U.S.NRC
United States Nuclear Regulatory Commission
Protecting People and the Environment

Technical Letter Report

TLR-RES/DE/CIB-2021-09

Reactor Pressure Vessel Fluence, DPA, and Uncertainty Quantification in Extended Beltline Locations

Date:

April 2021

Prepared in response to Tasks 5, 6, and 7 of User Need Request NRR-2015-002 by:

J. Risner
Oak Ridge National Laboratory

A. Alpan
Oak Ridge National Laboratory

NRC Project Manager:

Jay Wallace
Materials Engineer
Component Integrity Branch

Division of Engineering
Office of Nuclear Regulatory Research
U.S. Nuclear Regulatory Commission
Washington, DC 20555–0001

ORNL/SPR-2021/1988

Reactor Pressure Vessel Fluence, DPA, and Uncertainty Quantification in Extended Beltline Locations

Joel Risner
Arzu Alpan

April 2021

OAK RIDGE NATIONAL LABORATORY
MANAGED BY UT-BATTELLE FOR THE US DEPARTMENT OF ENERGY

ORNL/SPR-2021/1988

Nuclear Energy and Fuel Cycle Division

REACTOR PRESSURE VESSEL FLUENCE, DPA AND UNCERTAINTY QUANTIFICATION IN EXTENDED BELTLINE LOCATIONS

Joel Risner, Arzu Alpan

Date Published

April 2021

Prepared by
OAK RIDGE NATIONAL LABORATORY
Oak Ridge, TN 37831-6283
managed by
UT-BATTELLE, LLC
for the
US DEPARTMENT OF ENERGY
under contract DE-AC05-00OR2272

ABSTRACT

It has become increasingly challenging to accurately predict neutron fluence and displacements per atom (dpa) in reactor pressure vessels (RPVs) as plant life extensions and power uprates expand the area of concern, causing neutron damage to locations in the so-called *extended beltline region*. At this writing, the only available guidance on RPV fluence calculations is from analyses that only address the traditional beltline region. This study evaluated the impact of multiple physical parameters on fast fluence (E > 1 MeV) estimates to ascertain the degree to which extended beltline fluence evaluations are more sensitive to those parameters compared with traditional beltline evaluations. In addition, key calculational parameters in the widely used discrete ordinates method were evaluated to determine their impact on extended beltline fluence estimates. Hybrid radiation transport calculations, which employ the current state of the art in radiation transport simulations, were used as benchmark solutions in the absence of measured data in extended beltline locations. These hybrid calculations utilize continuous-energy Monte Carlo calculations and eliminate the discretizations in space, energy, and angle that impose accuracy limitations on discrete ordinates calculations. This report details the results of the physical and calculational parameter studies and provides insights into where modifications in analysis methodology may be necessary to obtain calculational uncertainty in the extended beltline region comparable to that specified for traditional beltline fluence analyses.

TABLE OF CONTENTS

LIST OF FIGURES

LIST OF TABLES

EXECUTIVE SUMMARY

Regulatory Guide (RG) 1.190, "Calculational and Dosimetry Methods for Determining Pressure Vessel Neutron Fluence," describes the application and qualification of a methodology acceptable to the U.S. Nuclear Regulatory Commission (NRC) for determining the best-estimate neutron fluence experienced by materials in the beltline region of light water reactor (LWR) reactor pressure vessels (RPVs). Although the beltline region is not explicitly defined in RG 1.190, NUREG/CR-1511, "Reactor Pressure Vessel Status Report," states that materials with a projected neutron fluence greater than 1.0×10^{17} neutrons per square centimeter (n/cm^2) at end of license experience sufficient neutron damage to be included in the beltline.

Subsequent to the issuance of RG 1.190, the continuing trend of plant life extension and power uprates for both pressurized water reactors (PWRs) and boiling water reactors (BWRs) has led to growing concern about lifetime fluence levels in materials outside the traditional beltline region and in the RPV internals. The regions of the RPV that lie outside the traditional beltline are referred to as the *extended beltline region*.

Although the fundamental radiation transport phenomena for fluence levels in the extended beltline region are the same as those for the traditional beltline region, the characteristics and limitations of the numerical methods used to solve the transport equation, as well as the different transport paths from the core to the reactor vessel, result in additional considerations when determining fluence outside the beltline region relative to calculations within the beltline region. In addition, calculation of other neutron responses of interest—including damage as measured by displacements per atom (dpa) and a variety of dosimetry reactions that serve as measured data for use in benchmarking transport methods—may be more sensitive to the selection of transport methods and parameters in the extended beltline.

Multigroup cross-section library sensitivity

One of the most significant areas of potential solution inaccuracy in discrete ordinates calculations is the use of multigroup (MG) cross-section libraries. With respect to RPV fluence calculations, this area is of particular concern for extended beltline regions where the neutron flux spectra may be significantly different from those used to generate an MG library. For instance, the flux weighting spectra that were used to develop the widely used BUGLE-B7 MG library are based on one-dimensional transport calculations at the core midplane of simplified PWR and BWR models.

The method chosen to evaluate MG libraries in this study uses hybrid Shift calculations. Because Shift can be run with either MG or continuous-energy (CE) cross-section data, these calculations provide a means of comparing various MG libraries with a more accurate CE solution. Various MG libraries were evaluated, including VITAMIN-B7 (199 neutron energy groups) and BUGLE-B7 (47 neutron groups), both of which were developed specifically for LWR shielding analyses. MG libraries from the SCALE code system containing from 200 to 1,597 neutron groups were evaluated. In addition, two libraries developed specifically to address neutron transport through energy ranges important for RPV flux and response calculations were also evaluated. All of these calculations were performed using the PWR model.

In addition to assessing the impact of MG libraries on fast fluence calculations in the extended beltline region, analyses were also performed to evaluate the ability of MG libraries to provide accurate calculation of neutron dpa rates and for nine dosimetry reaction rates that have been used in RPV fluence benchmark analyses. This set of 11 neutron responses (fast flux, dpa rate,

and dosimetry reaction rates) was used to assess the adequacy of MG libraries over a wide range of neutron energies. The results of these studies suggest that whereas the BUGLE-B7 library is generally adequate for the calculation of all these quantities at locations radially out through the inner portion of the RPV in the traditional beltline region, it is not well suited to the calculation of most of these 11 responses at locations in the extended beltline region.

The accuracy of MG solutions can be improved by using a very fine group structure. However, libraries with up to several hundred energy groups could increase the amount of computer memory required for cross-section storage by more than two orders of magnitude and would also lead to much longer run times. Therefore, MG solutions with very fine group libraries may not be practical for routine RPV analyses.

Recommendations for analysis methodology

Results from the analyses performed in this study suggest that the discretization of the energy variable in MG discrete ordinates transport calculations poses significant challenges for RPV fluence evaluations in the extended beltline region. The use of MG cross-section libraries—even with hundreds of energy groups—produced solutions that often underpredicted more accurate CE calculations in extended beltline locations, including the vessel supports in the PWR model. This underprediction is particularly noteworthy for calculation of dpa rates and of some dosimetry reaction rates.

Hybrid radiation transport methods provide a significant advantage in these analyses because the Monte Carlo calculations that are performed in the final stage of the hybrid calculational sequence are not subject to the approximations made in MG cross-section libraries.

ACKNOWLEDGMENTS

The work described in this report was sponsored by the U.S. Nuclear Regulatory Commission (NRC), Office of Nuclear Regulatory Research (RES). The authors thank Jay Wallace for his support and guidance as the NRC project manager. His insights, questions, and encouragement have been invaluable to the success of this project and report. A number of NRC staff contributed constructive comments on draft versions of this report, on earlier documents, and in public meetings held during the course of this project. Among those contributors, special thanks are due to Ben Parks, Nate Hudson, Dan Widrevitz, and Amrit Patel. The authors also thank Oak Ridge National Laboratory (ORNL) staff members Tara Pandya and Katherine Royston for their reviews of this work, and Rose Raney and Kathy Jones for final document preparation.

ABBREVIATIONS AND ACRONYMS

1D	one-dimensional
2D	two-dimensional
3D	three-dimensional
ADAMS	Agencywide Documents Access and Management System
ANS	American Nuclear Society
ANSI	American National Standards Institute
ASTM	American Society for Testing and Materials
B&W	Babcock and Wilcox
BAF	bottom of active fuel
BOL	beginning of life
BWR	boiling water reactor
CE	continuous energy
C/M	calculated-to-measured ratio
CPU	central processing unit
dpa	displacements per atom
DOM	the dominant axial zone in a GE14 BWR fuel assembly
DSA	diffusion synthetic acceleration
DTW	directional theta weighted
EFPY	effective full-power year
ENDF	Evaluated Nuclear Data File
EOL	end of life
EVND	ex-vessel neutron dosimetry
IAEA	International Atomic Energy Agency
IRDF	International Reactor Dosimetry File
LD	linear discontinuous
LWR	light water reactor
MCNP	Monte Carlo N-Particle
MG	multigroup
NAT	the natural U axial zone at the bottom of each rod in a GE14 BWR fuel assembly
NPP	nuclear power plant
NRC	United States Nuclear Regulatory Commission
N-T	the natural U axial zone at the top of each rod in a GE14 BWR fuel assembly
N-V	the natural uranium vanished rod axial zone in a GE14 BWR fuel assembly
ORNL	Oak Ridge National Laboratory
PNNL	Pacific Northwest National Laboratory
PCA	Pool Critical Assembly [Pressure Vessel Facility Benchmark]
PCR	partial-current rebalance
PDF	probability distribution function
PLE	the plenum axial zone in a GE14 BWR fuel assembly
PSZ	the power shaping axial zone in a GE14 BWR fuel assembly
PWR	pressurized water reactor
PWROG	PWR Owners Group
QR	quadruple range
RPV	reactor pressure vessel
RVI	reactor vessel internals
SC	step characteristic
SI	source iteration

SLR	subsequent license renewal
SPEO	subsequent period of extended operation
TAF	top of active fuel
TLD	trilinear discontinuous
TSA	transport synthetic acceleration
TW	theta weighted
Voxel	volume element
VAN	the vanished rod axial zone in a GE14 BWR fuel assembly
VF	void fraction
VR	variance reduction
WBN1	Watts Bar Nuclear Plant Unit 1
WDD	weighted diamond difference

1. INTRODUCTION

For the past several decades, the main region of concern for reactor pressure vessel (RPV) fluence calculations has been the portion of the RPV referred to as the *beltline region,* which can be defined [1] as "the region adjacent to the reactor core that must be evaluated to account for the effects of radiation on fracture toughness." With the continuing trend of plant life extension and power uprates for both pressurized water reactors (PWRs) and boiling water reactors (BWRs) throughout the United States, there is growing concern about lifetime fluence levels in regions above and below what has historically been considered the beltline region and in reactor vessel internals (RVI).

Regulatory Guide (RG) 1.190 [2] describes the application and qualification of a methodology acceptable to the U.S. Nuclear Regulatory Commission (NRC) for determining the best-estimate neutron fluence experienced by materials in the beltline region of light water reactor (LWR) RPVs. This methodology is also acceptable for determining the overall uncertainty associated with those best-estimate values. However, RG 1.190 does not specifically define the beltline region.

In Title 10 of the Code of Federal Regulations (CFR) Part 50 [3], Section II of Appendix G defines the beltline region as "The region of the reactor vessel (shell material including welds, heat affected zones, and plates or forgings) that directly surrounds the effective height of the active core and adjacent regions of the reactor vessel that are predicted to experience sufficient radiation damage to be considered in the selection of the most limiting material with regard to radiation damage." 10 CFR Part 50, Section III of Appendix H [3] requires that reactor vessels for which the peak neutron fluence at the end of the design life of the vessel exceeds 10^{17} cm^{-2} (E > 1 MeV) must have their beltline materials monitored by a surveillance program complying with American Society for Testing and Materials (ASTM) E185-82 [4], as modified by Appendix H.

Section 2.3 of NUREG/CR-1511 [5] states that "The NRC staff considered materials with a projected neutron fluence of greater than 1.0E17 neutrons per square centimeter (n/cm^2) at end of license to experience sufficient neutron damage to be included in the beltline."

An International Atomic Energy Agency (IAEA) Nuclear Energy Series report on the integrity of RPVs in nuclear power plants (NPPs) [6] refers to the beltline as "the region of shell material directly surrounding the effective height of the fuel element assemblies, plus an additional volume of shell material both below and above the active core, with an [end-of-life] fluence of more than 10^{21} m^{-2} (E > 1 MeV) (10^{17} cm^{-2})." This definition is consistent with that given in NUREG/CR-1511.

Chapter 12 of *Nuclear Power – Control, Reliability, and Human Factors* [7] states that typical end-of-life design neutron fluences are on the order of 10^{18} n/cm^2 for BWRs and on the order of 10^{19} n/cm^2 for PWRs. Values of 4×10^{18} n/cm^2 for BWRs, 4×10^{19} n/cm^2 for Westinghouse PWRs, and 1.2×10^{19} n/cm^2 for Babcock and Wilcox (B&W) PWRs are provided in the IAEA assessment [6]. The PWR fluence values are noted as corresponding to a lifetime of 32 effective full-power years (EFPYs). Lifetime is not noted for BWRs.

In the context of the current report, the portion of the RPV where the end-of license fluence would be expected to exceed 10^{17} n/cm^2 for plant operations consistent with those in the original

operating license is referred to as the *traditional beltline region*, or simply the *beltline region*. Locations above and below the traditional beltline region are referred to as the *extended beltline region*.

While the fundamental radiation transport phenomena for fluence levels in the extended beltline region are the same as those for the traditional beltline region, the characteristics and limitations of the numerical methods used to solve the transport equation, as well as the different transport paths from the core to the reactor vessel, result in additional considerations for the determination of fluence outside the beltline region relative to calculations within the beltline region.

A previous report [8] addressed sensitivities due to physical parameters and the selection of angular quadrature for discrete ordinates transport calculations using the Denovo code [9]. The analyses in this report are based on the reference PWR and BWR models described in [8].

2. DPA CONSIDERATIONS

While RG 1.190 is primarily directed toward calculations and measurement procedures for RPV fluence, the procedures it establishes are also applicable to analyses of displacements per atom (dpa). Calculation of dpa is somewhat more complex than calculation of fast fluence, as knowledge of the total neutron fluence and flux spectrum is required [10].

For calculations of fast fluence and dpa in extended beltline regions, the following issues must be considered:

1. The relationship between dpa rates and fast flux in the RPV varies as a function of location. This suggests that using fast fluence as a surrogate for dpa may have limitations with respect to locations in the RPV.
2. The rates of attenuation for fast flux and dpa rates change due to elevation and, to a lesser extent, the azimuthal location in the RPV. At elevations sufficiently far above or below the active fuel, the maximum values of the fast flux and dpa rate can occur at the outer edge of the RPV due to cavity streaming effects.
3. While the effects of gamma-induced dpa are known to be much less than the effects of neutron dpa in the traditional beltline region, it may be possible for gamma dpa effects to become important contributors at locations within vessel support structures [11].

2.1 Relationship between dpa and fast neutron fluence in the PWR and BWR models

Because the dpa cross section is a function of neutron energy, the relationship between dpa and fast fluence is inherently nonlinear. This nonlinearity can become problematic if fast neutron fluence is used as a surrogate for dpa in regions where the ratio of dpa to fast fluence deviates significantly from the ratio within the traditional beltline region.

In considering this effect, the fast flux and dpa rates are examined herein, as well as the ratio of the dpa rate to the fast flux at selected locations in the reference PWR and BWR models [8]. Calculations of fast flux and dpa rates in both models were performed using the pseudo-BOL sources described in Section 5.1 of [8]. All calculations were run using the Shift [12] Monte Carlo code with continuous energy (CE) cross-section data. The FW-CADIS hybrid methodology was used for variance reduction. More details of Shift and hybrid radiation transport calculations can be found in [8].

Much of the data analysis in this report is based on interpretation of mesh tally plots that provide information on the model geometry and the solution (or ratio of solutions in parameter studies) being plotted. Examples of mesh tally plots are provided in APPENDIX A. Examination of those plots will aid in understanding the features of the 2D data plots throughout Sections 2, 3, and 4.

2.1.1 PWR model

The fast (E > 1 MeV) neutron flux and total neutron dpa rate (i.e., the dpa rate integrated over all neutron energies) at the core midplane in the PWR model are shown in Figure 2-1 and Figure 2-2. In Figure 2-1 and all other 2D fast flux plots in Section 2, flooded contours are used for the flux in the RPV, vessel supports, and nozzles, while contour lines only are used in other materials (e.g., downcomer water, the cavity gap, and the bioshield). In Figure 2-2 and all other 2D dpa rate plots in Section 2, flooded contours are used for the dpa rate in the RPV, vessel supports, and nozzles.

No contour lines are present in any material other than the carbon steel, as dpa rates based on the dpa cross section data in [10] are valid only in carbon steel.

Based on these figures, it is immediately obvious that the relationship between fast fluence and dpa is not linear, as the variation (based on the ratio of the maximum to minimum flux or dpa rates in the RPV) is ~37 for the fast flux and ~16 for the dpa rate. This tendency of the dpa rate to attenuate less rapidly than the fast flux in the traditional beltline region has been shown in previous studies [13], [14].

The slower attenuation of the dpa rate is due to the contribution of neutrons with energies below 1 MeV. As neutrons penetrate into the RPV, their energies rapidly decrease due to scattering. Figure 2-3 illustrates the attenuation of the neutron flux as a function of energy through the RPV in a 1D representation of the PWR model. In this 1D model, which has no azimuthal variation (unlike the 3D model results in Figure 2-1), the flux for neutron energies greater than 1.0026 MeV decreases by nearly a factor of 20 in the RPV. Neutrons with energies between 111.09 keV and 1.0026 MeV enter the RPV with nearly the same magnitude as the fast (E > 1.0026 MeV) flux.[1] There is an initial increase in the flux of neutrons with energies from 111.09 keV to 1.0026 MeV, as fast neutrons are scattered to lower energies. The increase is followed by a gradual decrease, with a reduction of only about a factor of 2 between the inner and outer surfaces of the RPV.

The increasing contribution of neutrons with energy less than 1 MeV to the total dpa rate is also seen in Figure 2-4, where neutrons with energies greater than 1 MeV are responsible for ~70% of the total dpa rate near the inner radius of the RPV, but only 20–25% at the outer surface of the RPV.

The net result of these effects is an increase of more than a factor of two in the ratio of the dpa rate to the fast flux, as shown in Figure 2-5.

At the elevation of the vessel supports, significant differences occur in the relationship between the fast flux and the dpa rate. This behavior is illustrated in Figure 2-6 through Figure 2-9. As shown in Figure 2-8, the fraction of the dpa rate due to neutrons with energies greater than 1 MeV decreases from a peak value of 56.1% at the inner surface of the RPV to minimum values of 4.4% in the outer portion of the RPV and to values as low as 2.2% in the nozzle supports. Because of this significant increase in the contribution of neutrons with energies below 1 MeV to the dpa rate, the ratio of the dpa rate to the fast flux increases by more than an order of magnitude for locations in the nozzle supports (Figure 2-9).

Figure 2-10 through Figure 2-13 provide additional insights into the behavior of the fast flux and dpa rates in the PWR RPV. In Figure 2-10, the dpa rate displays an exponential attenuation with an attenuation coefficient of -0.23/inch. This value is nearly identical to the attenuation coefficient of -0.24/inch in Regulatory Guide (RG) 1.99, Eq. (3) [15]. The fast flux experiences a more rapid attenuation rate, confirming that the use of the dpa-based attenuation presented in RG 1.99 is conservative for use with fast fluence levels through the RPV in the traditional beltline region. Figure 2-10 also shows the trend of neutrons with energies less than 1 MeV becoming the dominant contributors to the total dpa rate at increasing distances through the RPV.

At an elevation of approximately 10 cm above the top of the fuel (Figure 2-11), the general characteristics of the fast flux and dpa rate are similar to those at the core midplane, but the rates

[1] The energy boundaries used in the 1D model are based on multigroup boundaries to facilitate comparison of the 1D Monte Carlo results with 1D discrete ordinates calculations.

of attenuation of the fast flux and total dpa rate have decreased slightly. At an elevation of approximately 50 cm above the top of the fuel (Figure 2-12), the fast flux and dpa rate profiles cannot be reasonably represented by a simple exponential attenuation through the full depth of the RPV. At an elevation of 470 cm (Figure 2-13), the concept of an exponential attenuation of the dpa rate is completely meaningless. Figure 2-13 also demonstrates that the dpa rate profile reverses (i.e., has a peak level on the outer surface of the RPV) sooner than the fast flux profile.

If the uniform power distribution used in this parameter study were realistic, then the peak neutron fluence in the vessel supports (Figure 2-6) for 80 years of operation with a capacity factor of 90% would be approximately 1.25×10^{17}, and the peak dpa value (Figure 2-7) would be approximately 9.7×10^{-4} dpa. The significance of these values lies in their relationship to the scope of ASTM E1035-18 [11], which is applicable to all PWRs with vessel supports that will experience a lifetime fluence (E > 1 MeV) exceeding 1×10^{17} n/cm^2, or a lifetime dpa exceeding 3.0×10^{-4} dpa. Based on the results of the calculations presented in this section, it is clear that the limiting dpa value from [11] may be more restrictive than the limiting fluence value for neutron exposure considerations in vessel supports.

2.1.2 BWR model

The fast neutron flux and total neutron dpa rate at the core midplane in the BWR model are shown in Figure 2-14 and Figure 2-15. As with the PWR model results in the preceding subsection, there is less attenuation of the dpa rate through the RPV relative to the attenuation of the fast flux. However, the differences in these two quantities (based on the ratio of the maximum-to-minimum values in the RPV) is less pronounced than in the PWR model. This behavior is consistent with the differences in the thicknesses of the RPVs: 22 cm for the PWR model and 14.9 cm for the BWR model. Because the BWR RPV thickness is significantly less than the PWR RPV thickness, there is less overall attenuation through the BWR RPV. In addition, there is less impact from changes in the neutron energy spectrum through the thickness of the BWR RPV. This can be seen in Figure 2-16. The fraction of the dpa rate due to neutrons with energies greater than 1 MeV decreases by a factor of ~1.7, whereas the same fraction at the core midplane of the PWR model decreases by a factor of ~3.6 (Figure 2-4). Similarly, the ratio of the total dpa rate to the fast flux in the PWR RPV at the core midplane increases by a factor of ~2.6 (Figure 2-5), whereas the corresponding ratio in the BWR RPV increases by a factor of ~1.4 (Figure 2-17).

Similar trends can be seen in the extended beltline regions of the PWR model (Figure 2-6 through Figure 2-9) and the BWR model (Figure 2-18 through Figure 2-21). In particular, the variation in the ratio of the dpa rate to the fast flux in the BWR extended beltline location (Figure 2-21) is ~3.5, whereas in the extended beltline region of the PWR model (Figure 2-9), the variation in that ratio is nearly a factor of 14.

In summary, there is significantly less variation in the relationship between fast flux and dpa in the BWR model compared to the PWR model. Thus, the question of whether fast flux is an acceptable surrogate for dpa rate in RPVs, nozzles, and vessel supports may be a concern primarily for PWR neutron exposure analyses.

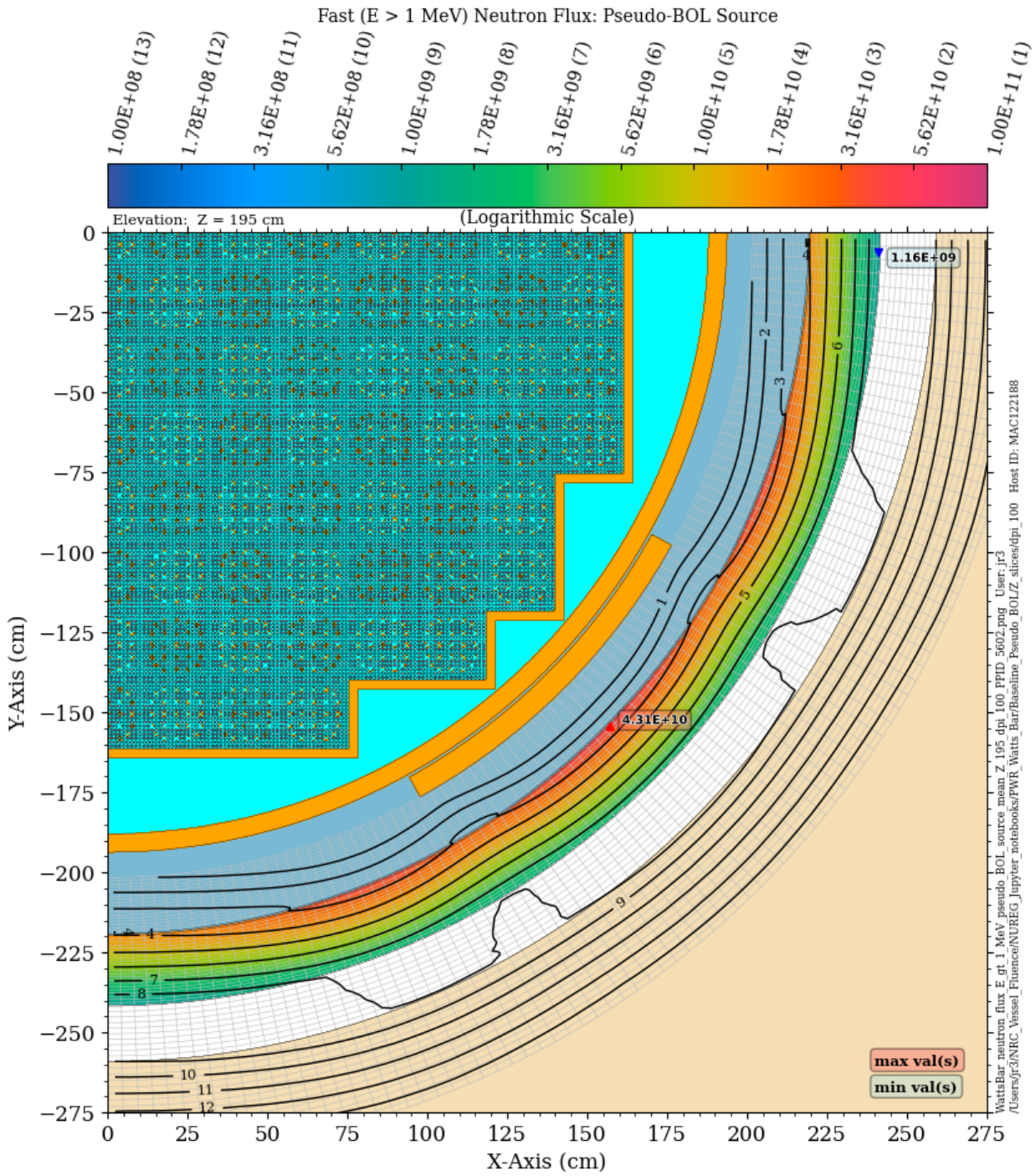

Figure 2-1 Fast neutron flux in the PWR model at the core midplane: pseudo-BOL source

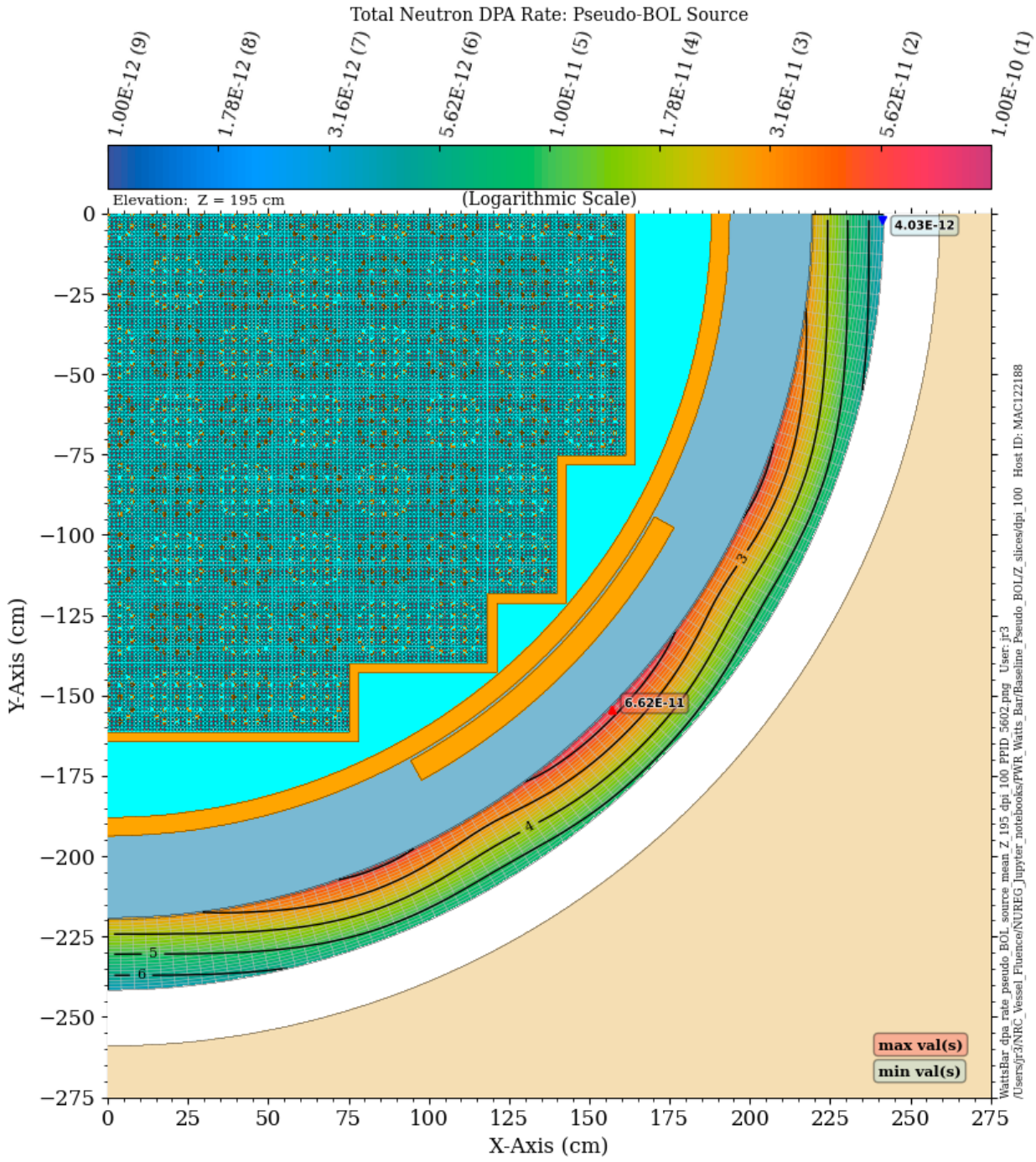

Figure 2-2 Total neutron dpa rate in the PWR model at the core midplane: pseudo-BOL source

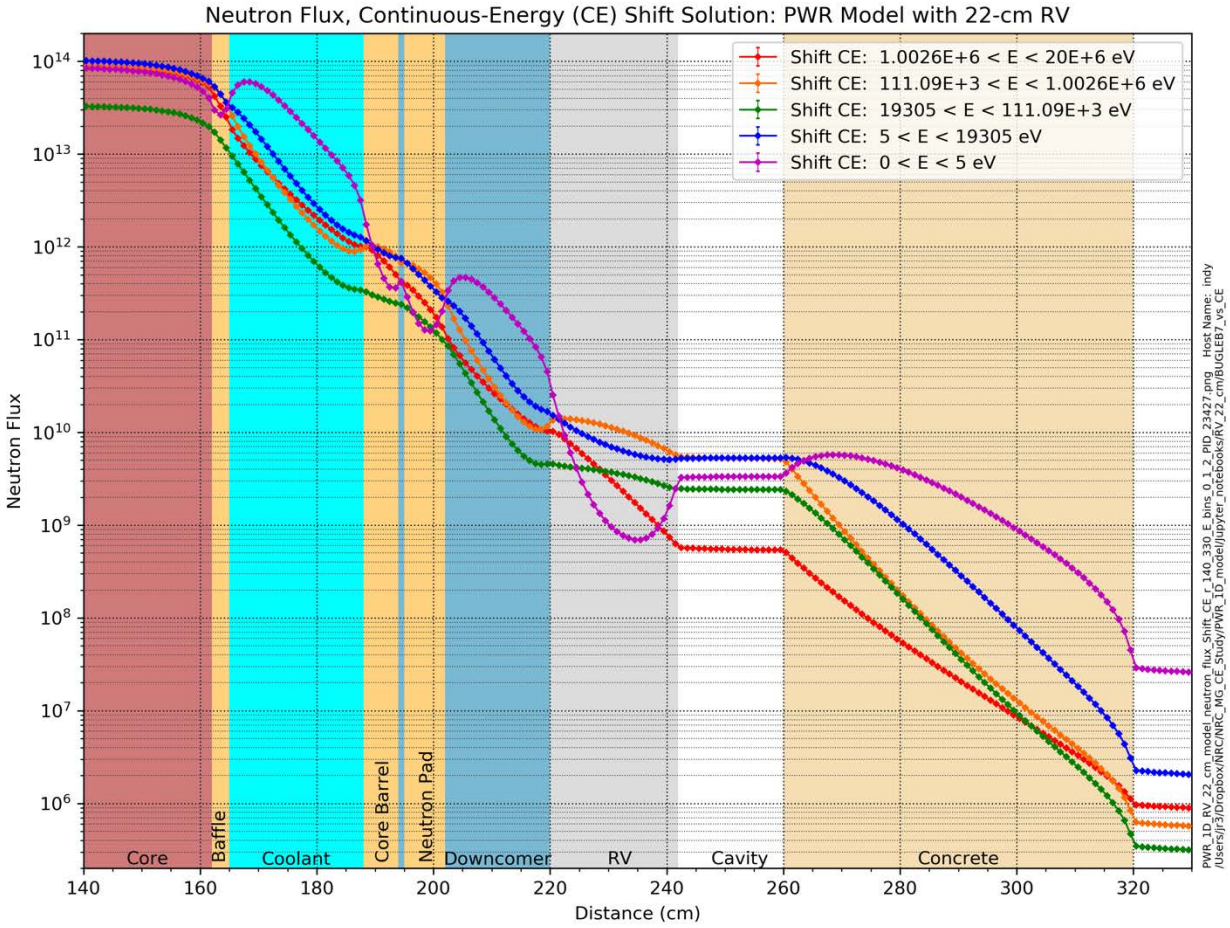

Figure 2-3 Neutron flux traverses for five energy ranges through a 1D mockup of the PWR reference model

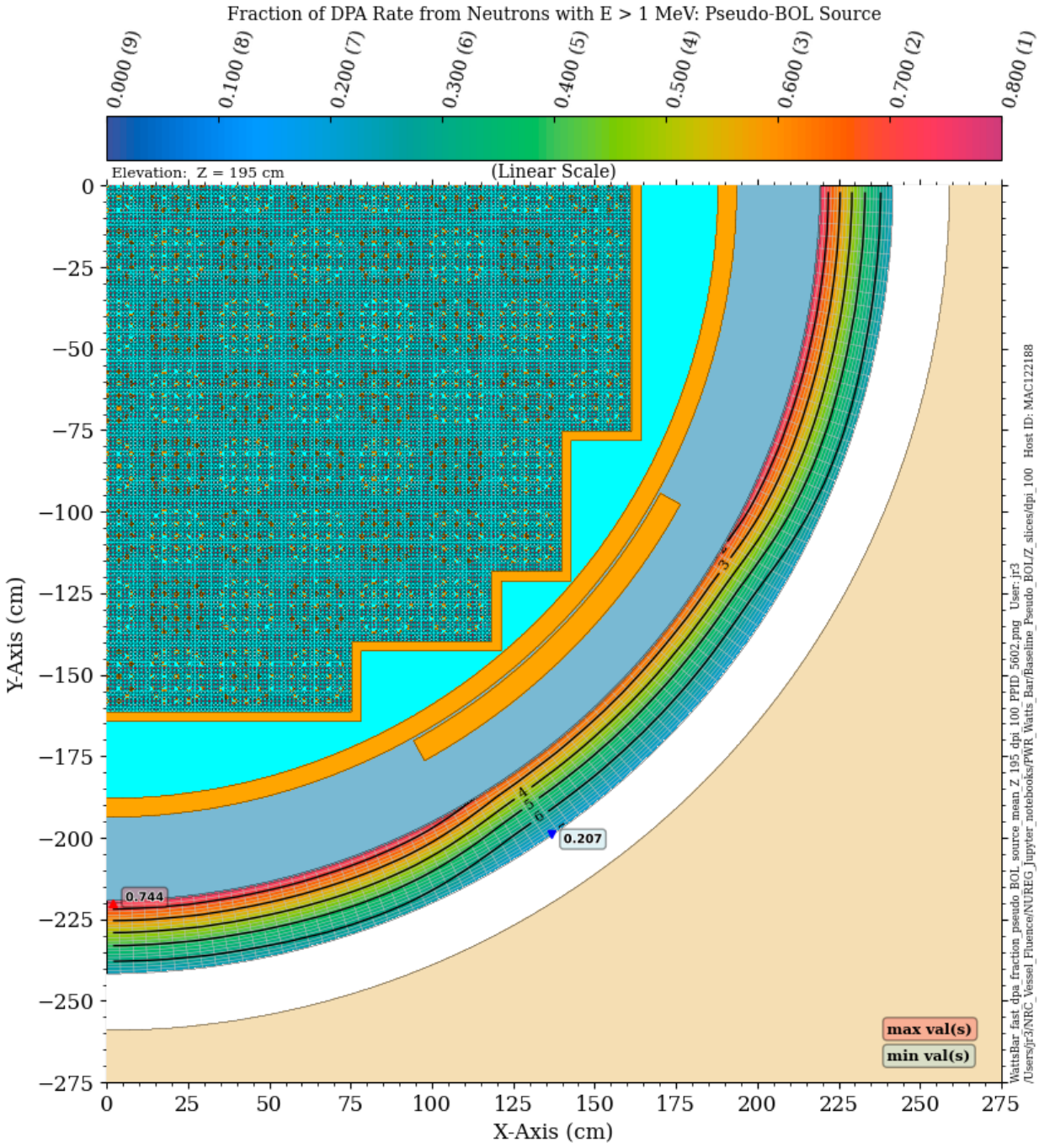

Figure 2-4 Fraction of the total neutron dpa rate due to neutrons with energy > 1 MeV in the PWR RPV. Plan view at the core midplane

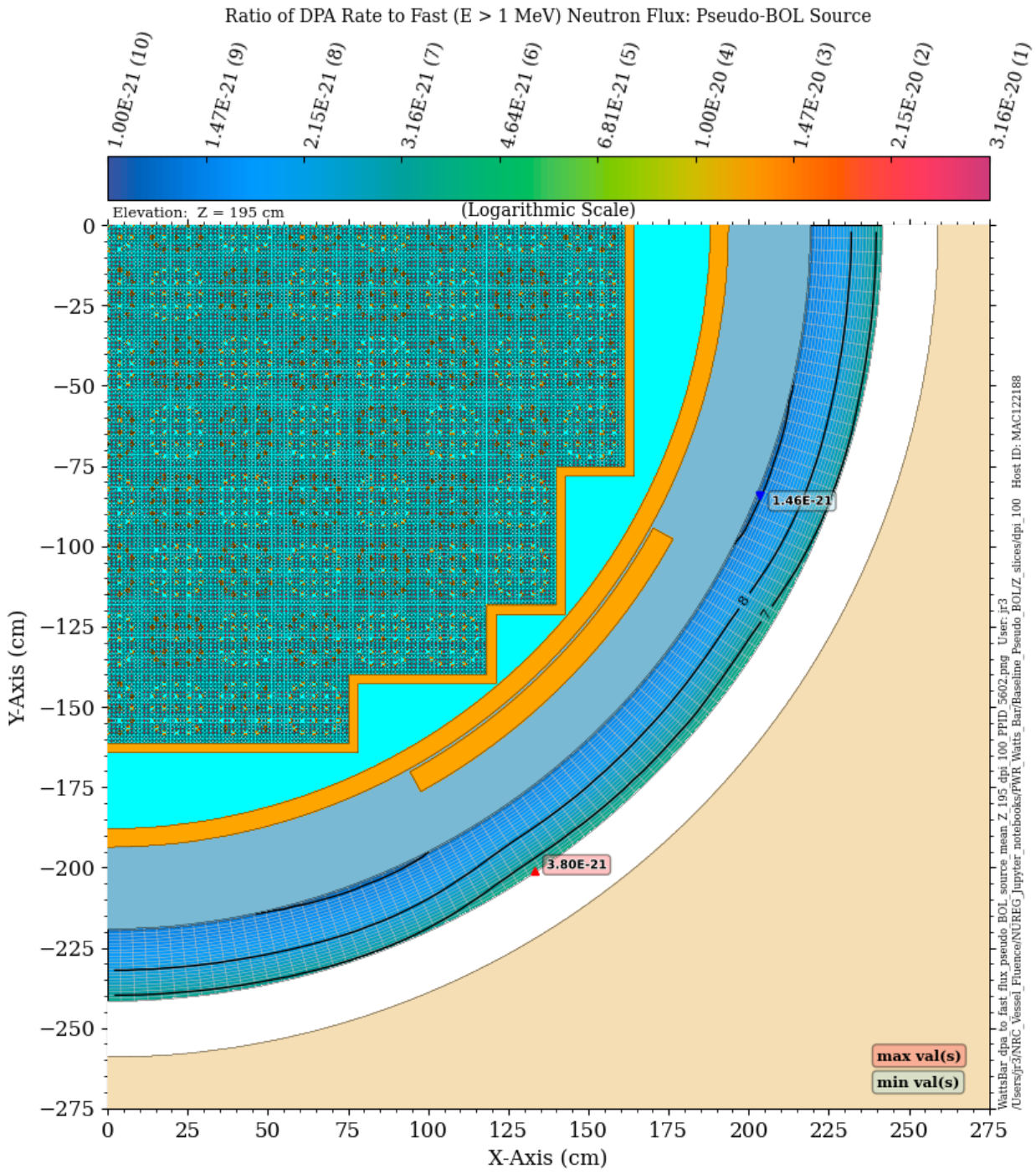

Figure 2-5 Ratio of the total neutron dpa rate to the fast (E > 1 MeV) neutron flux in the PWR RPV. Plan view at the core midplane

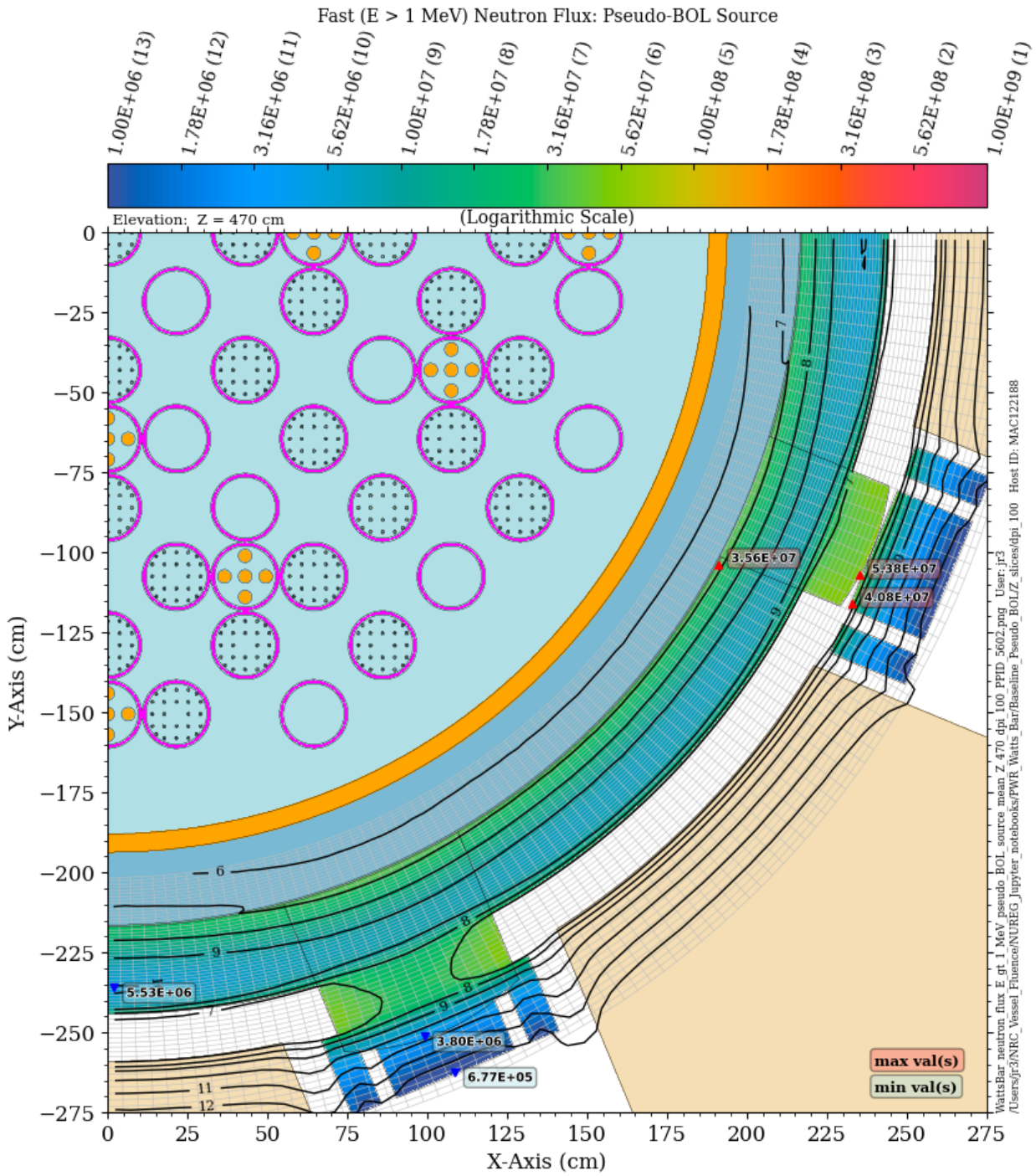

Figure 2-6 Fast neutron flux in the baseline PWR model at an elevation of Z = 470 cm

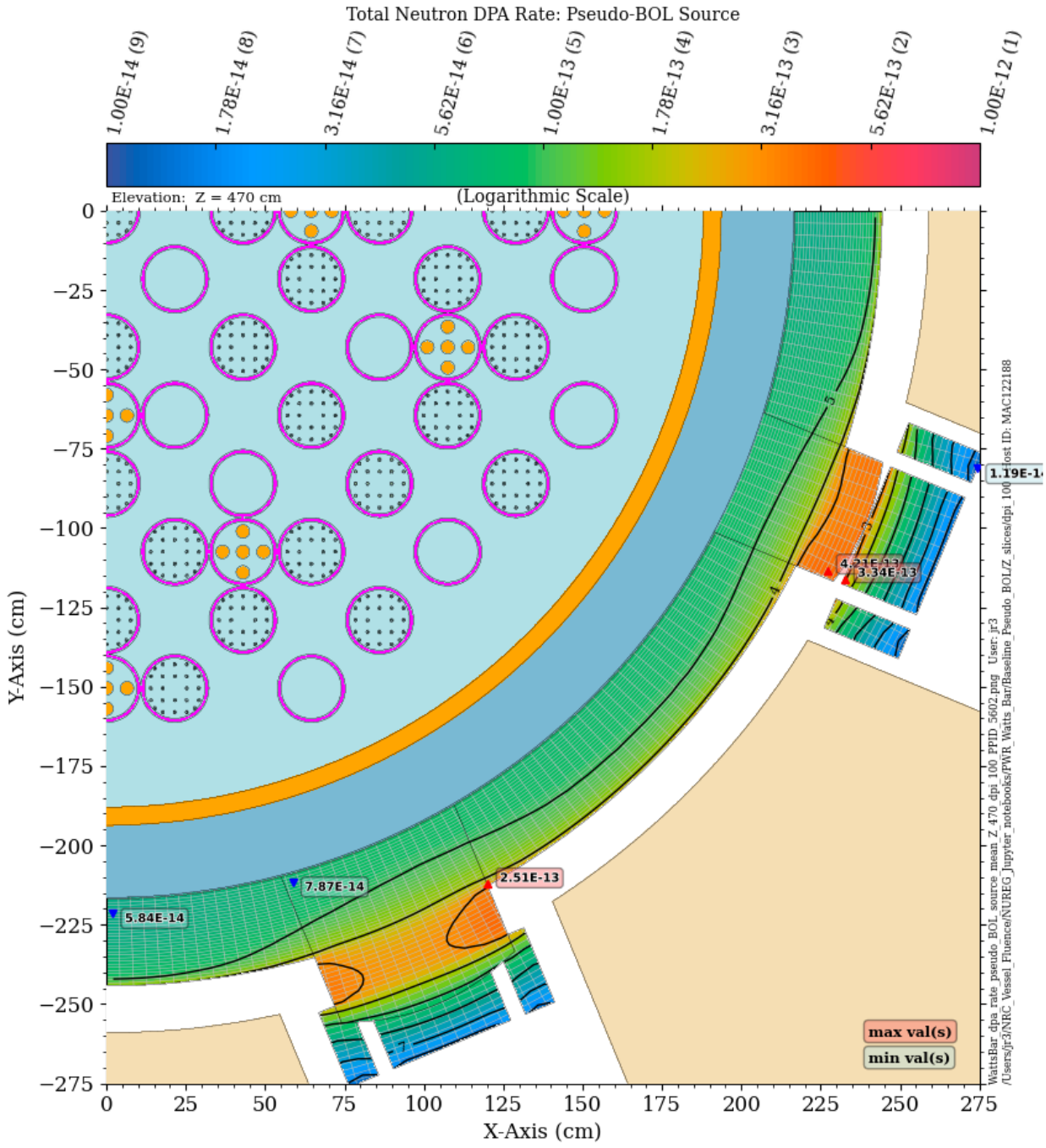

Figure 2-7 Total neutron dpa rate in the PWR RPV and vessel supports. Plan view at an elevation of 470 cm

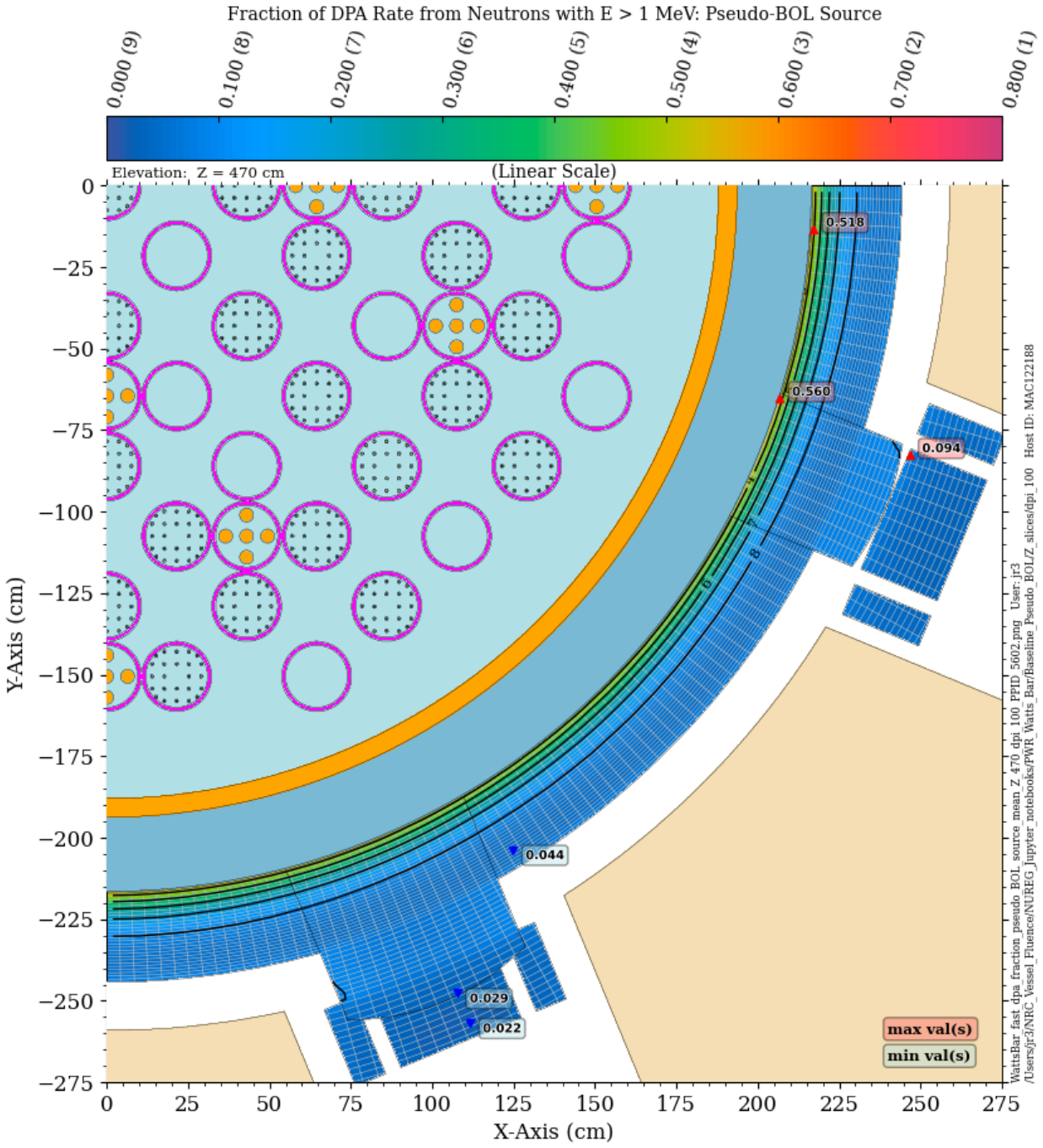

Figure 2-8 Fraction of the total neutron dpa rate due to neutrons with energy > 1 MeV in the PWR RPV, nozzles, and vessel supports. Plan view at an elevation of 470 cm

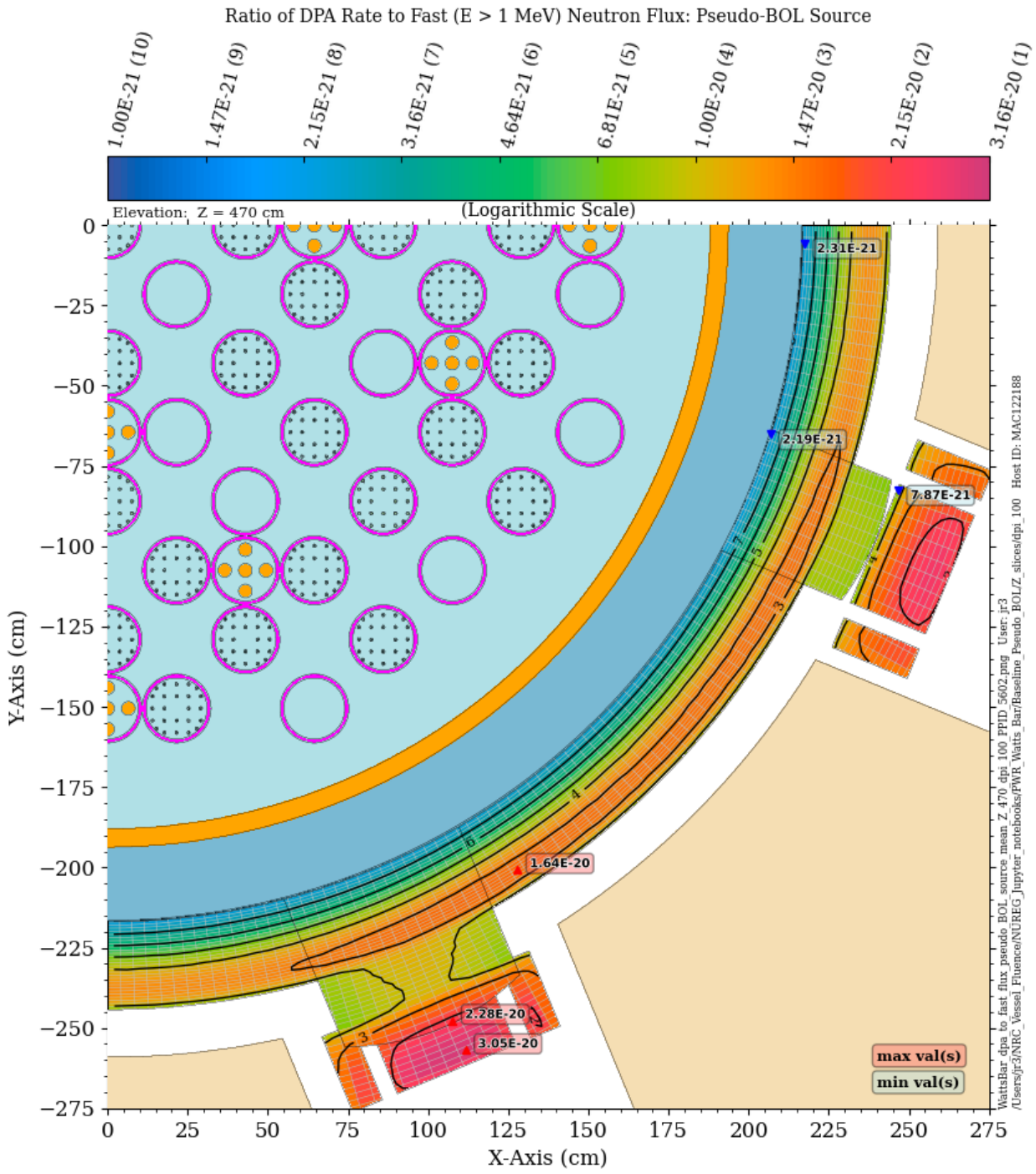

Figure 2-9 Ratio of the total neutron dpa rate to the fast (E > 1 MeV) neutron flux in the PWR RPV, nozzles, and vessel supports. Plan view at an elevation of 470 cm

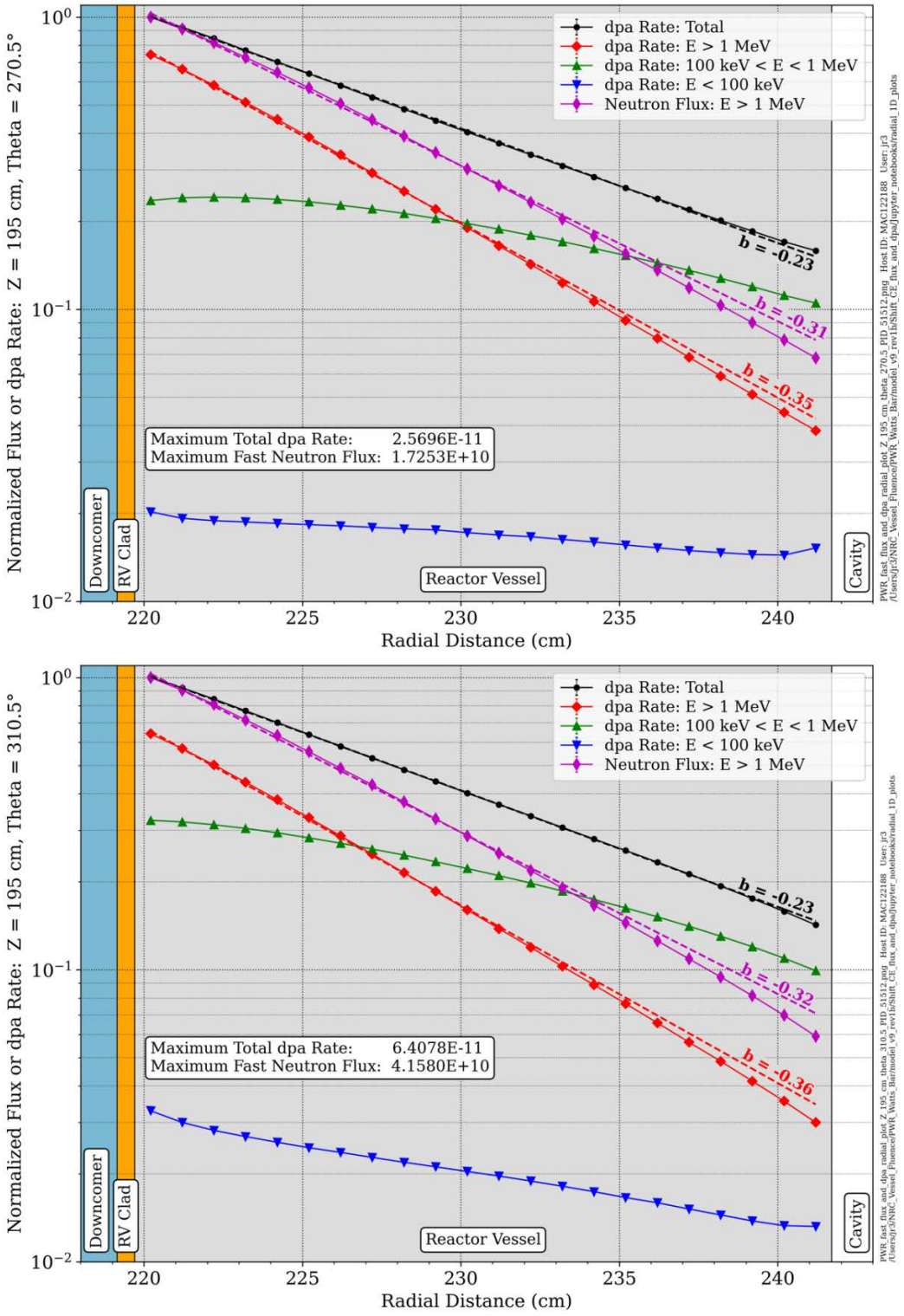

Figure 2-10 Normalized radial fast flux and dpa rate profiles in the PWR RPV at the core midplane. The dashed lines are exponential fits of the form e^{-bx}, where x is the depth in the RPV in inches. The profiles are normalized to the flux and dpa rates at the RPV inner diameter at each azimuthal location

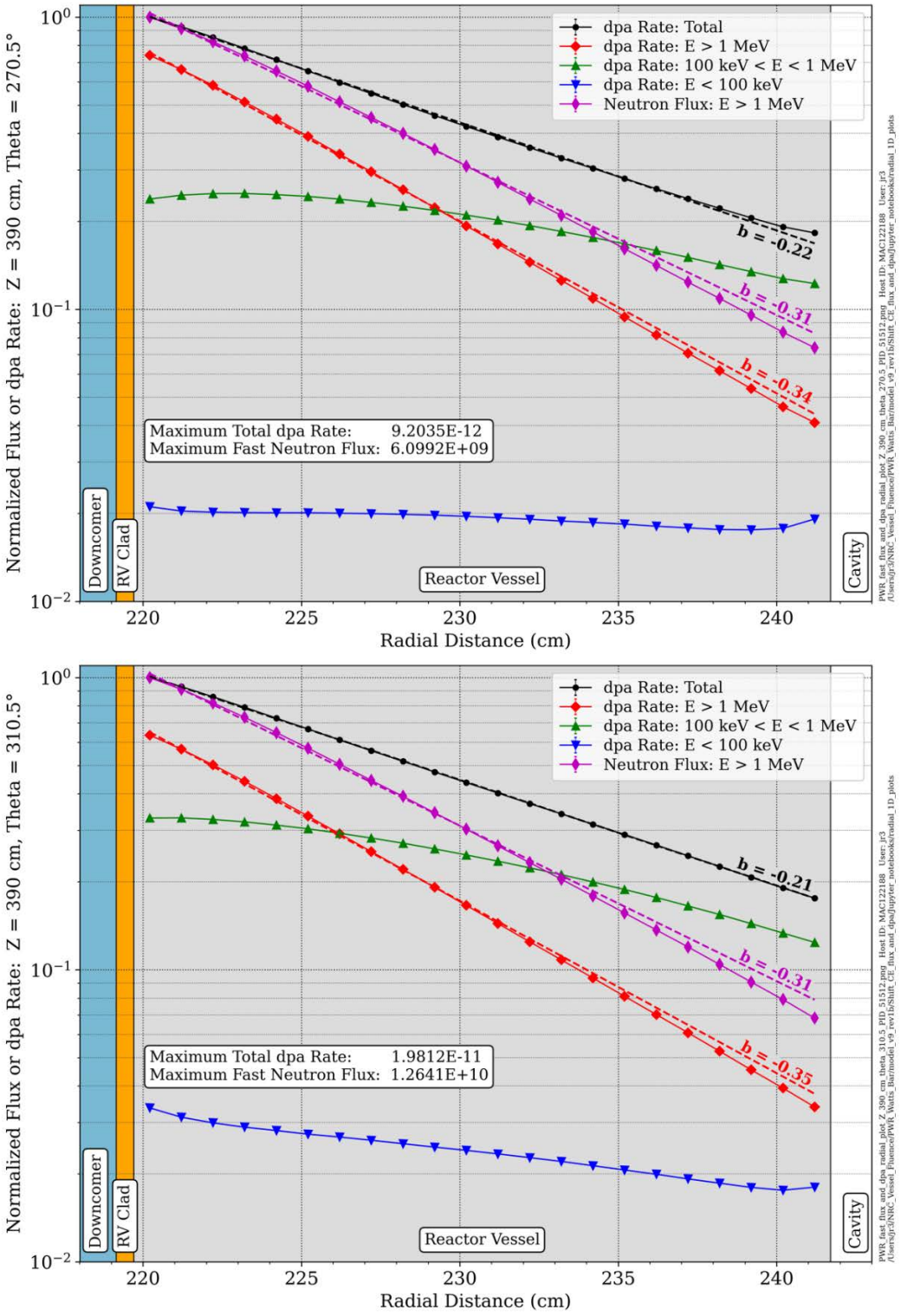

Figure 2-11 Normalized radial fast flux and dpa rate profiles in the PWR RPV at an elevation of 390 cm. The dashed lines are exponential fits of the form e^{-bx}, where x is the depth in the RPV in inches. The profiles are normalized to the flux and dpa rates at the RPV inner diameter at each azimuthal location

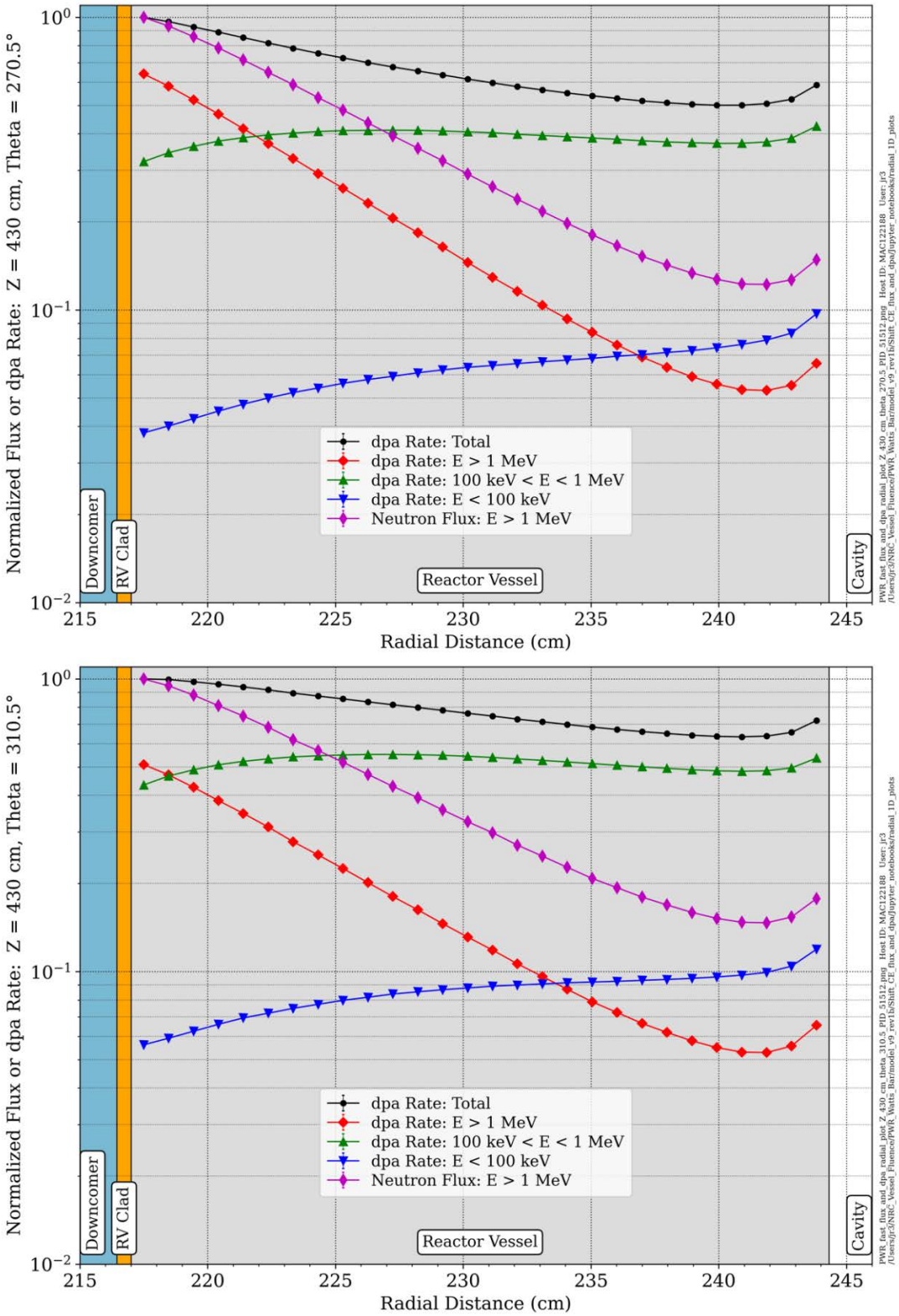

Figure 2-12 Normalized radial fast flux and dpa rate profiles in the PWR RPV at an elevation of 430 cm. The profiles are normalized to the flux and dpa rates at the RPV inner diameter at each azimuthal location

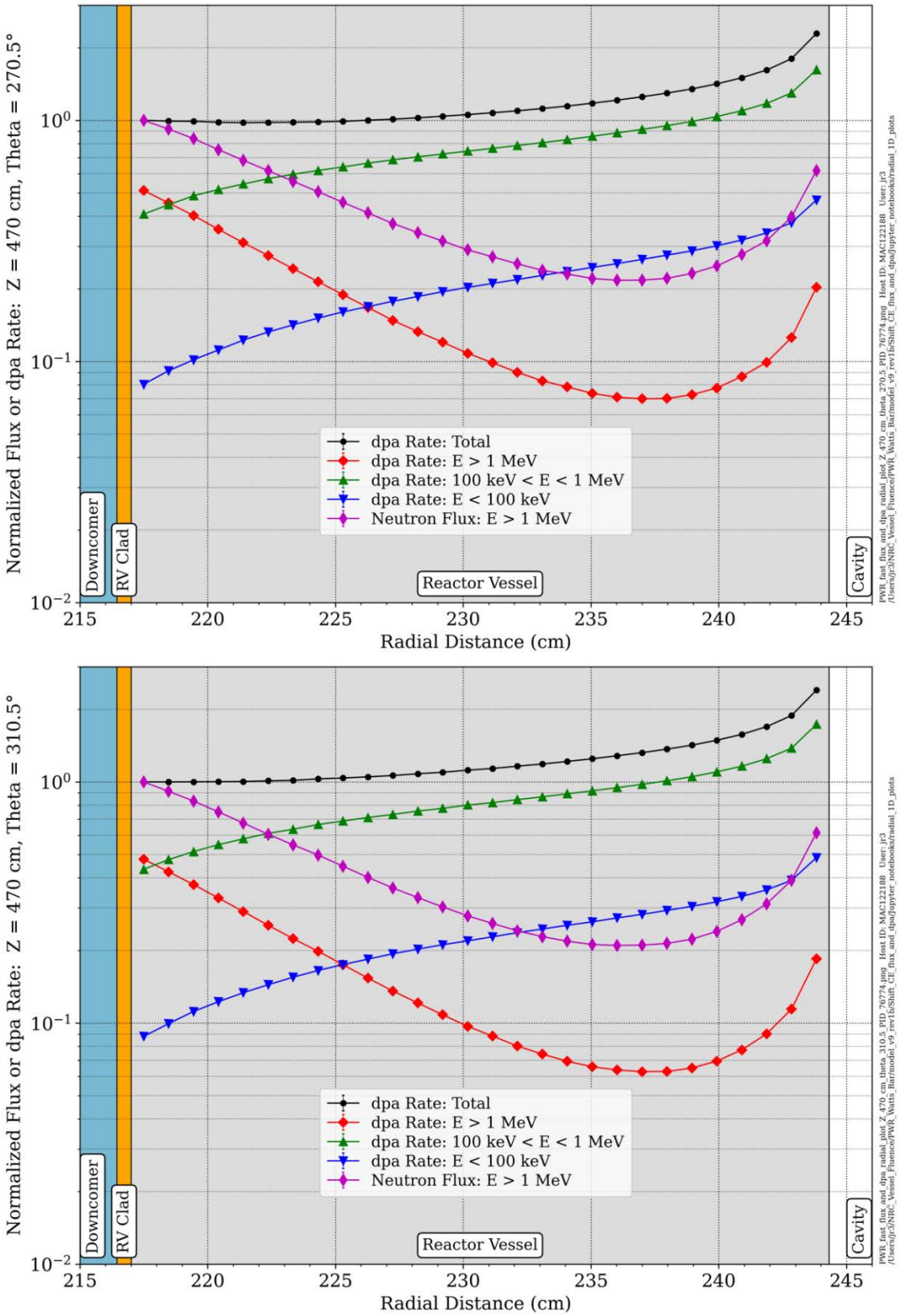

Figure 2-13 Normalized radial fast flux and dpa rate profiles in the PWR RPV at an elevation of 470 cm. The profiles are normalized to the flux and dpa rates at the RPV inner diameter at each azimuthal location

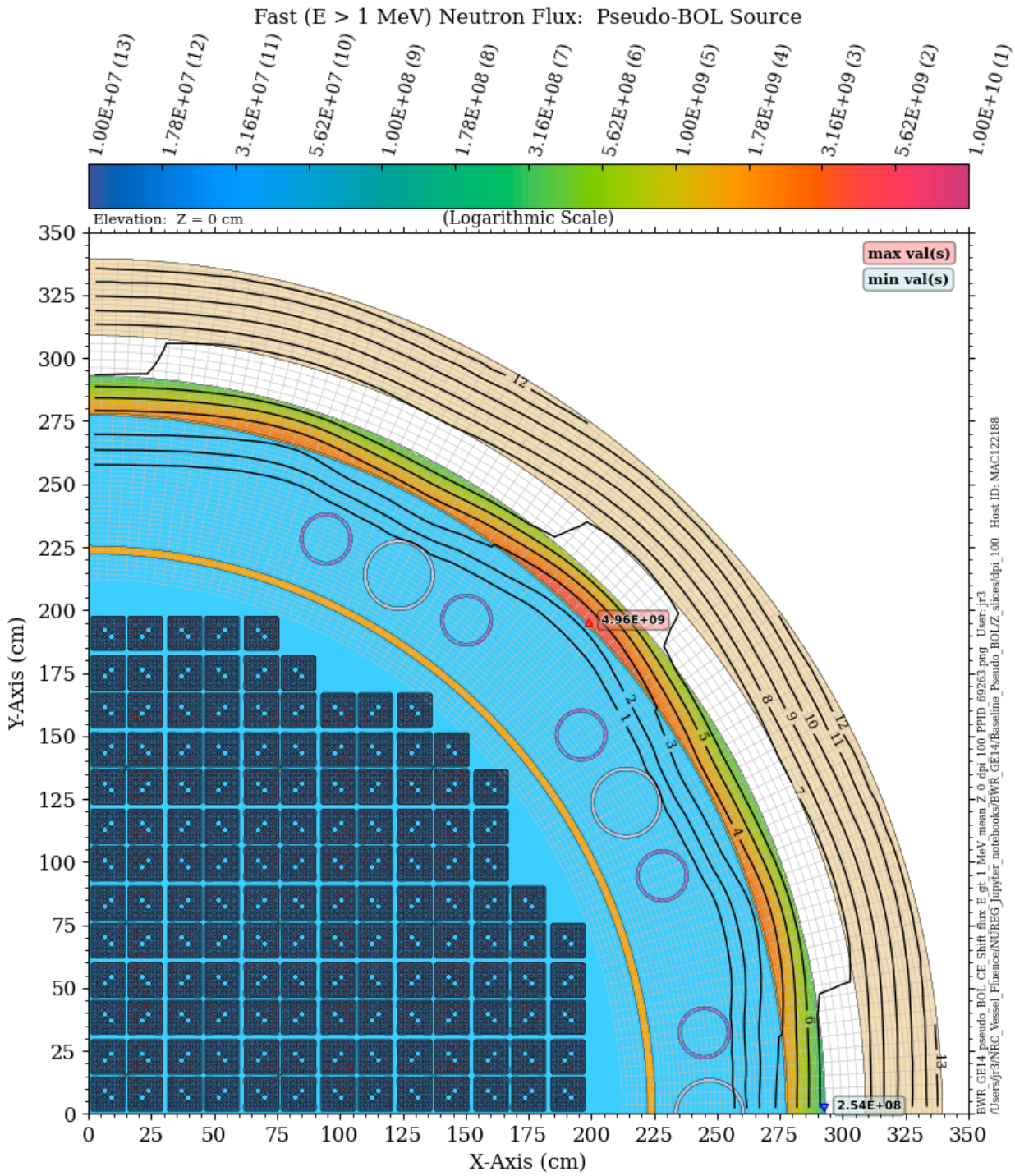

Figure 2-14 Fast neutron flux in the BWR model at the core midplane: pseudo-BOL source

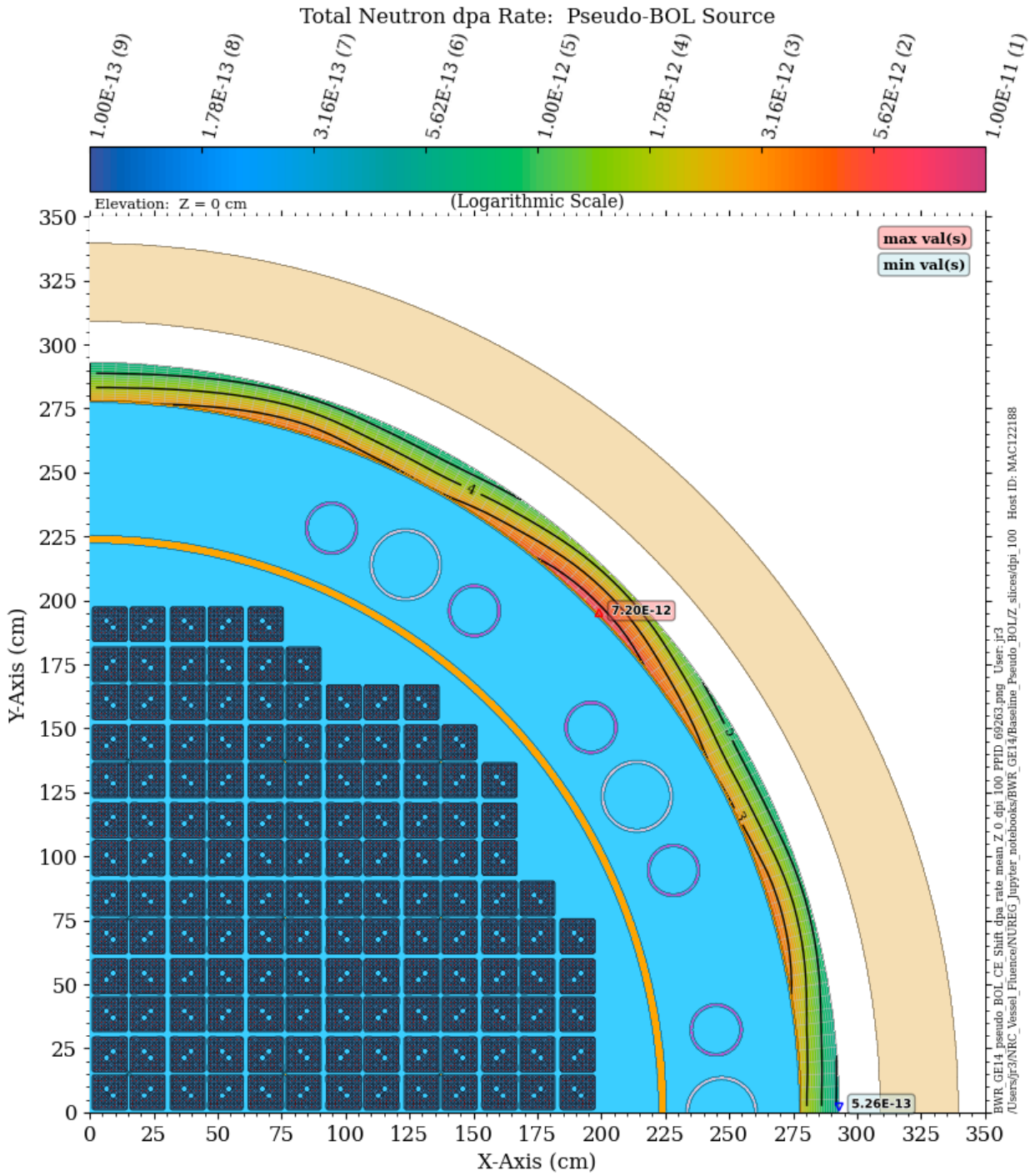

Figure 2-15 Total neutron dpa rate in the BWR model at the core midplane: pseudo-BOL source

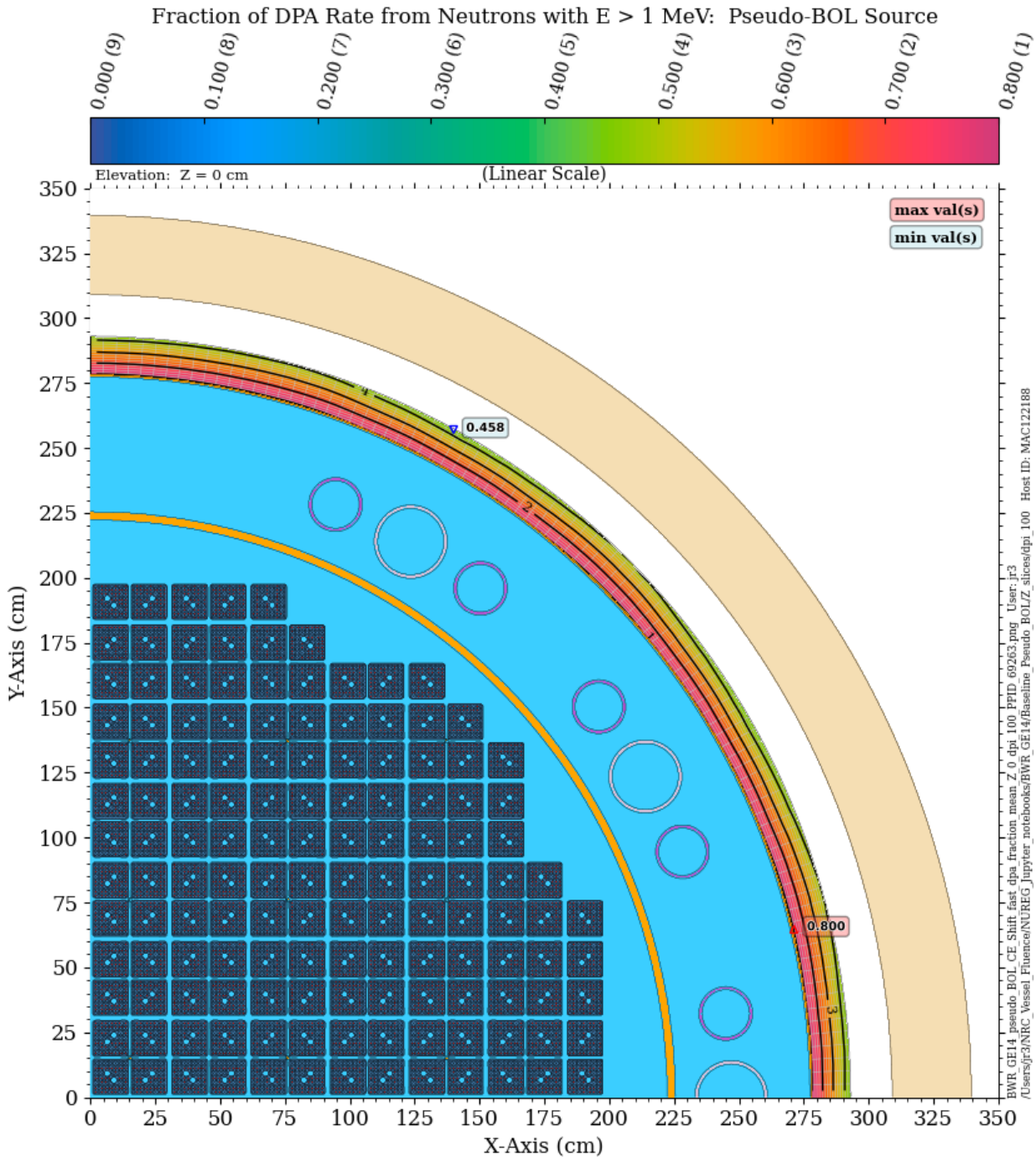

Figure 2-16 Fraction of the total neutron dpa rate due to neutrons with energy >1 MeV in the BWR at the core midplane: pseudo-BOL source

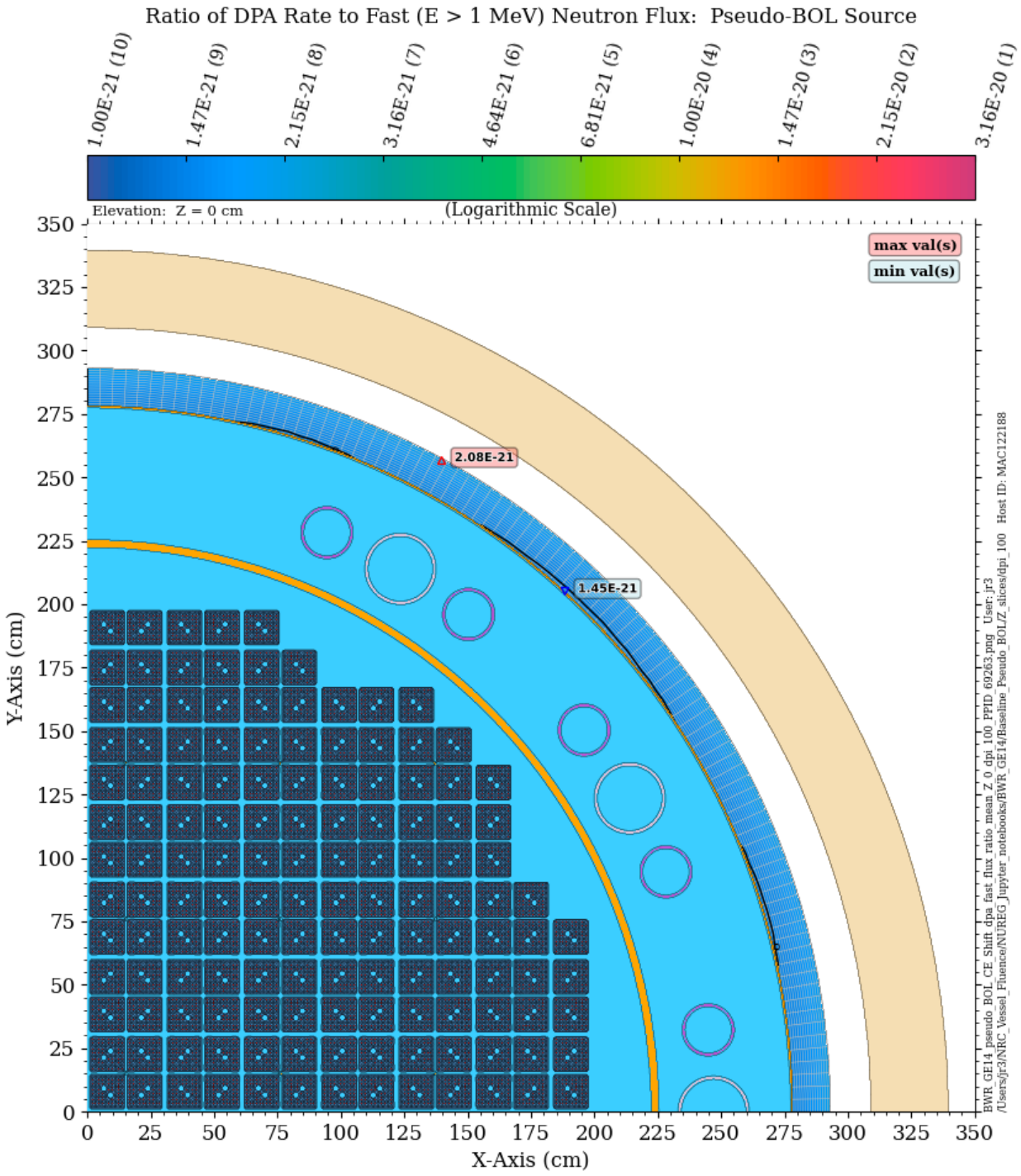

Figure 2-17 Ratio of the total neutron dpa rate to the fast (E > 1 MeV) neutron flux in the BWR RPV at the core midplane: pseudo-BOL source

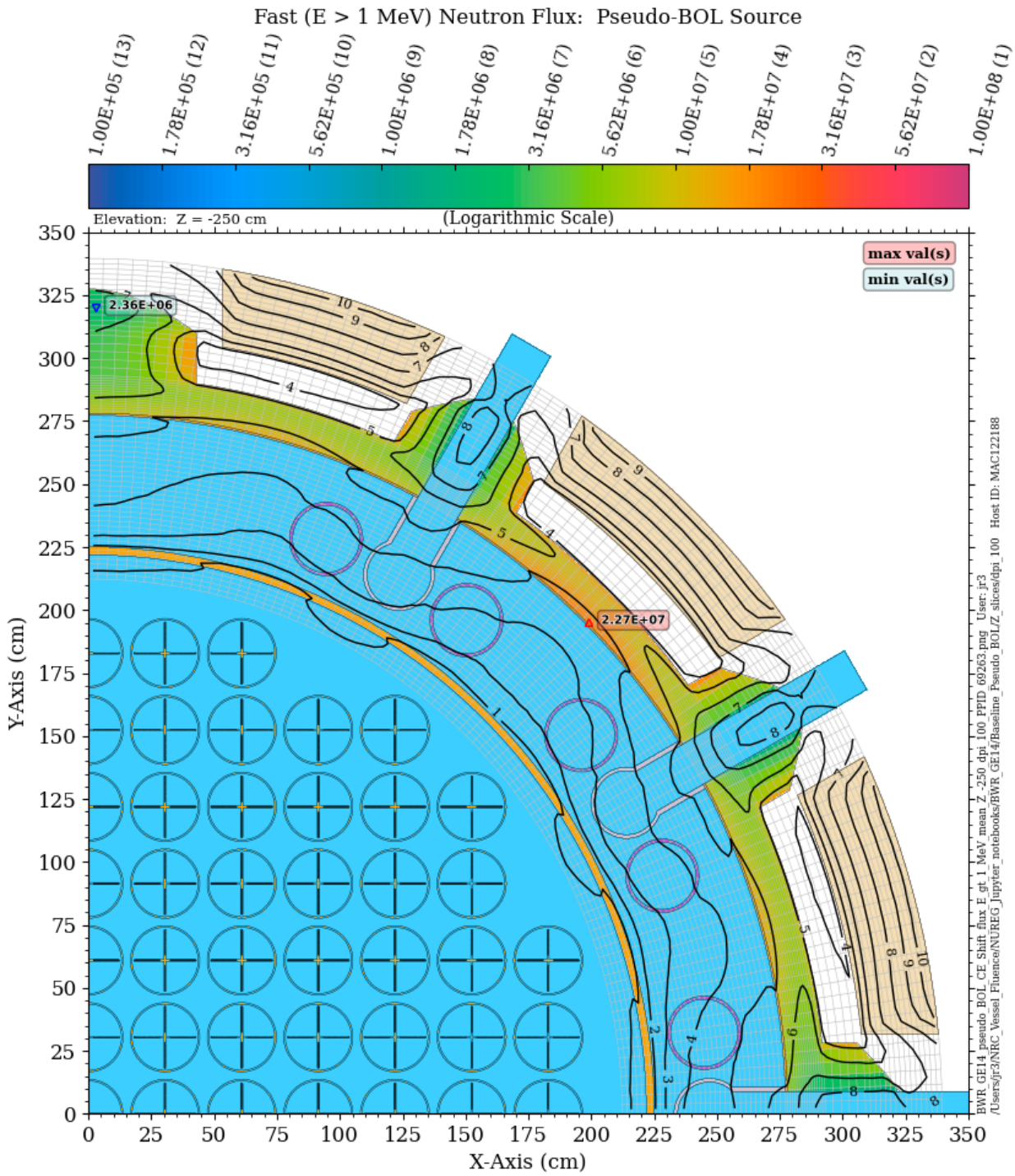

Figure 2-18 Fast neutron flux in the BWR model with a pseudo-BOL source. Plan view at an elevation of Z = -250 cm

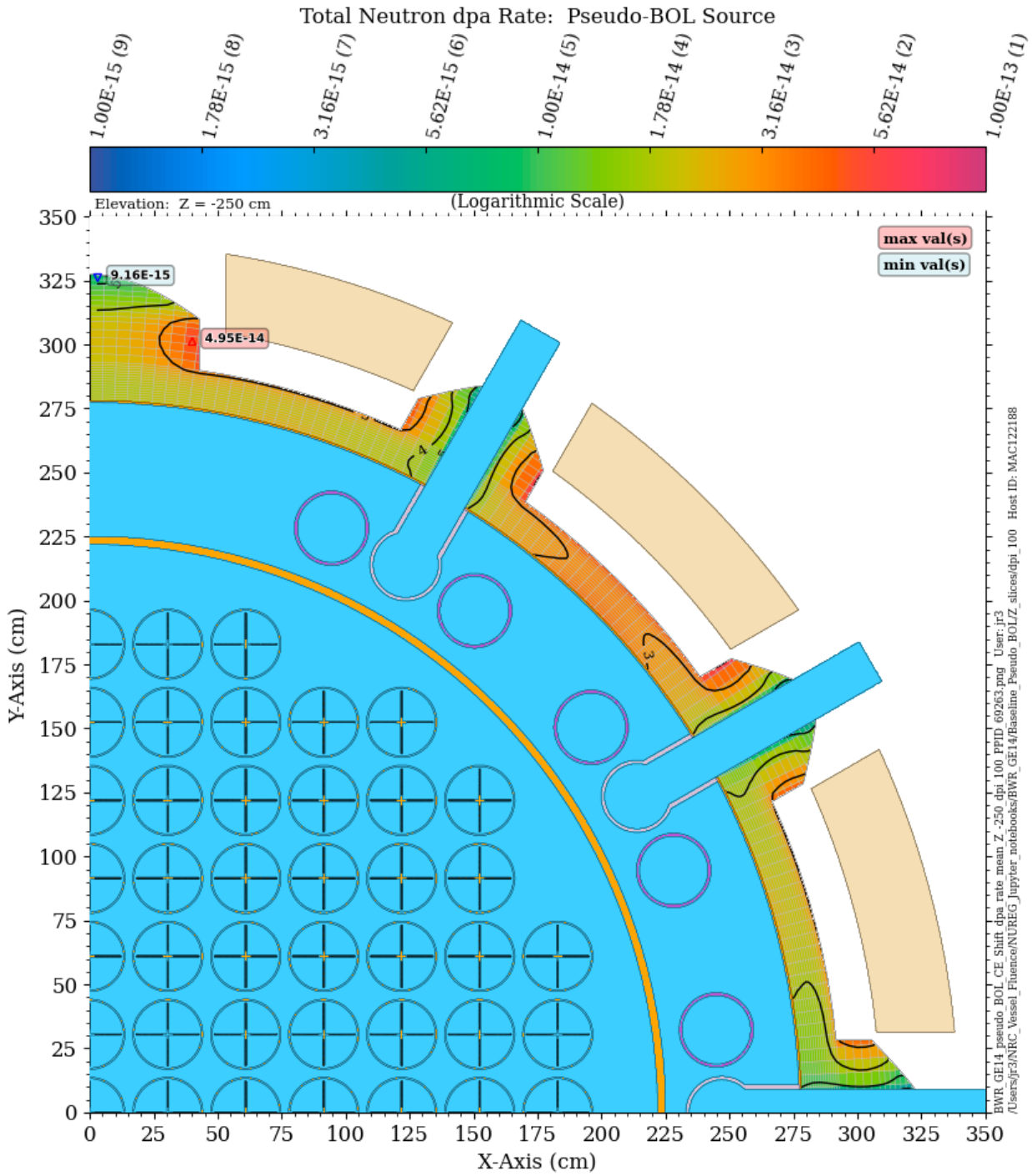

Figure 2-19 Total neutron dpa rate in the BWR model with a pseudo-BOL source. Plan view at an elevation of Z = -250 cm

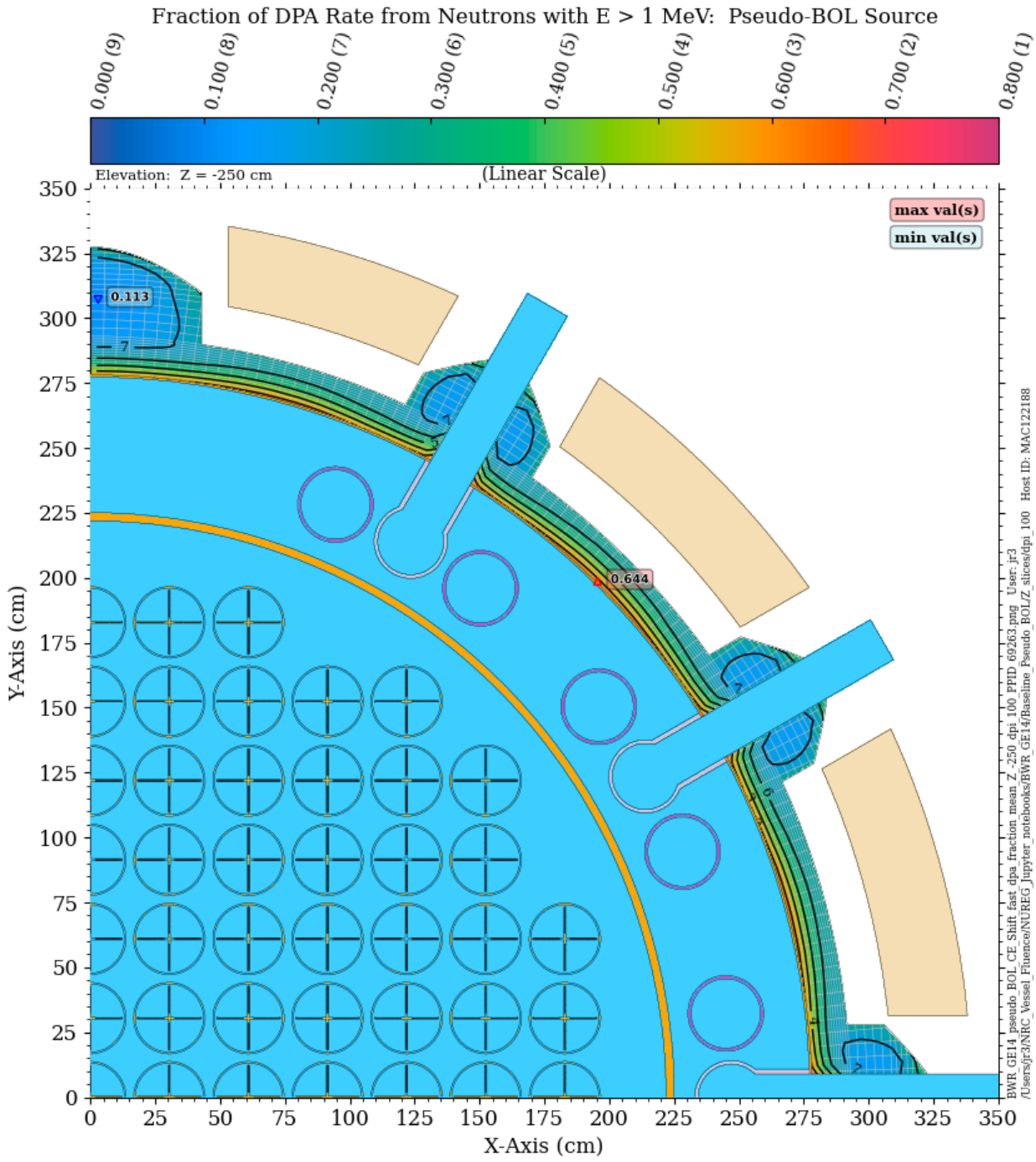

Figure 2-20 Fraction of the total neutron dpa rate due to neutrons with energy > 1 MeV in the BWR model with a pseudo-BOL source. Plan view at an elevation of Z = -250 cm

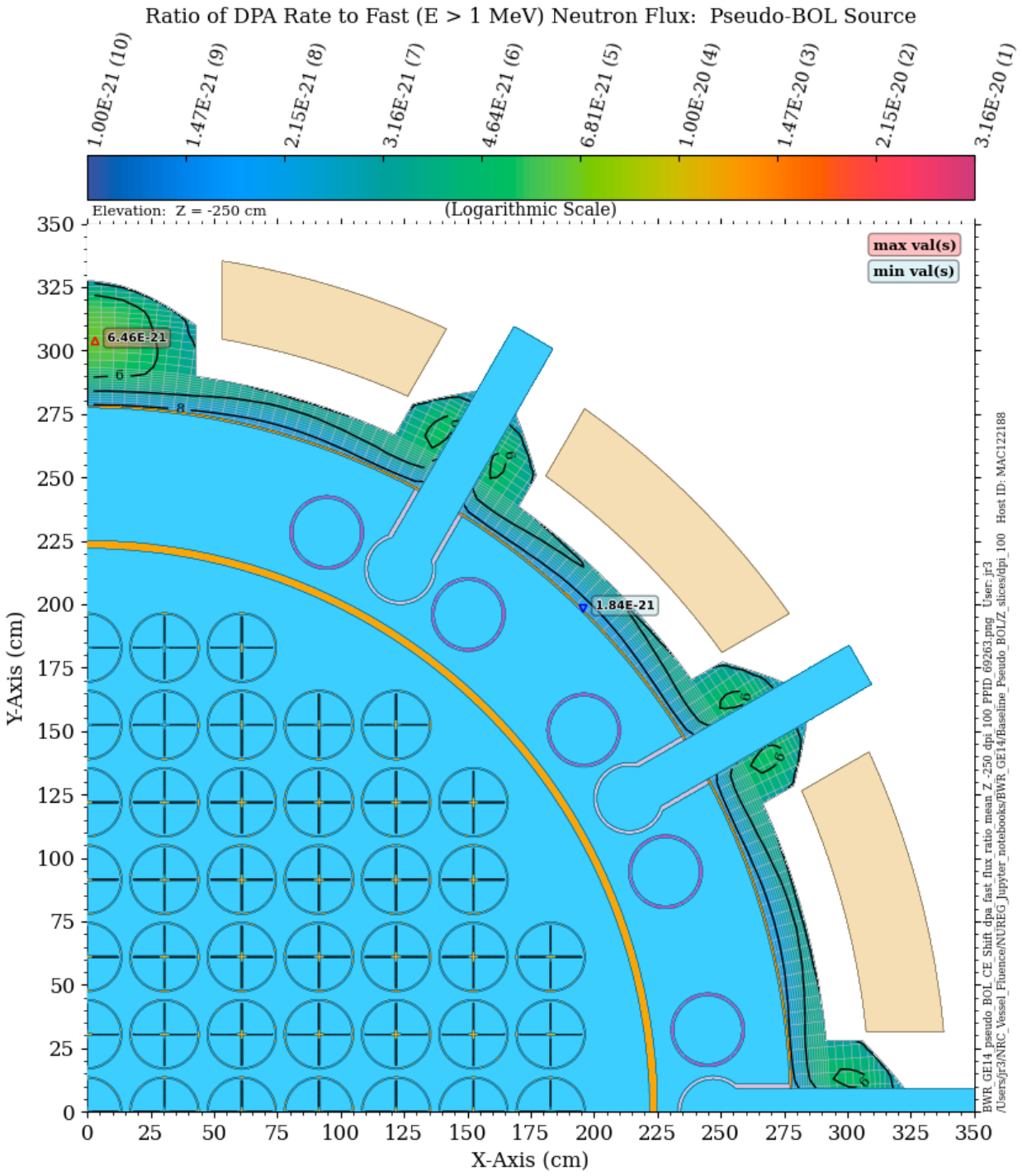

Figure 2-21 Ratio of the total neutron dpa rate to the fast (E > 1 MeV) neutron flux in the BWR model with a pseudo-BOL source. Plan view at an elevation of Z = -250 cm

2.2 Evaluation of gamma dpa rates in the extended beltline region

Predictions of radiation-induced embrittlement in LWR RPVs are typically performed using correlations of damage to either fast neutron fluence or neutron-induced dpa. While gamma rays are capable of producing dpa, the contribution of the gamma-induced dpa to the total dpa (neutron plus gamma) is generally a very small fraction and is consequently ignored. ASTM E1035-18 [11] states that it may be prudent to calculate gamma-induced dpa in vessel support structures using coupled neutron-gamma radiation transport calculations gamma dpa cross-section data.

Gamma dpa rates were calculated in the vessel supports for the PWR model. The gamma dpa cross sections were taken from the referenced work by Baumann [16]. While the fraction of the total dpa rate due to gamma-induced displacements does increase at the location of the vessel supports relative to the traditional beltline region, the increase is relatively minor, and the gamma dpa rate is significantly less than 1% of the neutron dpa rate.

Calculation of gamma dpa rates in the extended beltline region was also performed with the BWR model. As with the PWR model, the fraction of the total dpa rate due to gamma-induced displacements increases in the extended beltline region, but it is still well below 1% of the neutron dpa rate.

3. ASSESSMENT OF MULTIGROUP CROSS-SECTION LIBRARIES FOR RADIATION TRANSPORT CALCULATIONS IN THE EXTENDED BELTLINE REGION

The majority of RPV fluence calculations have been and continue to be performed using discrete ordinates transport codes with multigroup (MG) cross-section libraries. The adequacy of an MG library for transport applications is dependent on, among other factors, the energy structure (i.e., the group boundaries) and the weighting spectrum used to collapse either pointwise data to a fine-group library or a fine-group library to a broad-group library (see APPENDIX B).

The VITAMINB-B7 and BUGLE-B7 libraries [17] are widely used for LWR shielding analyses, with BUGLE-B7 being commonly used for RPV fluence applications. The VITAMIN-B7 library was created by collapsing pointwise ENDF/B-VII.0 data with (1) a weighting composed of a fission spectrum for neutron energies greater than 820.8 keV, (2) a 1/E slowing-down spectrum for energies between 0.125 eV and 820.8 keV, and (3) a Maxwellian spectrum for energies below 0.125 eV. For the BUGLE-B7 library, weighting spectra at several locations in representative 1D PWR and BWR models were calculated using the VITAMIN-B7 library. These spectra are shown in Figure 3-1.

The fine-group weighting spectrum used for generating the BUGLE-B7 library data for locations inside steel regions (especially the RPV) is taken at ¼ of the thickness of the RPV from a PWR model with an RPV thickness of 21.91 cm. As neutrons travel through the RPV, the spectrum changes substantially. Figure 3-2 shows how the neutron flux as a function of five energy ranges changes from the core radially outward through the concrete bioshield for a 1D mockup of the PWR reference model at the core midplane. Note that the flux for energies above 1 MeV is attenuated by a factor of ~20 from the inner surface of the RPV to the outer surface. In contrast, the flux profiles in the lower energy ranges (excluding the profile for $E < 5$ eV) decrease more slowly because high-energy neutrons are scattered into lower energy ranges. As a result of the down-scattering of high-energy neutrons (i.e., neutrons scattering to lower energies), the flux profile for neutron energies between 111.09 keV and 1.0026 MeV has a slight increase near the inner surface of the RPV before decreasing. This behavior is also shown in Figure 3-3, which illustrates how the neutron flux spectrum undergoes a significant change as neutrons are transported from the inner surface of the RPV to the outer surface.

In addition to the variation in the neutron spectrum as a function of radial distance into the RPV, significant changes also occur as a function of elevation. As a result, in an MG library such as BUGLE-B7, the data that are collapsed using the neutron spectrum from a single location may not be appropriate for use in other locations, even though the material composition (e.g., steel) may be identical.

Furthermore, the appropriateness of an MG library depends on the specific neutron response (e.g. flux, dpa rate, reaction rate) being considered in an analysis. For example, calculation of the rate of a neutron dosimetry reaction with a high threshold energy is likely to be less sensitive to MG structures compared to a reaction that occurs primarily at lower energies, when neutron transport through energy ranges with significant resonance regions is important.

The calculations presented in this section were performed with the objective of comparing neutron fluxes, dpa rates, and dosimetry reaction rates calculated using the Shift Monte Carlo

code with both continuous energy (CE) and MG physics treatments. The aim of this study is not to compare calculated and measured data (which is difficult to do due to the lack of adequate measurement data in the extended beltline region), but rather to assess how well a given MG library performs compared to the more exact CE cross sections. For this purpose, the following neutron responses are considered:

1. Fast neutron flux (E > 1 MeV)
2. Neutron dpa rate using dpa cross-section data from ASTM E693-17 [10]
3. ^{27}Al (n,α) reaction rate
4. ^{63}Cu-63 (n,α) reaction rate
5. ^{46}Ti (n,p) reaction rate
6. ^{54}Fe (n,p) reaction rate
7. ^{58}Ni (n,p) reaction rate
8. ^{115}In (n,n′) ^{103m}In reaction rate
9. ^{103}Rh (n,n′) ^{103m}Rh reaction rate
10. ^{237}Np (n,f) reaction rate
11. ^{238}U (n,f) reaction rate

The (n,α), (n,p), and (n,n′) reactions have threshold energies ranging from 3.25 MeV to 40.14 keV. They are listed in decreasing order of the threshold energy. The cross-section data for these reactions are shown in Figure C-1 and Figure C-2 of APPENDIX C.

3.1 Selection of multigroup cross-section libraries

For the purposes of this study, seven MG libraries were evaluated. Scoping studies were performed using XSDRNPM [18] 1D deterministic calculations based on the PWR reference model. Based on the results of the 1D studies, 3D Shift calculations were performed using selected MG libraries for comparison to Shift CE solutions. The CE calculations were all run using Shift with the SCALE [18] ENDF/B-VII.1 CE library.

The following MG libraries were considered in the 1D calculations:

1. **VITAMIN-B7**: a fine-group library with 197 neutron energy groups.
2. **BUGLE-B7:** a broad-group library with 47 neutron energy groups which was created by collapsing the VITAMIN-B7 library using representative weighting spectra from 1D PWR and BWR models; widely used in LWR shielding applications.
3. **X200N47G:** One of two fine-group shielding libraries with energy structures identical to VITAMIN-B7, except for an additional group from 19.64 to 20.0 MeV. There are X200N47G libraries based on ENDF/B-VII.0 and ENDF/B-VII.1.
4. **X999N:** an experimental SCALE MG library with 999 neutron groups; developed primarily for reactor physics applications.
5. **X1597N:** an experimental SCALE MG library with 1,597 neutron energy groups; developed primarily for reactor physics applications.
6. **X642N:** a library with 642 neutron groups. For energies below 1.0026 MeV, the groups are identical to the SCALE X200N47G structure. There are 440 equal-lethargy groups from 1.0026 to 3.0119 MeV. The intent of these fine groups is to provide improved MG accuracy over an energy range that is particularly significant for neutron transport through thick iron regions. There are 48 equal-lethargy groups from 3.0119 to 10.0 MeV. Above 10.0 MeV, the groups are identical to the SCALE X200N47G structure.

7. **X956N:** a library with 956 neutron groups that is a refinement of the X642N library. This library has 100 equal-lethargy groups for the energy range from 3.0119 to 10.0 MeV. For energies from 10.595 keV to 1.0026 MeV, the group structure of the X999N library is used.

The energy group structures for these libraries are shown in Figure 3-4.

Results of the 1D calculations showed that the X642N and X956N libraries, which were developed specifically for modeling neutron transport through iron, are superior to the X999N and X1597N libraries for LWR shielding applications. Consequently, the X999N and X1597N libraries were used only on a limited basis for the 3D calculations.

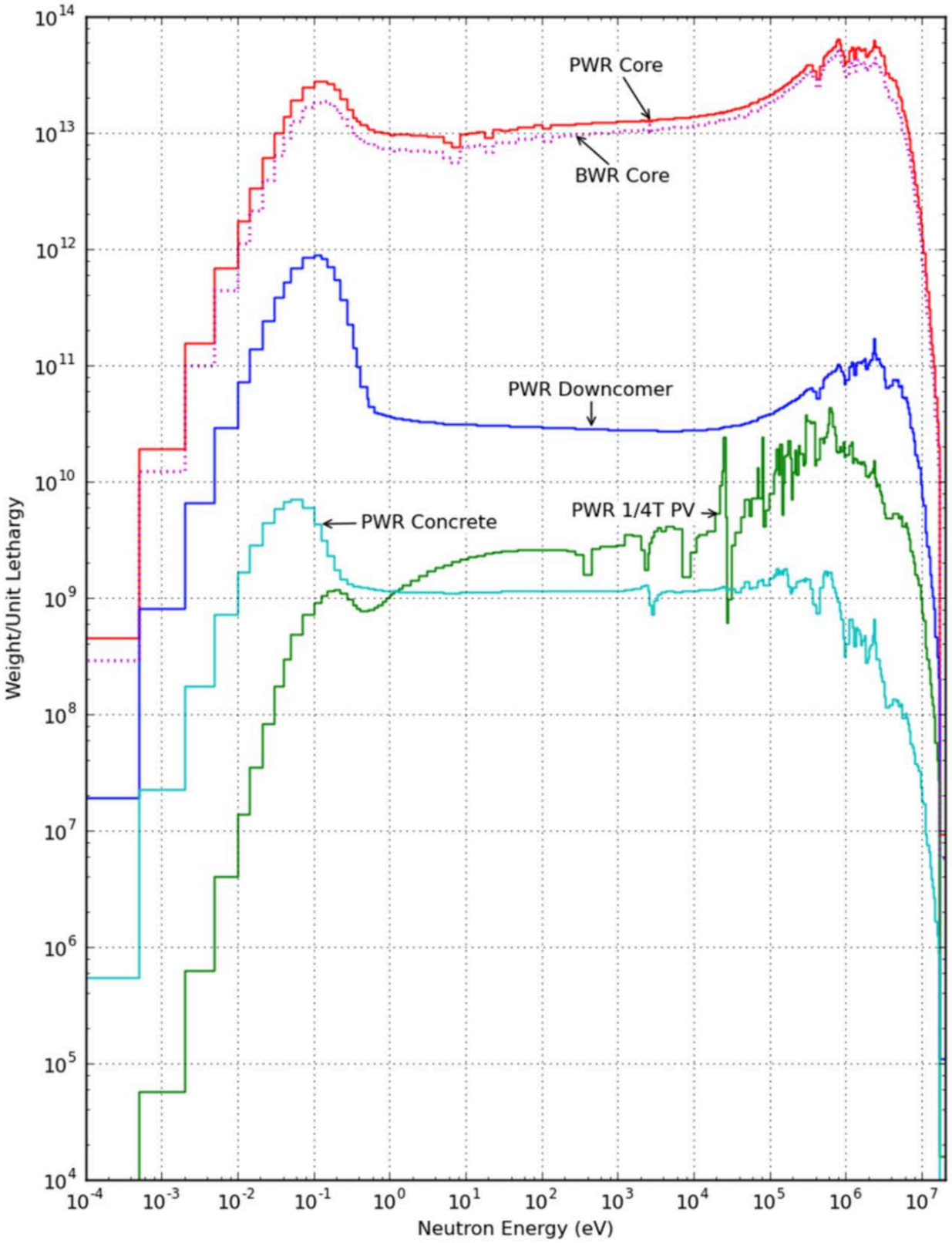

Figure 3-1 Weighting spectra used to generate the BUGLE-B7 MG library for LWR shielding analyses

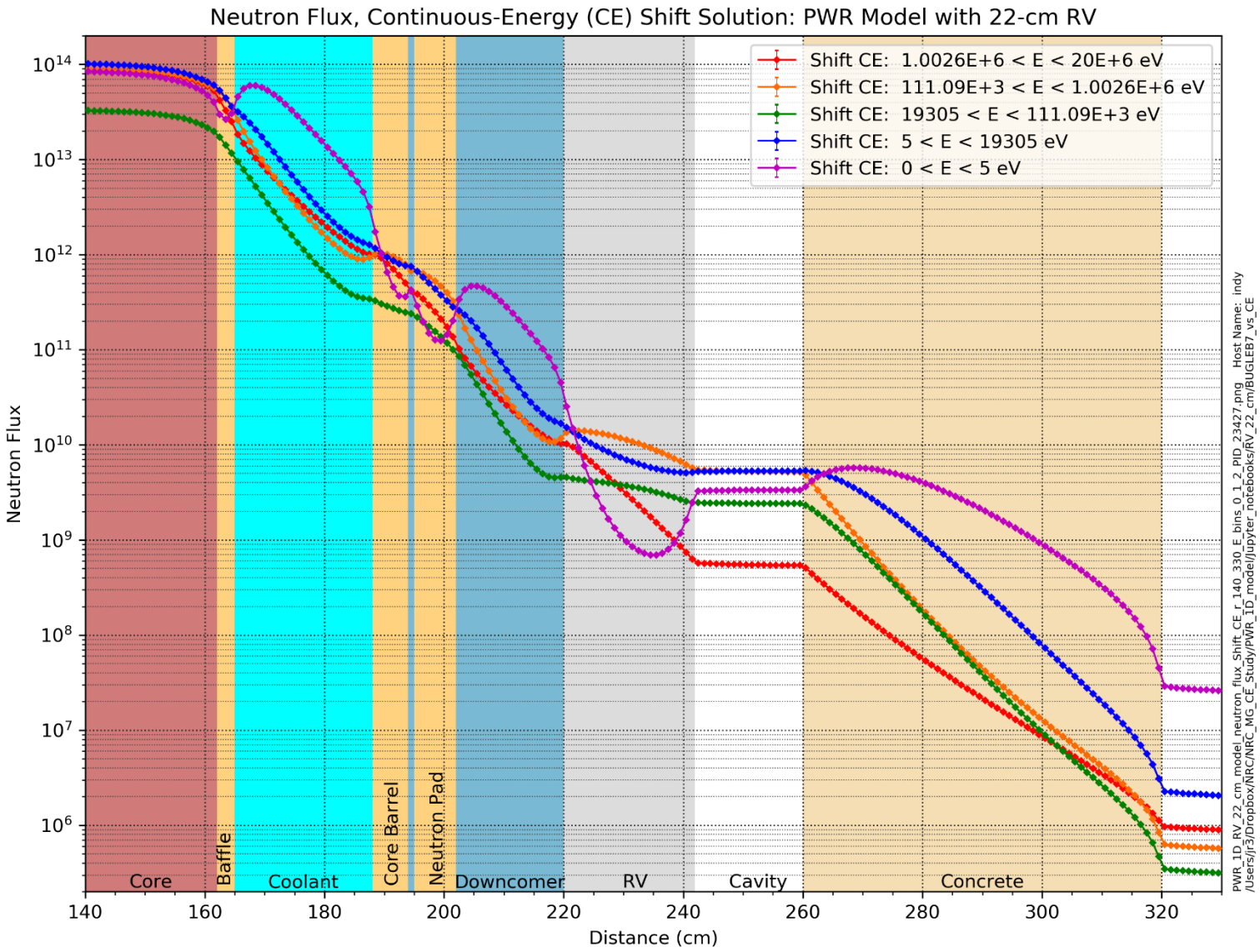

Figure 3-2 Neutron flux traverses for five energy ranges in a 1D mockup of the PWR reference model at the core midplane

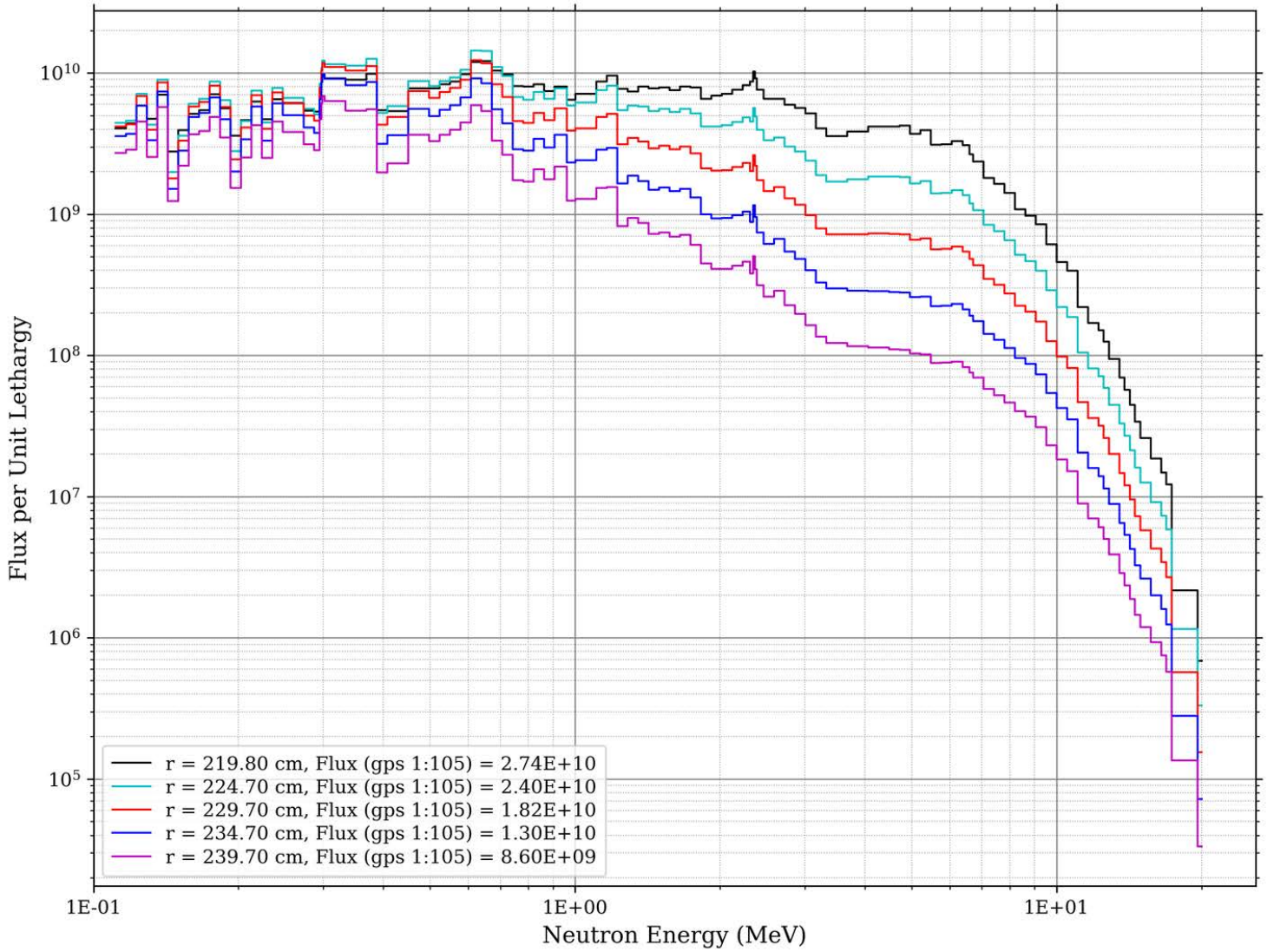

Figure 3-3 Neutron spectra for groups 1 to 105 (111.09 keV < E < 20 MeV) of the VITAMIN-B7 library at five locations through the thickness of the RPV for the 1D mockup of the PWR reference model

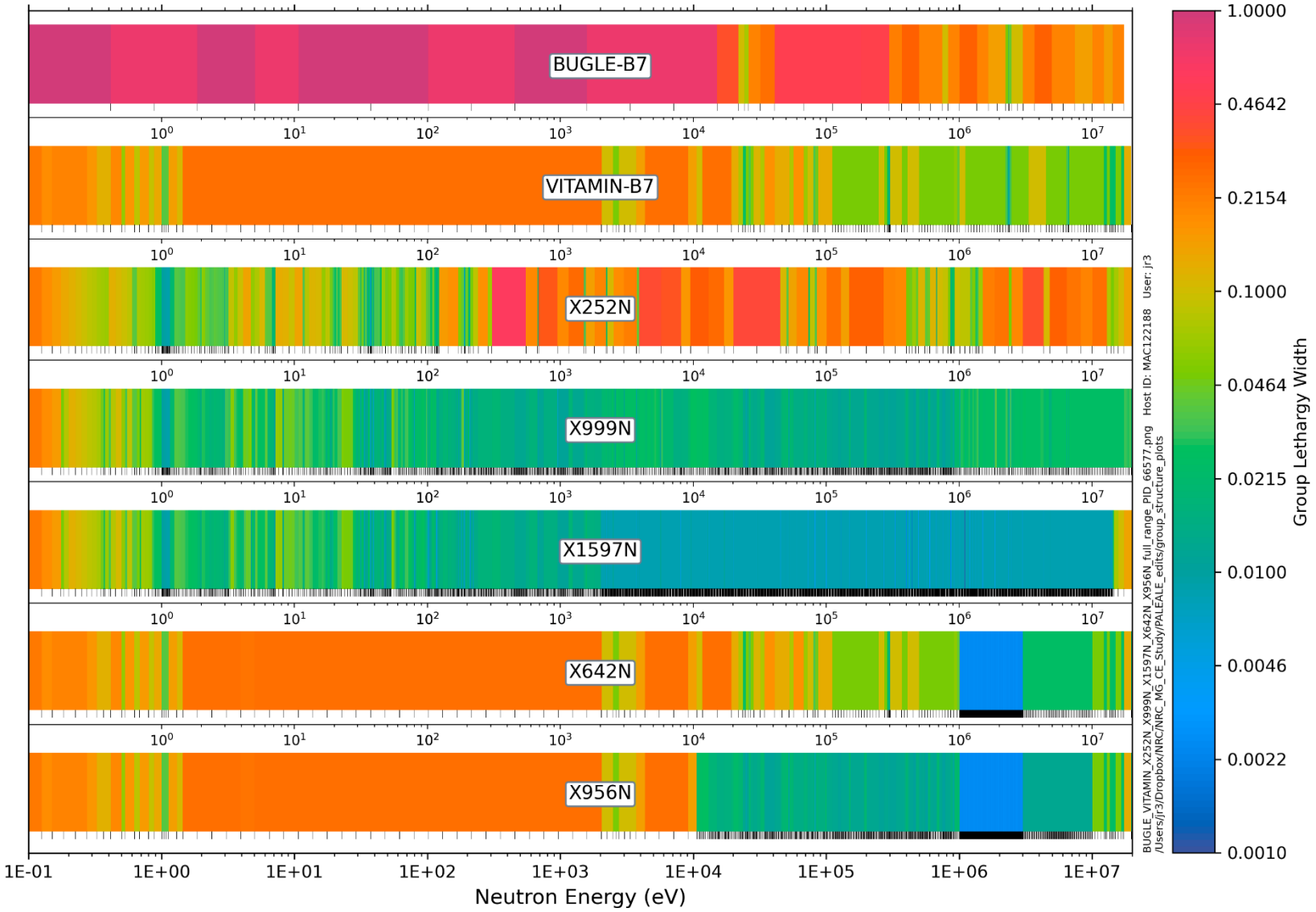

Figure 3-4 Group lethargy widths for the BUGLE-B7, VITAMIN-B7, X999N, X642N, X956N, and X1597N cross-section libraries

3.2 Fast flux calculations

Because the fast neutron fluence is a widely used metric for correlations of radiation damage in carbon steel RPVs, the first set of Shift MG/CE comparisons addresses how well an MG calculation can match a CE calculation of the neutron fast flux at locations in the traditional and extended beltline regions for a ^{235}U source. For calculational consistency, an energy cutoff of 1.0026 MeV was used in the CE calculations, as that is the nearest group boundary in each of the MG libraries considered in this analysis.

The results in this section demonstrate the performance of several MG libraries for fast neutron flux calculations at two elevations in the PWR reference model: at the core midplane at Z = 195 cm, and at an elevation of Z = 470 cm. These elevations are representative of the traditional beltline region and an extended beltline location near the RPV nozzles and vessel supports.

Figure 3-5 and Figure 3-6 show the MG/CE fast flux ratios when the BUGLE-B7 library is used with Shift. While the solutions agree well near the maximum flux in the RPV at the core midplane, they deviate more at azimuthal locations where the distance between the outer edge of the core and the RPV is maximized. At the outer edge of the RPV, the BUGLE-B7 solution underpredicts the CE solution by up to 10%. This is not significant for fast fluence in the traditional beltline region, where the peak fast flux levels occur at the inner surface of the RPV, but it suggests that cavity streaming neutron flux levels in extended beltline regions may be underpredicted using the BUGLE-B7 library, as the cavity streaming flux is driven by neutrons that escape the RPV and scatter from the bioshield back into the cavity gap. At the extended beltline elevation of 470 cm, the fast flux is underpredicted by ~5–14% throughout the RPV, and by as much as nearly 18% in the vessel supports. As noted in Section 5.6 of [8], at this location the EOL fast fluence is likely to be below 1×10^{17} n/cm^2, but the dpa rate may exceed the monitoring standard practice of 3×10^{-4} from ASTM E1035-18 [11]. Consequently, underprediction of the fast flux using the BUGLE-B7 library may be significant for vessel supports.

Figure 3-7 and Figure 3-8 show the MG/CE fast flux ratios when the VITAMIN-B7 library is used with Shift. It is somewhat surprising that the VITAMIN-B7/CE agreement is not noticeably improved compared to the BUGLE-B7/CE ratios. Use of the SCALE X200N47Gv71 MG library, which has the same group structure as the VITAMIN-B7 library, with the exception of an added group for energies between 19.64 MeV (the upper limit of the VITAMIN-B7 library), provides a slightly improved agreement relative to VITAMIN-B7 (Figure 3-9 and Figure 3-10). However, there is still an underprediction of ~9% at the outer surface of the RPV at the core midplane, and fast flux levels in the vessel support are underpredicted by up to nearly 20%.

Use of the Shift X999N library (Figure 3-11 and Figure 3-12), which was developed for reactor physics applications, yields an MG Shift solution that offers essentially no improvement, although the number of groups is increased by a factor of five. In contrast to the X999N library, the X956N library, which was developed specifically to improve MG accuracy over the energy range above 1 MeV, where there is resolved resonance data in the iron isotope cross sections, provides significantly improved solutions at the core midplane (Figure 3-13) and in the extended beltline region (Figure 3-14). At the core midplane, the X956N solution agrees with the CE solution within 2.5% at all mesh tally voxels. At the extended midplane elevation, the differences in the X956N and CE solutions are less than 5% in over 99% of the mesh tally voxels.

The final MG/CE fast flux comparison was made using the X642N library. Like the X956N library, it was developed to improve MG accuracy over the energy range above 1 MeV. The differences between the X642N and X956N libraries are primarily at energies below 1.0026 MeV, so they are likely to produce very similar results for fast flux calculations. This is shown in Figure 3-15 and Figure 3-16.

In summary, MG flux solutions obtained with today's commonly used libraries—BUGLE-B7, VITAMIN-B7, and Shift X200N47Gv71—tend to systematically underpredict fast flux levels in the outer portion of the RPV within the traditional beltline region and at all locations in the extended beltline region at the elevation of the vessel supports.

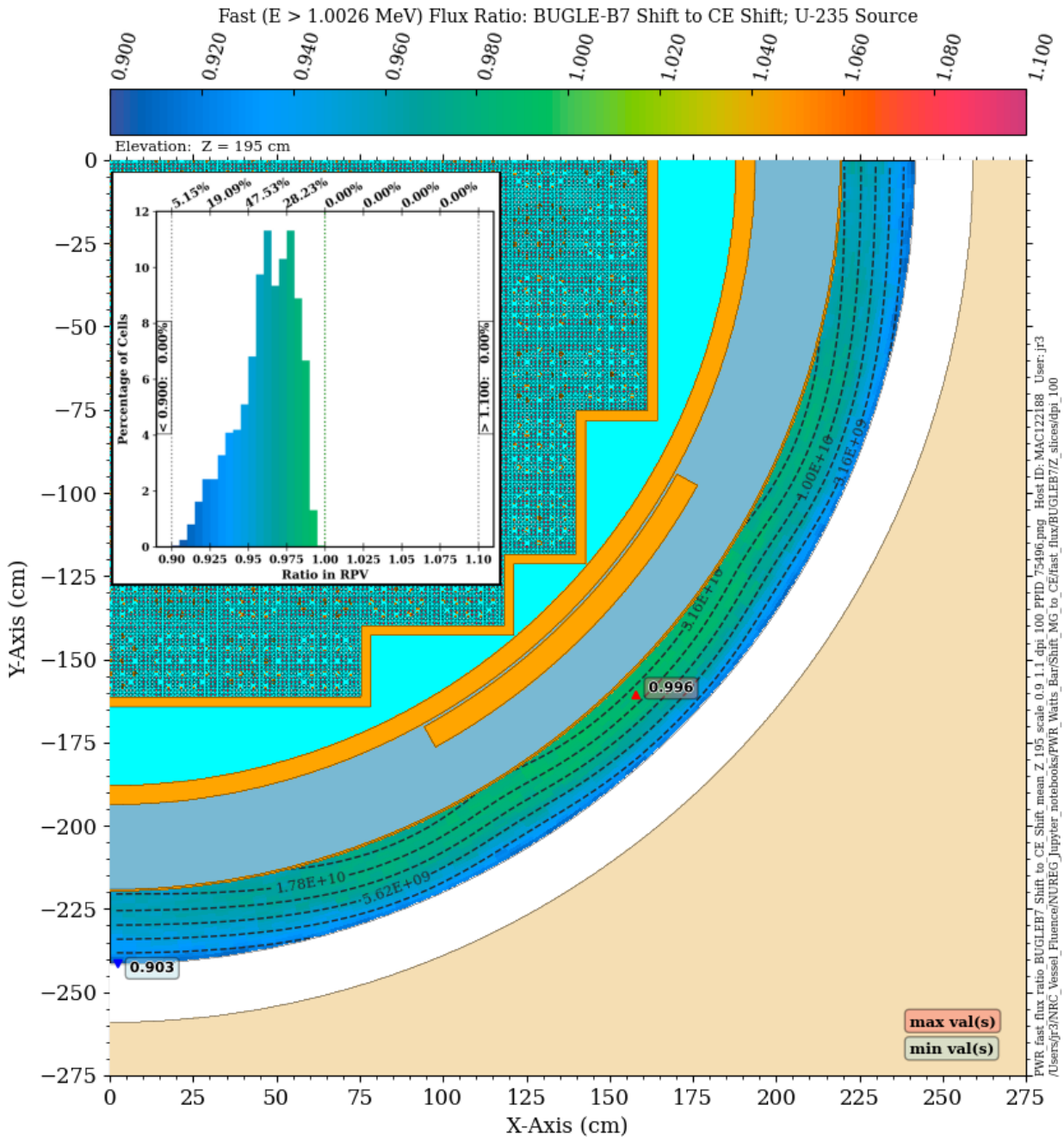

Figure 3-5 Fast neutron flux ratio in the PWR RPV: BUGLE-B7 Shift/CE Shift. Plan view at Z = 195 cm. The contour lines are the fast flux from the CE solution

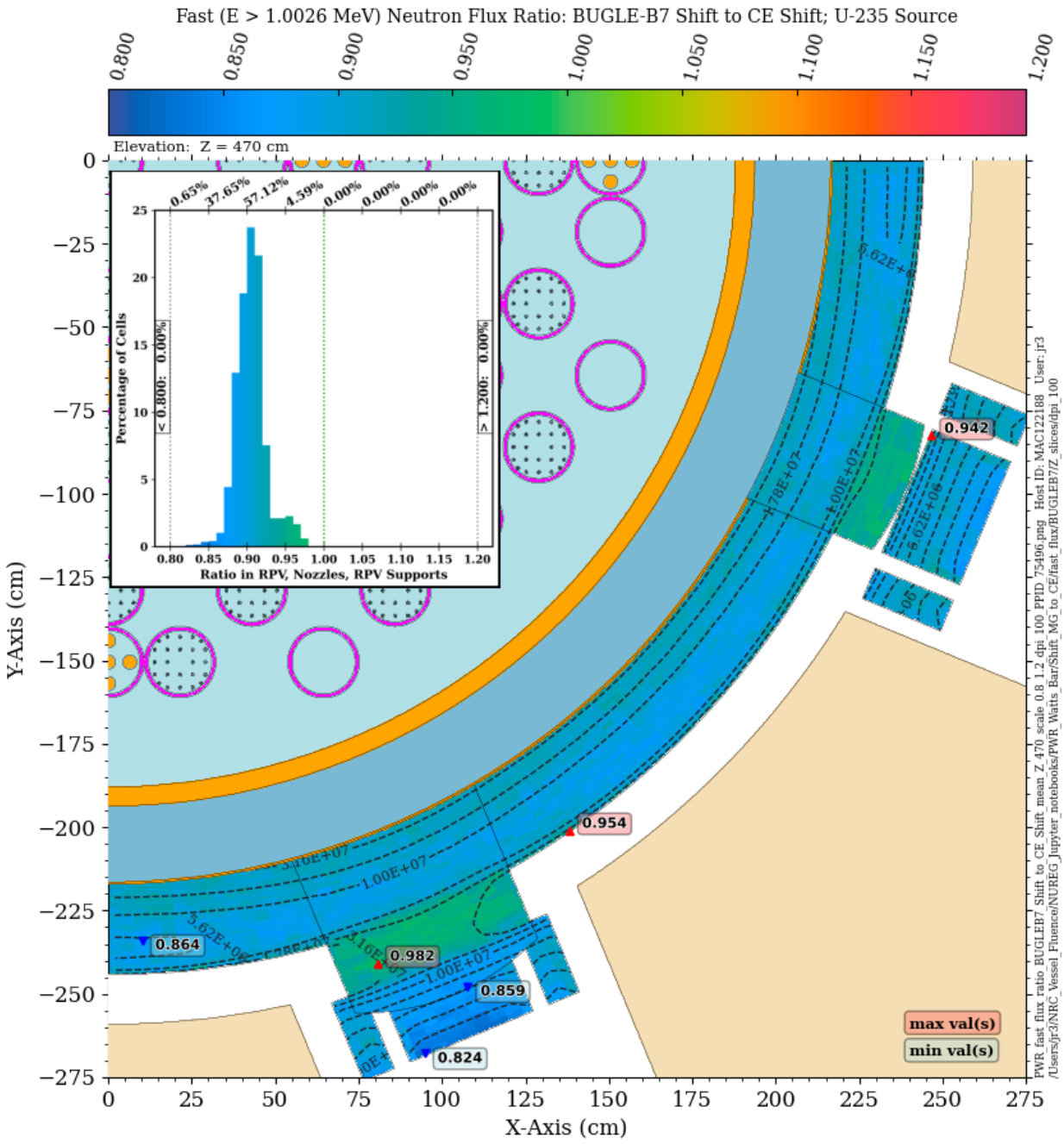

Figure 3-6 Fast neutron flux ratio in the PWR RPV: BUGLE-B7 Shift/CE Shift. Plan view at Z = 470 cm. The contour lines are the fast flux from the CE solution. Note the change in scale relative to Figure 3-5

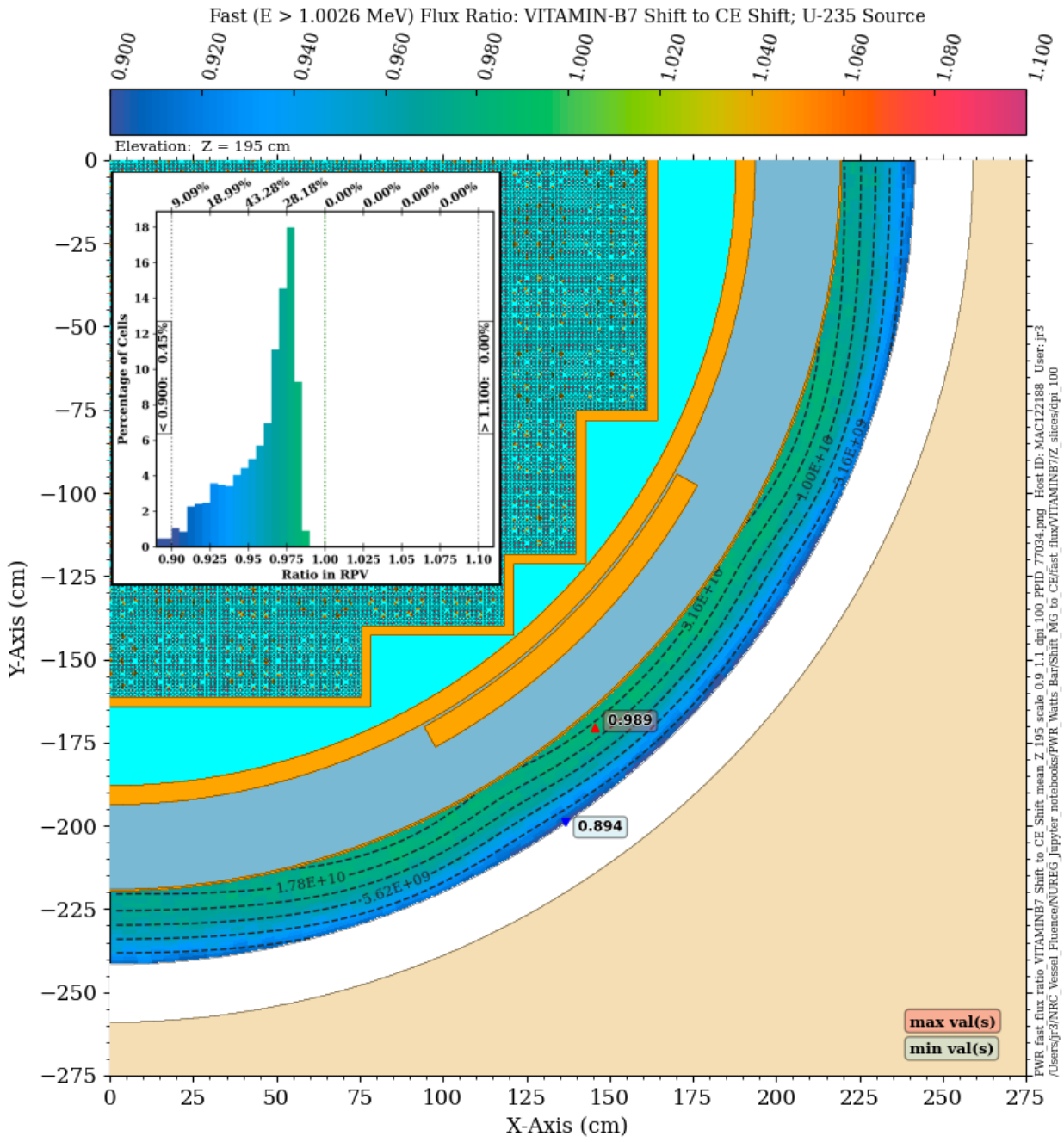

Figure 3-7 Fast neutron flux ratio in the PWR RPV: VITAMIN-B7 Shift/CE Shift. Plan view at Z = 195 cm. The contour lines are the fast flux from the CE solution

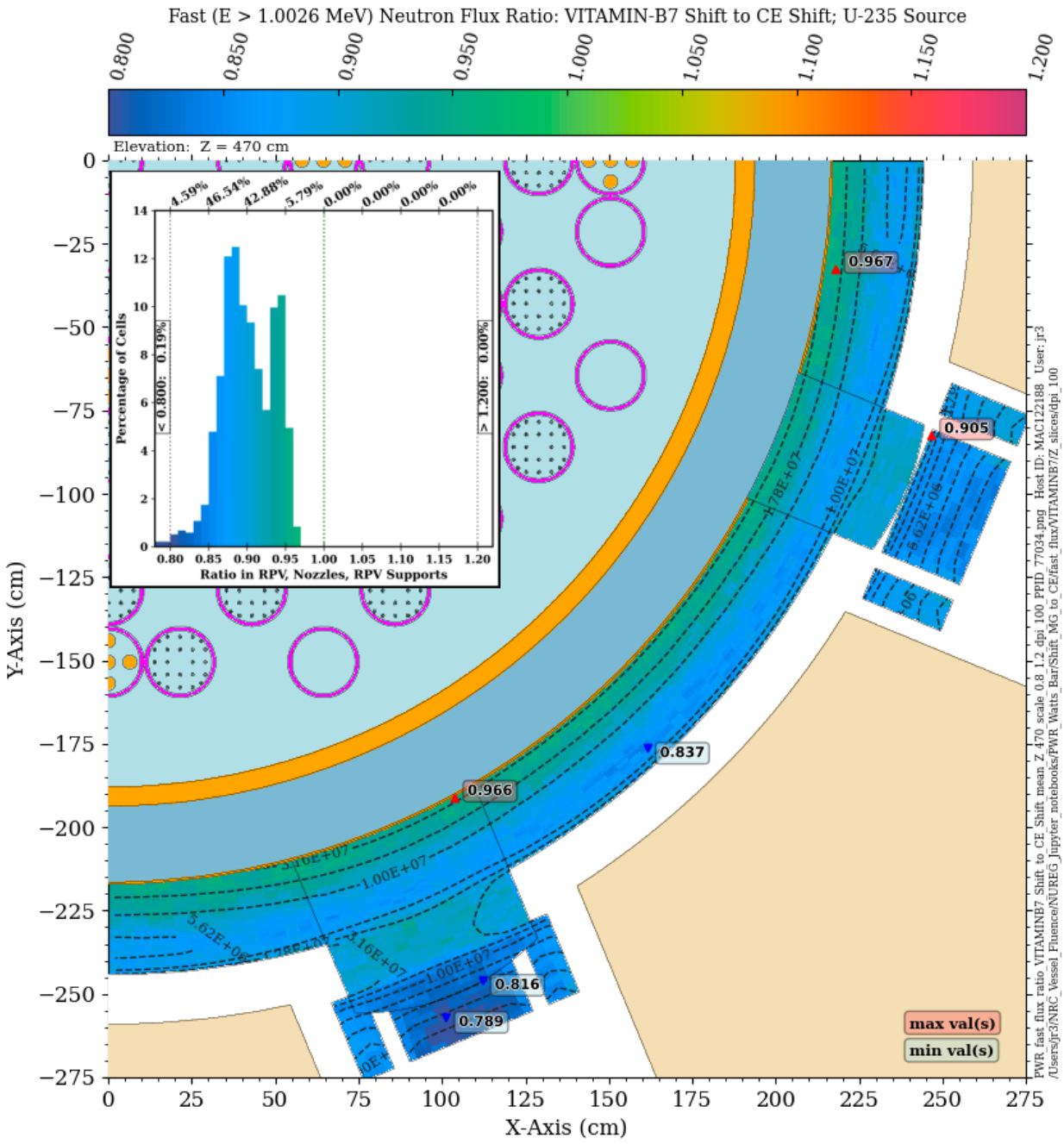

Figure 3-8 Fast neutron flux ratio in the PWR RPV: VITAMIN-B7 Shift/CE Shift. Plan view at Z = 470 cm. The contour lines are the fast flux from the CE solution. Note the change in scale relative to Figure 3-7

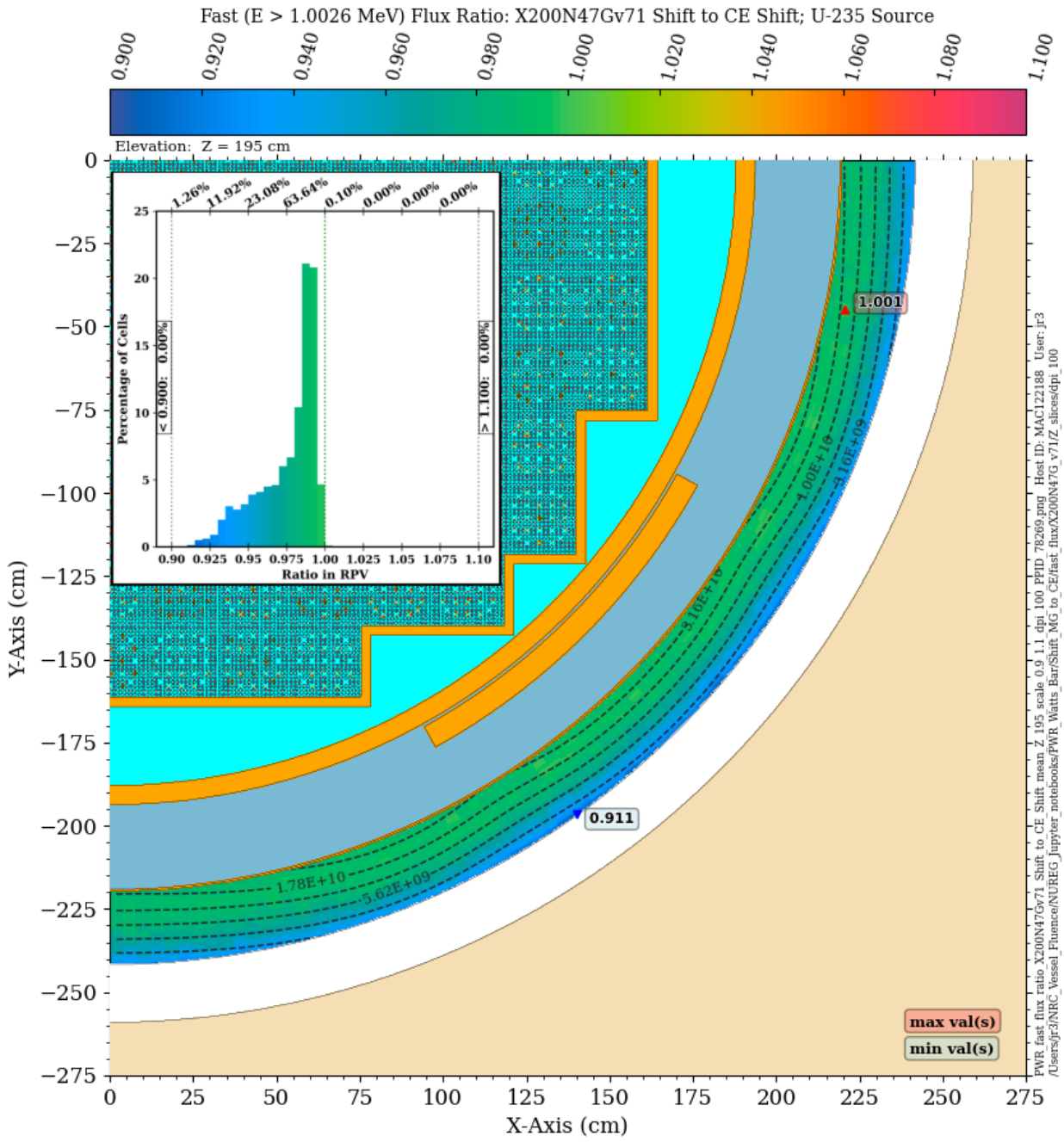

Figure 3-9 Fast neutron flux ratio in the PWR RPV: X200N47Gv71 Shift/CE Shift. Plan view at Z = 195 cm. The contour lines are the fast flux from the CE solution

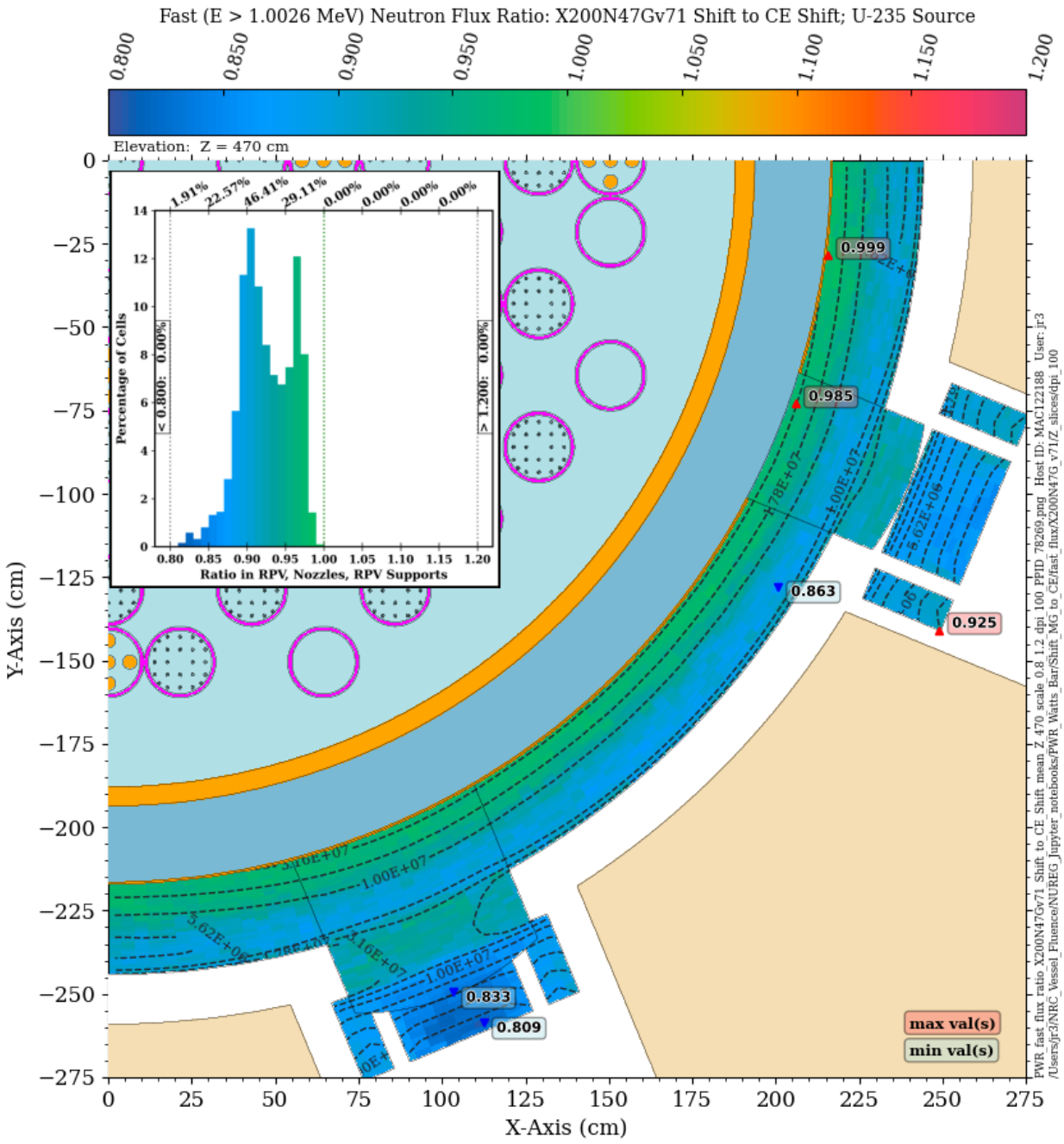

Figure 3-10 Fast neutron flux ratio in the PWR RPV: X200N47Gv71 Shift/CE Shift. Plan view at Z = 470 cm. The contour lines are the fast flux from the CE solution. Note the change in scale relative to Figure 3-9

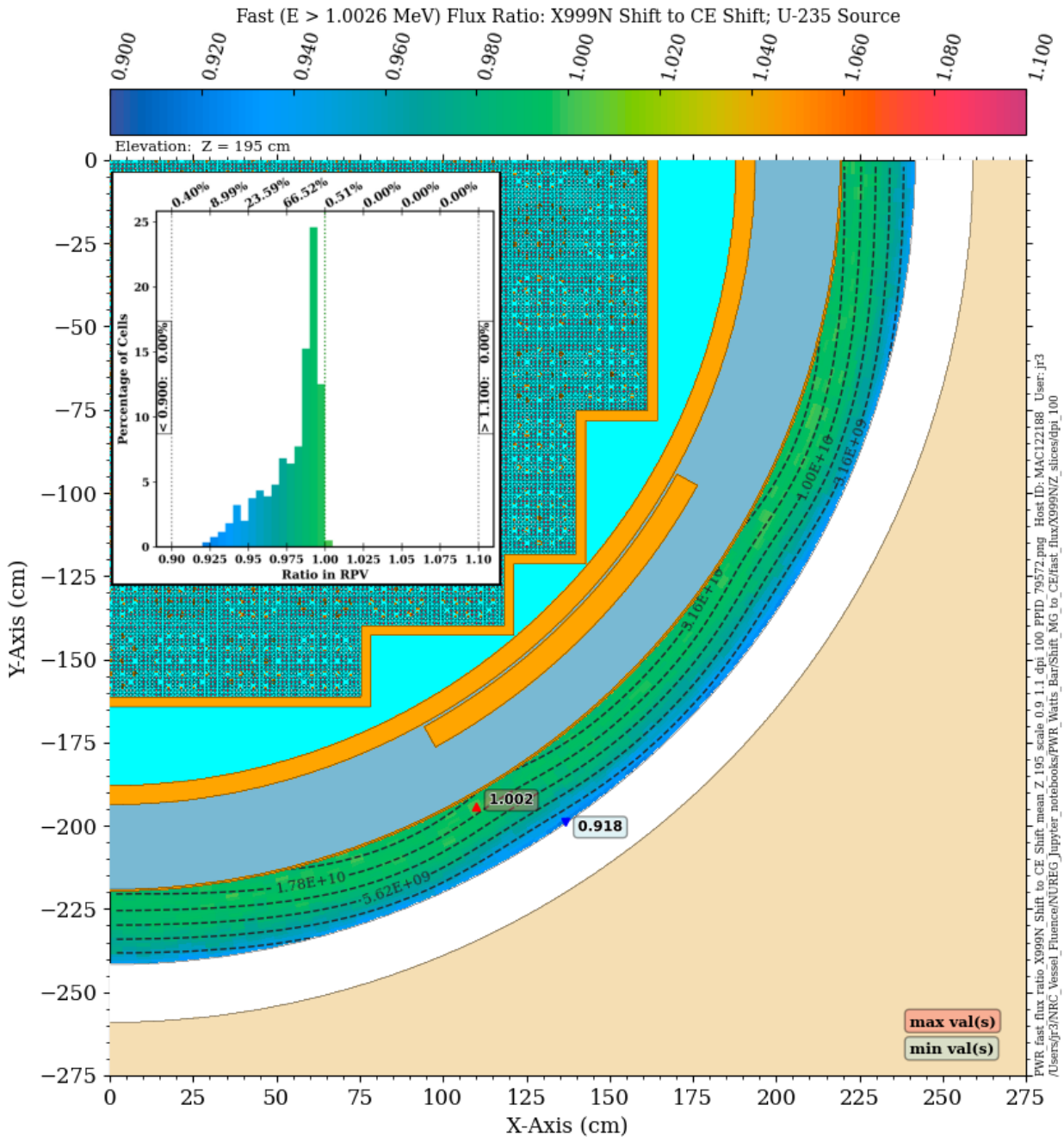

Figure 3-11 Fast neutron flux ratio in the PWR RPV: X999N Shift/CE Shift. Plan view at Z = 195 cm. The contour lines are the fast flux from the CE solution

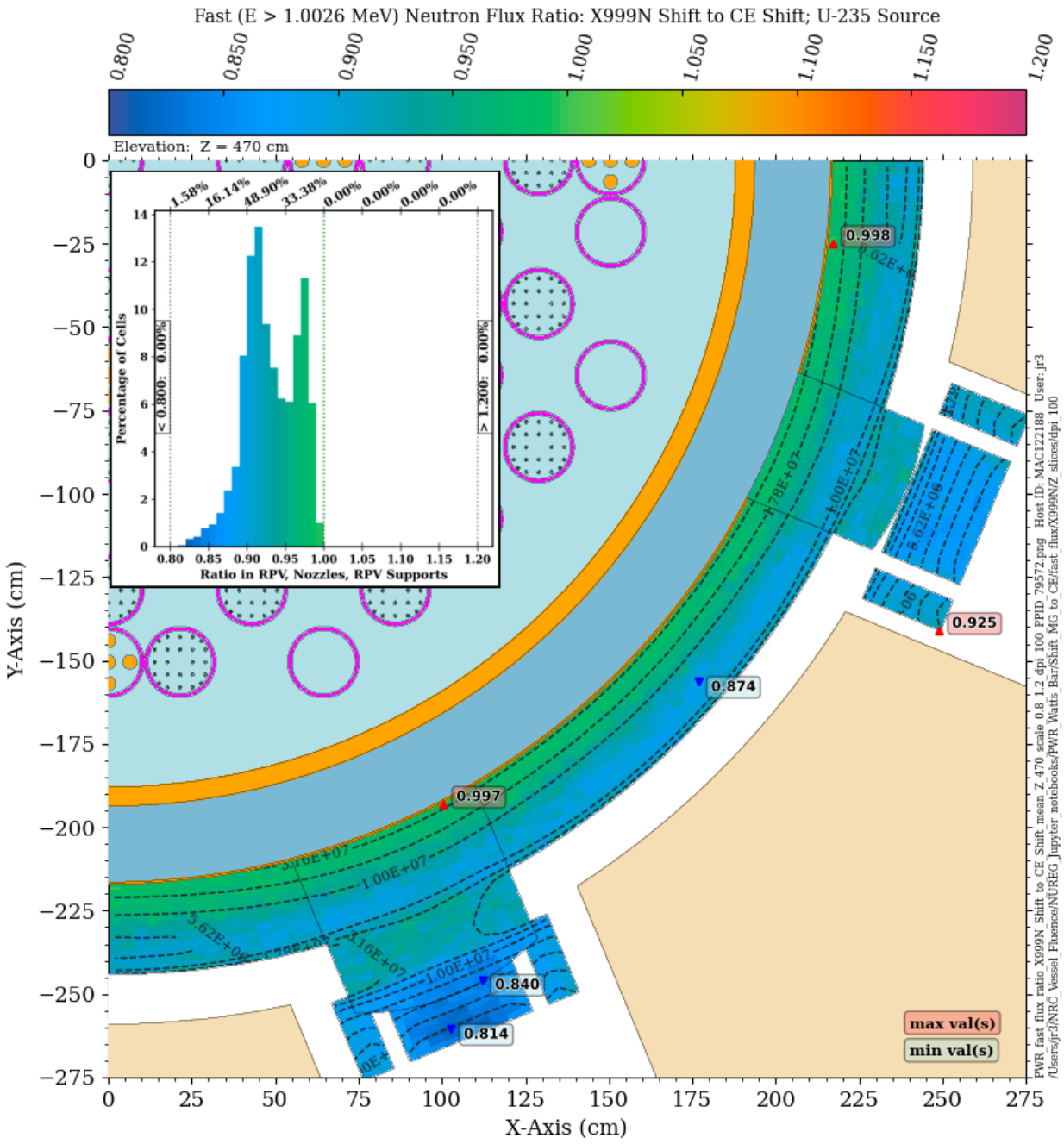

Figure 3-12 Fast neutron flux ratio in the PWR RPV: X999N Shift/CE Shift. Plan view at Z = 470 cm. The contour lines are the fast flux from the CE solution. Note the change in scale relative to Figure 3-11

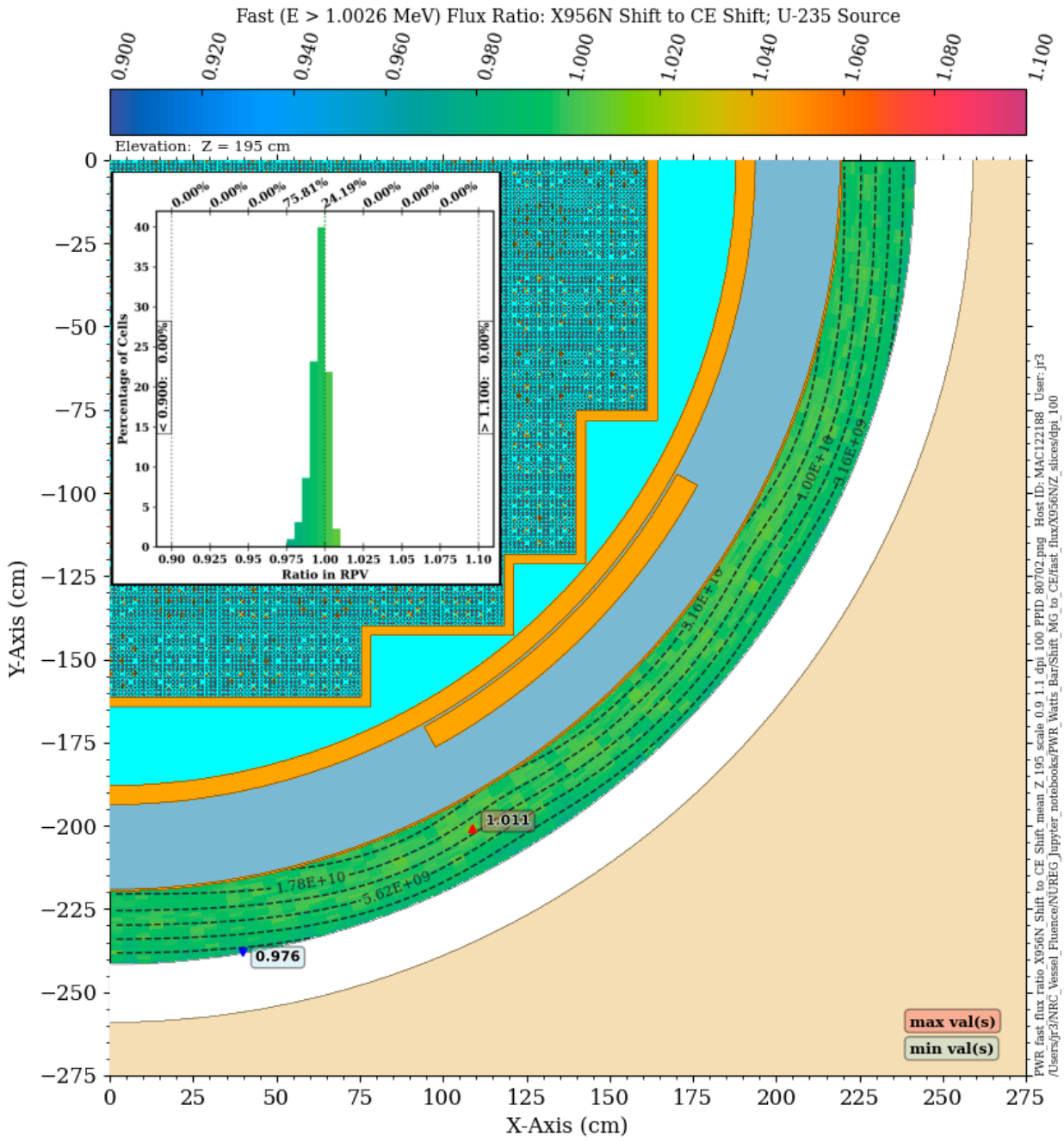

Figure 3-13 Fast neutron flux ratio in the PWR RPV: X956N Shift/CE Shift. Plan view at Z = 195 cm. The contour lines are the fast flux from the CE solution

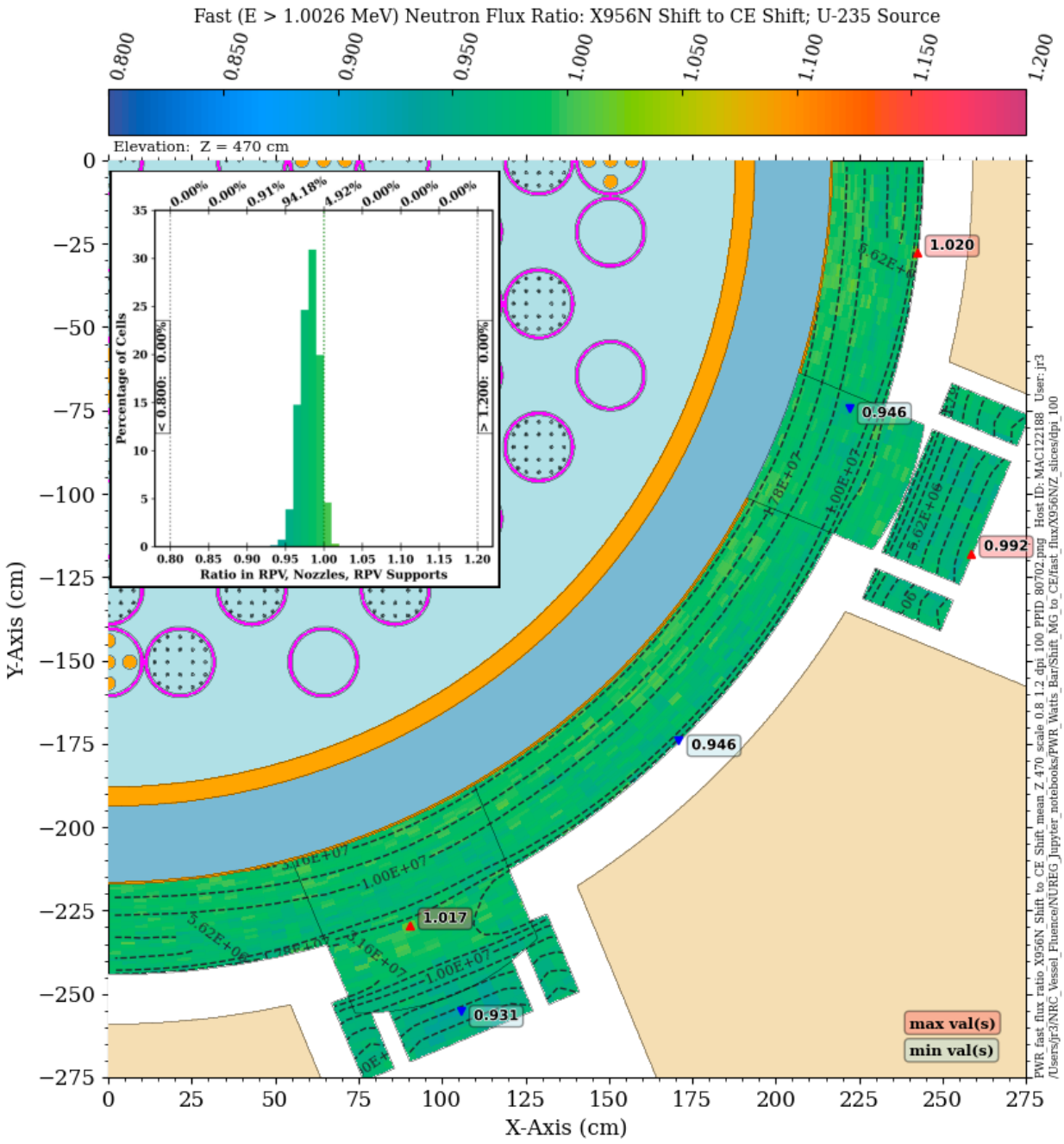

Figure 3-14 Fast neutron flux ratio in the PWR RPV: X956N Shift/CE Shift. Plan view at Z = 470 cm. The contour lines are the fast flux from the CE solution. Note the change in scale relative to Figure 3-13

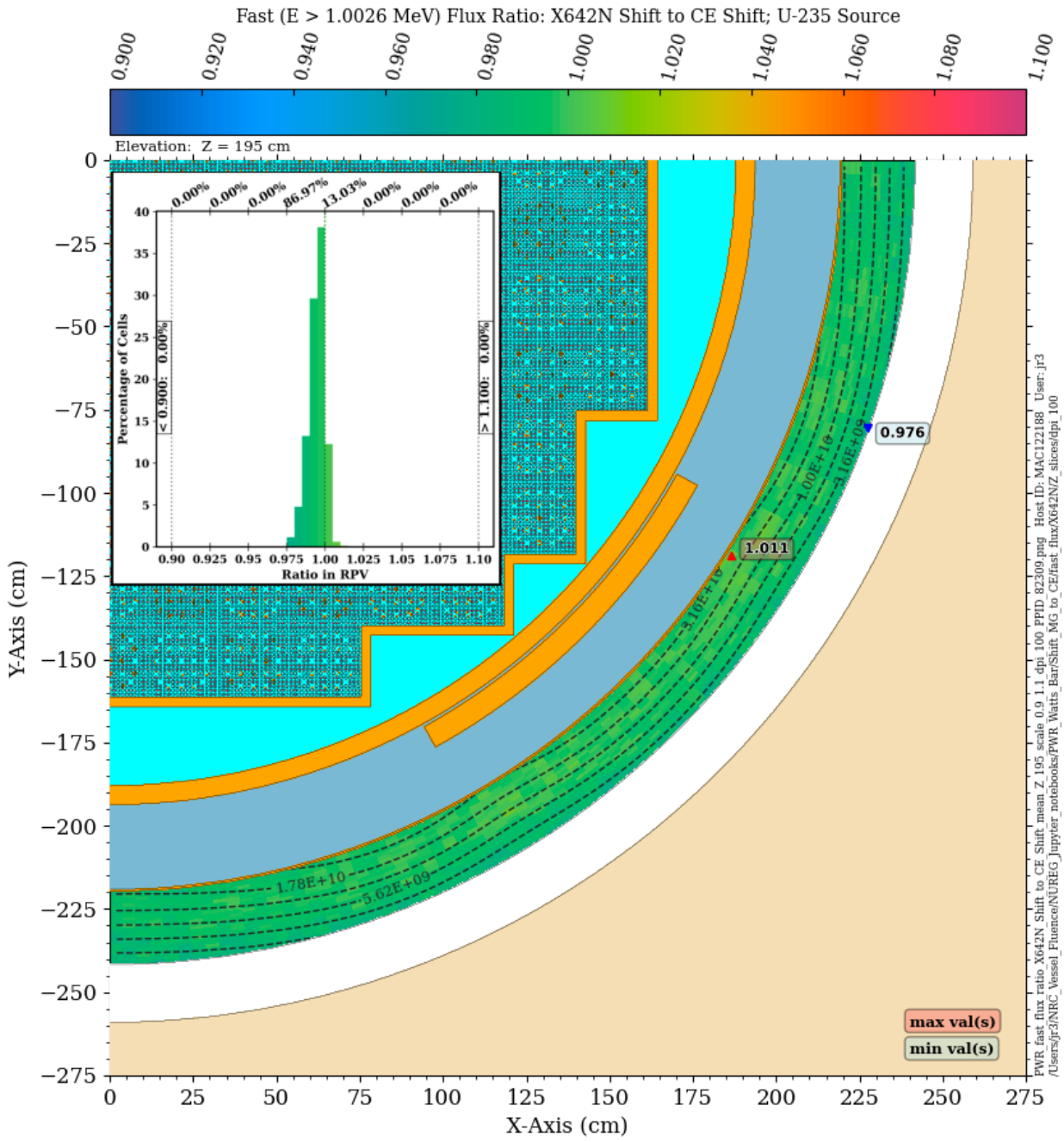

Figure 3-15 Fast neutron flux ratio in the PWR RPV: X642N Shift/CE Shift. Plan view at Z = 195 cm. The contour lines are the fast flux from the CE solution

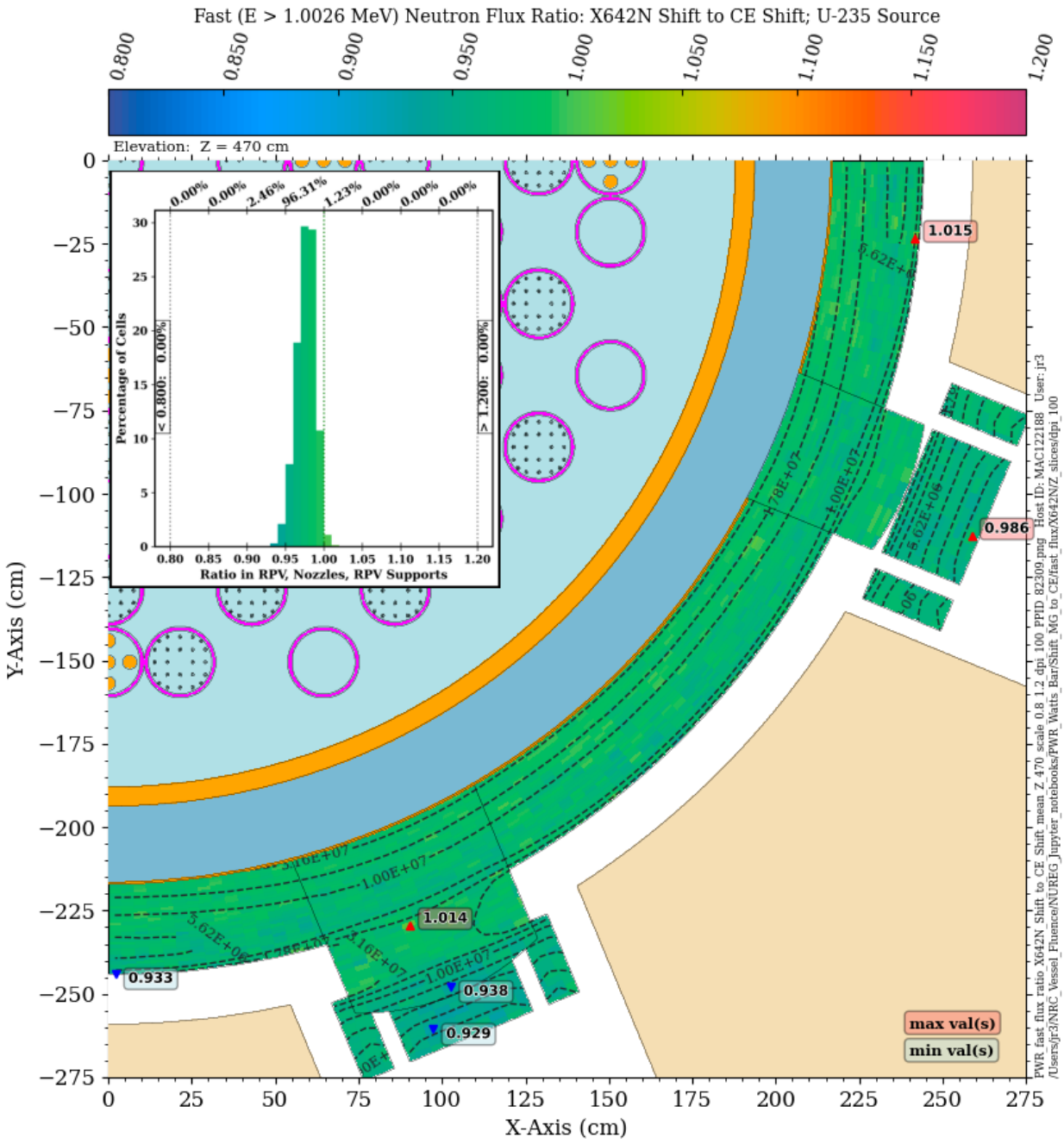

Figure 3-16 Fast neutron flux ratio in the PWR RPV: X642N Shift/CE Shift. Plan view at Z = 470 cm. The contour lines are the fast flux from the CE solution. Note the change in scale relative to Figure 3-15

3.3 DPA rate calculations

While the fast neutron fluence is often used for neutron damage estimates in RPVs, the accumulated dpa metric is often considered to be a more physically justified for neutron radiation damage effects [19], [20]. Unlike the fast neutron flux, the dpa rate is sensitive to spatial variations of the neutron energy spectrum over the entire neutron energy range. The dpa cross-section data [10] are shown in Figure 3-17. Because of variations in the neutron energy spectrum at different RPV locations (Figure 3-3), the fraction of the dpa rate due to neutrons in a specified energy interval will change as a function of location, as shown in Section 2.1.

As a result of these spectral effects, the difference in dpa rates calculated using MG and CE cross-section data will not mirror the difference in fast flux levels. For the BUGLE-B7 library, the difference in dpa rates compared to a CE solution is significantly greater than the difference in fast neutron flux rates. This can be seen when comparing Figure 3-5 with Figure 3-18 and Figure 3-6 with Figure 3-19. Even at the inner surface of the RPV near the core midplane, the BUGLE-B7 dpa rate is more than 5% lower than the dpa rate from a CE solution. At the outer surface of the RPV at the same elevation, the BUGLE-B7 solution underpredicts the CE solution by 20%. At the elevation of the vessel supports, the BUGLE-B7 solution is more than 20% lower than the CE solution in nearly all mesh tally voxels in the RPV, nozzle, and nozzle supports, with differences of more than 35% at some locations in the nozzle supports. As noted previously, this is an area where the EOL dpa in the nozzle supports could exceed the dpa monitoring threshold given in ASTM E1035-18 [11], even though the EOL fluence is likely to be below the neutron fluence monitoring threshold.

The MG/CE dpa rate ratios for calculations using the VITAMIN-B7 and X200N47Gv71 libraries are shown in Figure 3-20 through Figure 3-23. The MG/CE agreement with these libraries is significantly improved at the core midplane elevation relative to the BUGLE-B7 comparisons, but there are still substantial differences at Z = 470 cm, particularly in nozzle supports. The improvement relative to the BUGLE-B7 solution is likely due in part to the much finer energy-group widths for neutron energies below 1.0026 MeV in the VITAMIN-B7 and X200N47G libraries compared to the BUGLE-B7 library (Figure 3-4). The finer group structure at these energies is important because of the increasing contribution to the dpa rate from neutrons with energies below 1.0026 MeV in the outer part of the RPV, and especially at the elevation of the vessel supports.

The Shift solution with the X999N library shows further improvements at the core midplane (Figure 3-24) and the vessel support elevation (Figure 3-25). Results for the X956N and X642N libraries are shown in Figure 3-26 through Figure 3-29. The X956N library provides excellent agreement with the CE solution at the core midplane, with nearly all mesh tally voxels agreeing within 2.5%. At the elevation of the vessel supports, the deviation is greater, but all mesh tally voxels are within 10% of the CE solution, even in the vessel supports. The accuracy of the X642N solution is degraded relative to the X956N solution, likely due to the coarser group structure of the X642N library for energies below 1.0026 MeV.

Results of these comparisons suggest that dpa rates calculated using the BUGLE-B7 library may be slightly nonconservative in the beltline region and substantially nonconservative in the extended beltline region. Even the VITAMIN-B7 and X200N47Gv71 libraries tend to underpredict the dpa rate (by factors of up to 20% or more) at the elevation of the vessel supports. Only the X956N library provides solutions that agree within 10% of the CE solution at both elevations.

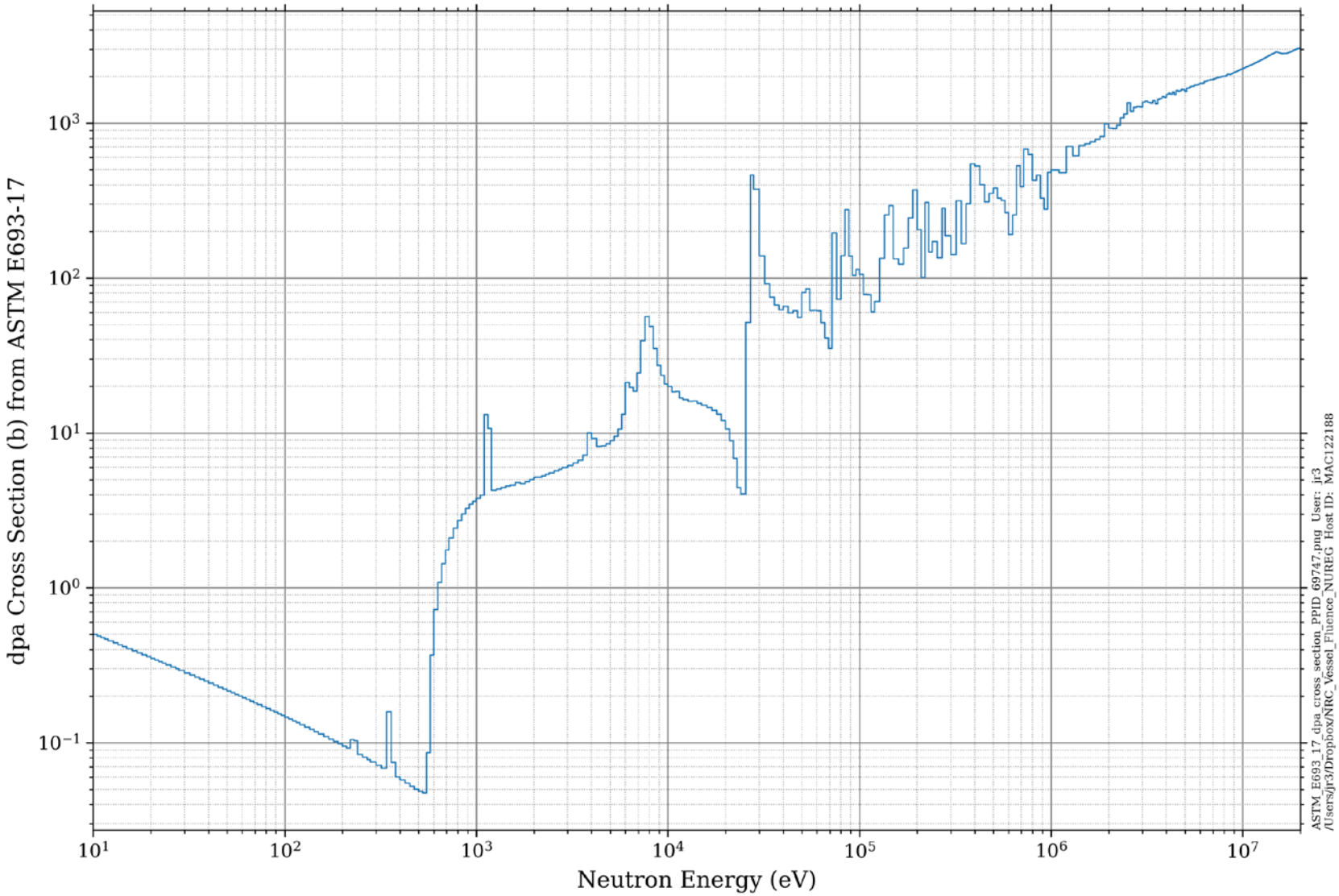

Figure 3-17 Neutron dpa cross section data from ASTM E693-17(reproduced with permission. ASTM E693-17, copyright ASTM International, 100 Barr Harbor Drive, West Conshohocken, PA 19428)

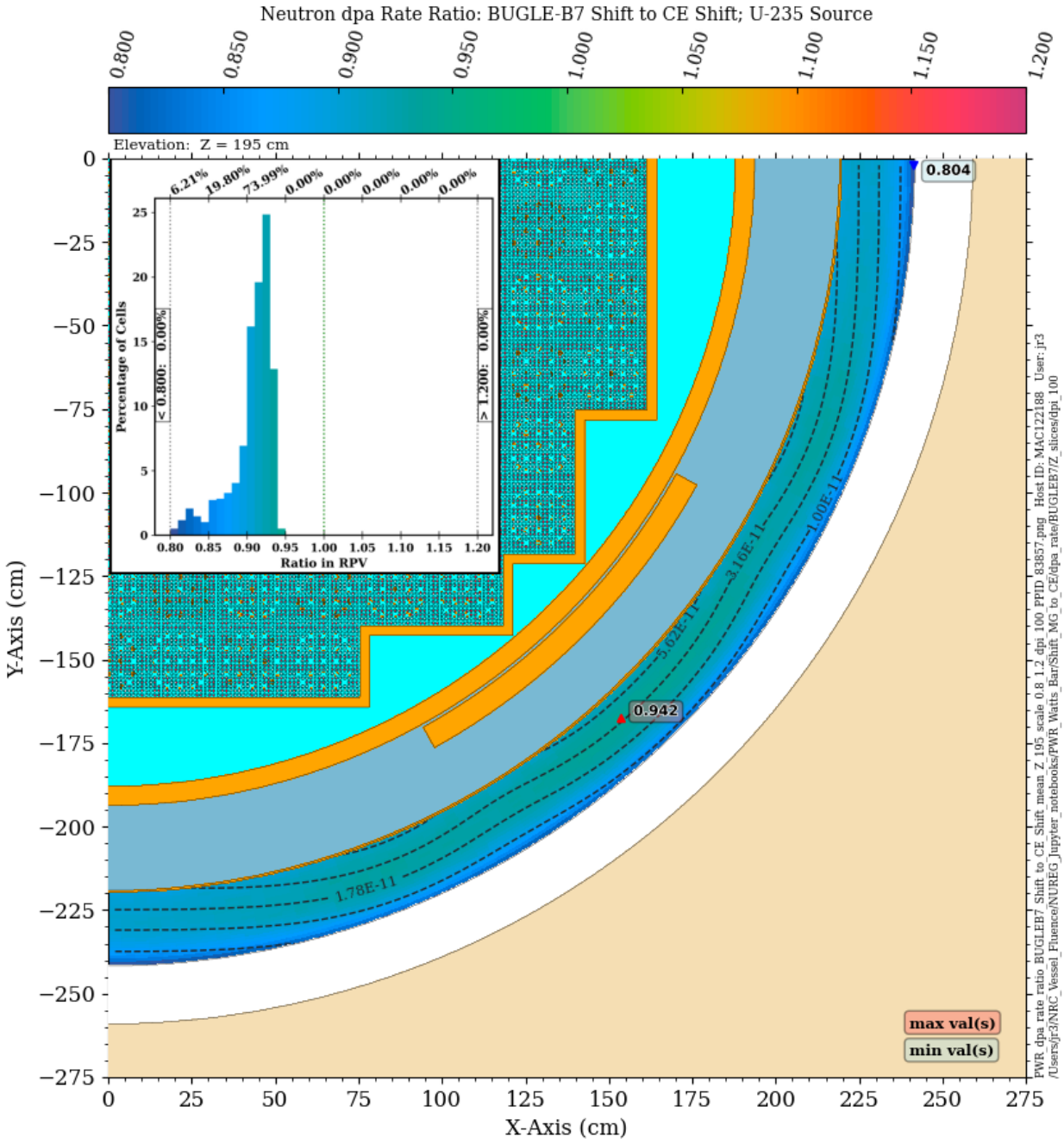

Figure 3-18 DPA rate ratio in the PWR model: BUGLE-B7 Shift/CE Shift. Plan view at Z = 195 cm. The contour lines are the dpa rate from the CE solution

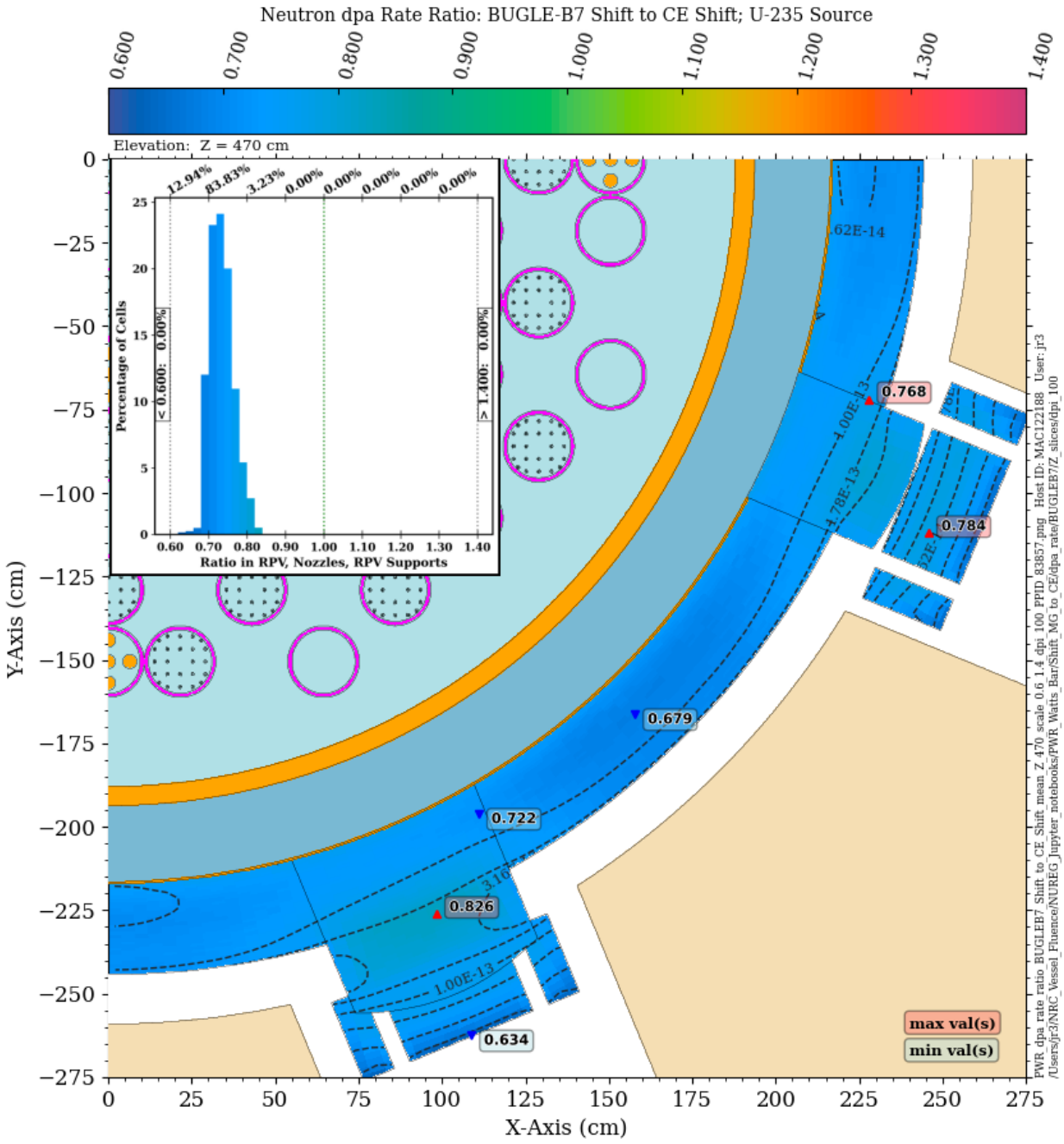

Figure 3-19 DPA rate ratio in the PWR model: BUGLE-B7 Shift/CE Shift. Plan view at Z = 470 cm. The contour lines are the dpa rate from the CE solution. Note the change in scale relative to Figure 3-18

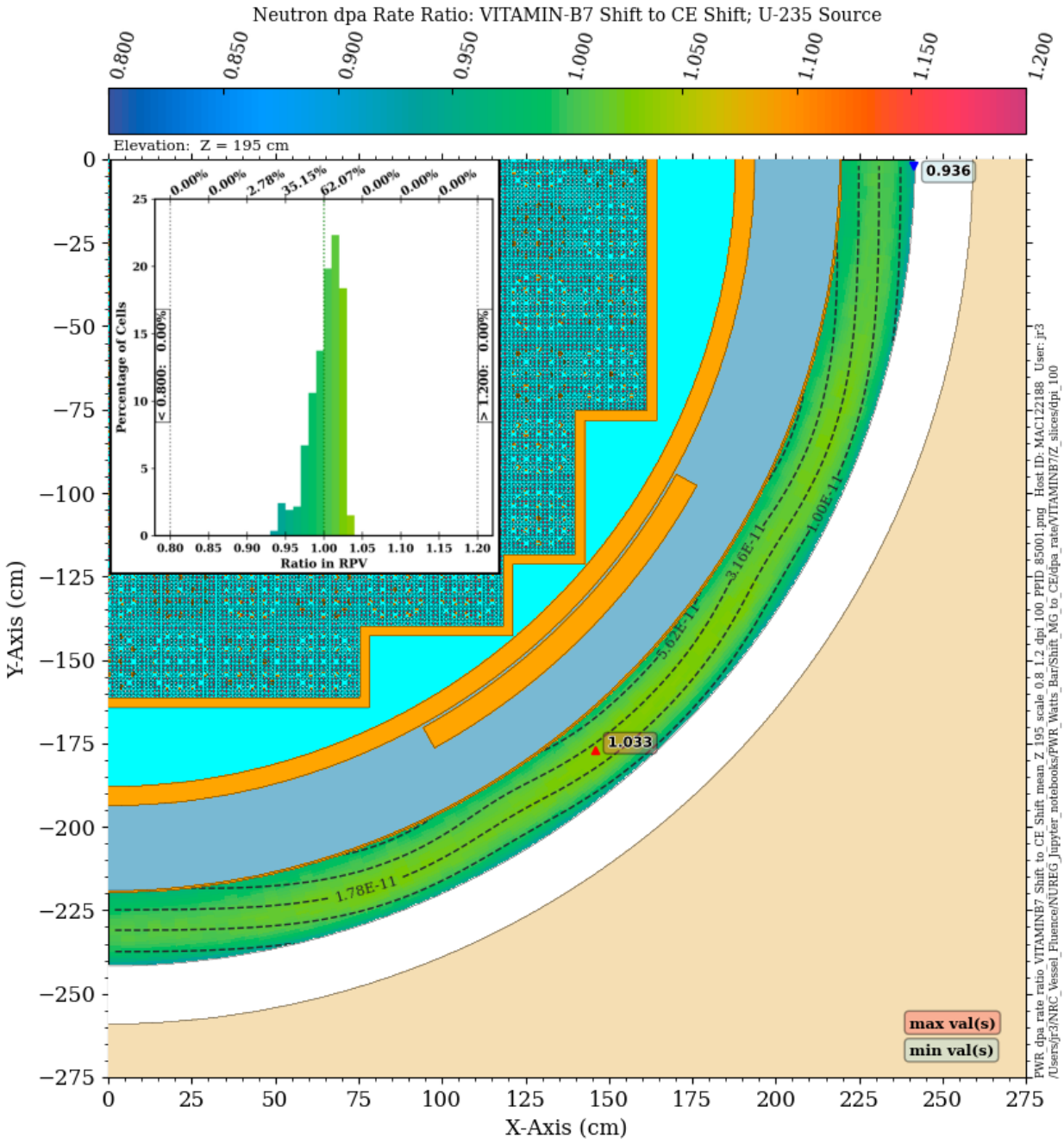

Figure 3-20 DPA rate ratio in the PWR model: VITAMIN-B7 Shift/CE Shift. Plan view at Z = 195 cm. The contour lines are the dpa rate from the CE solution

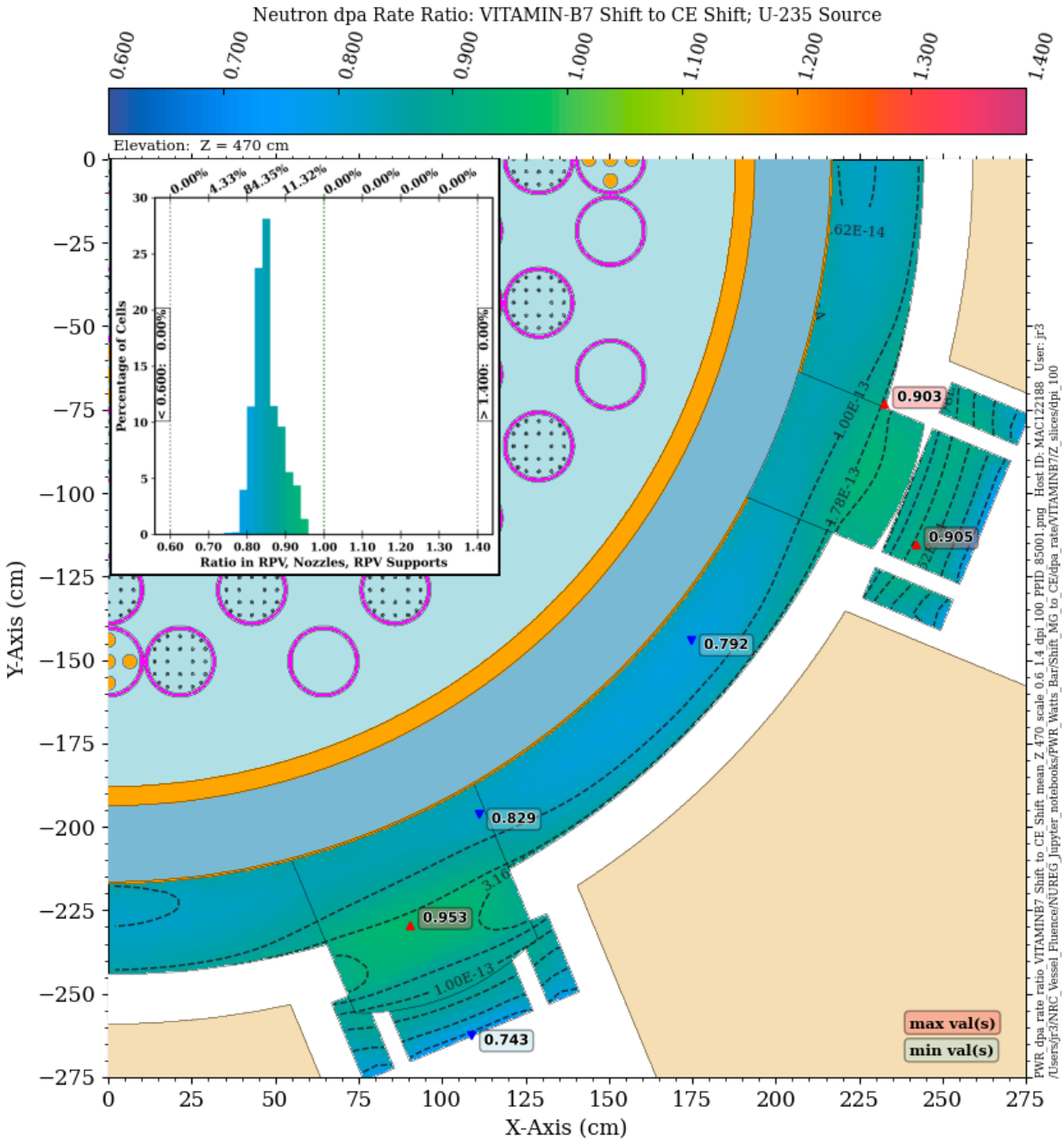

Figure 3-21 DPA rate ratio in the PWR model: VITAMIN-B7 Shift/CE Shift. Plan view at Z = 470 cm. The contour lines are the dpa rate from the CE solution. Note the change in scale relative to Figure 3-20

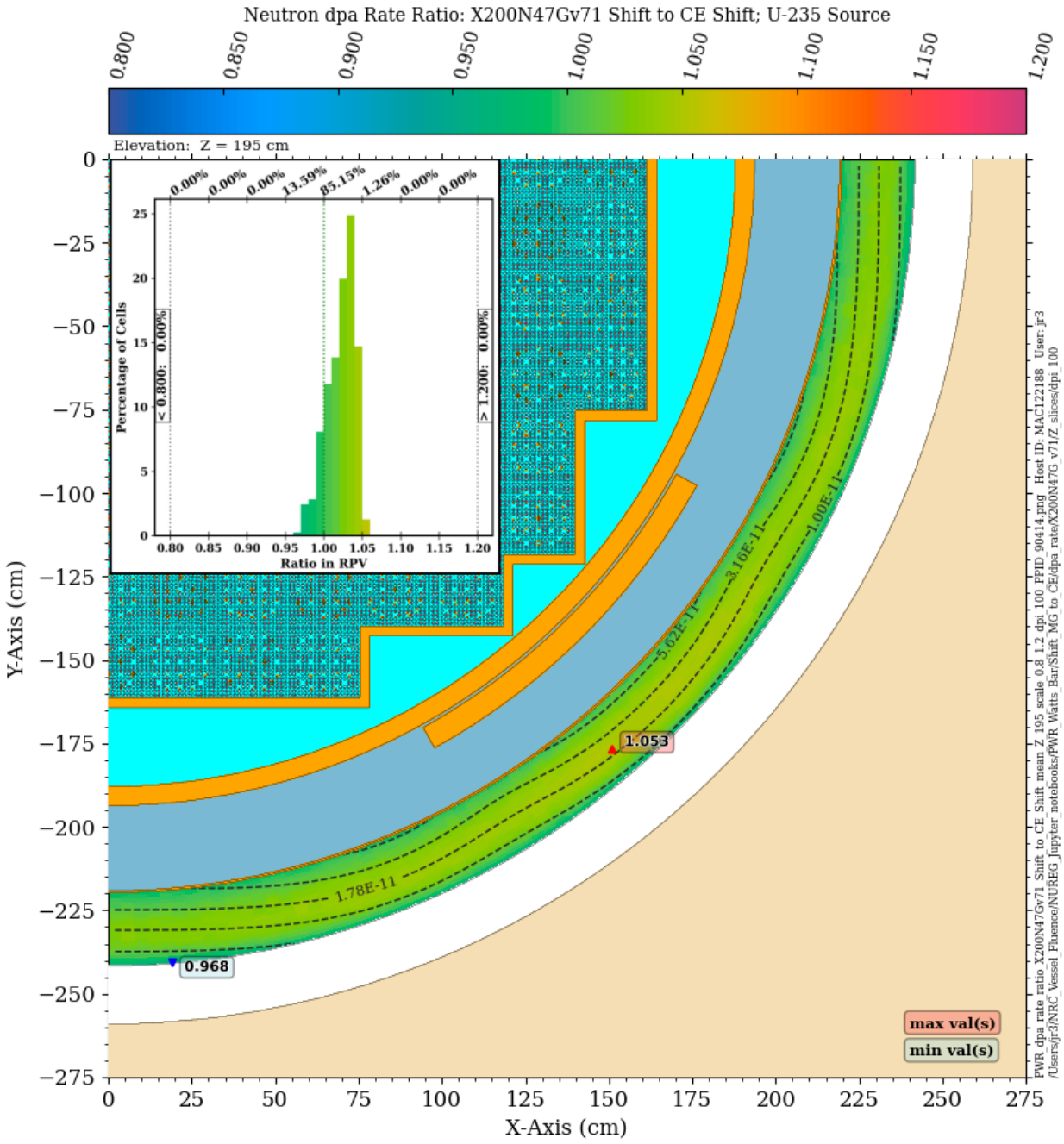

Figure 3-22 DPA rate ratio in the PWR model: X200N47Gv71 Shift/CE Shift. Plan view at Z = 195 cm. The contour lines are the dpa rate from the CE solution

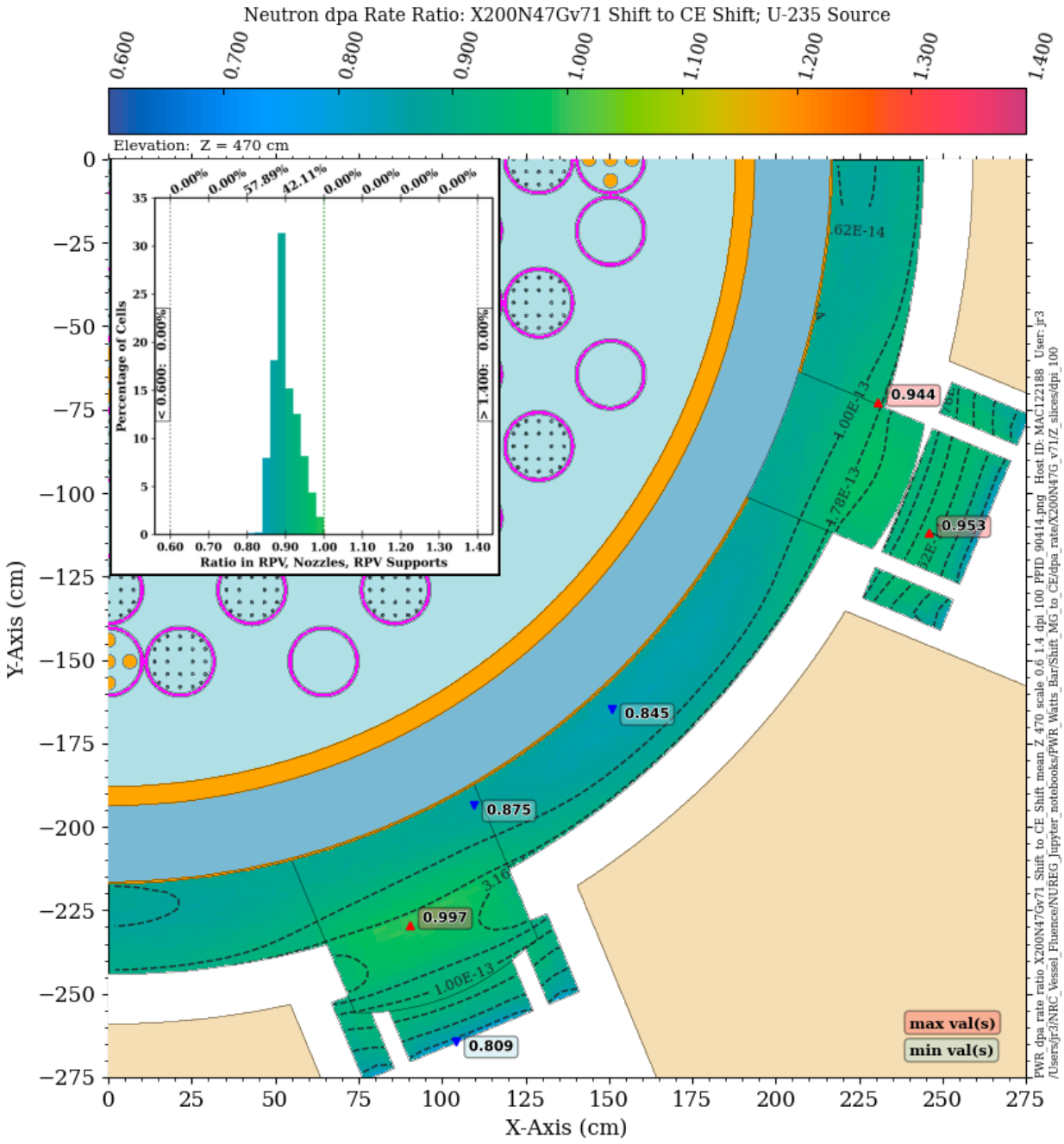

Figure 3-23 DPA rate ratio in the PWR model: X200N47Gv71 Shift/CE Shift. Plan view at Z = 470 cm. The contour lines are the dpa rate from the CE solution. Note the change in scale relative to Figure 3-22

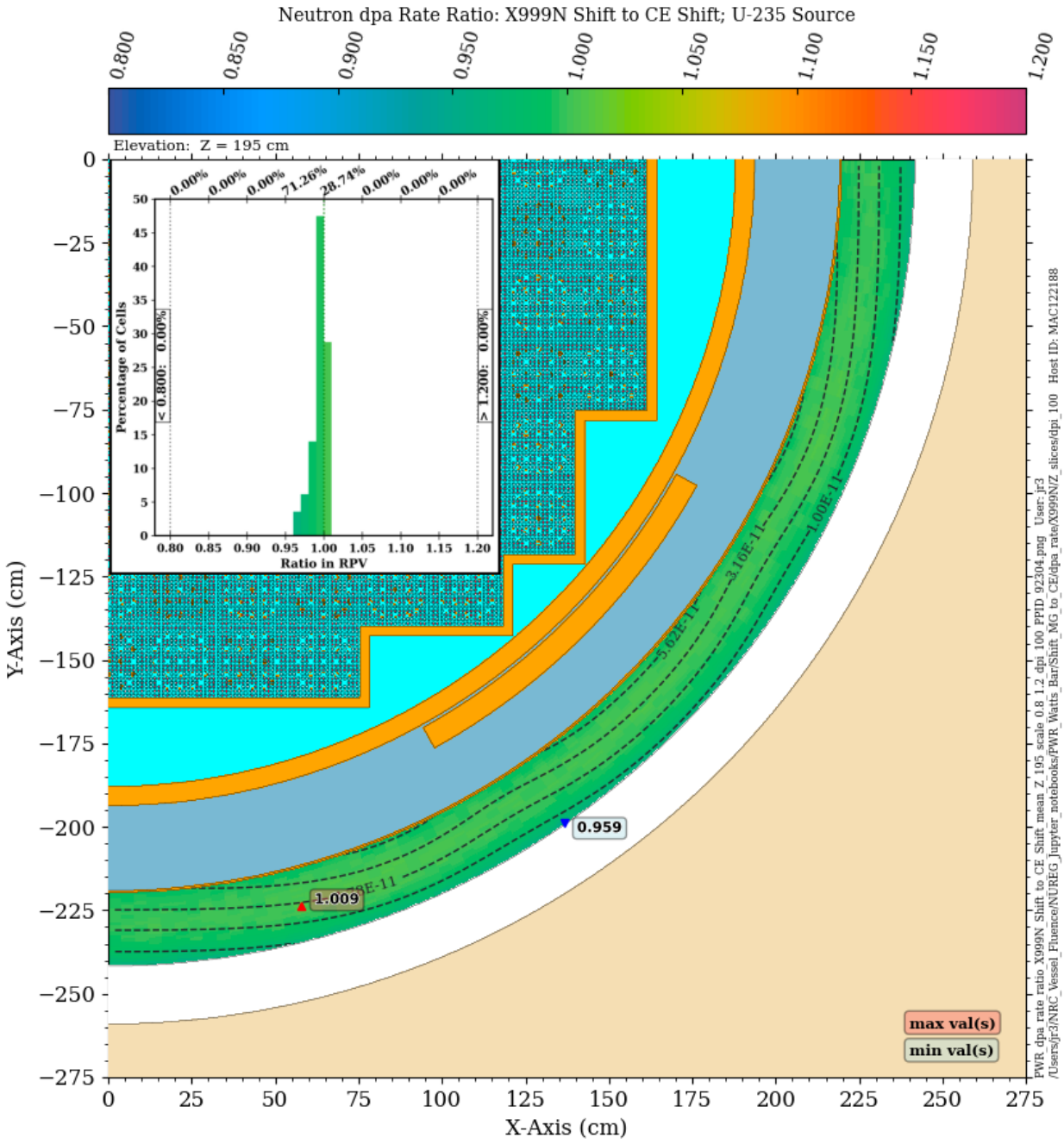

Figure 3-24 DPA rate ratio in the PWR model: X999N Shift/CE Shift. Plan view at Z = 195 cm. The contour lines are the dpa rate from the CE solution

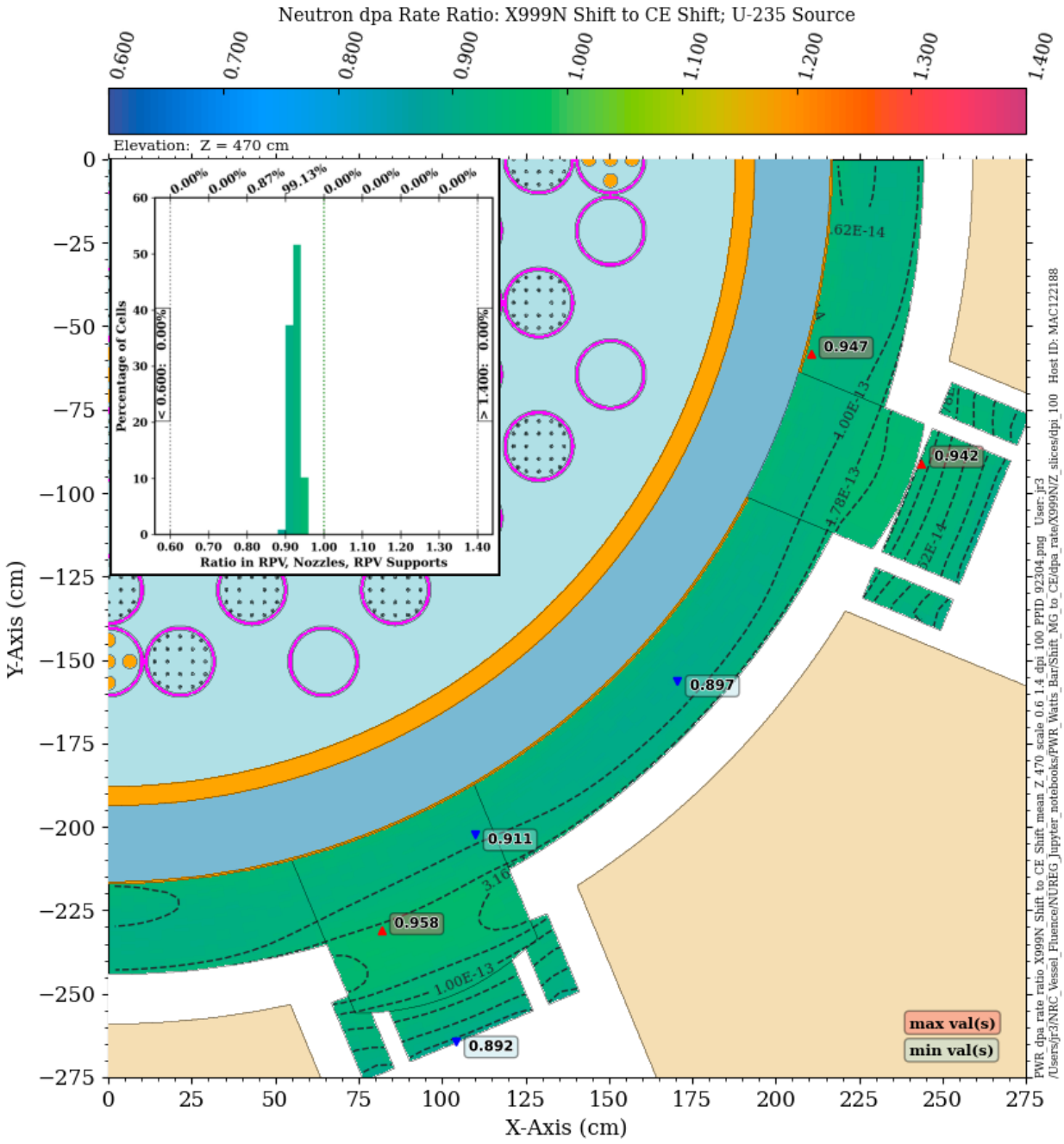

Figure 3-25 DPA rate ratio in the PWR model: X999N Shift/CE Shift. Plan view at Z = 470 cm. The contour lines are the dpa rate from the CE solution. Note the change in scale relative to Figure 3-24

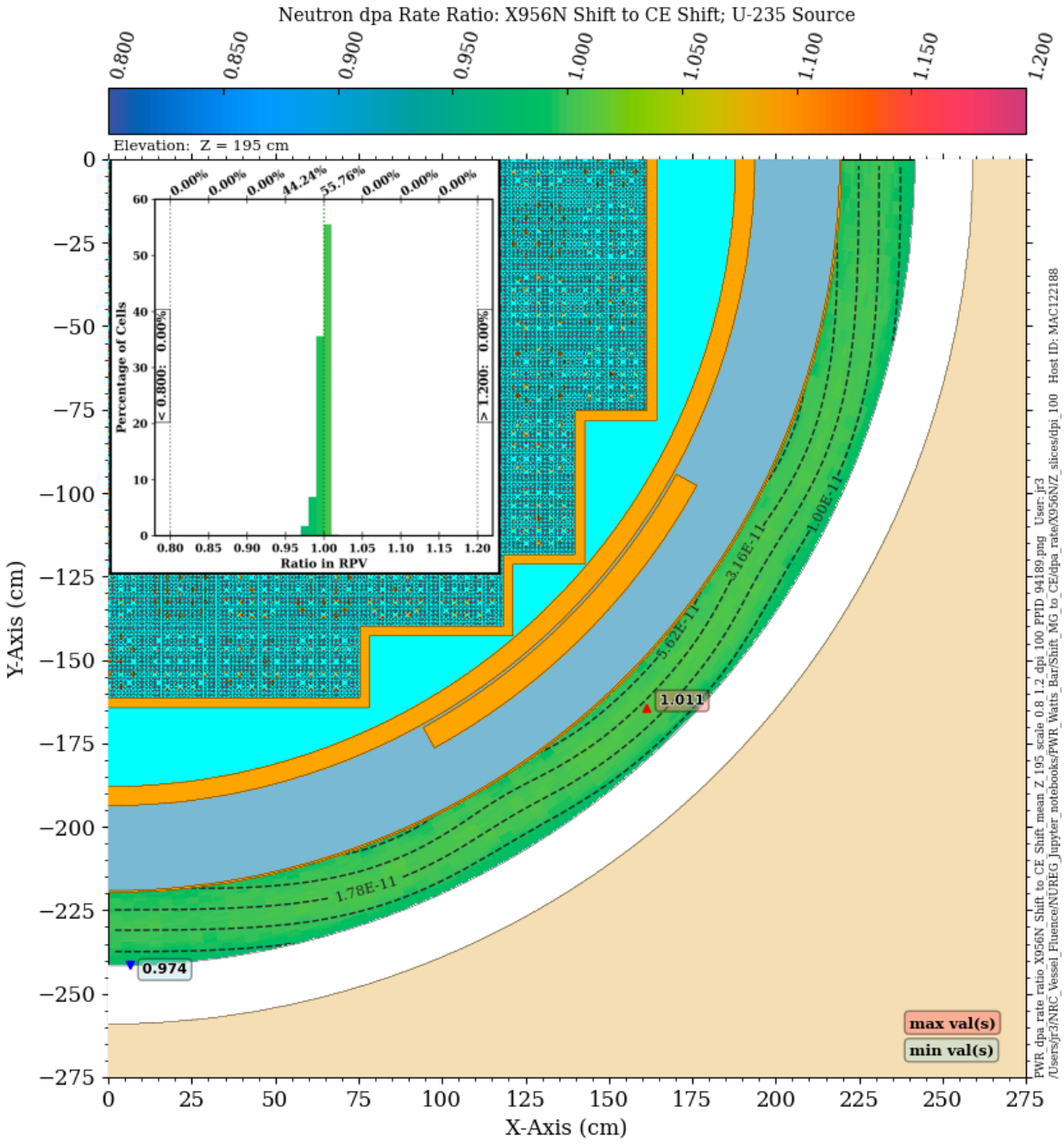

Figure 3-26 DPA rate ratio in the PWR model: X956N Shift/CE Shift. Plan view at Z = 195 cm. The contour lines are the dpa rate from the CE solution

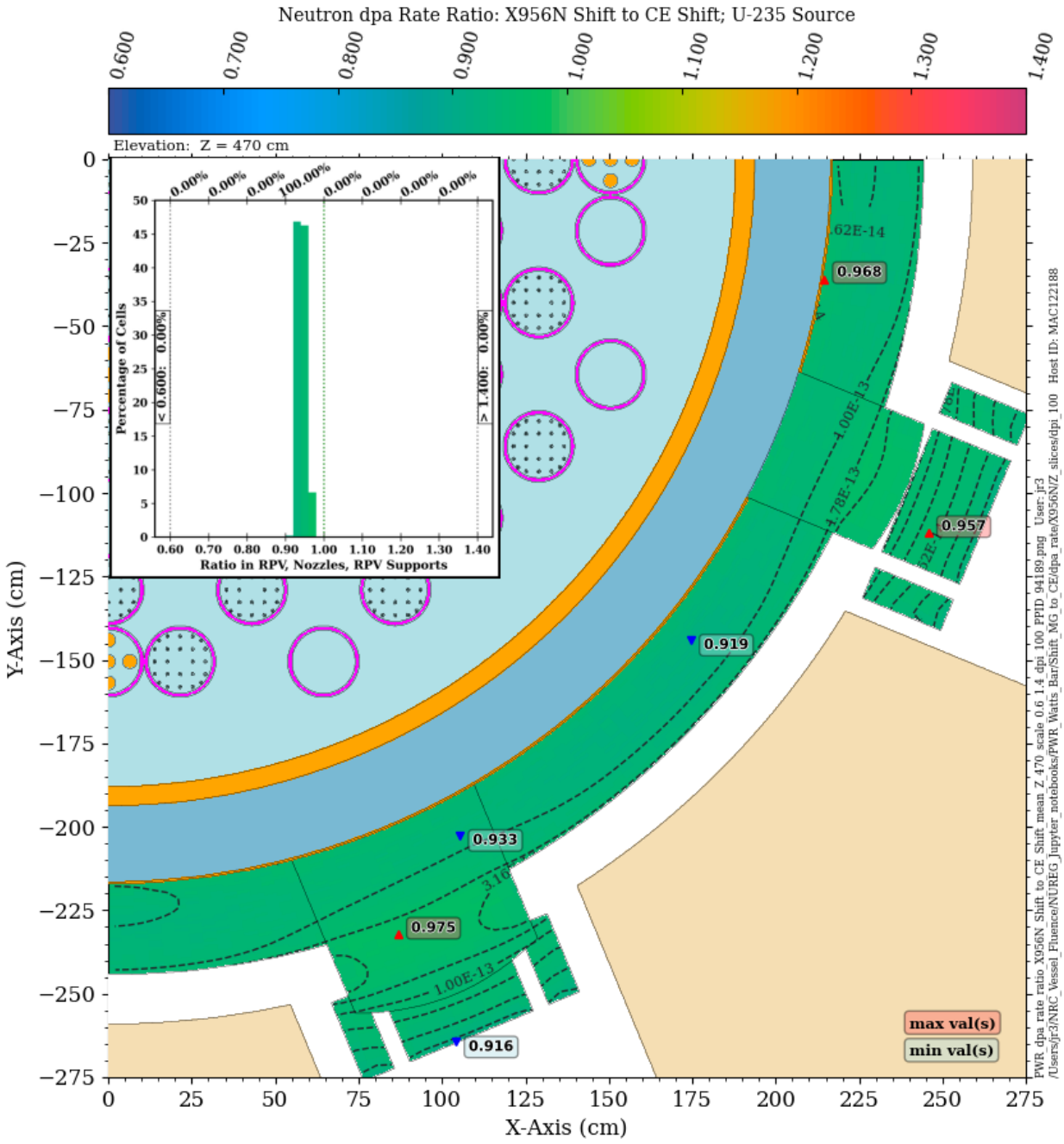

Figure 3-27 DPA rate ratio in the PWR model: X956N Shift/CE Shift. Plan view at Z = 470 cm. The contour lines are the dpa rate from the CE solution. Note the change in scale relative to Figure 3-26

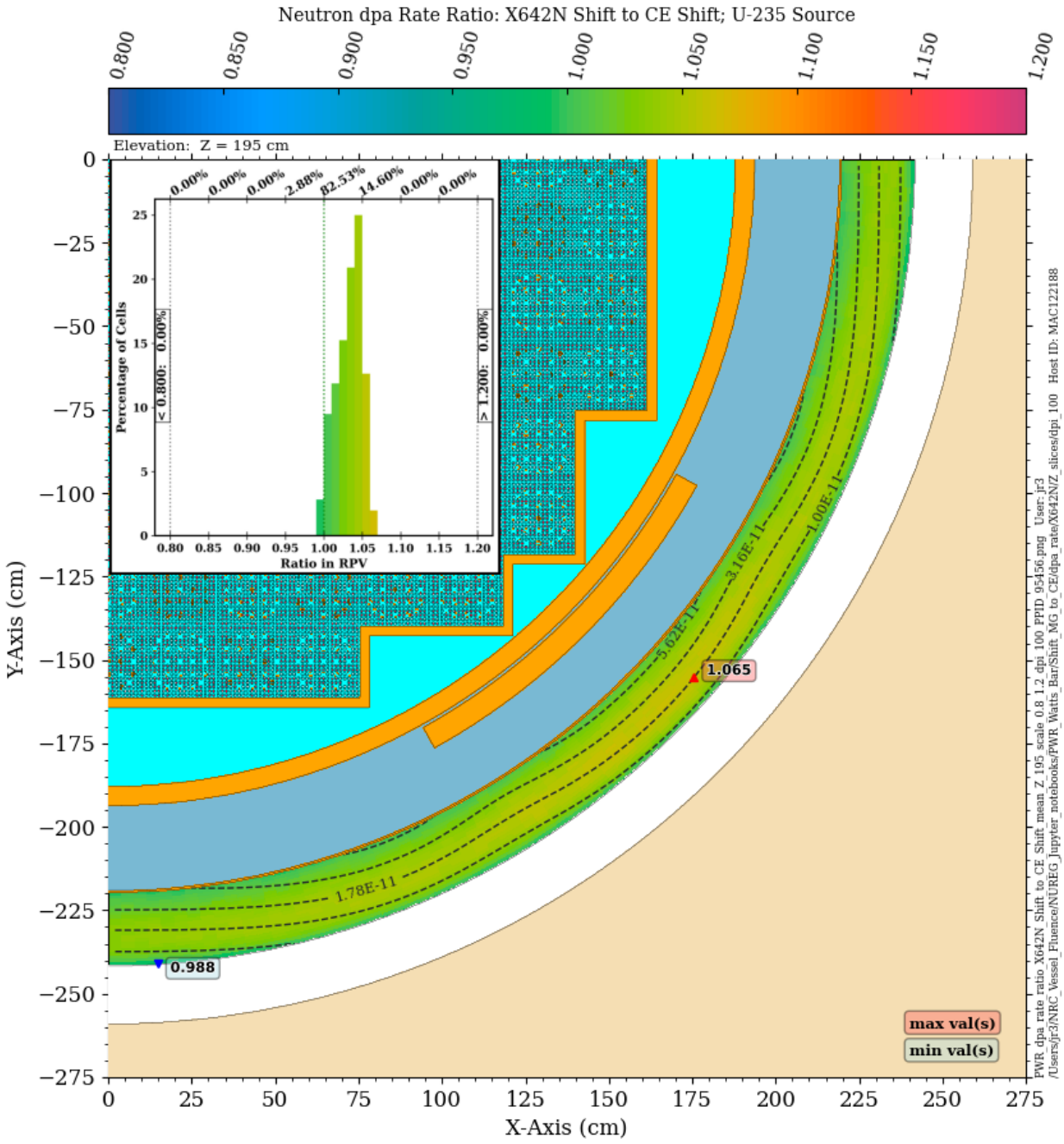

Figure 3-28 DPA rate ratio in the PWR model: X642N Shift/CE Shift. Plan view at Z = 195 cm. The contour lines are the dpa rate from the CE solution

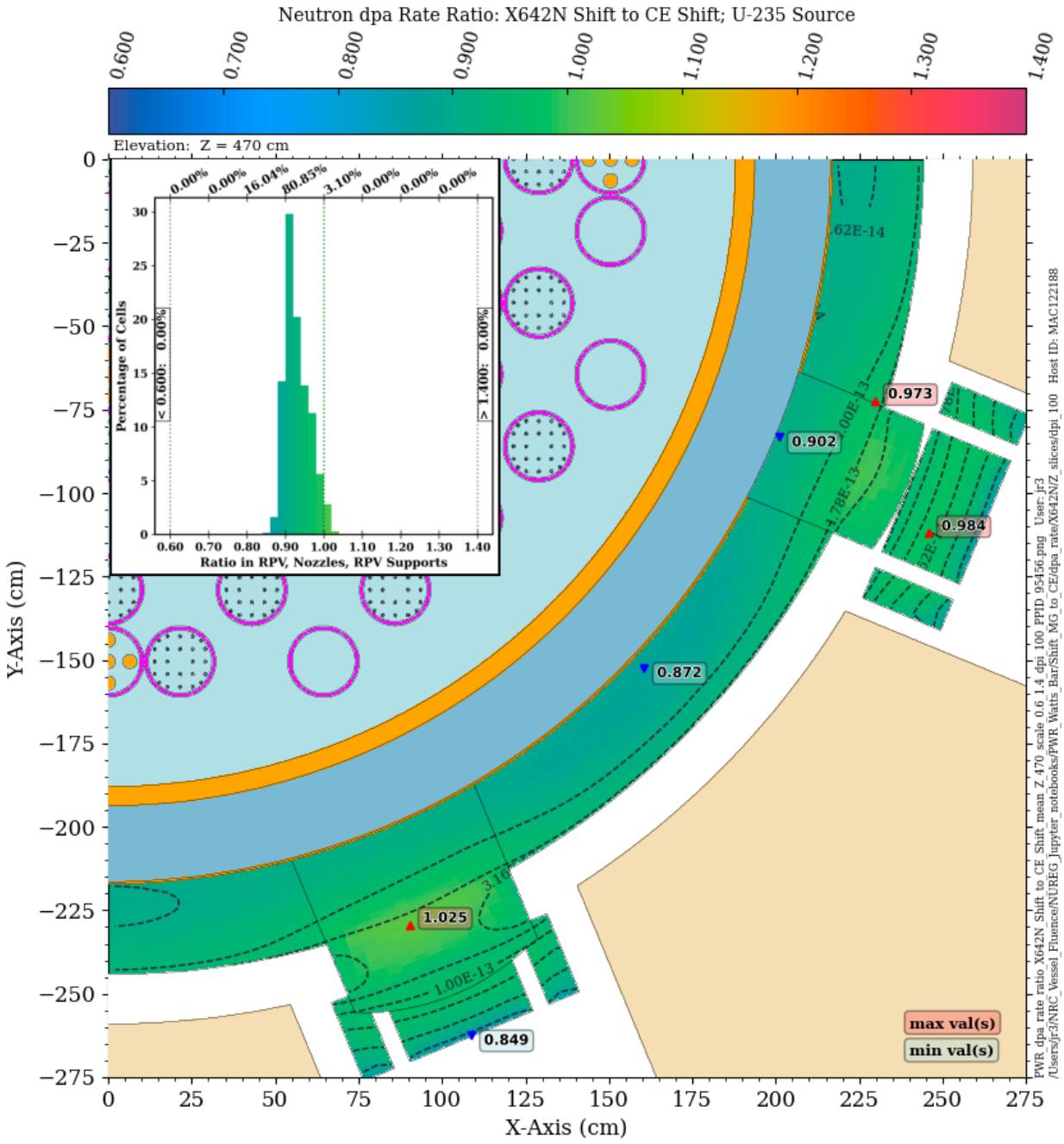

Figure 3-29 DPA rate ratio in the PWR model: X642N Shift/CE Shift. Plan view at Z = 470 cm. The contour lines are the dpa rate from the CE solution. Note the change in scale relative to Figure 3-28

3.4 Dosimetry reaction rates

The dosimetry reaction rates considered in this study are based on dosimetry measurements that were used in the validation of the VITAMIN-B7 and BUGLE-B7 libraries for locations within the traditional beltline region. These reactions have a broad range of threshold energies, and consequently can be used to assess the ability of radiation transport calculations to accurately model neutron transport over the energies of concern for radiation damage. Cross sections for the dosimetry reactions are shown in Figure C-1 and Figure C-2 of APPENDIX C.

For all of the MG/CE ratio plots in this section, ratio values are shown in the cavity gap as well as in the RPV, nozzles, and nozzle supports. The cavity gap is included in the ratios because any ex-vessel dosimetry measurements would be made within the gap.

3.4.1 ^{27}Al (n,α)

The ^{27}Al (n,α) reaction has a threshold energy of 3.25 MeV and a 90% energy response range of 6.45 to 11.9 MeV (Table C-1). For this dosimetry reaction, the Shift solution using the BUGLE-B7 library is in relatively good agreement with the CE Shift solution. At the core midplane elevation (Figure 3-30), all of the mesh tally voxels from the BUGLE-B7 solution are within 5% of the CE solution, and over 93% are within 2.5%. At an elevation of 470 cm (Figure 3-31), the BUGLE-B7 solution appears to have a bias of ~3.5% below the CE solution.

The Shift solution using the VITAMIN-B7 (Figure 3-32 and Figure 3-33) library shows no significant differences relative to the BUGLE-B7 solution.

The Shift solution using the X200N47G library is in excellent agreement with the CE solution. Nearly 98% of the ratio values at the core midplane (Figure 3-34) are within 2.5% of unity. At Z = 470 cm (Figure 3-35) nearly 95% of the X200N47G values are within 5% of the CE solution. Results using the X956N library (not shown) are very consistent with those using the X200N47G library.

The relatively good agreement between the MG and CE Shift solutions may not be surprising, as the majority of the ^{27}Al (n,α) reaction rate occurs at energies where the iron cross section is slowing varying (Figure B-1), so energy groups can be relatively broad compared to lower neutron energies where resonance effects are important and finer group widths are needed.

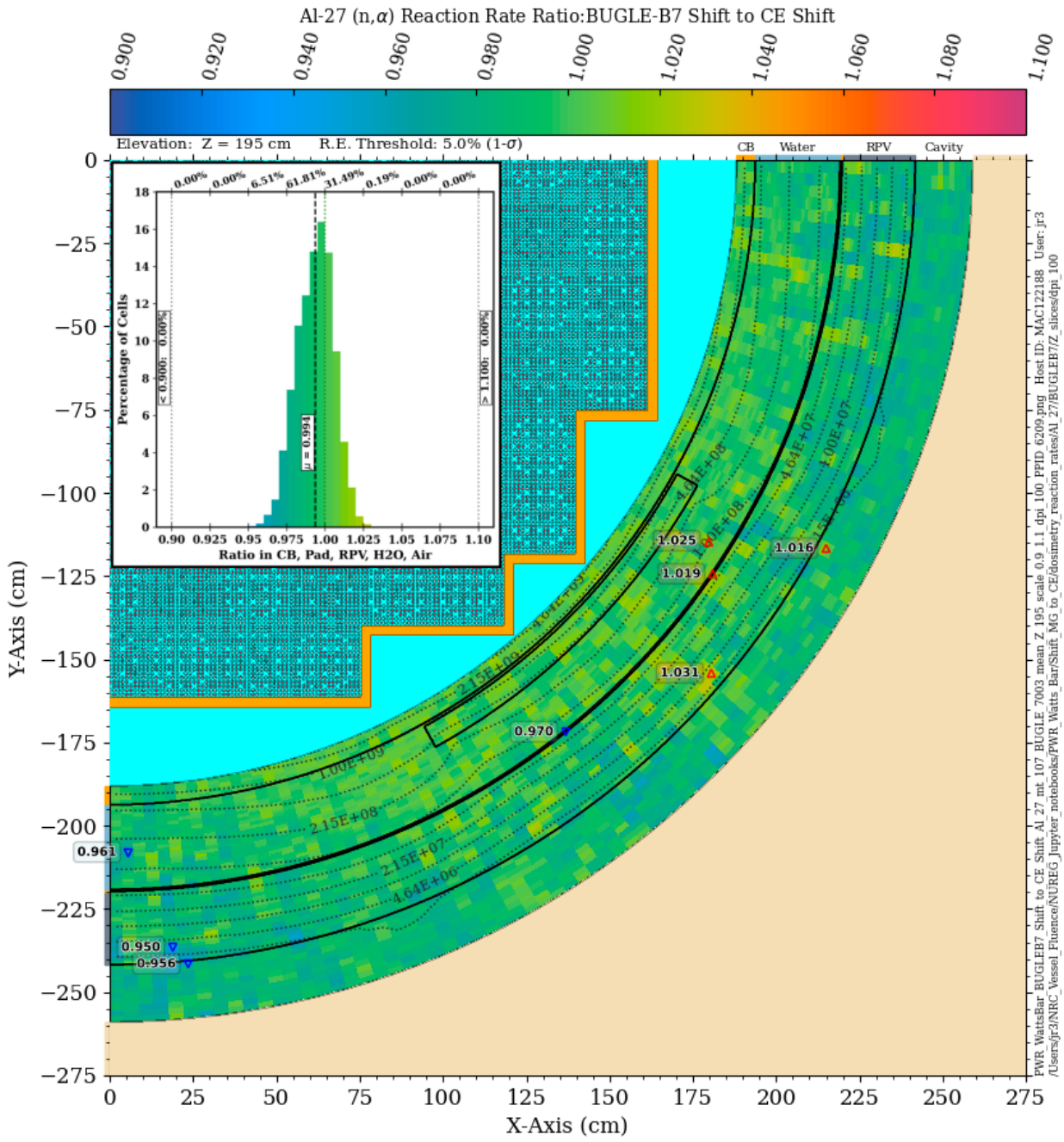

Figure 3-30 **^{27}Al (n,α) reaction rate ratio in the PWR model: BUGLE-B7 Shift/CE Shift. Plan view at Z = 195 cm. The contour lines are the reaction rate values from the CE solution**

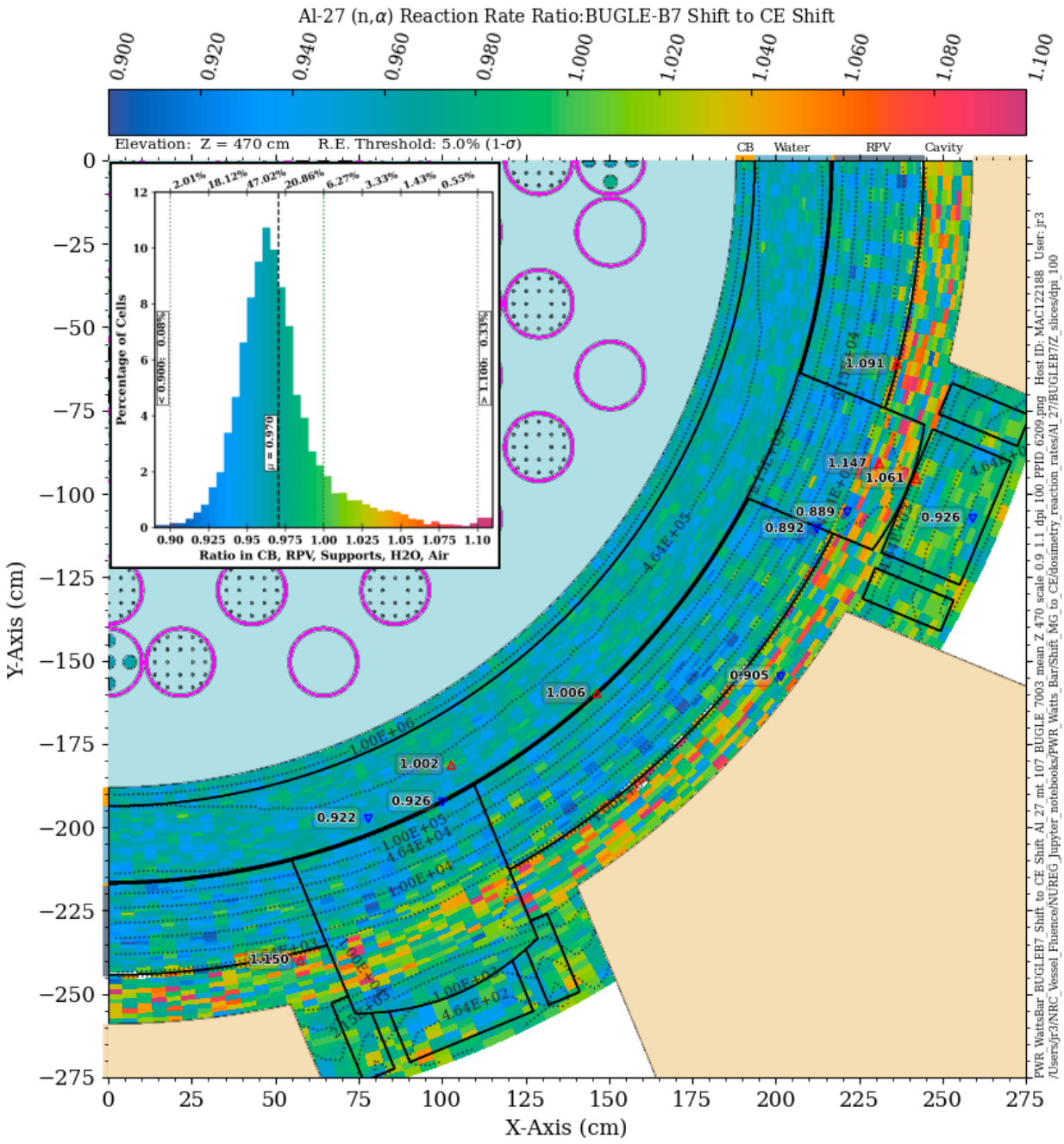

Figure 3-31 **^{27}Al (n,α) reaction rate ratio in the PWR model: BUGLE-B7 Shift/CE Shift. Plan view at Z = 470 cm. The contour lines are the reaction rate values from the CE solution. Note the change in scale relative to Figure 3-30**

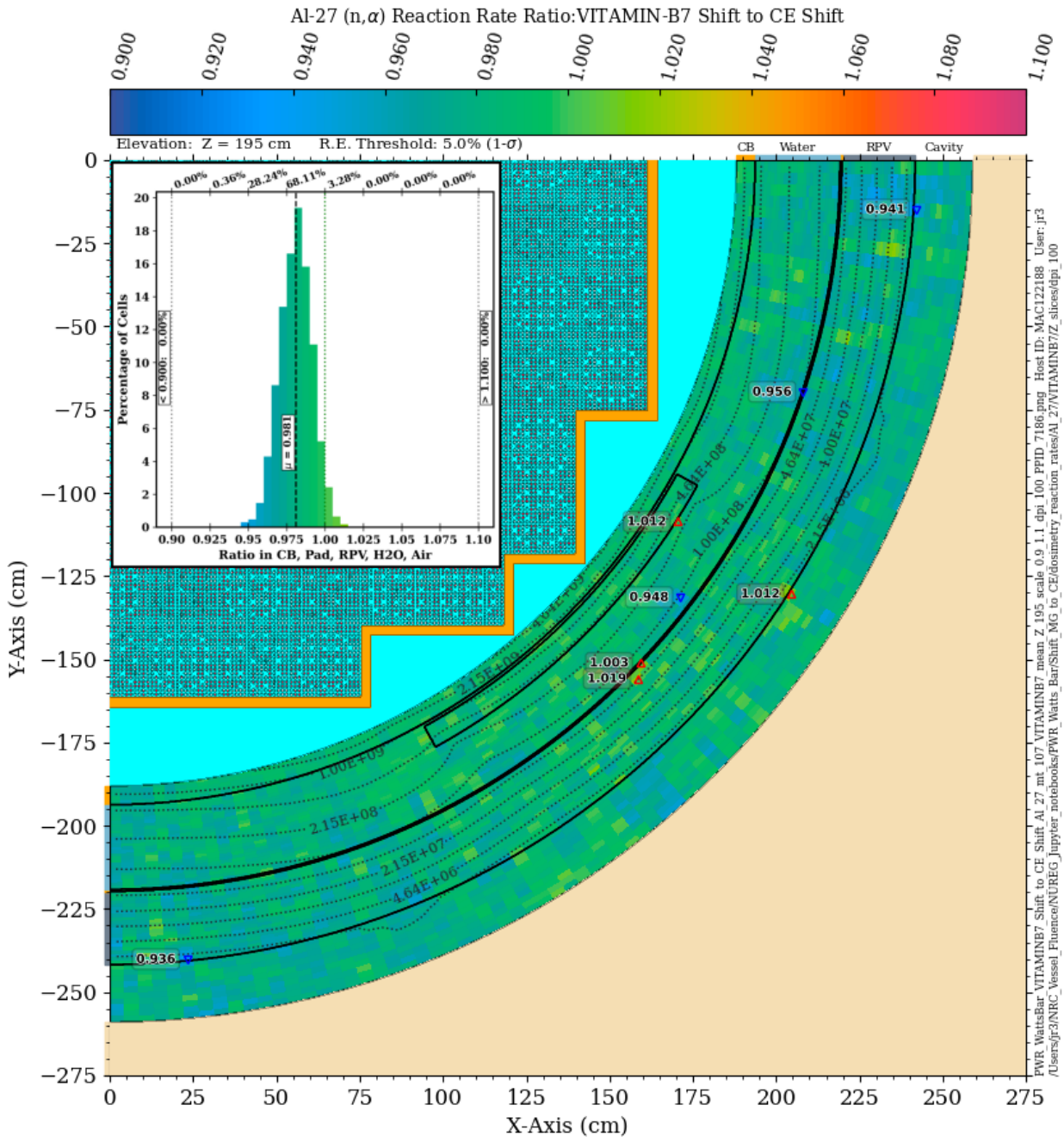

Figure 3-32 **^{27}Al (n,α) reaction rate ratio in the PWR model: VITAMIN-B7 Shift/CE Shift. Plan view at Z = 195 cm. The contour lines are the reaction rate values from the CE solution**

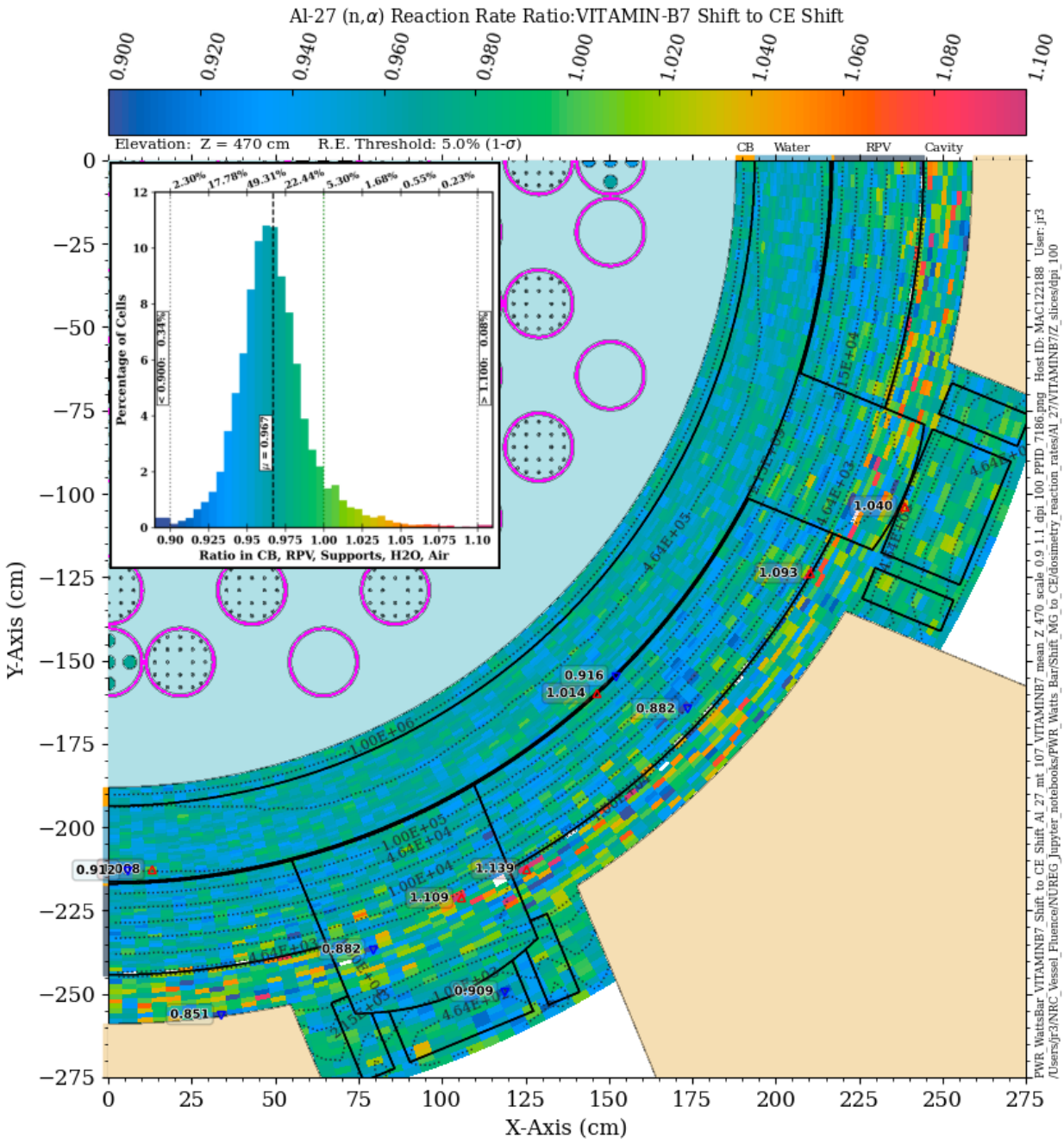

Figure 3-33 **^{27}Al (n,α) reaction rate ratio in the PWR model: VITAMIN-B7 Shift/CE Shift. Plan view at Z = 470 cm. The contour lines are the reaction rate values from the CE solution**

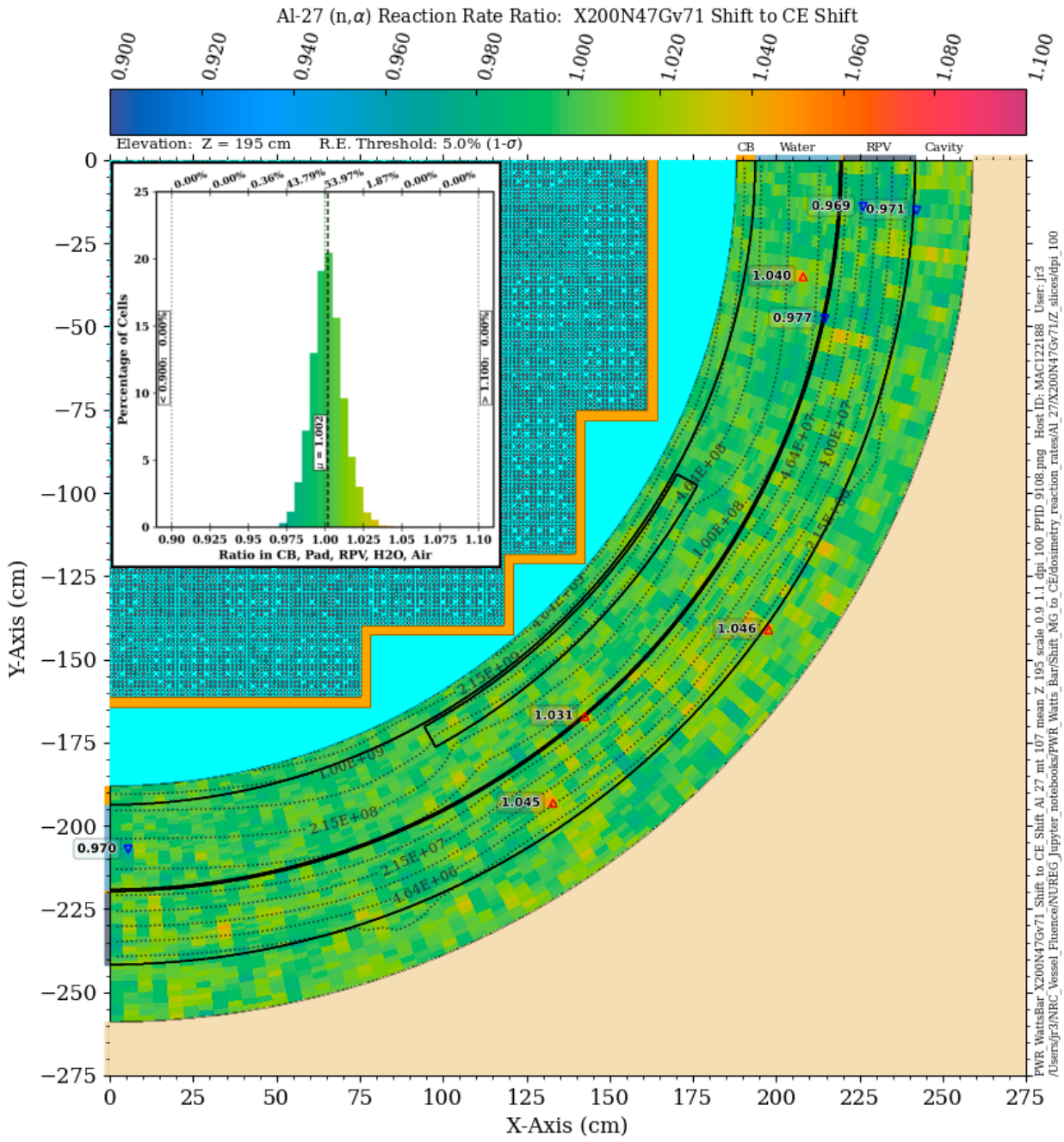

Figure 3-34 ^{27}Al (n,α) reaction rate ratio in the PWR model: X200N47Gv71 Shift/CE Shift. Plan view at Z = 195 cm. The contour lines are the reaction rate values from the CE solution

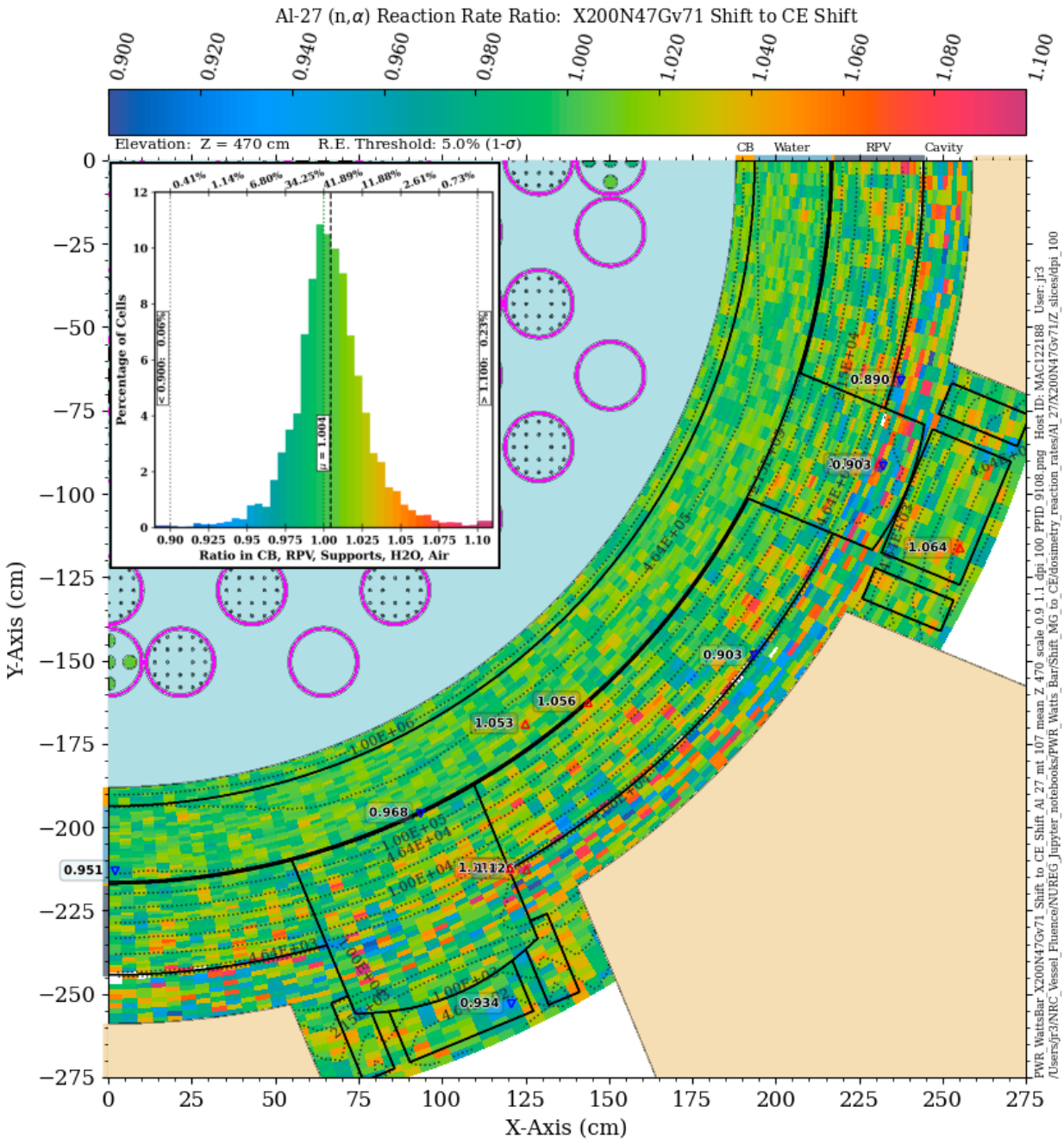

Figure 3-35 **^{27}Al (n,α) reaction rate ratio in the PWR model: X200N47Gv71 Shift/CE Shift. Plan view at Z = 470 cm. The contour lines are the reaction rate values from the CE solution**

3.4.2 ^{63}Cu (n,α)

The ^{63}Cu (n,α) reaction has a threshold energy of 2.25 MeV and a 90% energy response range of 4.53 to 11.0 MeV (Table C-1). For this dosimetry reaction, the Shift solution using the BUGLE-B7 library is in relatively good agreement with the CE Shift solution. At the core midplane elevation (Figure 3-36), over 99% of the mesh tally voxels from the BUGLE-B7 solution are within 5% of the CE solution, and nearly 90% are within 2.5%. At Z = 470 cm (Figure 3-37), the BUGLE-B7 solution appears to have a bias of ~5% below the CE solution.

As was the case with the ^{27}Al (n,α) reaction, the Shift solution using the VITAMIN-B7 library (Figure 3-38 and Figure 3-39) library shows no significant differences relative to the BUGLE-B7 solution.

The Shift MG solution using the X200N47G library is in excellent agreement with the CE solution at both elevations. At the core midplane (Figure 3-40), the X200N47G solution is within 2.5% of the CE solution in nearly 99% of the mesh tally voxels. At Z = 470 cm (Figure 3-41), the agreement is slightly degraded, but the solutions agree within 5% in over 94% of the mesh tally voxels. Results using the X956N library (not shown) are very consistent with those using the X200N47G library.

As with the ^{27}Al MG/CE comparisons (Section 3.4.1), the generally good agreement between the MG and CE solutions is likely due to the fact that the majority of the ^{63}Cu (n,α) reaction rate occurs at energies in which the iron cross section is slowly varying.

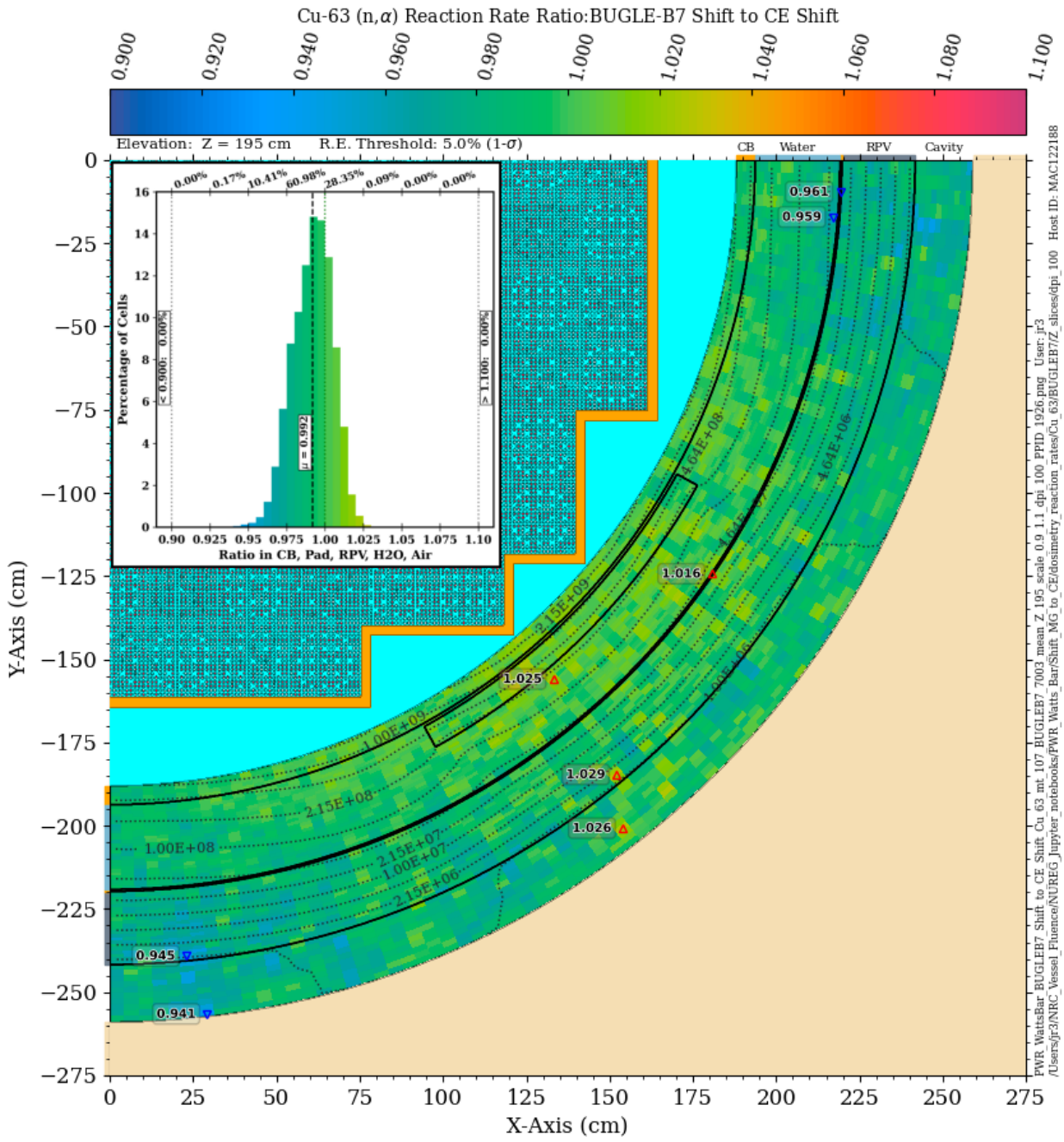

Figure 3-36 **^{63}Cu (n,α) reaction rate ratio in the PWR model: BUGLE-B7 Shift/CE Shift. Plan view at Z = 195 cm. The contour lines are the reaction rate values from the CE solution**

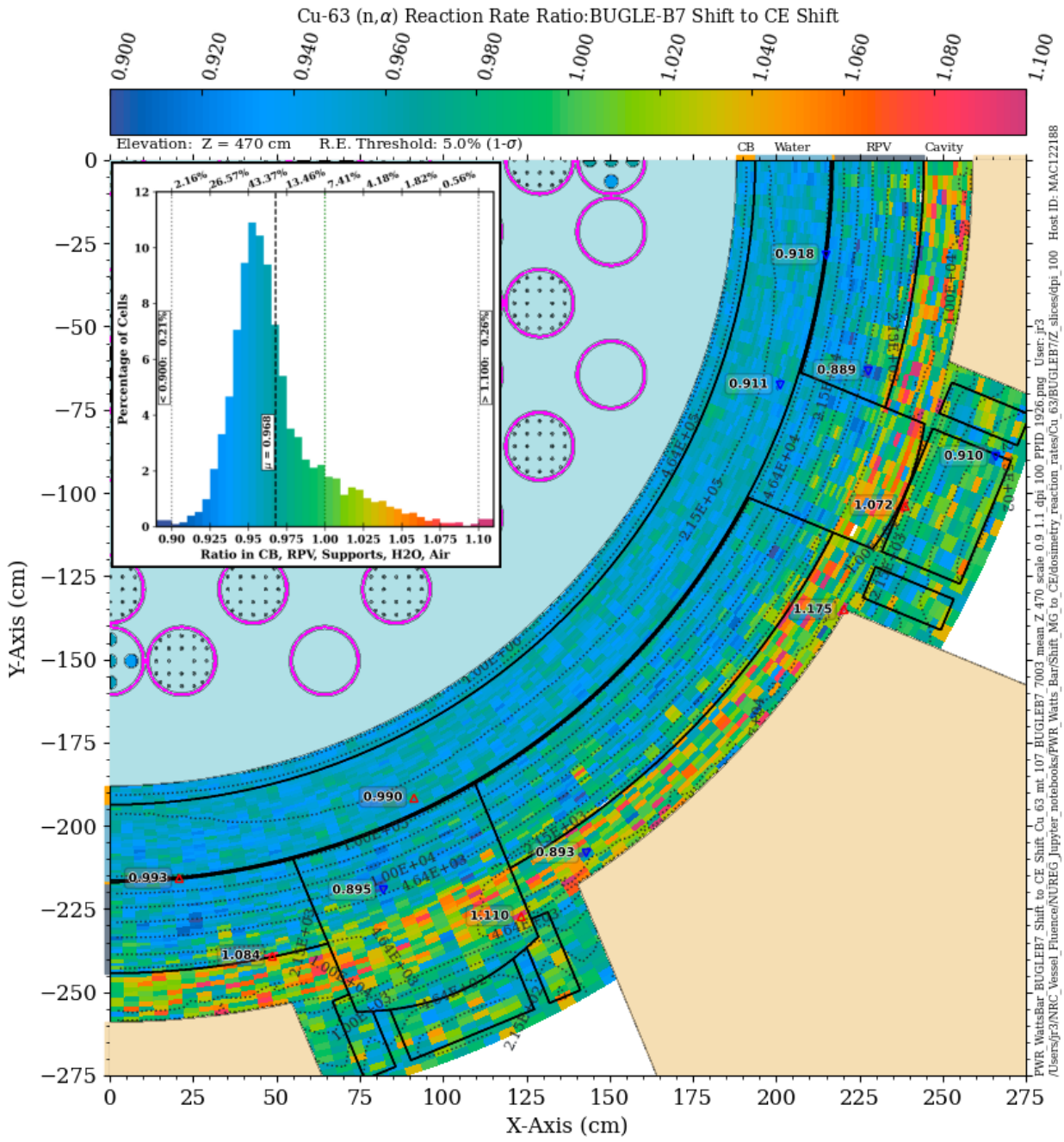

Figure 3-37 ^{63}Cu (n,α) reaction rate ratio in the PWR model: BUGLE-B7 Shift/CE Shift. Plan view at Z = 470 cm. The contour lines are the reaction rate values from the CE solution

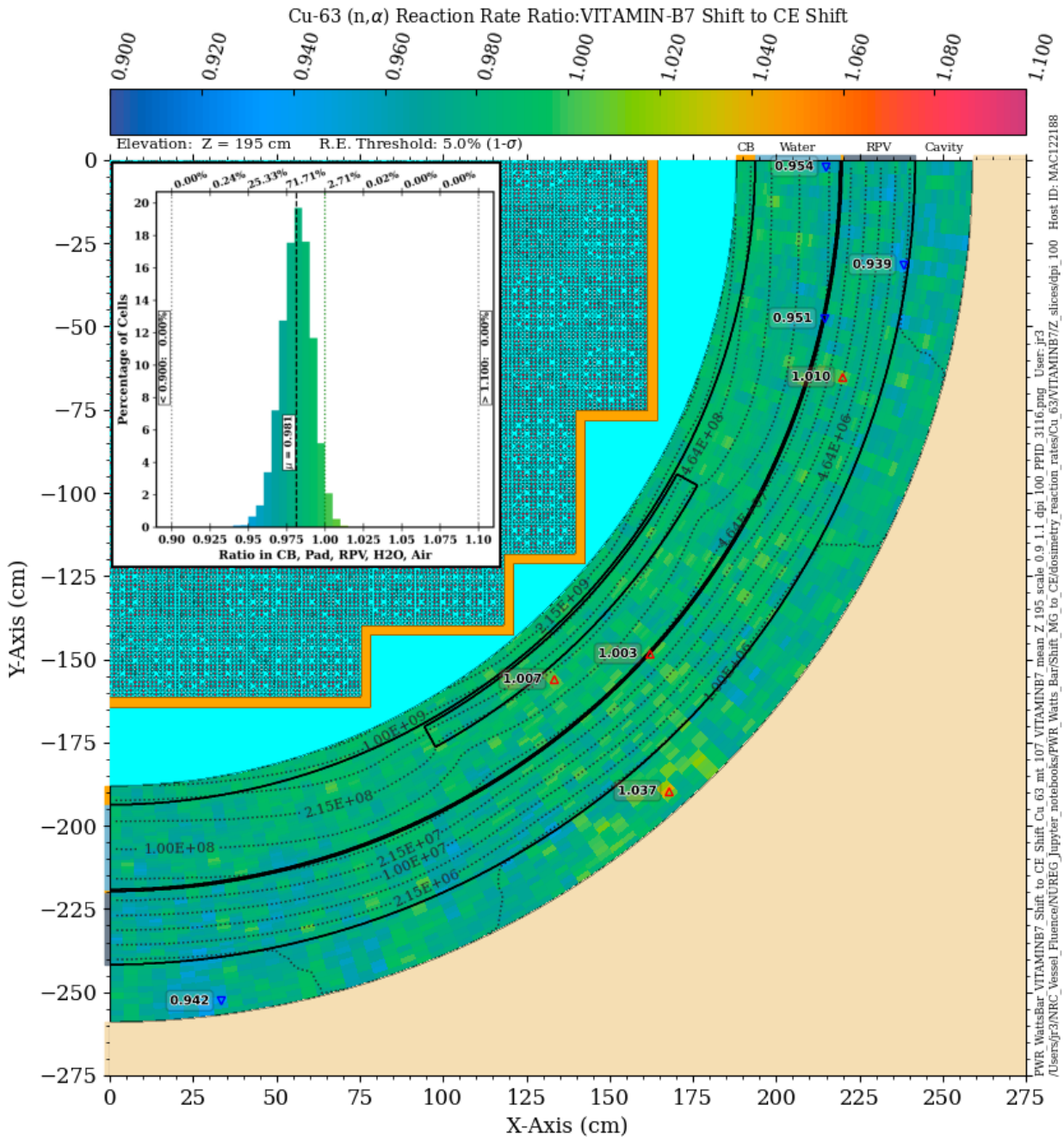

Figure 3-38 **^{63}Cu (n,α) reaction rate ratio in the PWR model: VITAMIN-B7 Shift/CE Shift. Plan view at Z = 195 cm. The contour lines are the reaction rate values from the CE solution**

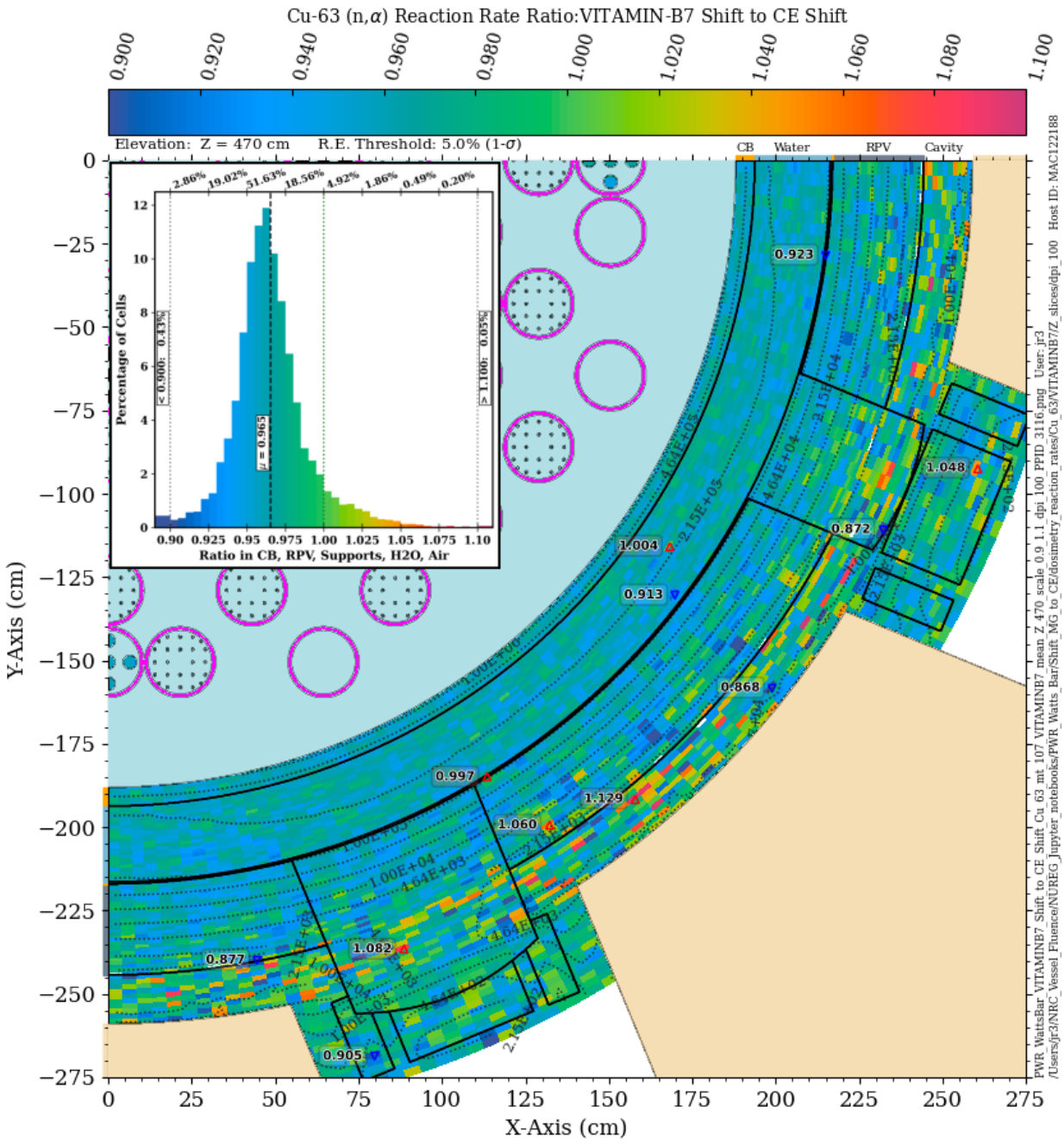

Figure 3-39 ^{63}Cu (n,α) reaction rate ratio in the PWR model: VITAMIN-B7 Shift/CE Shift. Plan view at Z = 470 cm. The contour lines are the reaction rate values from the CE solution

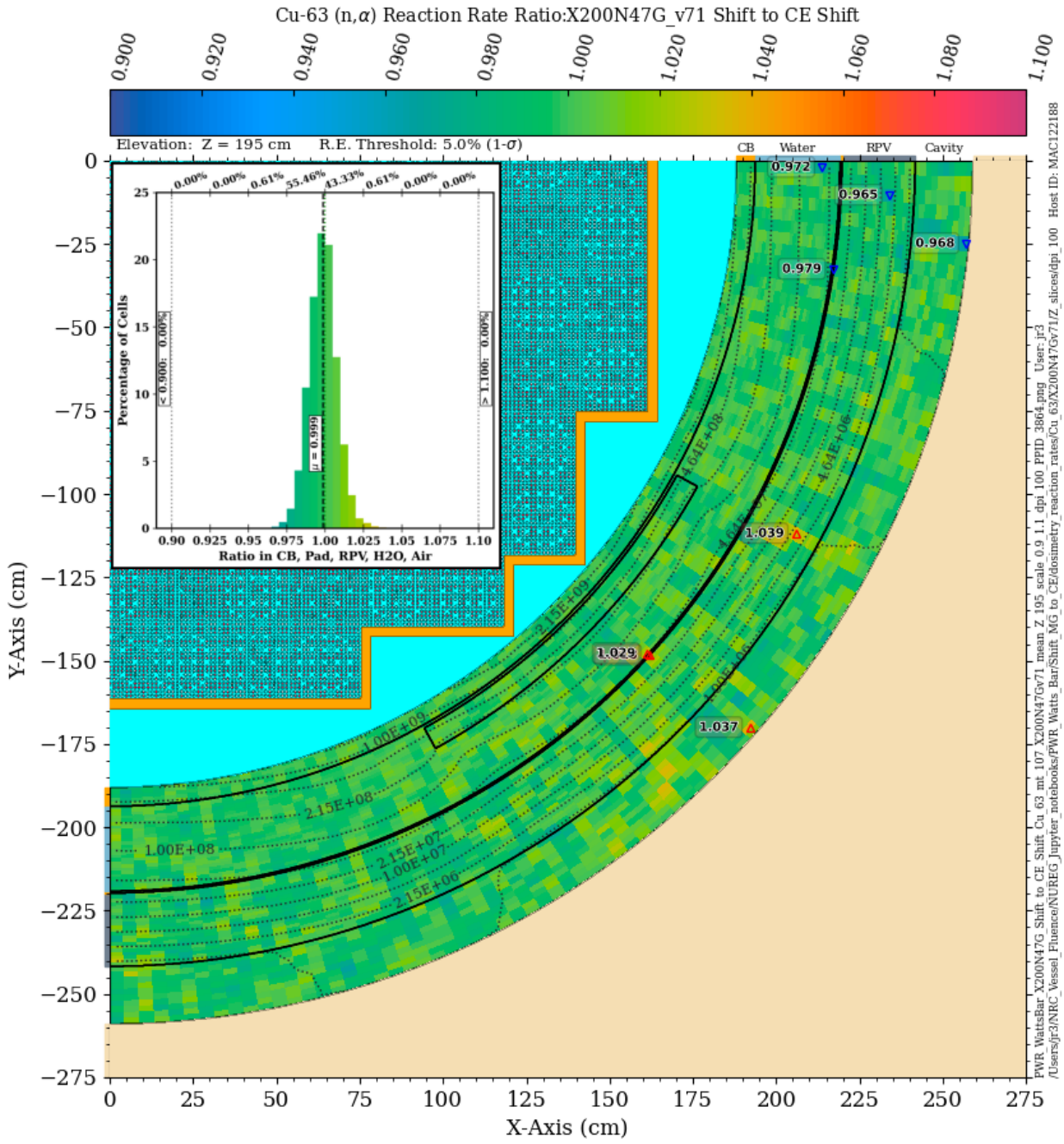

Figure 3-40 **^{63}Cu (n,α) reaction rate ratio in the PWR model: X200N47Gv71 Shift/CE Shift. Plan view at Z = 195 cm. The contour lines are the reaction rate values from the CE solution**

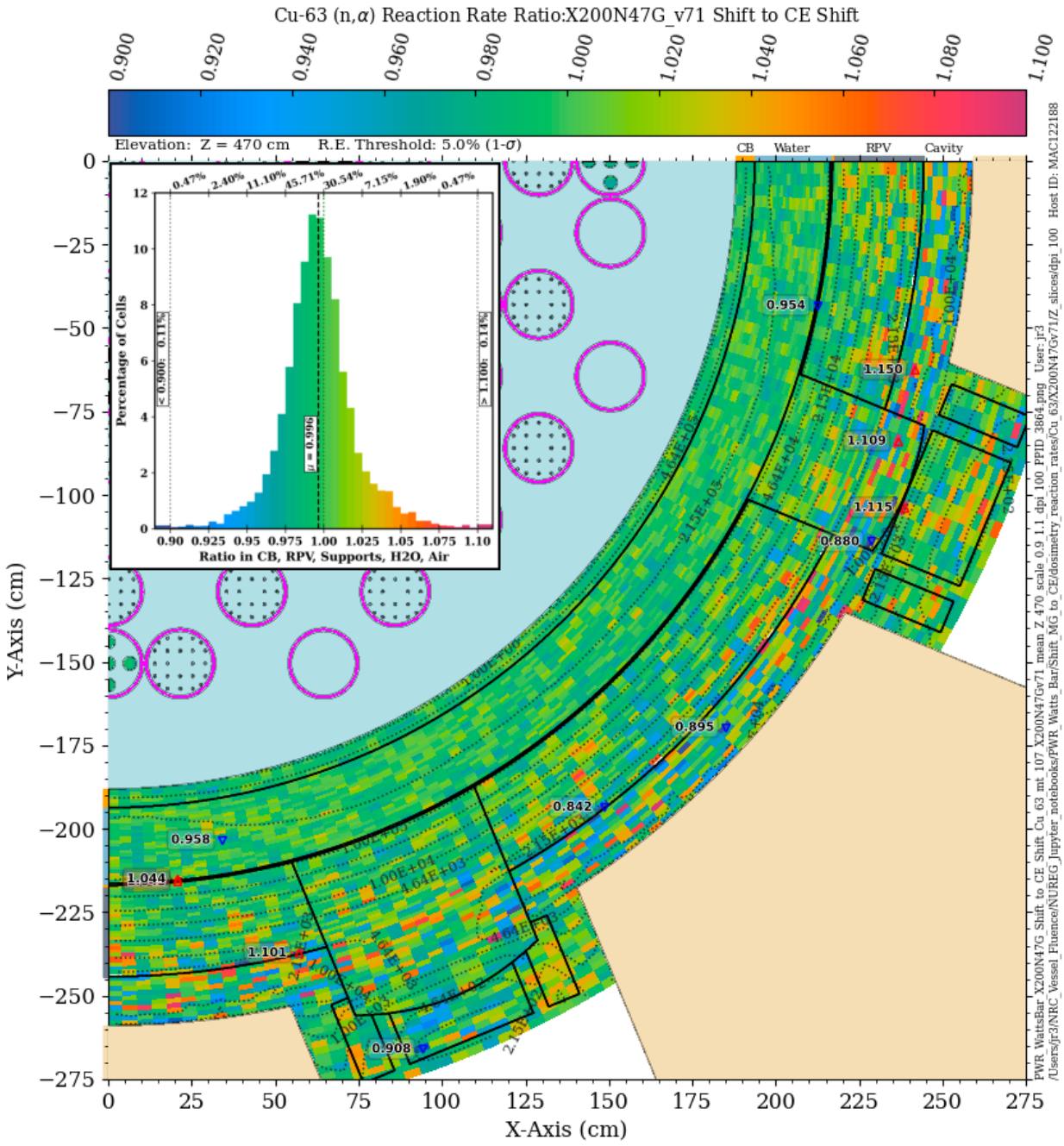

Figure 3-41 **^{63}Cu (n,α) reaction rate ratio in the PWR model: X200N47G Shift/CE Shift. Plan view at Z = 470 cm. The contour lines are the reaction rate values from the CE solution**

3.4.3 ^{46}Ti (n,p)

The ^{46}Ti (n,p) reaction has a threshold energy of 2.10 MeV and a 90% energy response range of 3.70 to 9.43 MeV (Table C-1). The agreement between a Shift solution with BUGLE-B7 cross-section data and a Shift solution with CE data for this reaction is poor. At the core midplane (Figure 3-42), the BUGLE-B7 solution is uniformly higher, with a bias centered at ~15%. At Z = 470 cm (Figure 3-43), the BUGLE-B7/CE agreement at locations within the outer radius of the RPV is improved, but agreement is very poor outside the RPV, where flux levels are dominated by cavity streaming. MG/CE ratios with the VITAMIN-B7 library (Figure 3-44 and Figure 3-45) are very similar to those for the BUGLE-B7 library.

An MG solution with the X200N47G library shows substantially improved agreement with the CE solution. At the core midplane (Figure 3-46), the solutions agree to within 2.5% in over 99% of the mesh tally voxels. At Z = 470 cm (Figure 3-47), the solutions agree to within 5% in over 98% of the mesh tally voxels. Results using the X956N library (not shown) are very consistent with those using the X200N47G library.

The marked difference between the VITAMIN-B7 and X200N47G results suggests that the difference in the reaction rates calculated using these two libraries is not in the transport cross sections but rather in the ^{46}Ti (n,p) dosimetry cross-section data from these two libraries. Figure 3-48 shows the cross-section data for this reaction from several CE and MG libraries, as well as the ratio of the VITAMIN-B7 data to the X200N47G data. This comparison is consistent with the behavior seen in the reaction rates and indicates that the (n,p) cross-section data for this reaction should be carefully examined when performing MG calculations.

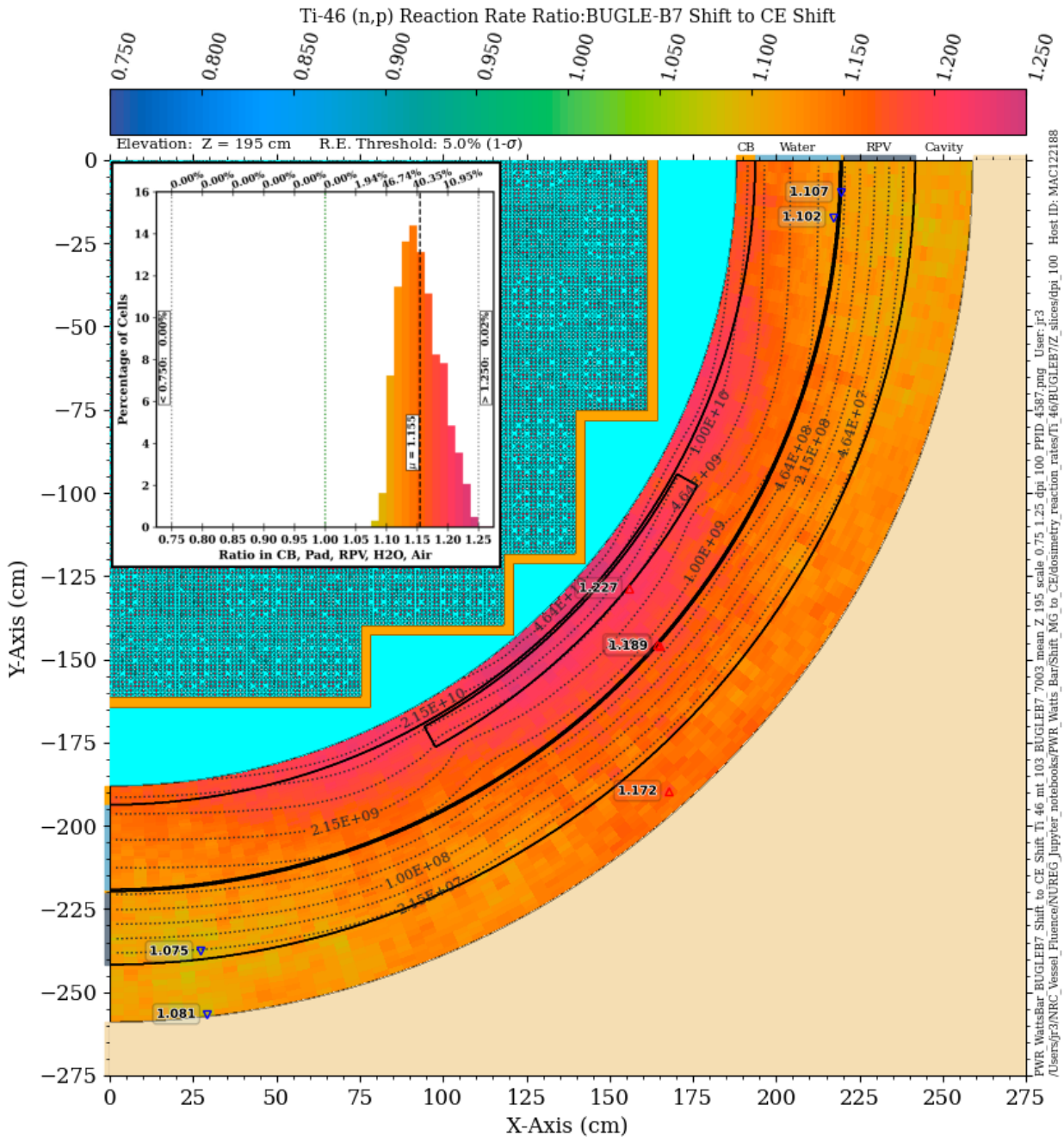

Figure 3-42 ^{46}Ti (n,p) reaction rate ratio in the PWR model: BUGLE-B7 Shift/CE Shift. Plan view at Z = 195 cm. The contour lines are the reaction rate values from the CE solution

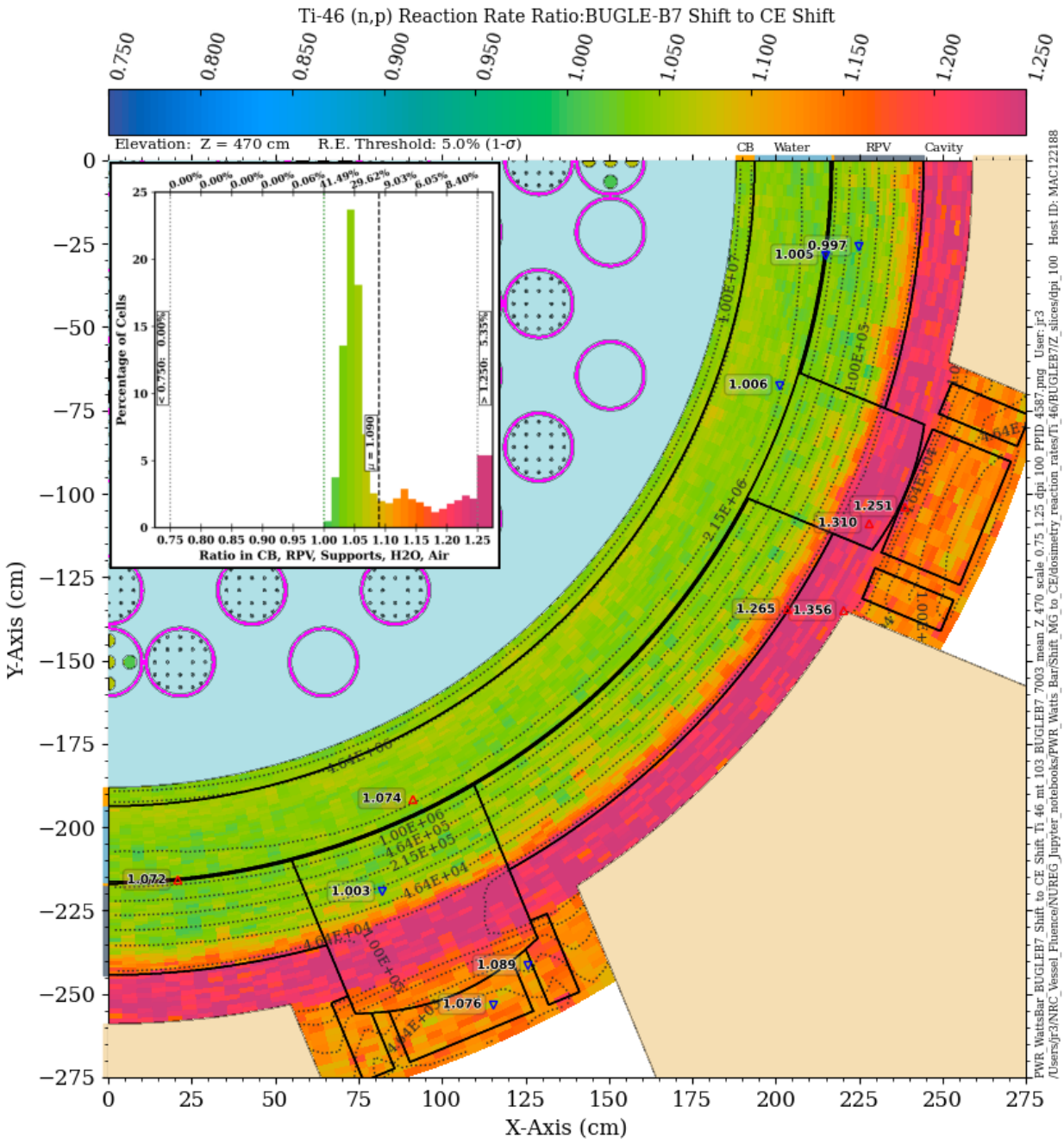

Figure 3-43 **^{46}Ti (n,p) reaction rate ratio in the PWR model: BUGLE-B7 Shift/CE Shift. Plan view at Z = 470 cm. The contour lines are the reaction rate values from the CE solution**

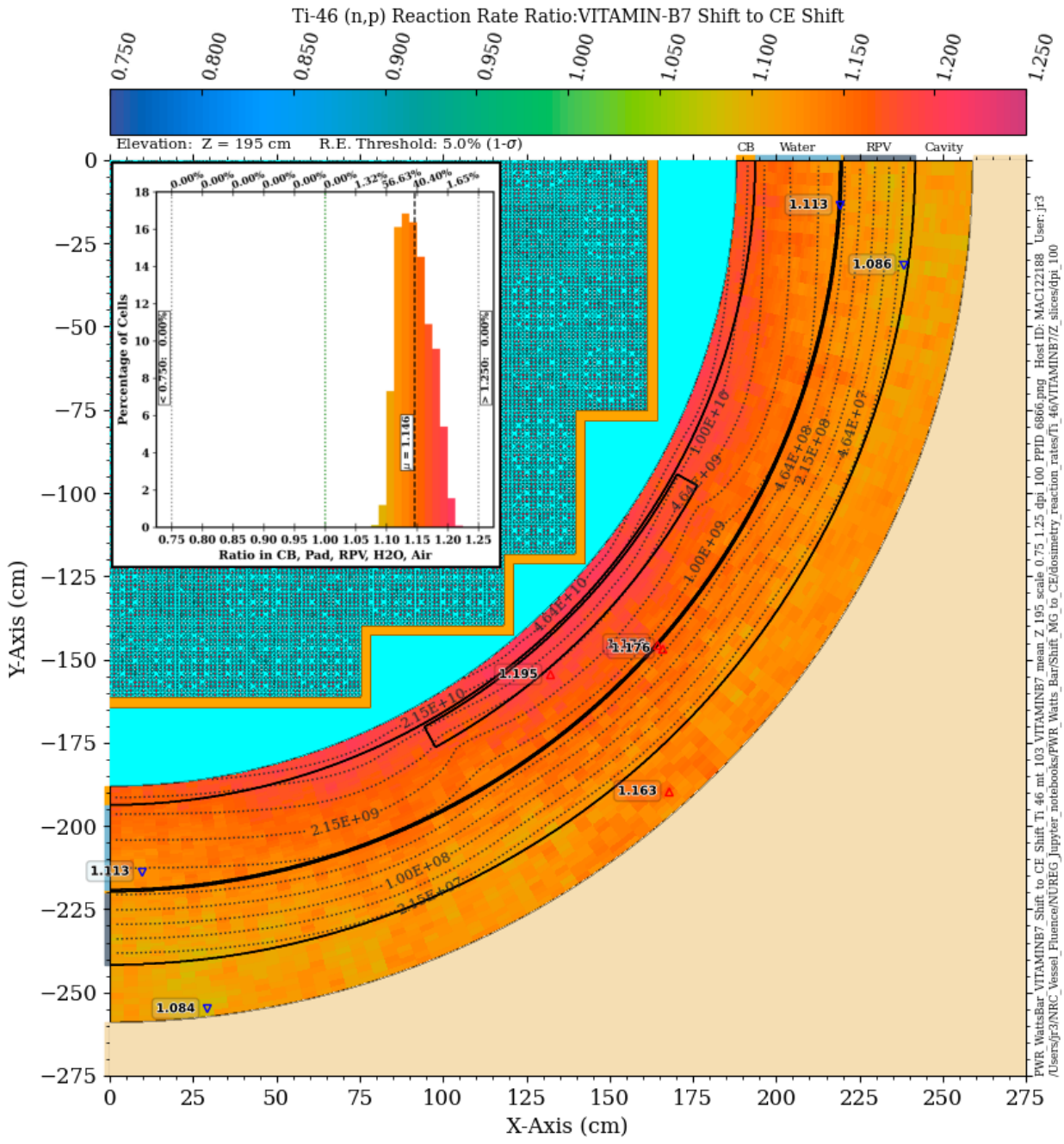

Figure 3-44 ^{46}Ti (n,p) reaction rate ratio in the PWR model: VITAMIN-B7 Shift/CE Shift. Plan view at Z = 195 cm. The contour lines are the reaction rate values from the CE solution

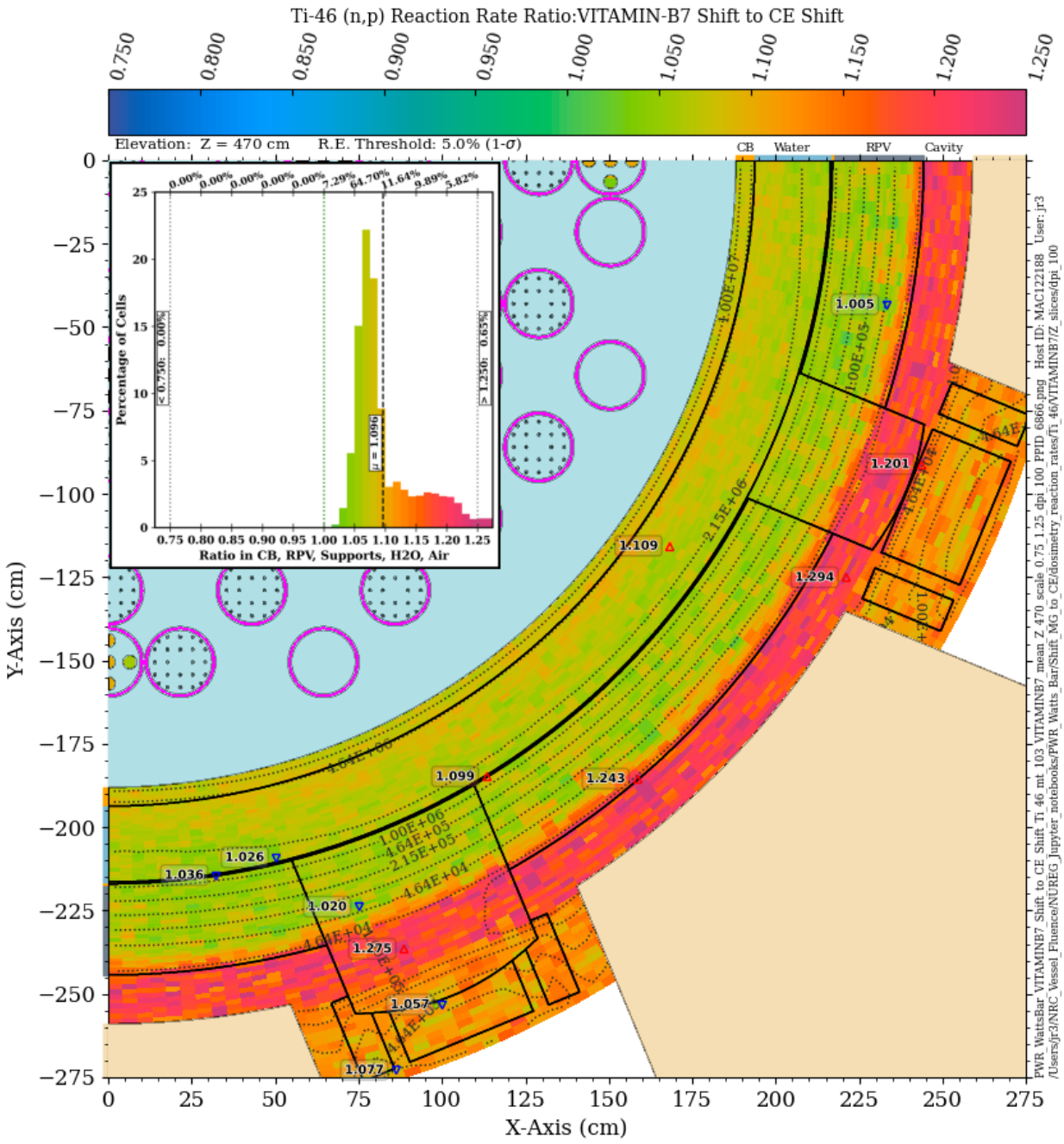

Figure 3-45 ^{46}Ti (n,p) reaction rate ratio in the PWR model: VITAMIN-B7 Shift/CE Shift. Plan view at Z = 470 cm. The contour lines are the reaction rate values from the CE solution

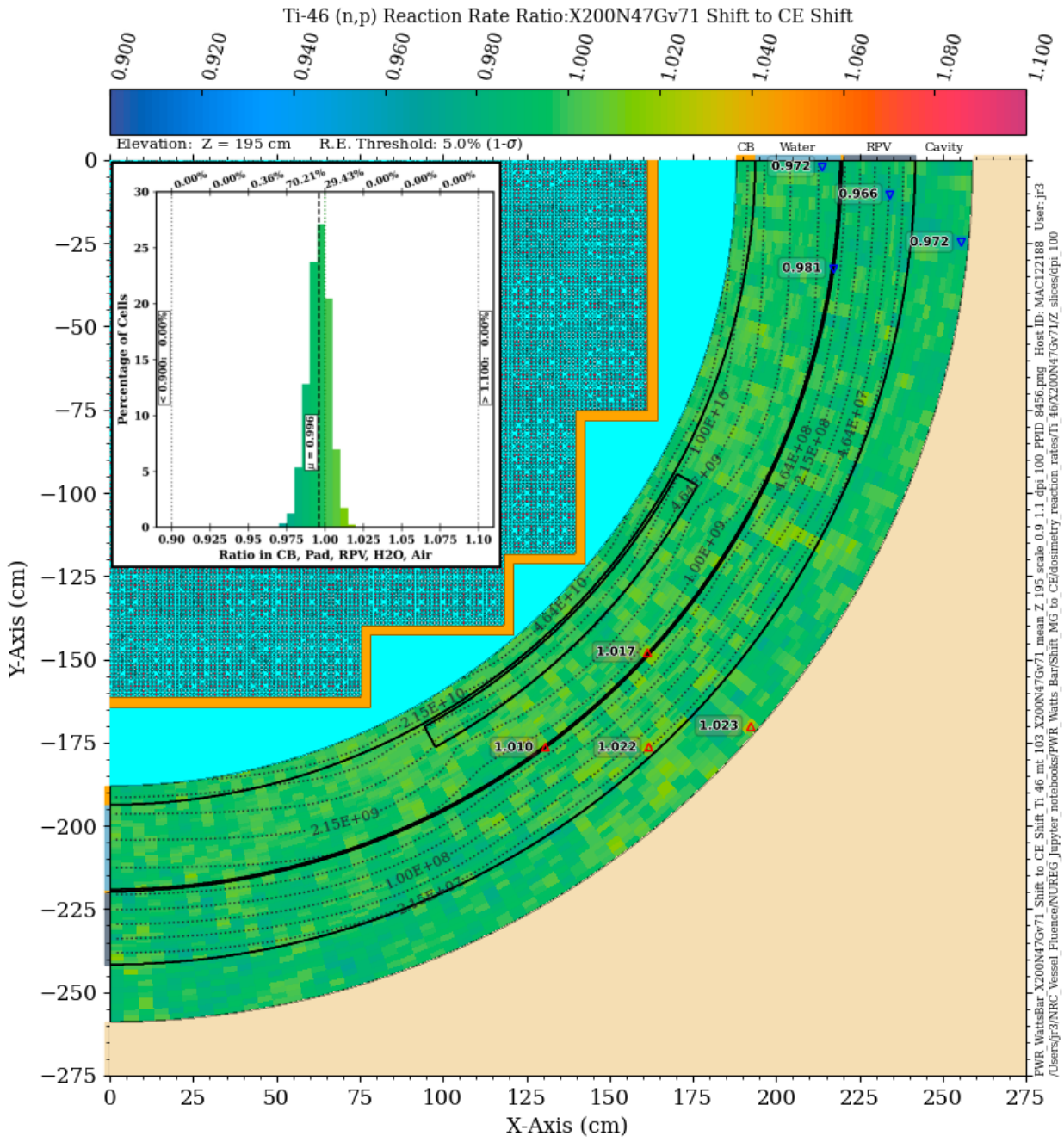

Figure 3-46 ^{46}Ti (n,p) reaction rate ratio in the PWR model: X200N47Gv71 Shift/CE Shift. Plan view at Z = 195 cm. The contour lines are the reaction rate values from the CE solution

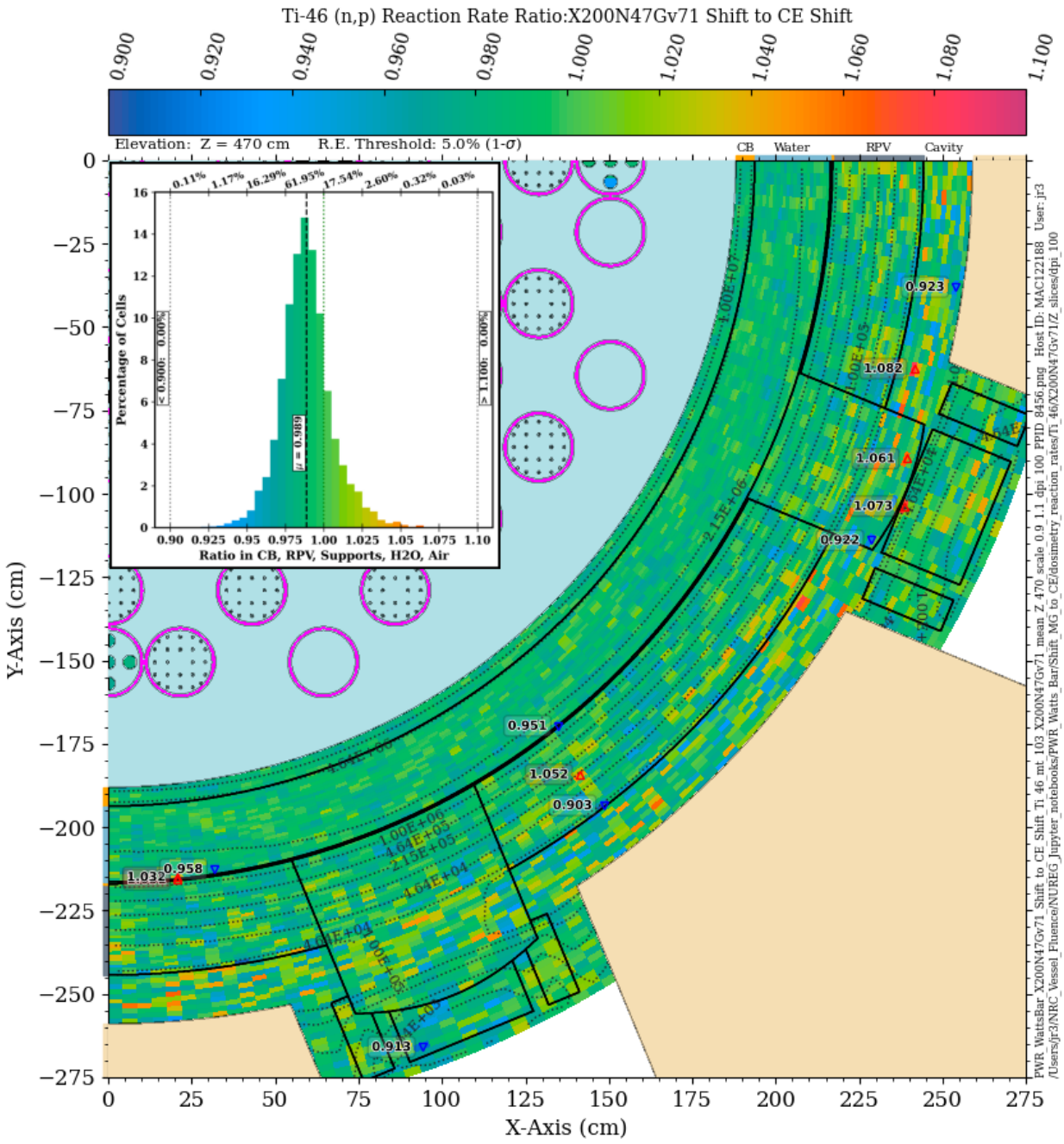

Figure 3-47 ^{46}Ti (n,p) reaction rate ratio in the PWR model: X200N47Gv71 Shift/CE Shift. Plan view at Z = 470 cm. The contour lines are the reaction rate values from the CE solution

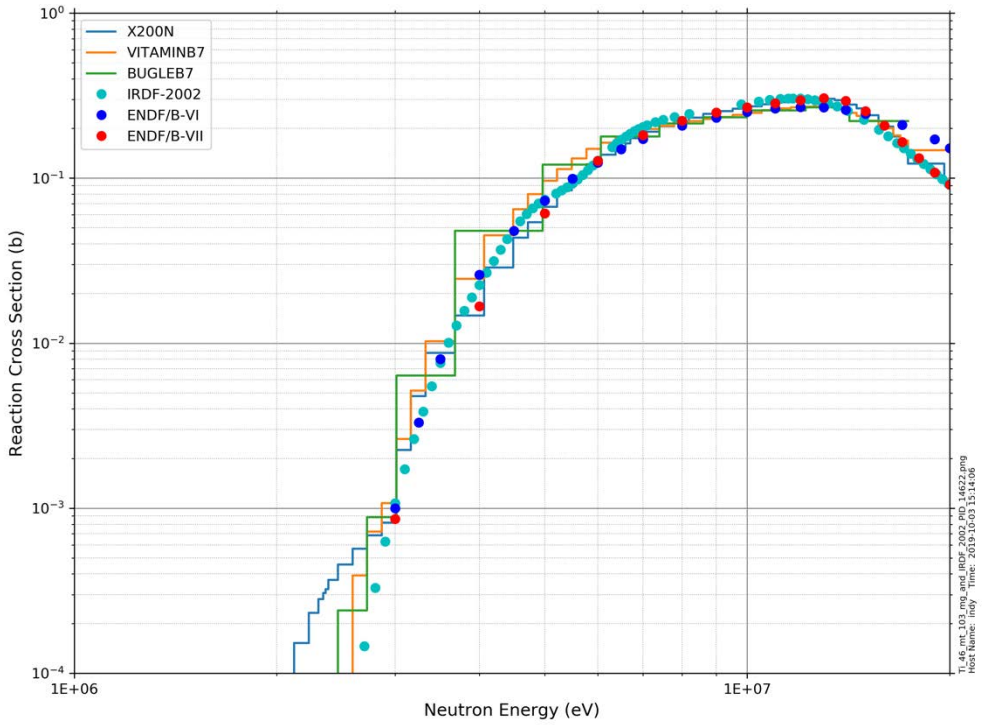

(a) Multigroup and CE cross-section data for the ^{46}Ti (n,p) reaction

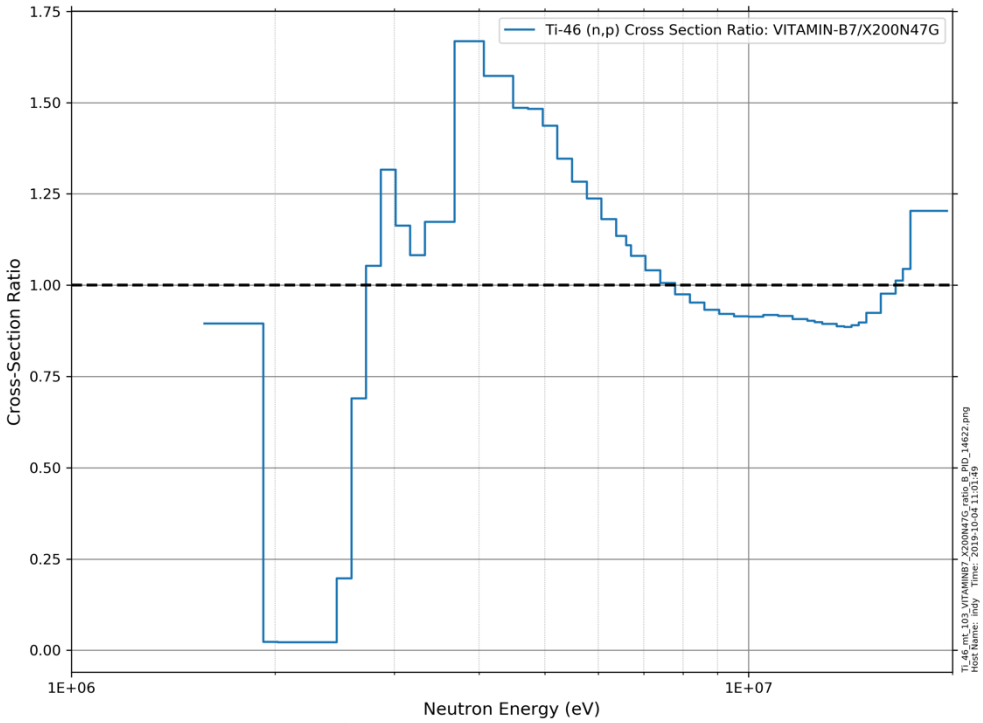

(b) Ratio of the VITAMIN-B7 ^{46}Ti (n,p) cross section to the X200N47Gv71 cross section

Figure 3-48 Cross-section data for the ^{46}Ti (n,p) reaction from MG and CE cross-section libraries and the ratio of the VITAMIN-B7 data to the X200N47G data

3.4.4 ^{54}Fe (n,p)

The ^{54}Fe (n,p) reaction has a threshold energy of 700 keV and a 90% energy response range of 2.27 to 7.54 MeV (Table C-1). For this dosimetry reaction, the Shift solution using the BUGLE-B7 library is in relatively good agreement with the CE Shift solution. At the core midplane (Figure 3-49), over 99% of the mesh tally voxels from the BUGLE-B7 solution are within 5% of the CE solution. It is also apparent that the MG/CE agreement is better at azimuthal locations which have the minimum amount of water between the baffle plates and the RPV. At an elevation of 470 cm (Figure 3-50), the BUGLE-B7 solution is lower than the CE solution in nearly 95% of the mesh tally voxels, with the majority of those locations have MG/CE ratios between 0.9 and 0.95.

Shift solutions using the VITAMIN-B7 library (Figure 3-51 and Figure 3-52) and the X200N47Gv71 library (Figure 3-53 and Figure 3-54) provide improved MG/CE ratios, with the X200N47Gv71 solution again showing better agreement than the VITAMIN-B7 solution. The distribution of ratio values at the core midplane with the X200N47G solution is centered at approximately 0.99, and over 99% of the X200N47G values are within 2.5% of the CE solution. At Z = 470 cm, the distribution is shifted slightly (~2%) below unity, and nearly 98% of the X200N47Gv71 values are within 5% of the CE solution. Results using the X956N library (not shown) are slightly improved relative to those using the X200N47Gv71 library.

3.4.5 ^{58}Ni (n,p)

The ^{58}Ni (n,p) reaction has a threshold energy of 400 keV and a 90% energy response range of 1.98–7.51 MeV (Table C-1). The MG/CE comparisons for this reaction (Figure 3-55 through Figure 3-60) are very similar to those for the ^{54}Fe (n,p) reaction. This consistency is likely due to the similarity in the energy thresholds and shapes of these two reaction cross sections (Figure C-2).

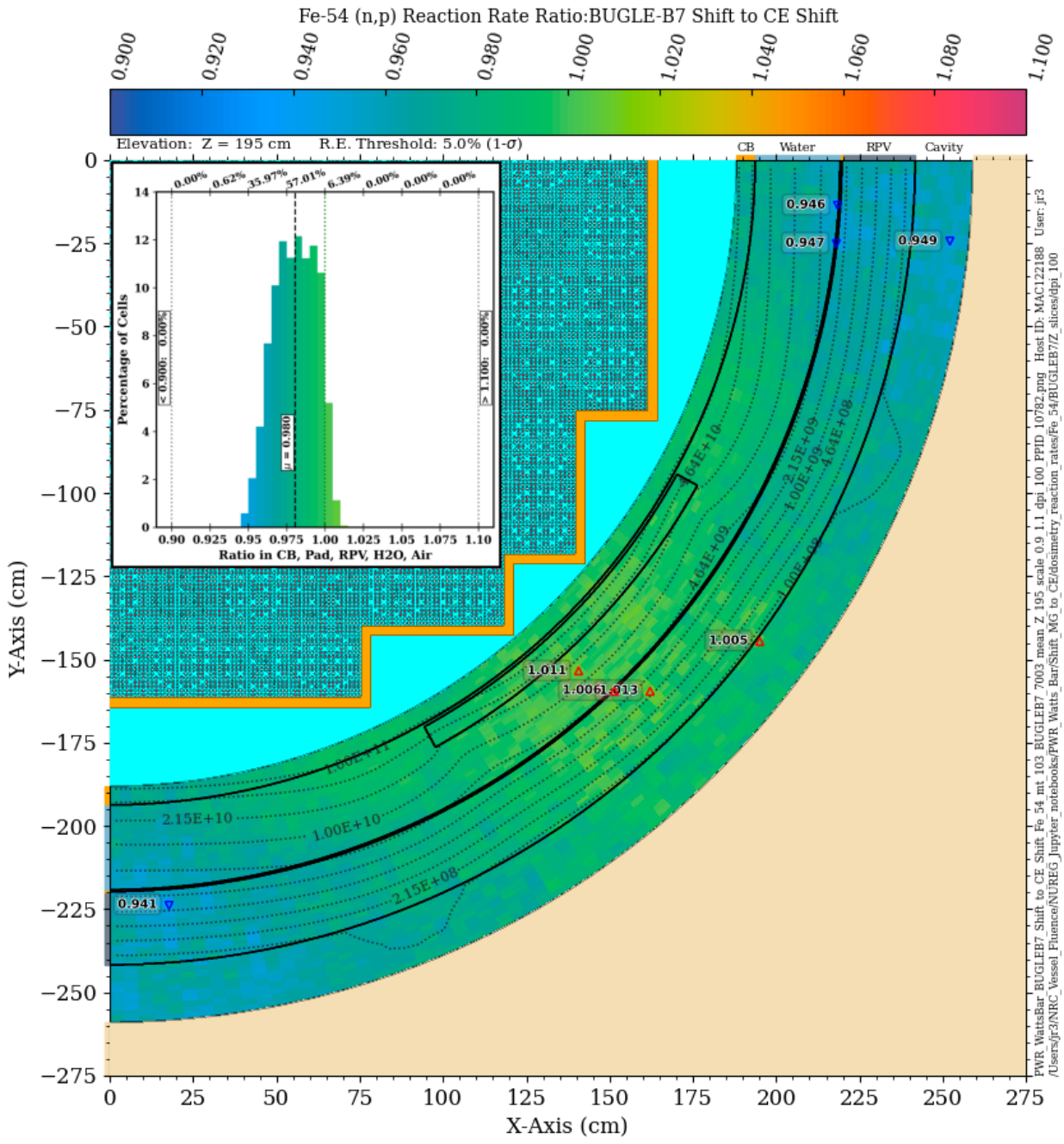

Figure 3-49 ^{54}Fe (n,p) reaction rate ratio in the PWR model: BUGLE-B7 Shift/CE Shift. Plan view at Z = 195 cm. The contour lines are the reaction rate values from the CE solution

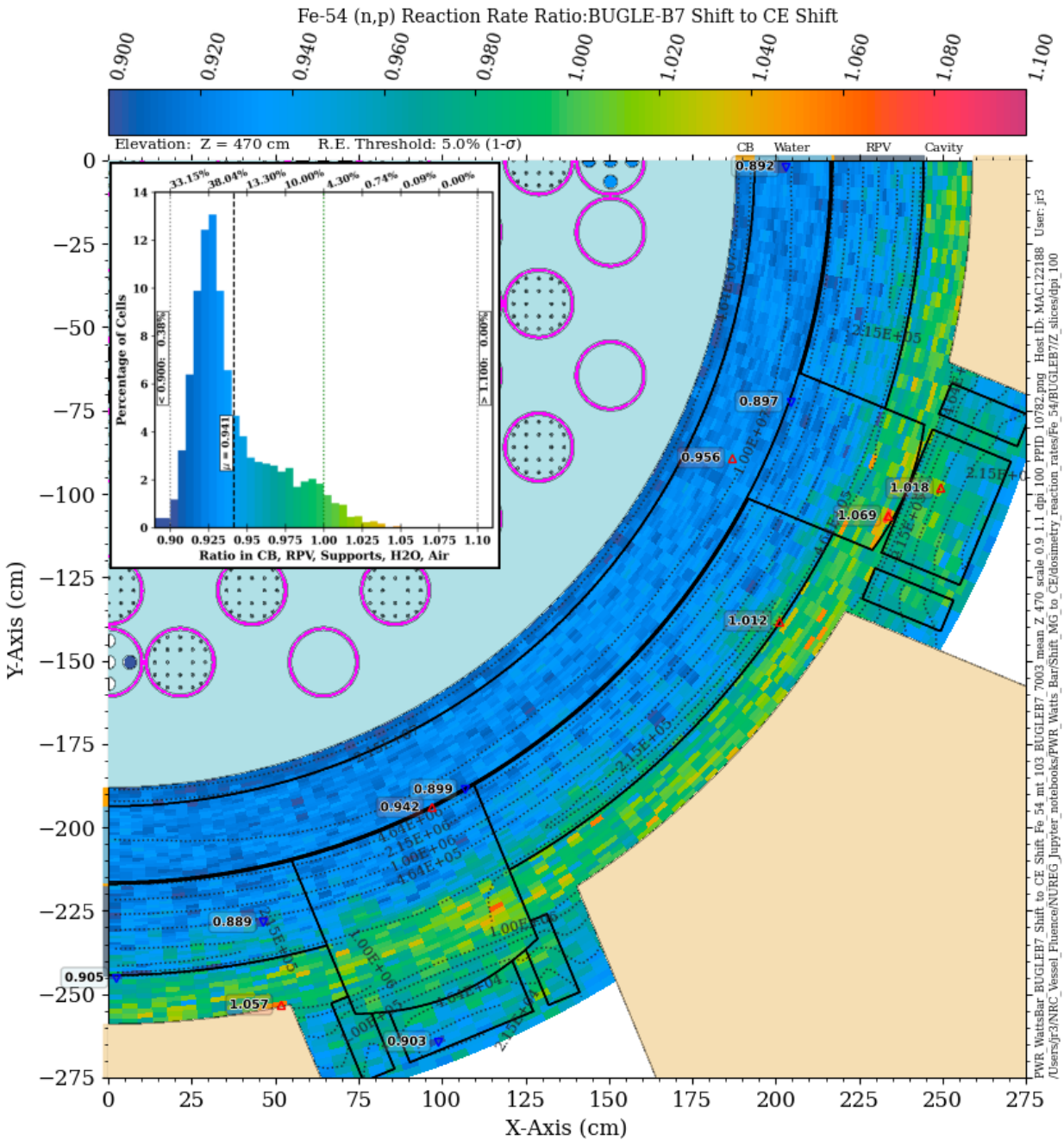

Figure 3-50 ^{54}Fe (n,p) reaction rate ratio in the PWR model: BUGLE-B7 Shift/CE Shift. Plan view at Z = 470 cm. The contour lines are the reaction rate values from the CE solution

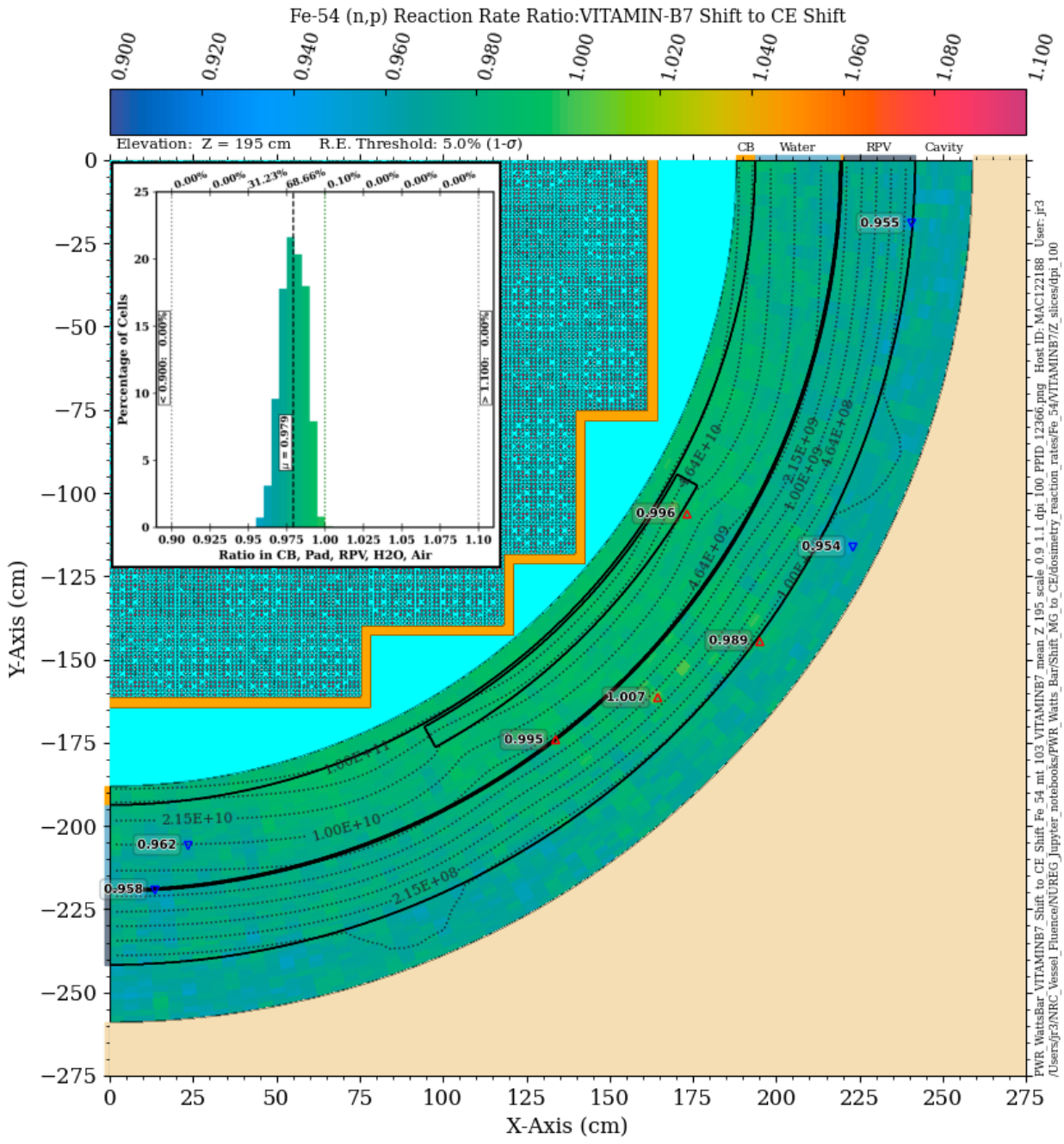

Figure 3-51 ^{54}Fe (n,p) reaction rate ratio in the PWR model: VITAMIN-B7 Shift/CE Shift. Plan view at Z = 195 cm. The contour lines are the reaction rate values from the CE solution

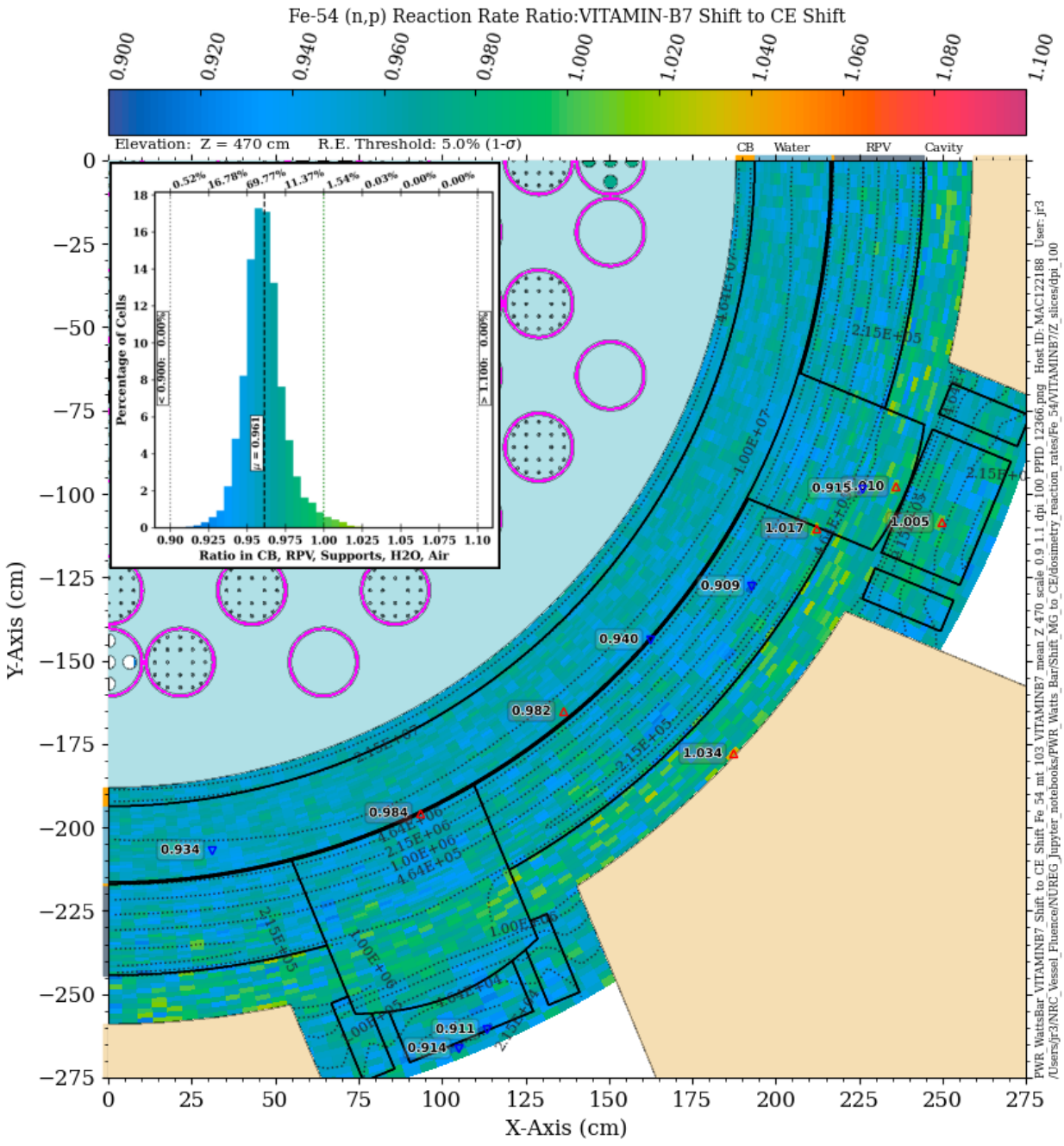

Figure 3-52 ^{54}Fe (n,p) reaction rate ratio in the PWR model: VITAMIN-B7 Shift/CE Shift. Plan view at Z = 470 cm. The contour lines are the reaction rate values from the CE solution

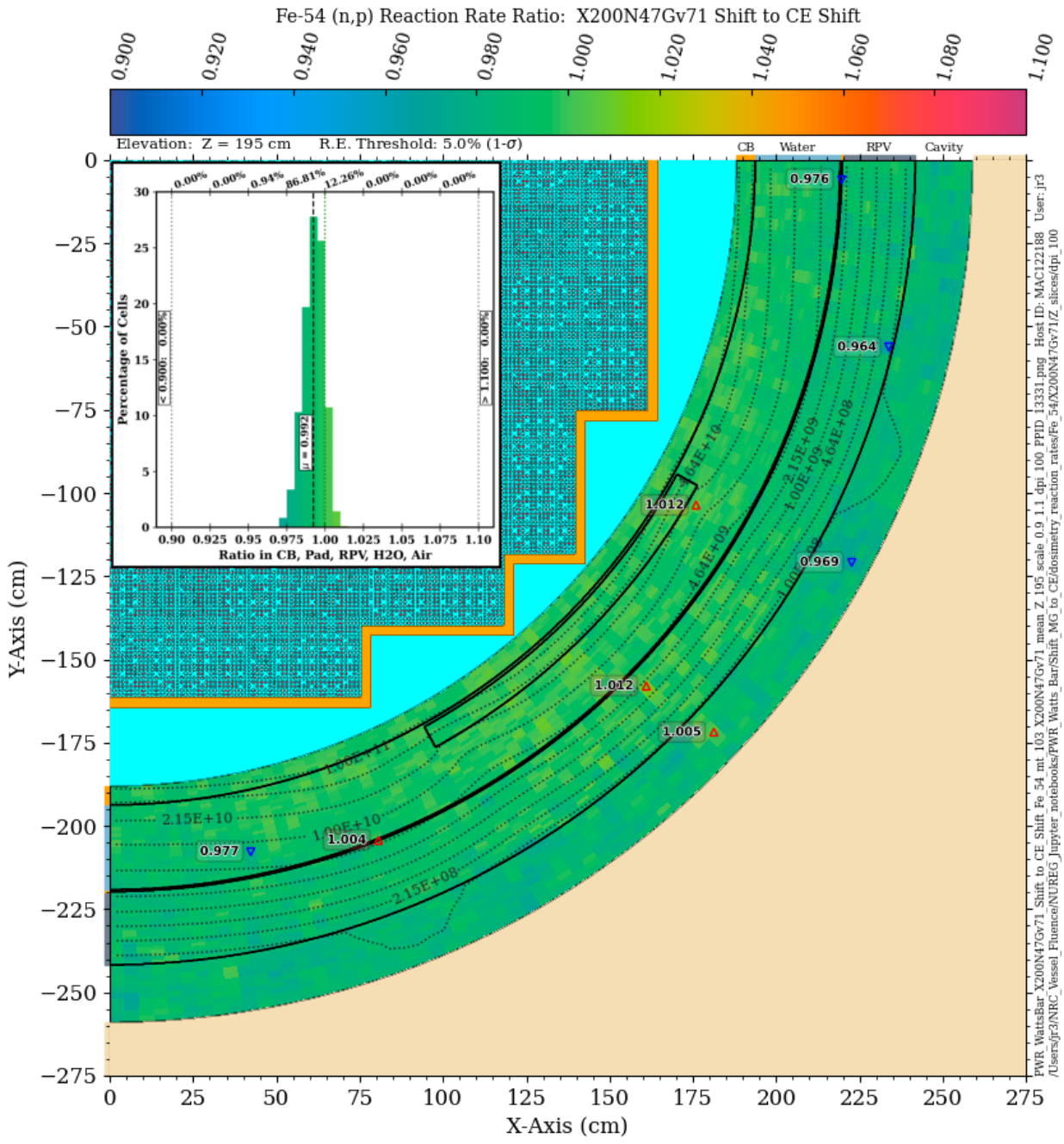

Figure 3-53 ^{54}Fe (n,p) reaction rate ratio in the PWR model: X200N47Gv71 Shift/CE Shift. Plan view at Z = 195 cm. The contour lines are the reaction rate values from the CE solution

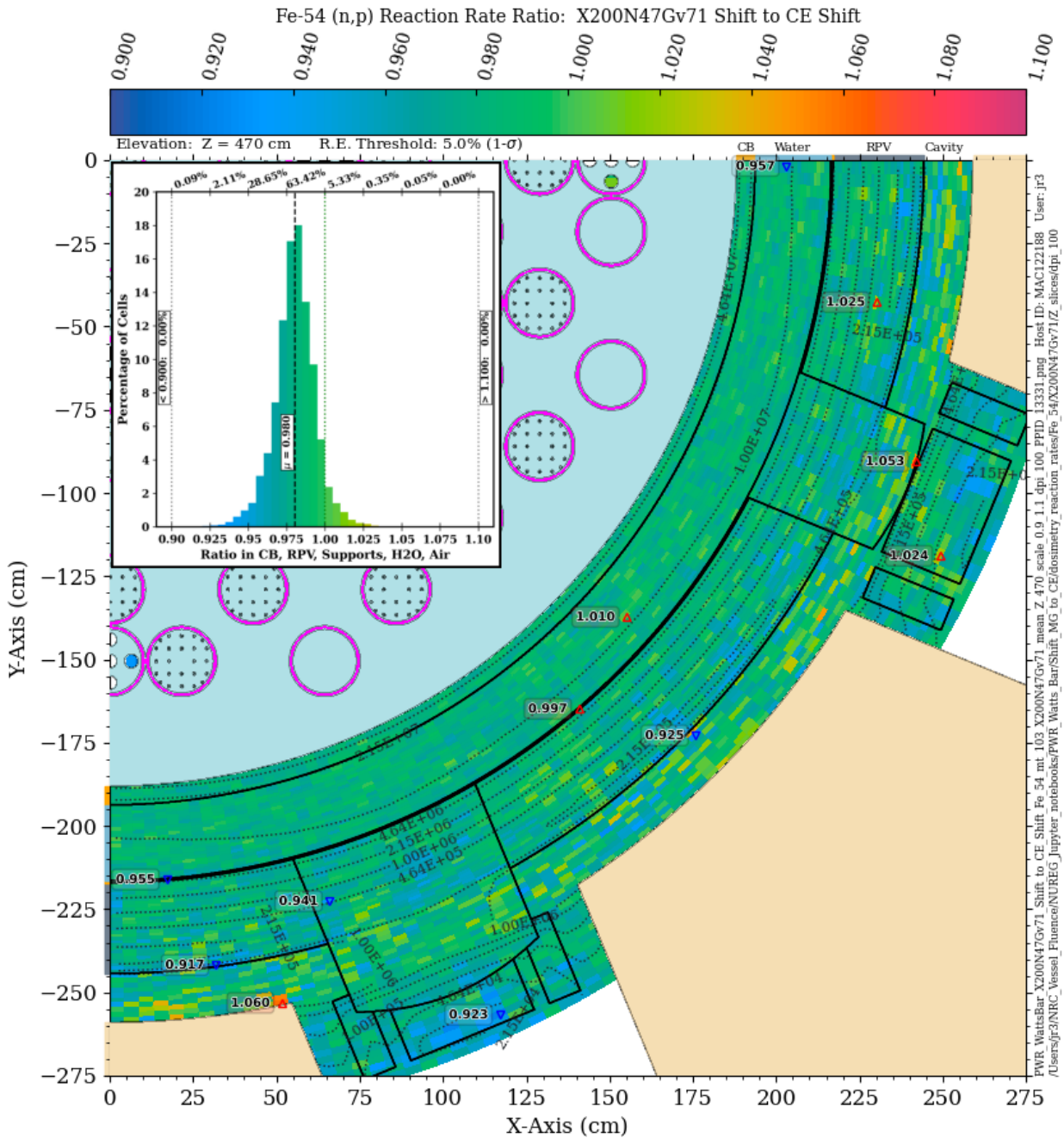

Figure 3-54 **^{54}Fe (n,p) reaction rate ratio in the PWR model: X200N47Gv71 Shift/CE Shift. Plan view at Z = 470 cm. The contour lines are the reaction rate values from the CE solution**

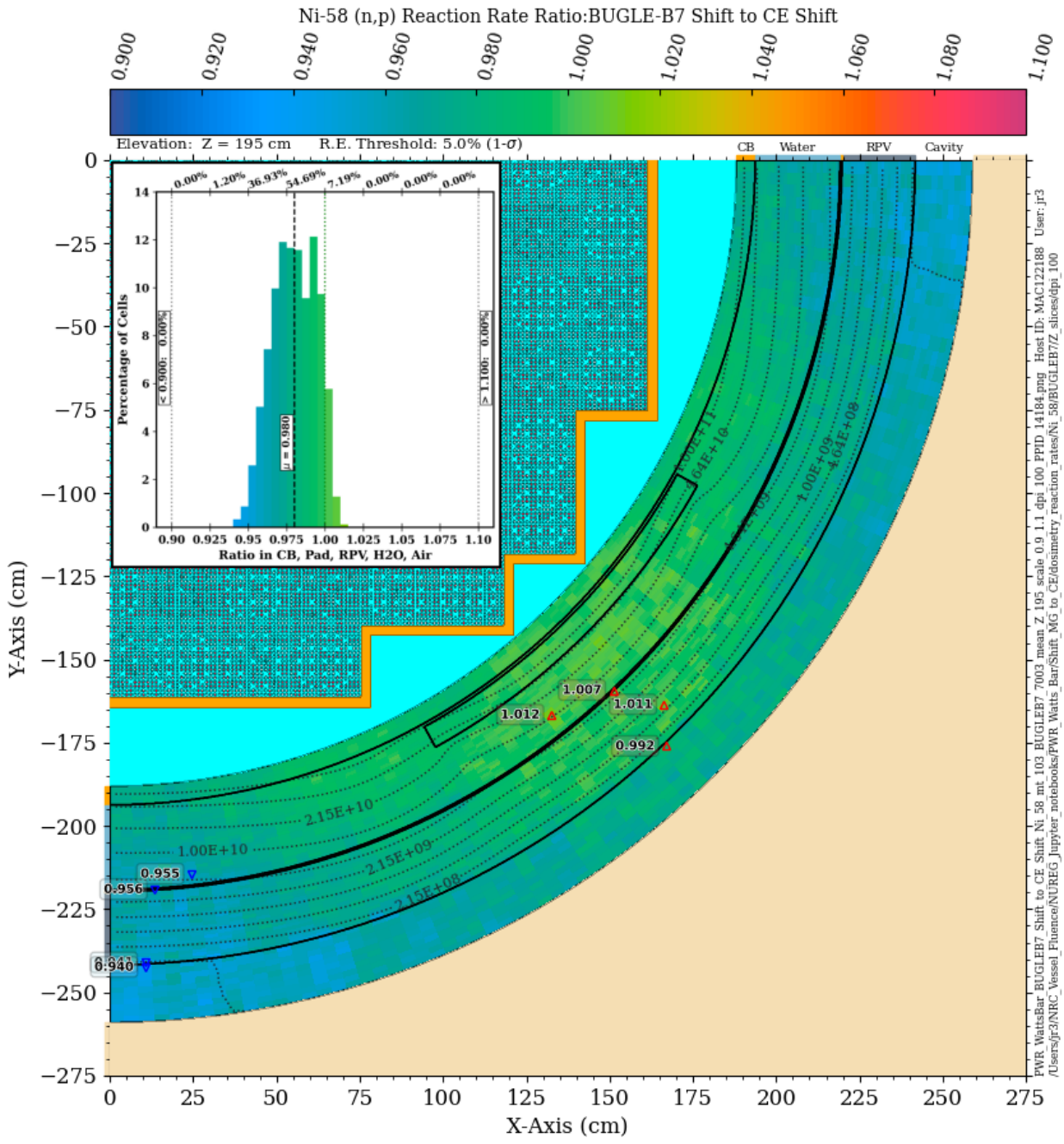

Figure 3-55 ^{58}Ni (n,p) reaction rate ratio in the PWR model: BUGLE-B7 Shift/CE Shift. Plan view at Z = 195 cm. The contour lines are the reaction rate values from the CE solution

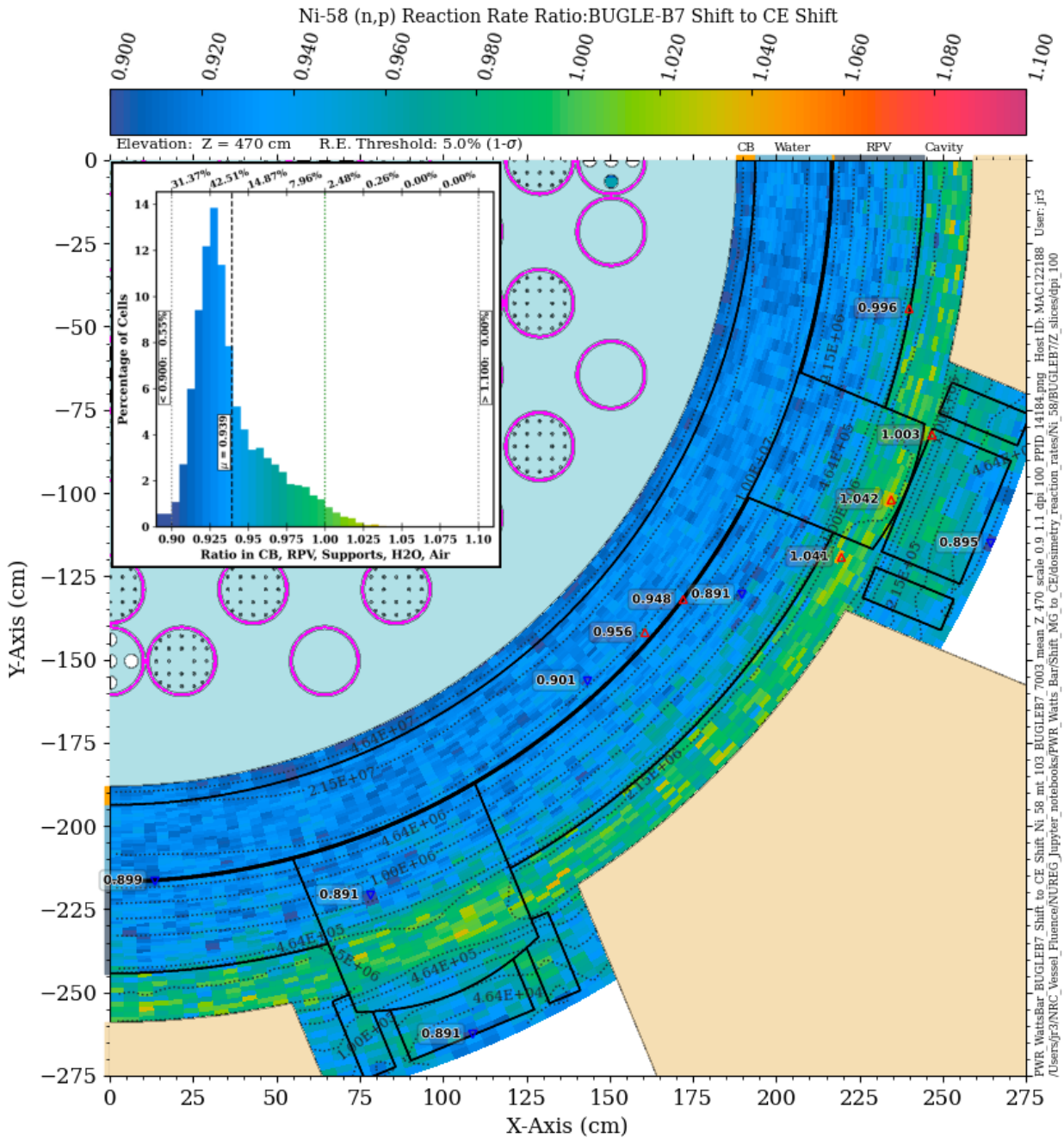

Figure 3-56 ^{58}Ni (n,p) reaction rate ratio in the PWR model: BUGLE-B7 Shift/CE Shift. Plan view at Z = 470 cm. The contour lines are the reaction rate values from the CE solution

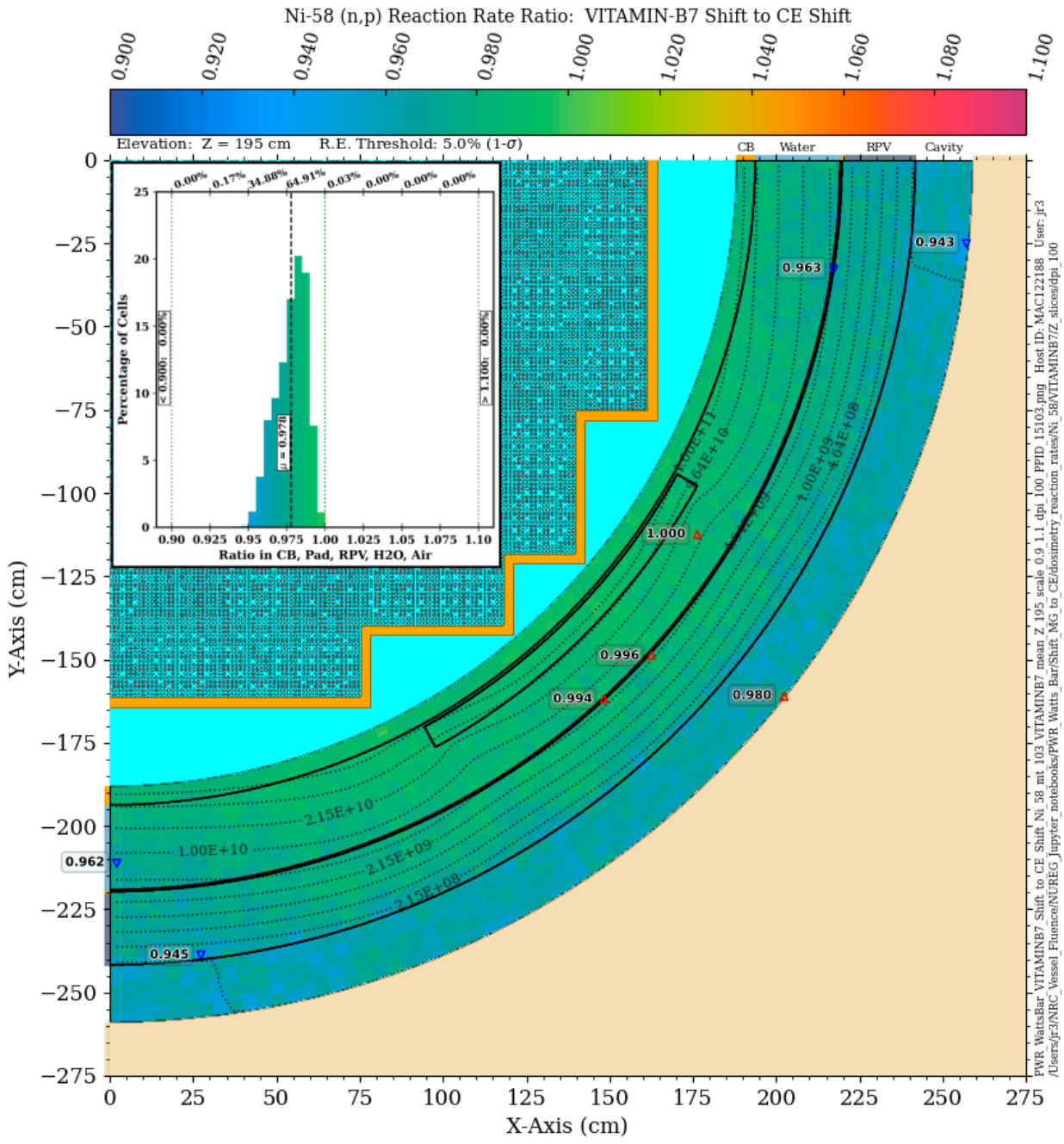

Figure 3-57 ^{58}Ni (n,p) reaction rate ratio in the PWR model: VITAMIN-B7 Shift/CE Shift. Plan view at Z = 195 cm. The contour lines are the reaction rate values from the CE solution

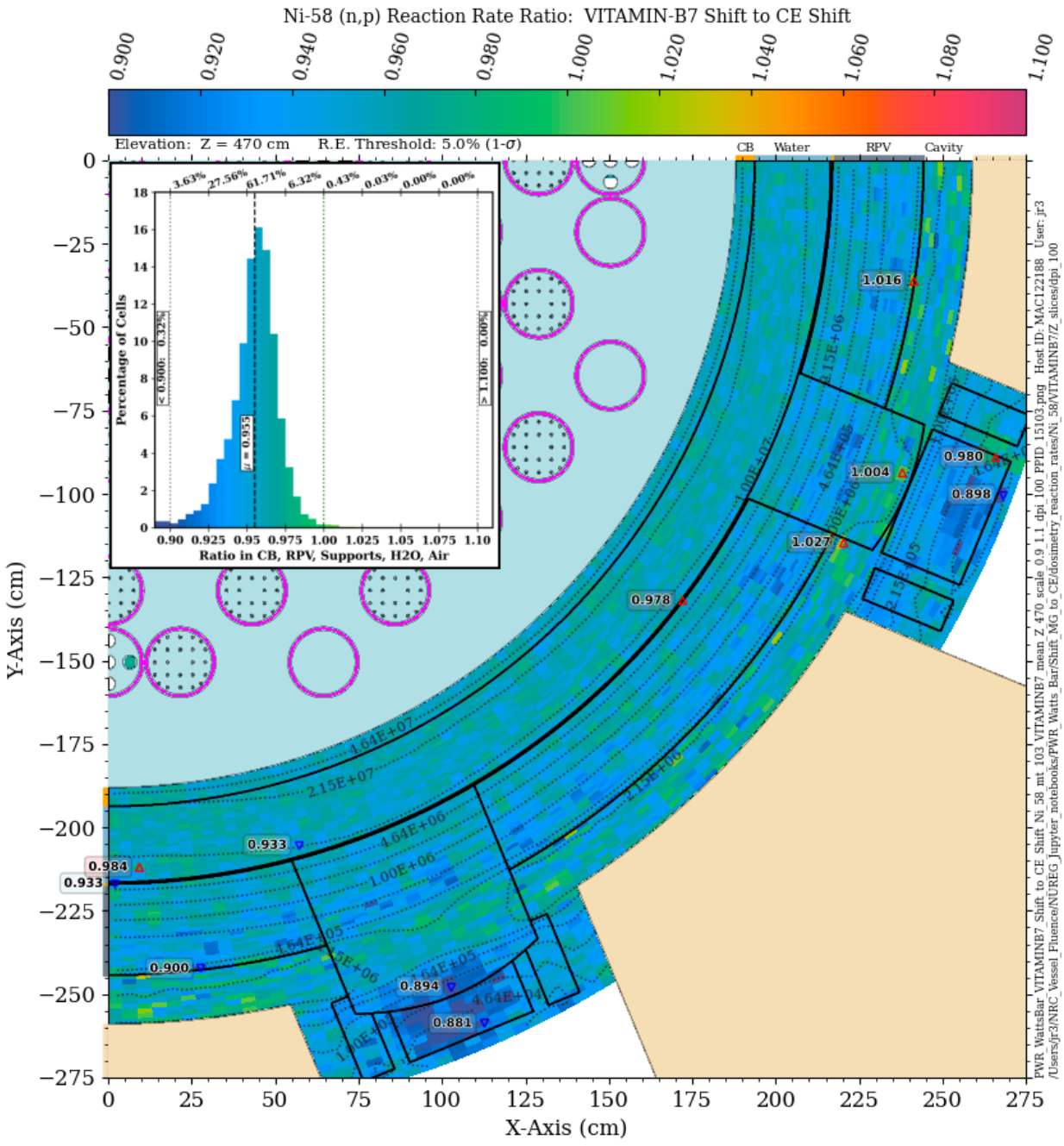

Figure 3-58 ^{58}Ni (n,p) reaction rate ratio in the PWR model: VITAMIN-B7 Shift/CE Shift. Plan view at Z = 470 cm. The contour lines are the reaction rate values from the CE solution

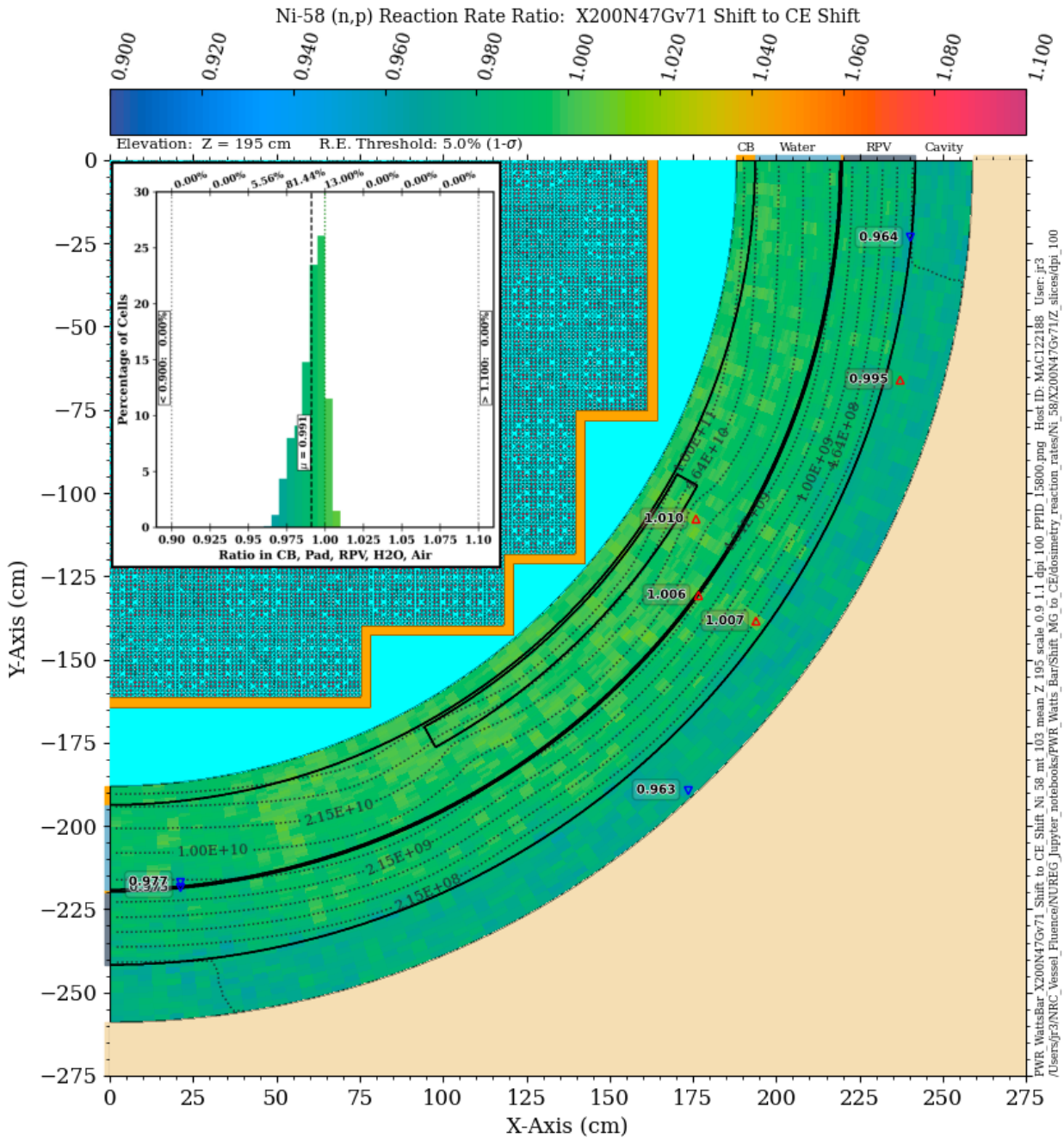

Figure 3-59 ^{58}Ni (n,p) reaction rate ratio in the PWR model: X200N47Gv71 Shift/CE Shift. Plan view at Z = 195 cm. The contour lines are the reaction rate values from the CE solution

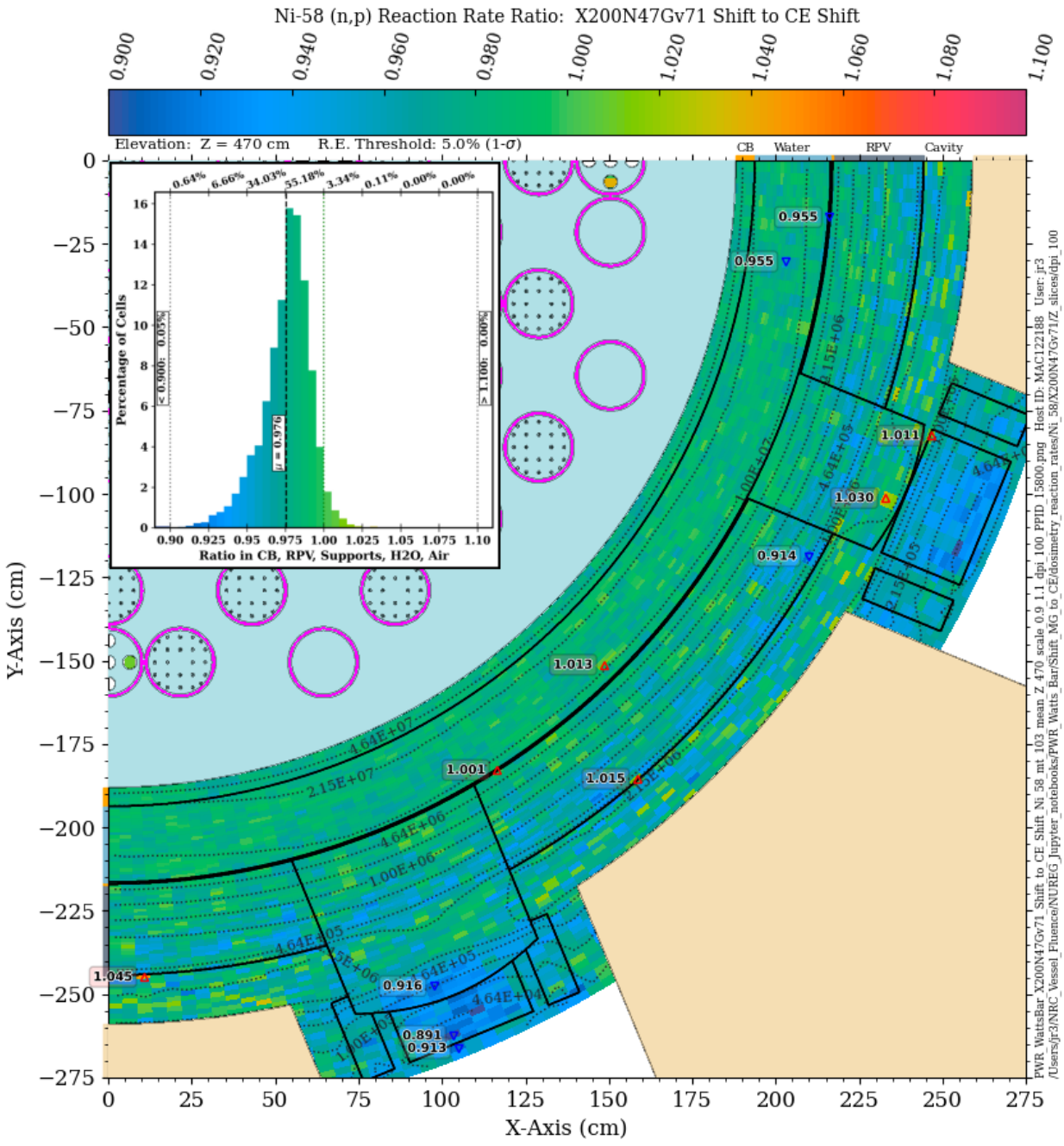

Figure 3-60 ^{58}Ni (n,p) reaction rate ratio in the PWR model: X200N47Gv71 Shift/CE Shift. Plan view at Z = 470 cm. The contour lines are the reaction rate values from the CE solution

3.4.6 ^{115}In (n,n′) ^{115m}In

The ^{115}In (n,n′) ^{115m}In reaction has a threshold energy of 339.2 keV and a 90% energy response range of 1.12 to 5.86 MeV (Table C-1). Note that the cross-section data for this reaction is based on the International Reactor Dosimetry File 2002 (IRDF-2002) [21]. There is no single ENDF reaction type (MT value) that can be used to compute the production rate of the metastable isomer. The BUGLE-B7 library contains response function data for this reaction, but the remainder of the MG libraries considered in this study do not. A comparison of the X956N solution to the CE solution was made based on convolving the X956N flux with the pointwise IRDF-2002 cross-section data. While a similar approach could have been taken with the remaining MG libraries, it was not because of the way in which Shift applies a pointwise response function to a MG flux solution. The flux in each group is treated as though it is all at the group lower energy bound when interpolating a value of the pointwise cross-section data. This approximation has a minor effect for very fine group structures (such as the X956N library), but it can have a substantial effect on the calculated reaction rate when a relatively coarse MG library is used.

The BUGLE-B7 solution agrees well with the CE solution near the core midplane (Figure 3-61) from the core barrel radially out through the inner portion of the RPV. However, at the outer edge of the RPV and in the cavity gap, the BUGLE-B7 solution is 5–10% lower than the CE solution. At the elevation of the vessel supports (Figure 3-62), the BUGLE-B7 solution underpredicts the CE solution at all locations, with an apparent bias of 8–9%. The BUGLE-B7 reaction rate underpredicts the CE solution by more than 20% in some vessel support mesh tally voxels.

The MG solution with the X956N library is in excellent agreement with the CE solution near the core midplane (Figure 3-63), with MG/CE agreement within 5% in 99.9% of the mesh tally voxels. At the elevation of the vessel supports (Figure 3-64), the agreement between the X956N and CE solutions is somewhat degraded, but the solutions agree to within 10% in more than 99% of the mesh tally voxels.

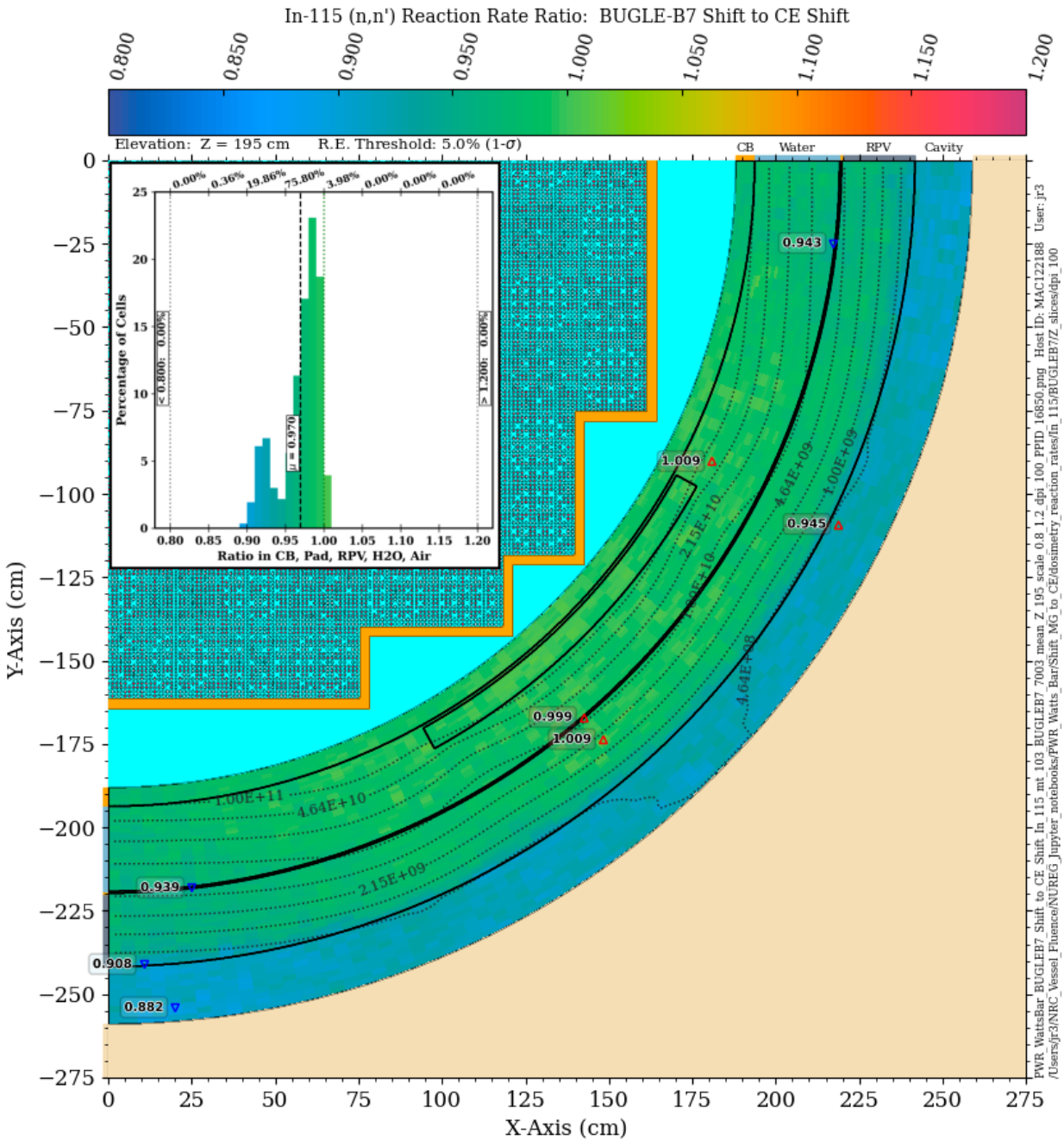

Figure 3-61 **^{115}In (n,n') ^{115m}In reaction rate ratio in the PWR model: BUGLE-B7 Shift/CE Shift. Plan view at Z = 195 cm. The contour lines are the reaction rate values from the CE solution**

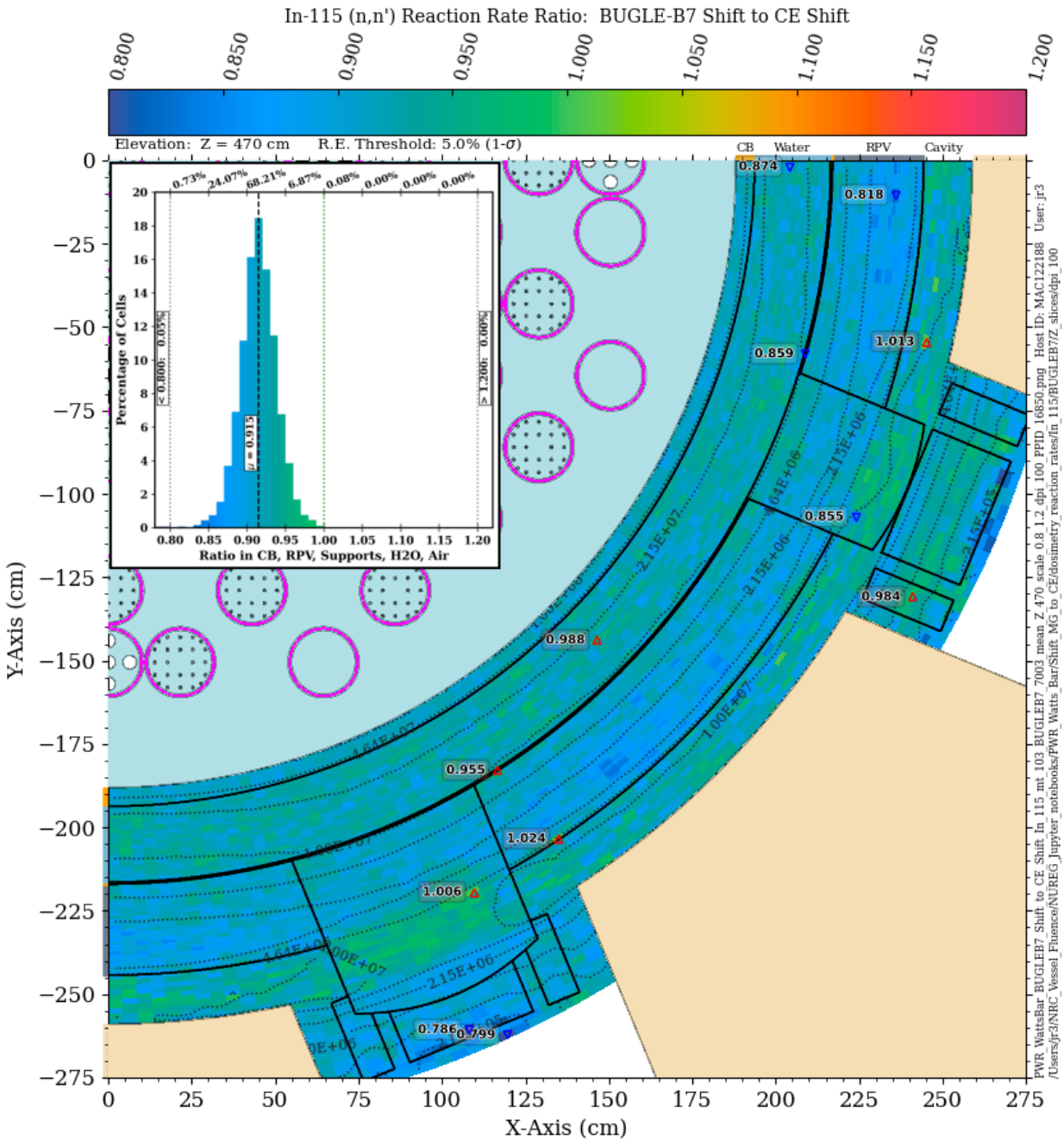

Figure 3-62 **^{115}In (n,n') ^{115m}In reaction rate ratio in the PWR model: BUGLE-B7 Shift/CE Shift. Plan view at Z = 470 cm. The contour lines are the reaction rate values from the CE solution**

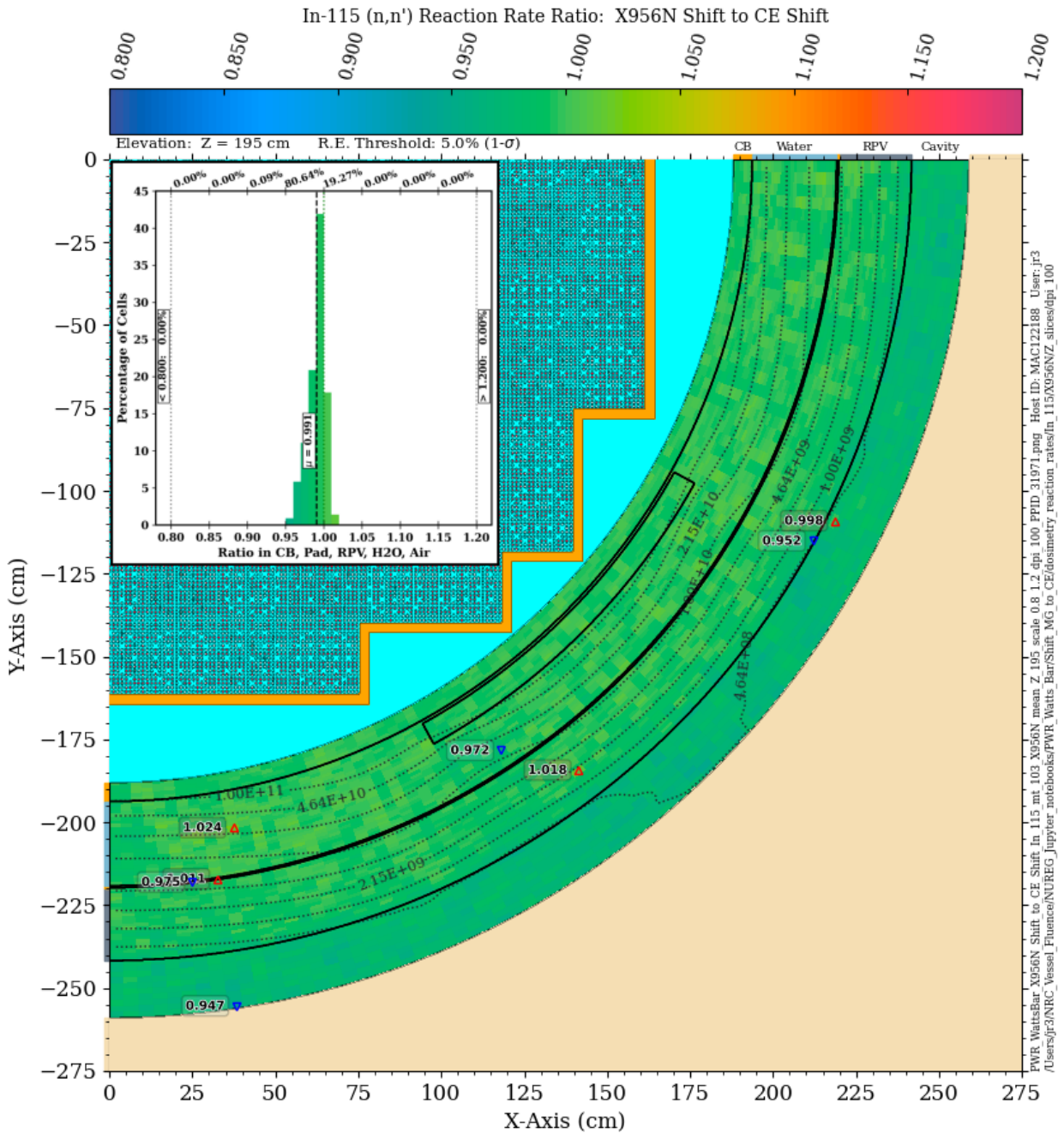

Figure 3-63 **^{115}In (n,n') ^{115m}In reaction rate ratio in the PWR model: X956N Shift/CE Shift. Plan view at Z = 195 cm. The contour lines are the reaction rate values from the CE solution**

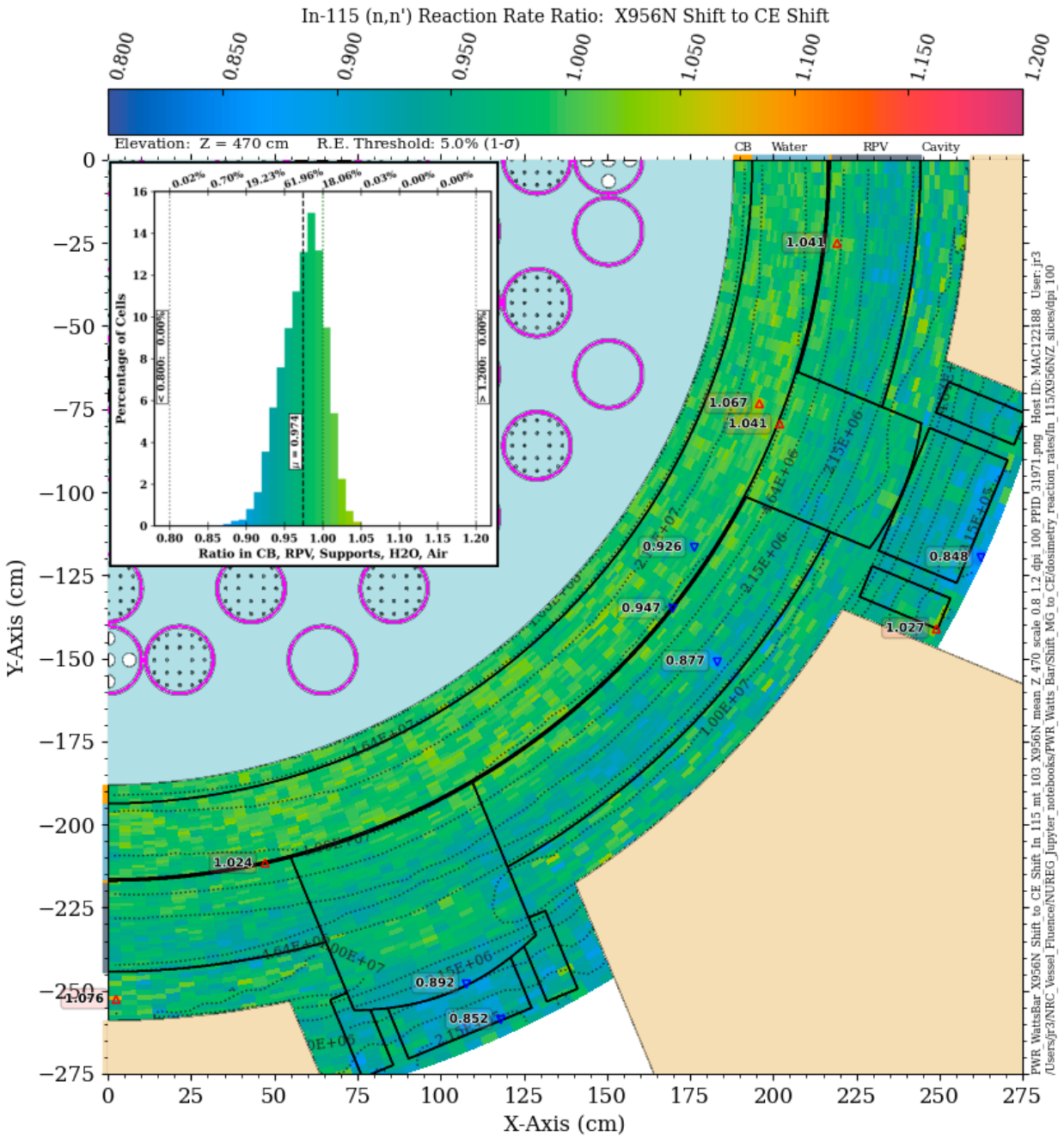

Figure 3-64 **^{115}In (n,n') ^{115m}In reaction rate ratio in the PWR model: X956N Shift/CE Shift. Plan view at Z = 470 cm. The contour lines are the reaction rate values from the CE solution**

3.4.7 ^{103}Rh (n,n′) ^{103m}Rh

The ^{103}Rh (n,n′) ^{103m}Rh reaction has a threshold energy of 40.14 keV and a 90% energy response range of 0.731 to 5.73 MeV (Table C-1). As with the ^{115}In (n,n′) ^{115m}In reaction, there is no single ENDF reaction type (MT value) which can be used to compute the production rate of the metastable isomer, and IRDF-2002 cross-section data are used. Consistent with the discussion in Section 3.4.6, only the BUGLE-B7 and X956N MG libraries were used.

The BUGLE-B7 solution agrees well with the CE solution at the core midplane (Figure 3-65) from the core barrel radially out through much of the RPV. At the outer edge of the RPV and in the cavity gap, though, the BUGLE-B7 solution underpredicts the CE solution by ~10–12%. At the elevation of the vessel supports (Figure 3-66), the BUGLE-B7 solution underpredicts the CE solution at all locations, with the difference exceeding 10% in ~55% of the mesh tally voxels, and differences exceeding 20% in some vessel support locations.

The MG solution with the X956N library is in excellent agreement with the CE solution near the core midplane (Figure 3-67), with nearly 100% of the mesh tally voxels agreeing within 5%. At Z = 470 cm, the agreement between the X956N and CE solutions is degraded (Figure 3-68), with differences of up to ~10% in the RPV, cavity gap, and vessel supports.

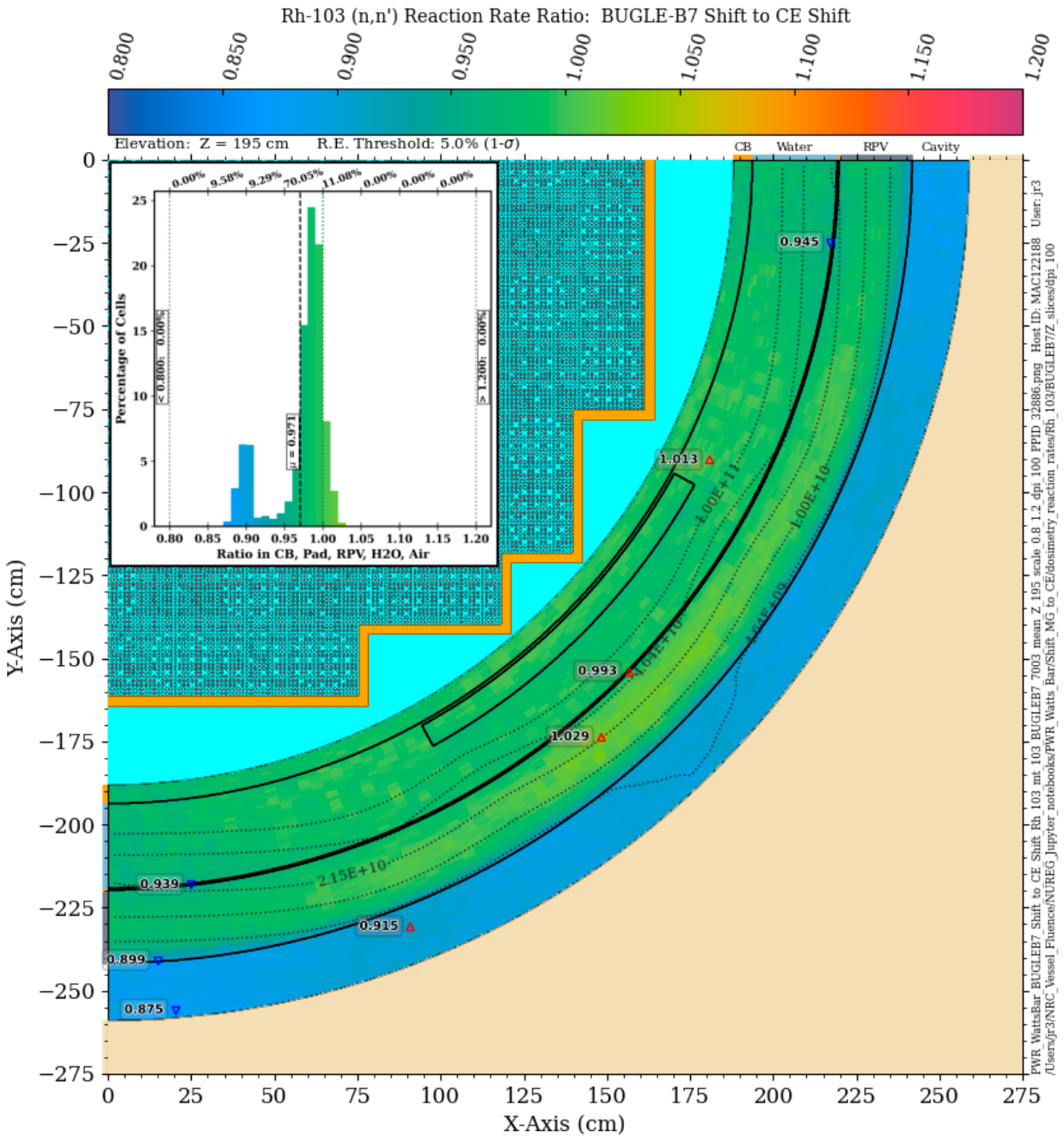

Figure 3-65 **^{103}Rh (n,n') ^{103m}Rh reaction rate ratio in the PWR model: BUGLE-B7 Shift/CE Shift. Plan view at Z = 195 cm. The contour lines are the reaction rate values from the CE solution**

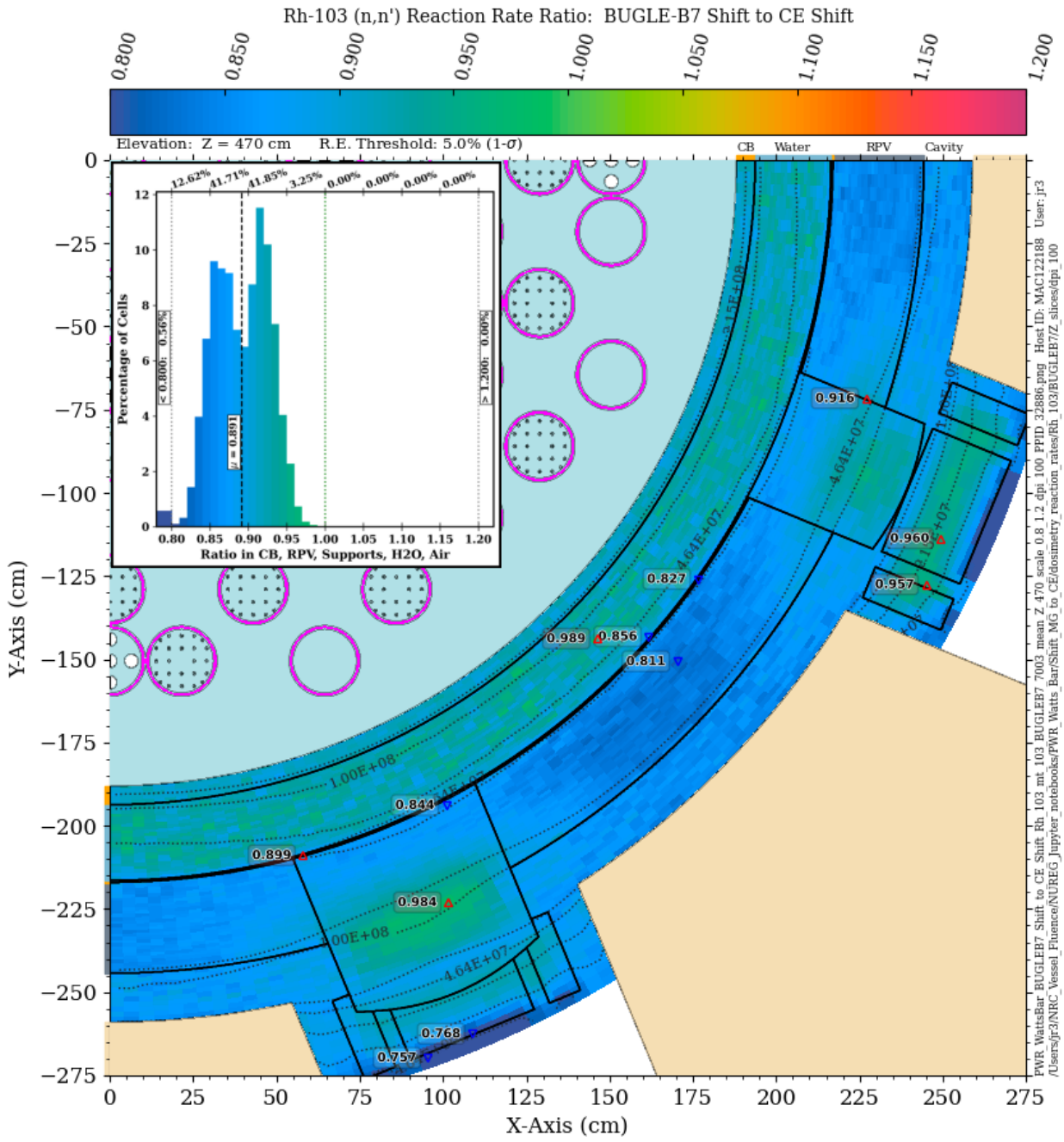

Figure 3-66 **^{103}Rh (n,n') ^{103m}Rh reaction rate ratio in the PWR model: BUGLE-B7 Shift/CE Shift. Plan view at Z = 470 cm. The contour lines are the reaction rate values from the CE solution**

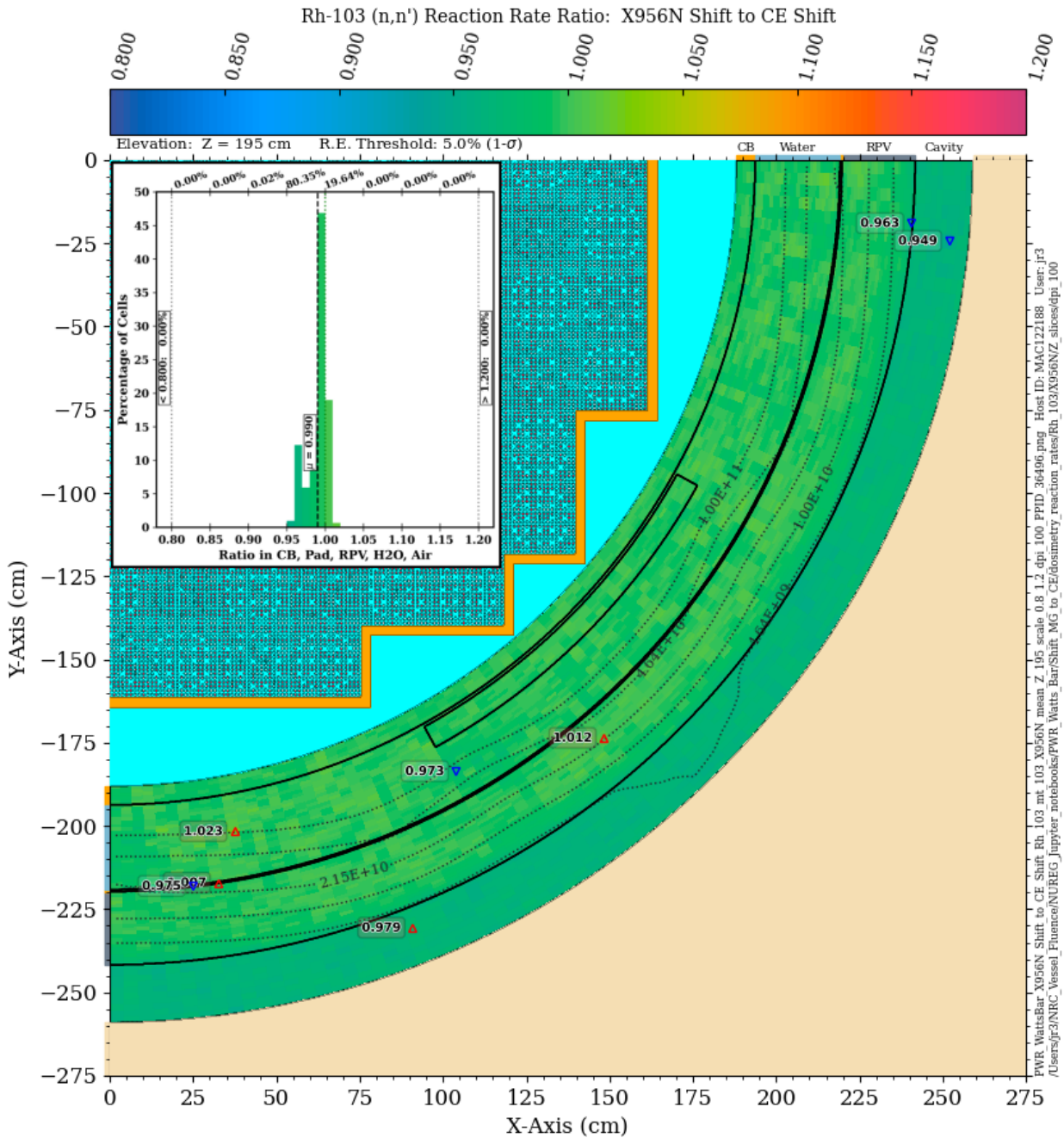

Figure 3-67 **^{103}Rh (n,n') ^{103m}Rh reaction rate ratio in the PWR model: X956N Shift/CE Shift. Plan view at Z = 195 cm. The contour lines are the reaction rate values from the CE solution**

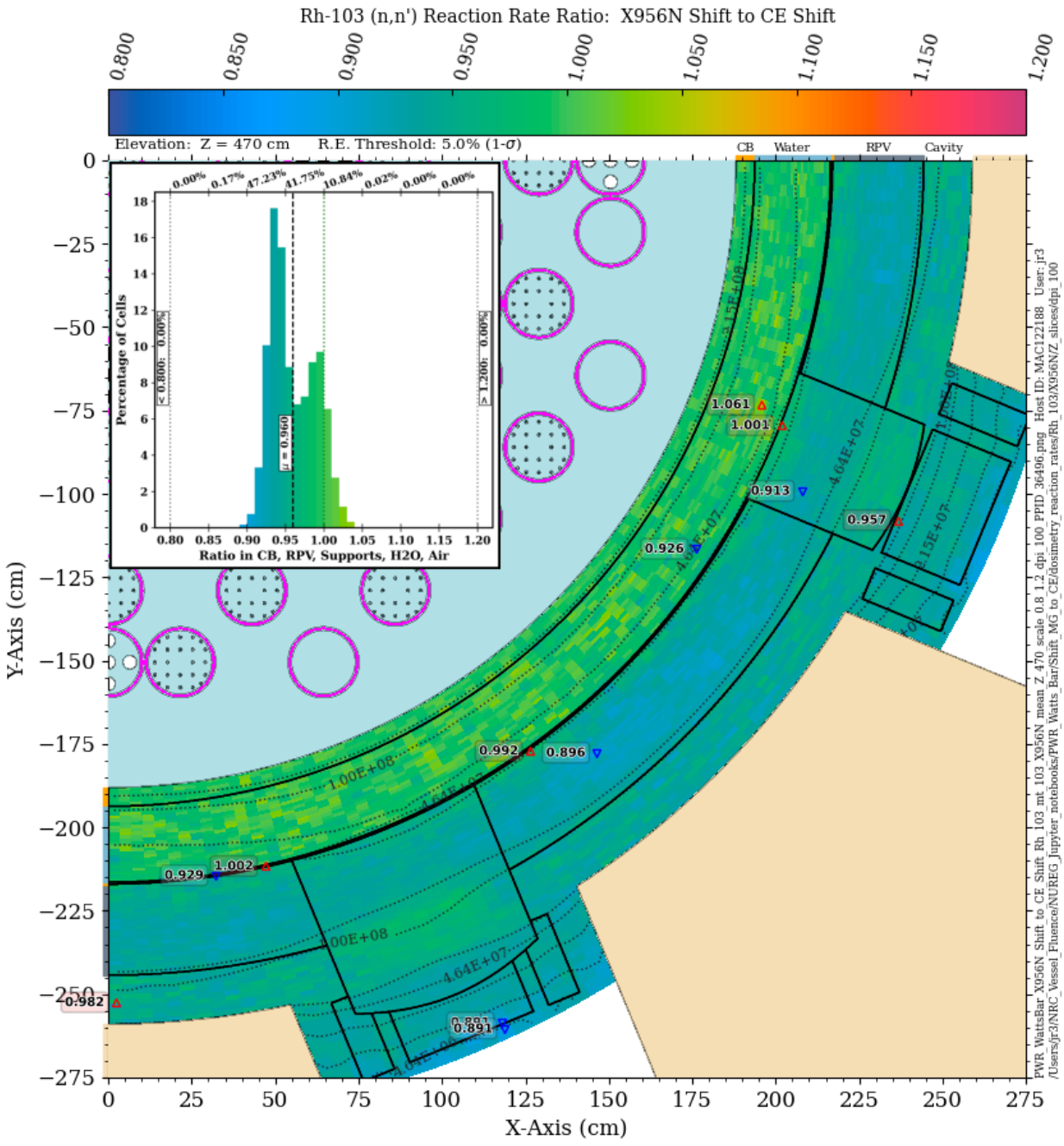

Figure 3-68 **^{103}Rh (n,n') ^{103m}Rh reaction rate ratio in the PWR model: X956N Shift/CE Shift. Plan view at Z = 470 cm. The contour lines are the reaction rate values from the CE solution**

3.4.8 ^{238}U (n,f)

The ^{238}U (n,f) reaction has no threshold energy and a 90% energy response range of 1.44 to 6.69 MeV (Table C-1). The fission rates calculated at the core midplane using the BUGLE-B7 library generally agree well with the CE solution at locations within the outer radius of the RPV, but they underpredict the CE values by up to 10% and more in the cavity gap (Figure 3-69). At Z = 470 cm (Figure 3-70), the BUGLE-B7 solution is almost uniformly lower than the CE solution in all locations other than the cavity gap, with an apparent bias of ~7–8%.

At the core midplane elevation, the X200N47G solution agrees well with the CE solution (typically within 5%) except for in the cavity gap, where the X200N47Gv71 solution underpredicts the CE solution by up to nearly 10% (Figure 3-71). At Z = 470 cm, the agreement is degraded, particularly in the outer portion of the RPV and the vessel supports, where the underprediction can reach 20% (Figure 3-72).

An MG calculation with the X956N library shows significant improvement in the MG/CE ratios. At the core midplane, the X956N solution and the CE solution agree, with the MG and CE solutions agreeing within 3% in over 98% of the mesh tally voxels (Figure 3-73). At Z = 470 cm, the MG/CE agreement is still very good, with more than 99% of the mesh tally voxels agreeing within 10%, and nearly 91% agreeing within 5%.

3.4.9 ^{237}Np (n,f)

The ^{237}Np (n,f) reaction has no threshold energy and a 90% energy response range of 0.684 to 5.61 MeV (Table C-1). The fission rates calculated using the BUGLE-B7 library agree with the CE solution within ~10% from the core barrel through the RPV (Figure 3-75), but they underpredict the CE solution by ~10–13% in the cavity gap. At Z = 470 cm (Figure 3-76), the differences between the BUGLE-B7 and CE solutions are substantially greater, with differences from 10–20% in the RPV, nozzles, and cavity gap, as well as locations in the vessel supports where the MG/CE ratio differs by more than 20%.

The Shift solution using the X200N47Gv71 library has better CE agreement than the BUGLE-B7 solution, but there are still differences of ~10% in the cavity gap at the core midplane elevation (Figure 3-77). At an elevation of 470 cm, the MG/CE differences are substantially larger (Figure 3-78), with differences of up to 20% and more in portions of the RPV, cavity gap, and vessel supports.

An MG calculation with the X956N library shows excellent agreement at the core midplane (Figure 3-79), with approximately 94% of the mesh tally voxels agreeing with the CE solution within 2.5%. At the elevation of the vessel supports (Figure 3-80), there are differences of 10–15% at locations in the RPV, cavity gap, and vessel supports.

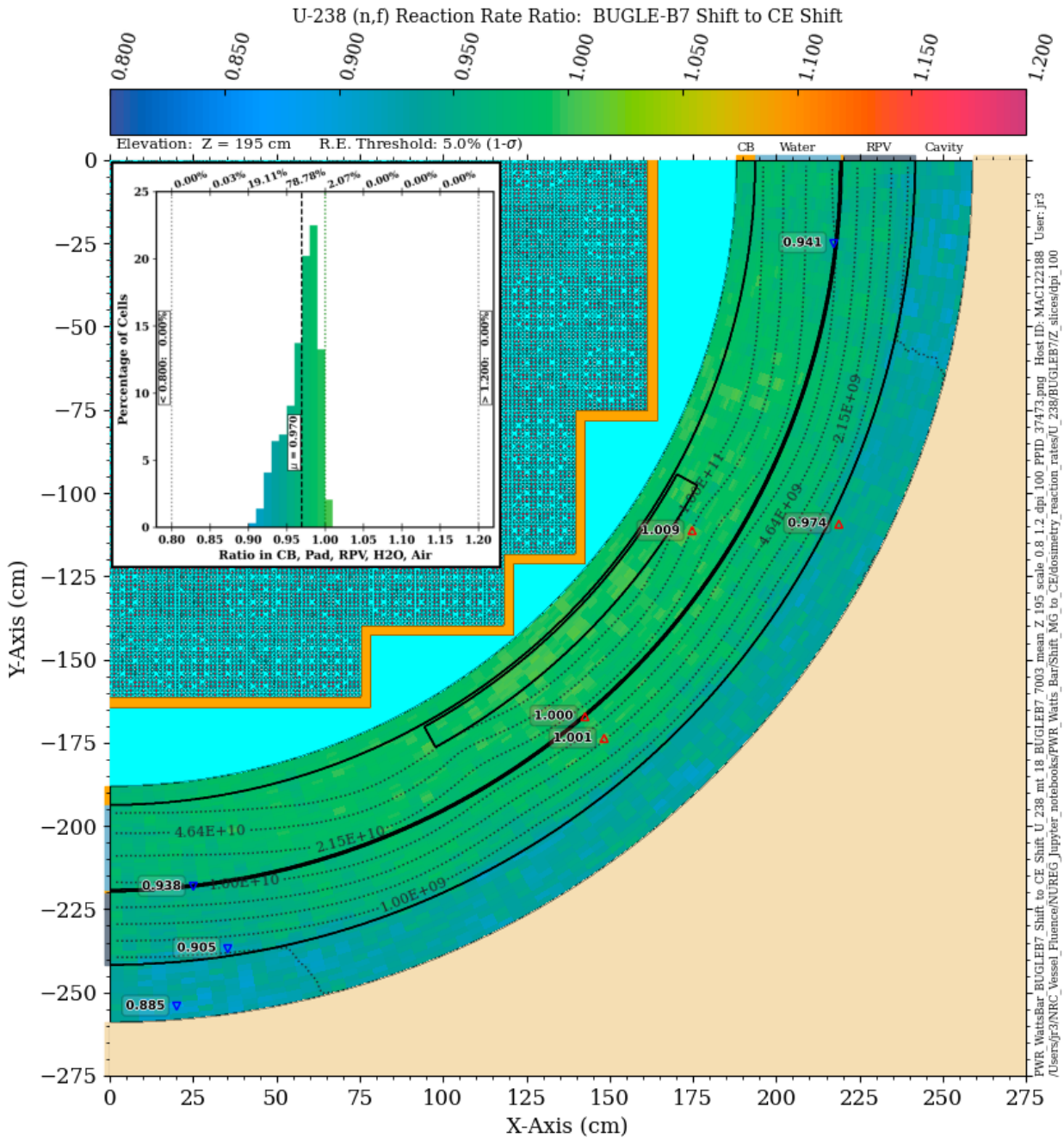

Figure 3-69 **^{238}U (n,f) reaction rate ratio in the PWR model: BUGLE-B7 Shift/CE Shift. Plan view at Z = 195 cm. The contour lines are the reaction rate values from the CE solution**

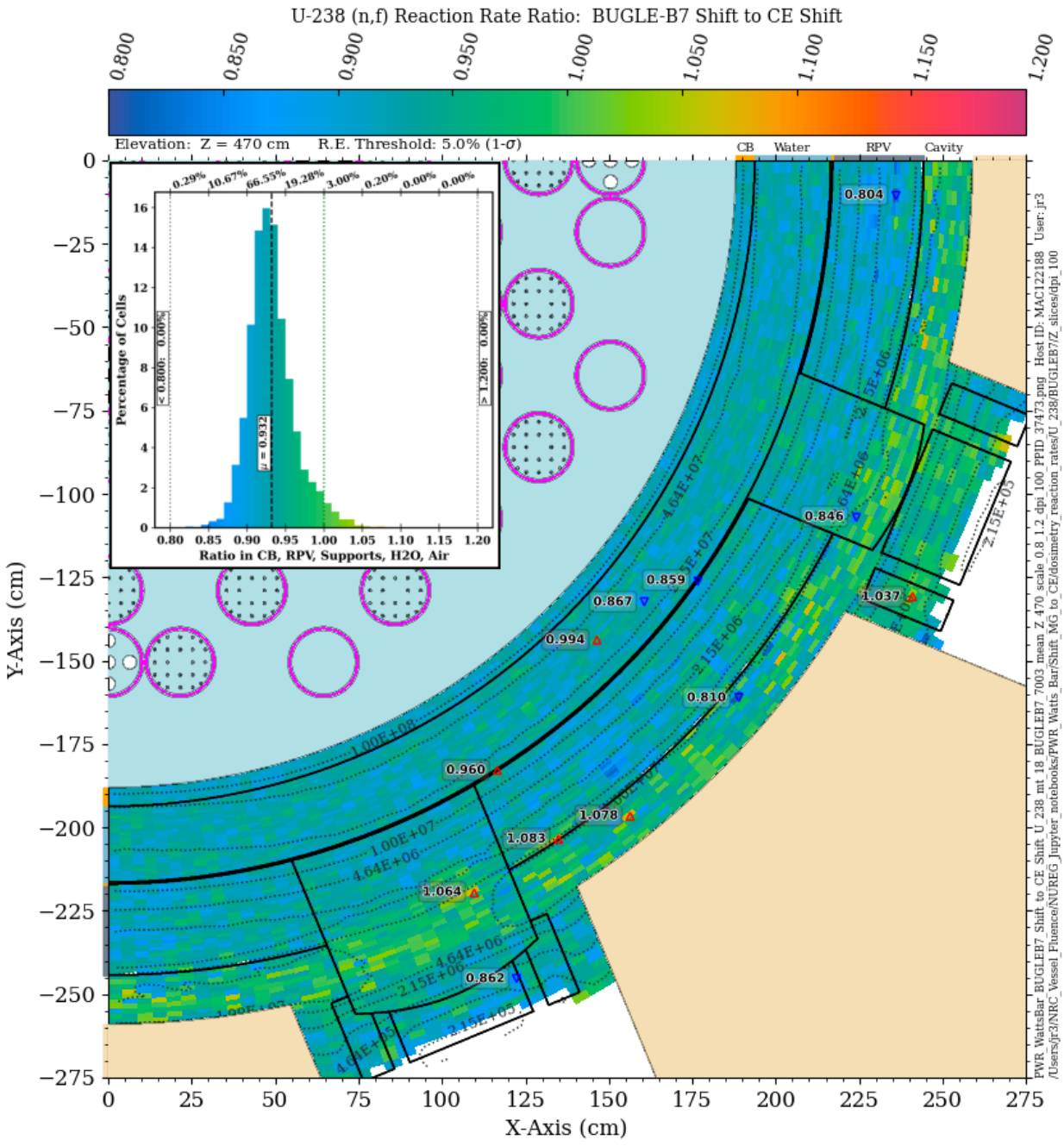

Figure 3-70 **^{238}U (n,f) reaction rate ratio in the PWR model: BUGLE-B7 Shift/CE Shift. Plan view at Z = 470 cm. The contour lines are the reaction rate values from the CE solution**

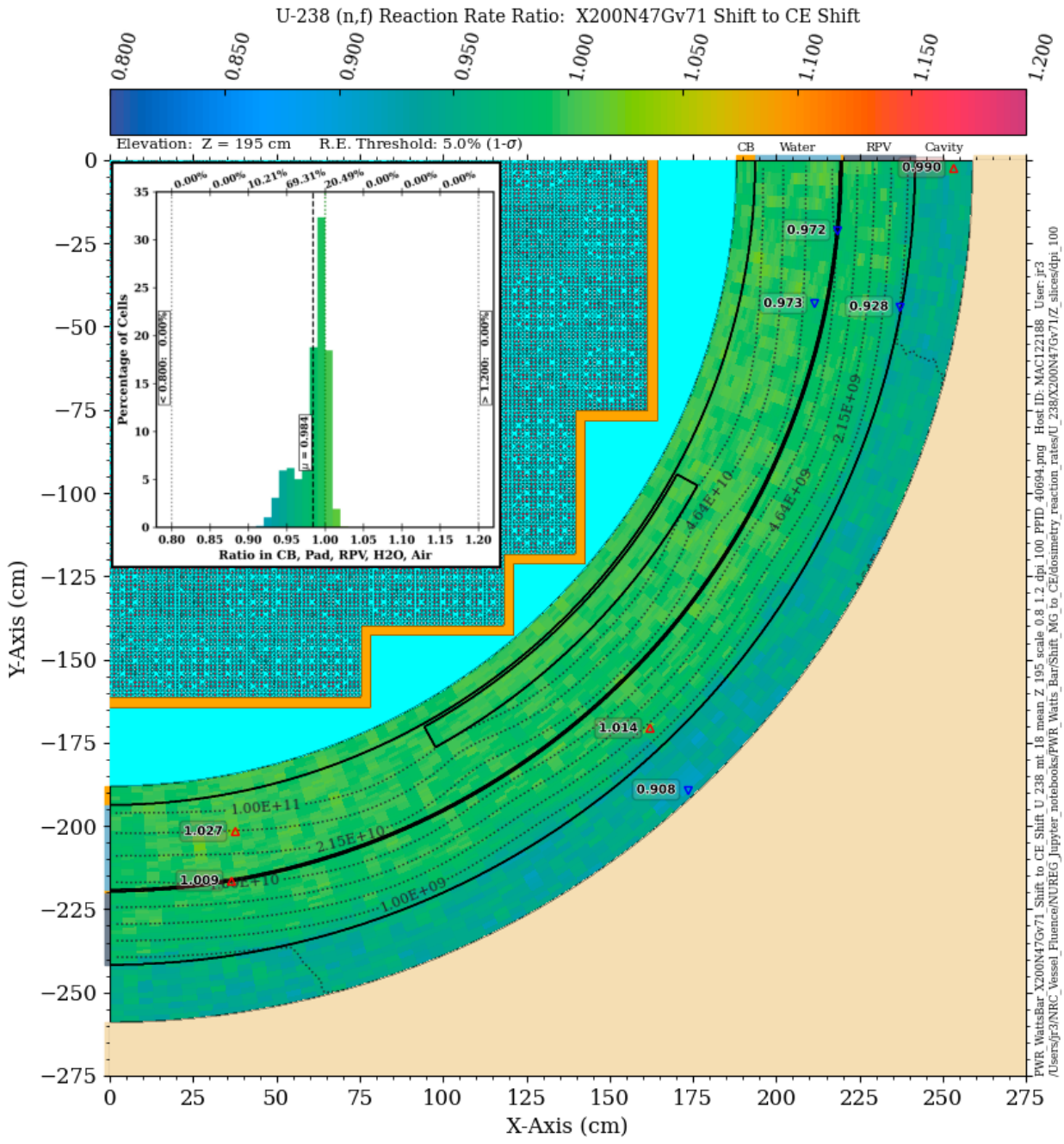

Figure 3-71 **^{238}U (n,f) reaction rate ratio in the PWR model: X200N47Gv71 Shift/CE Shift. Plan view at Z = 195 cm. The contour lines are the reaction rate values from the CE solution**

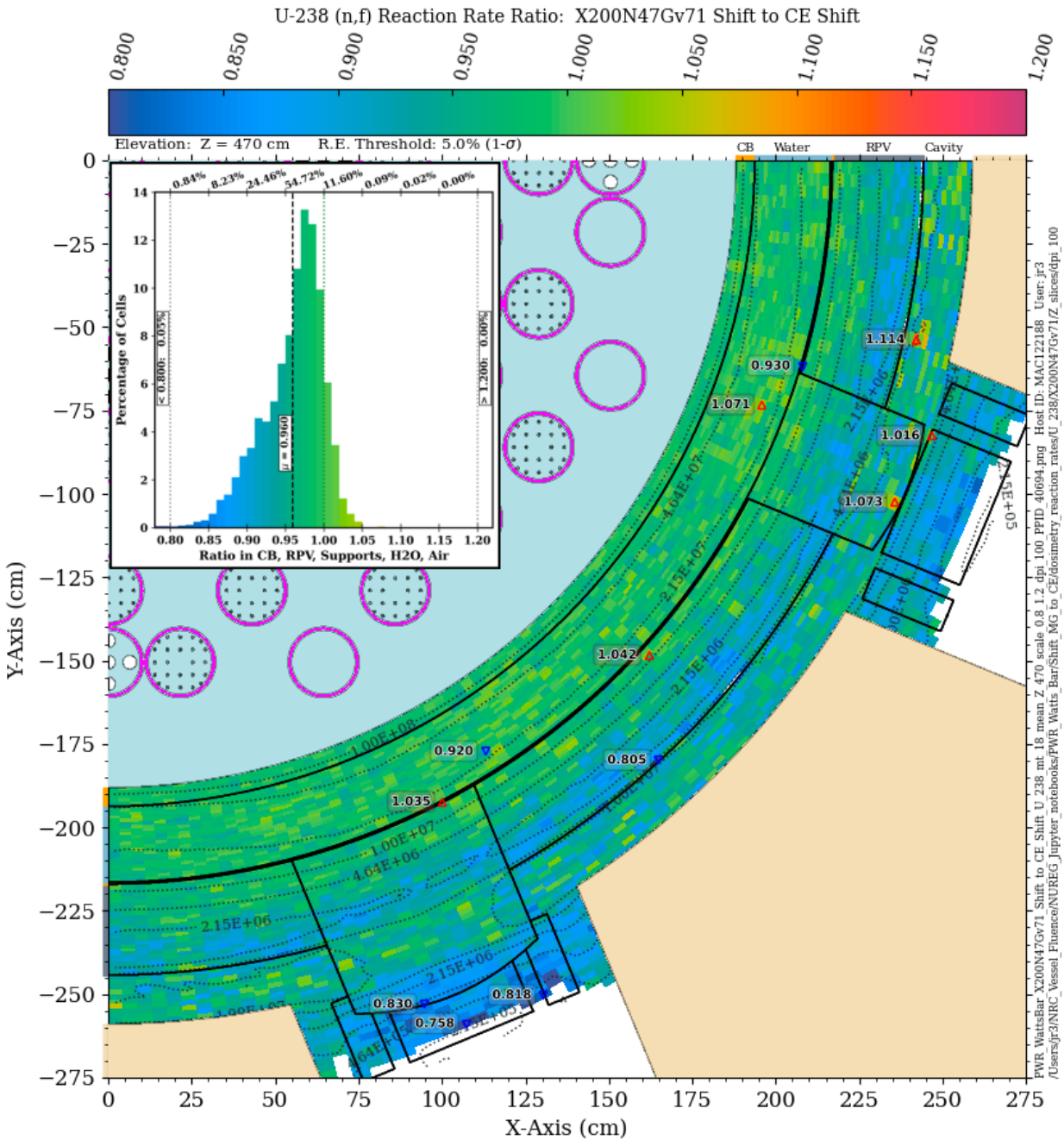

Figure 3-72 **^{238}U (n,f) reaction rate ratio in the PWR model: X200N47Gv71 Shift/CE Shift. Plan view at Z = 470 cm. The contour lines are the reaction rate values from the CE solution**

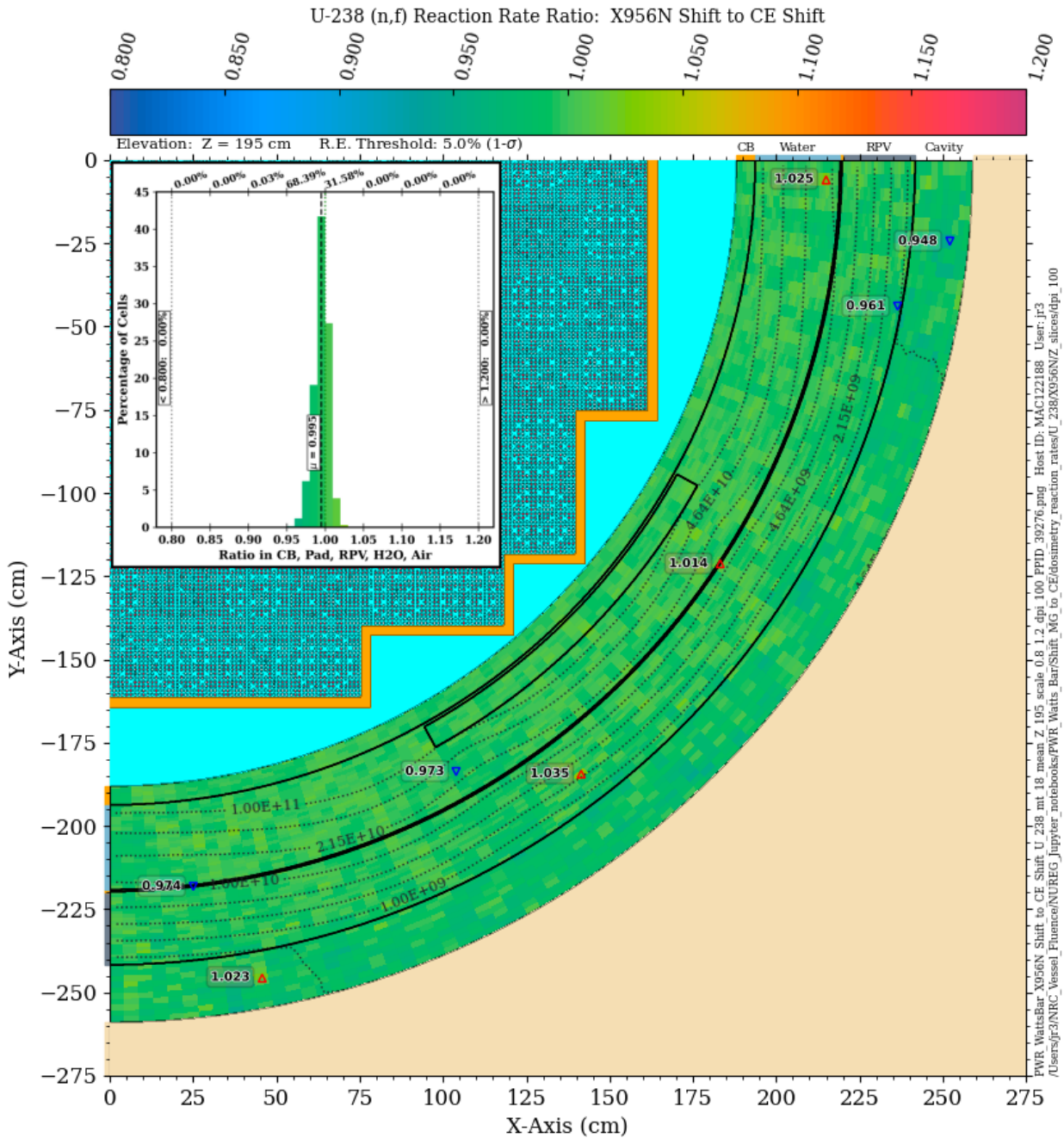

Figure 3-73 ^{238}U (n,f) reaction rate ratio in the PWR model: X956N Shift/CE Shift. Plan view at Z = 195 cm. The contour lines are the reaction rate values from the CE solution

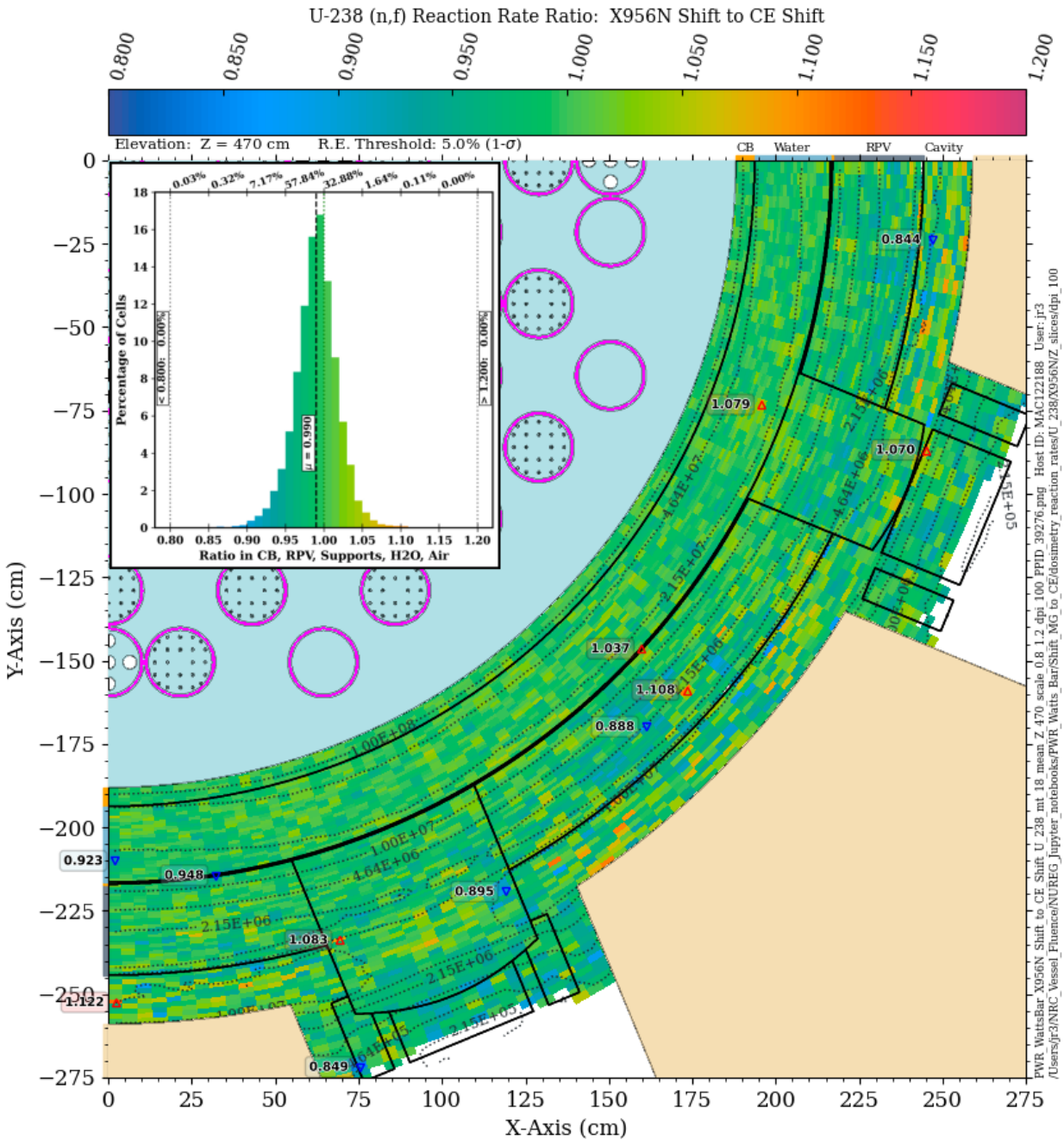

Figure 3-74 **^{238}U (n,f) reaction rate ratio in the PWR model: X956N Shift/CE Shift. Plan view at Z = 470 cm. The contour lines are the reaction rate values from the CE solution**

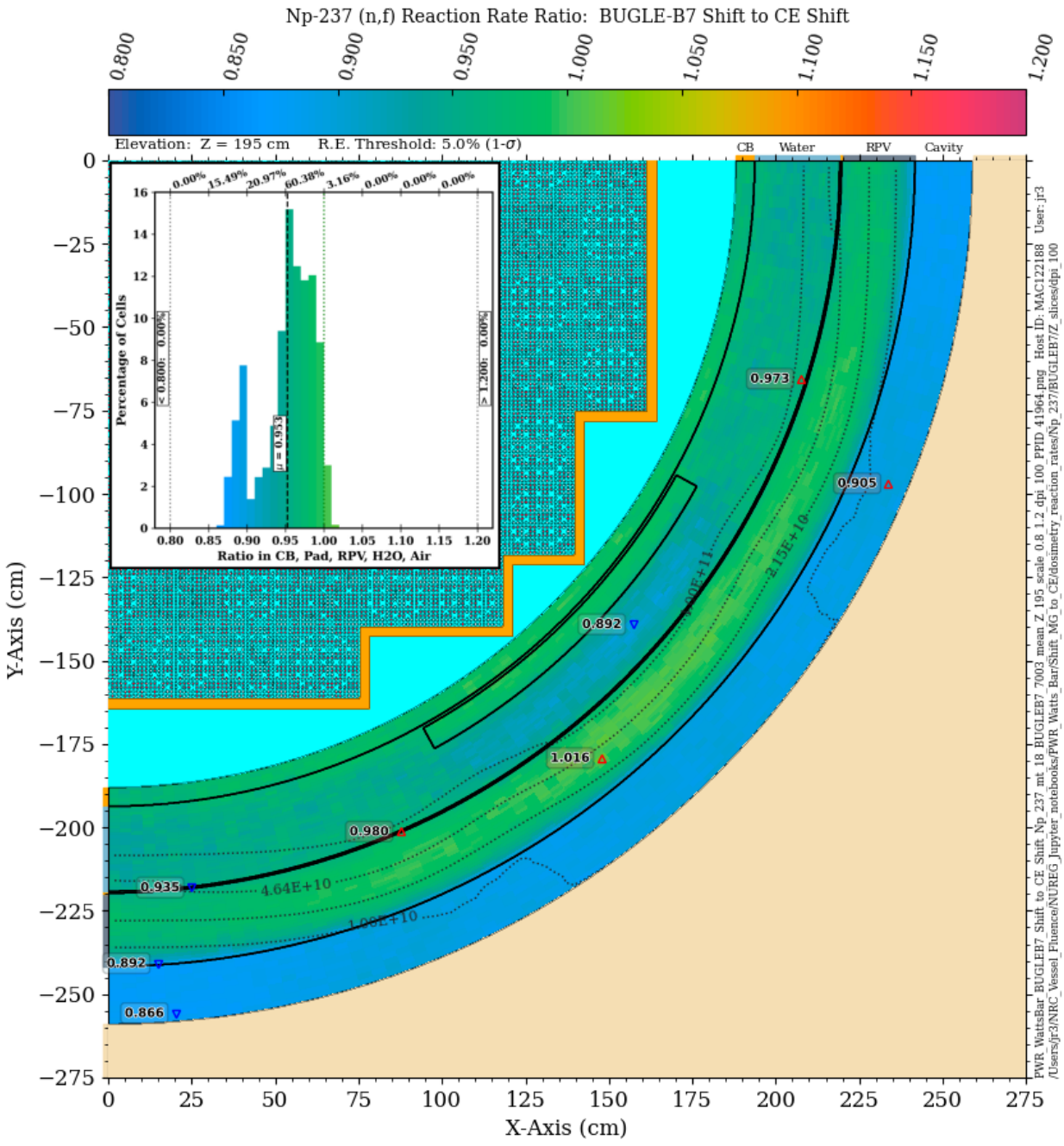

Figure 3-75 **^{237}Np (n,f) reaction rate ratio in the PWR model: BUGLE-B7 Shift/CE Shift. Plan view at Z = 195 cm. The contour lines are the reaction rate values from the CE solution**

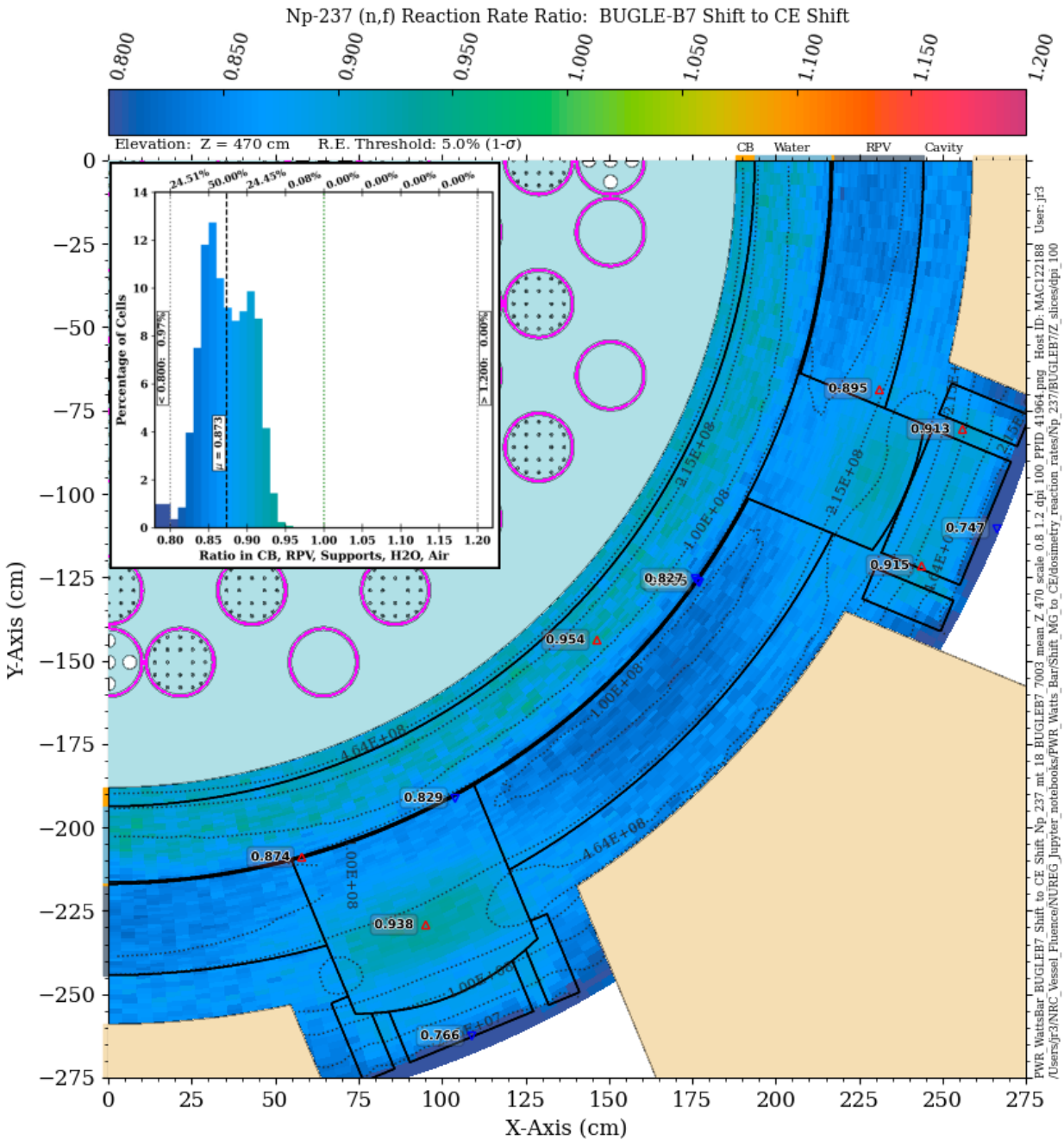

Figure 3-76 **^{237}Np (n,f) reaction rate ratio in the PWR model: BUGLE-B7 Shift/CE Shift. Plan view at Z = 470 cm. The contour lines are the reaction rate values from the CE solution**

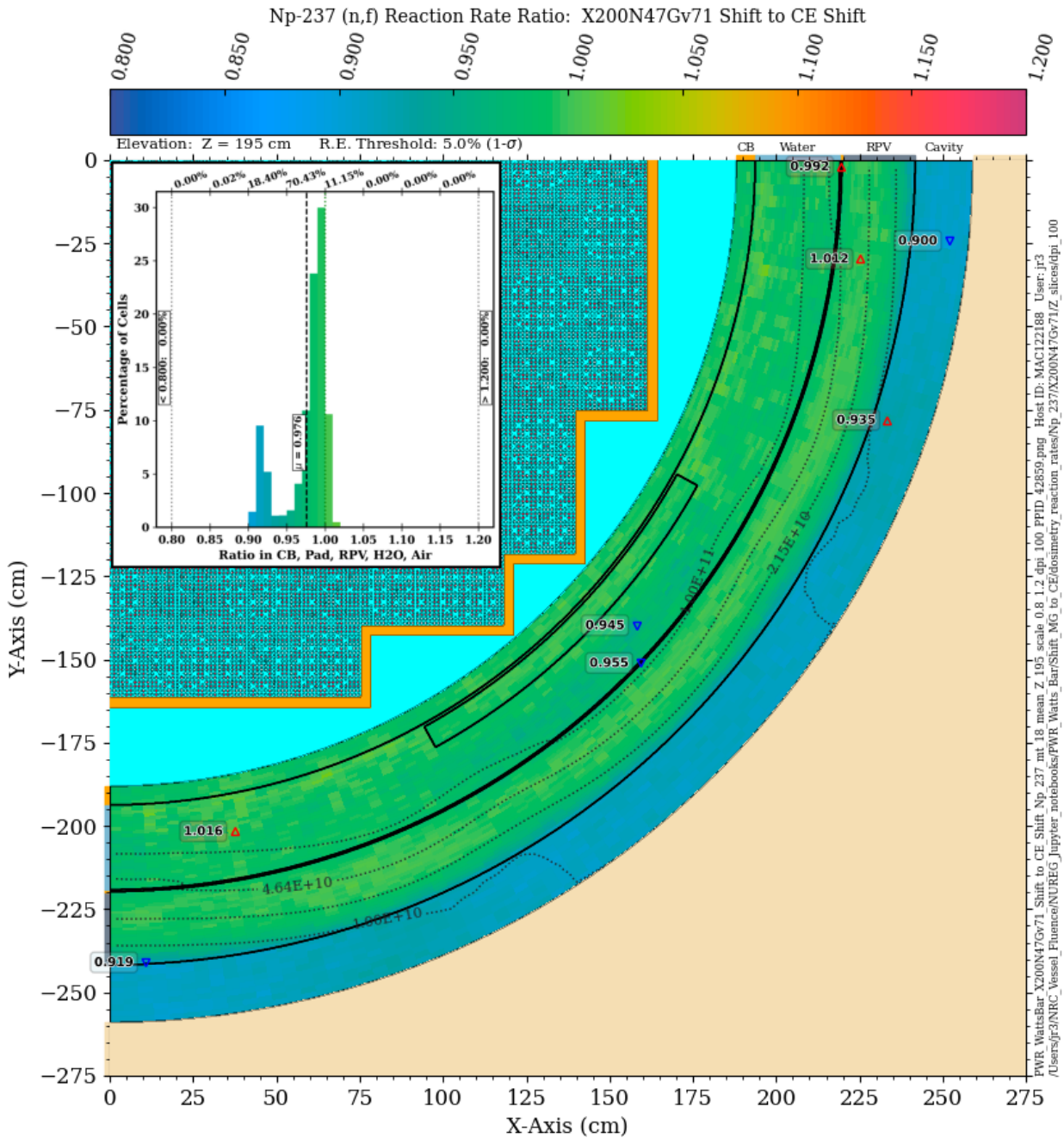

Figure 3-77 **^{237}Np (n,f) reaction rate ratio in the PWR model: 200N47Gv71 Shift/CE Shift. Plan view at Z = 195 cm. The contour lines are the reaction rate values from the CE solution**

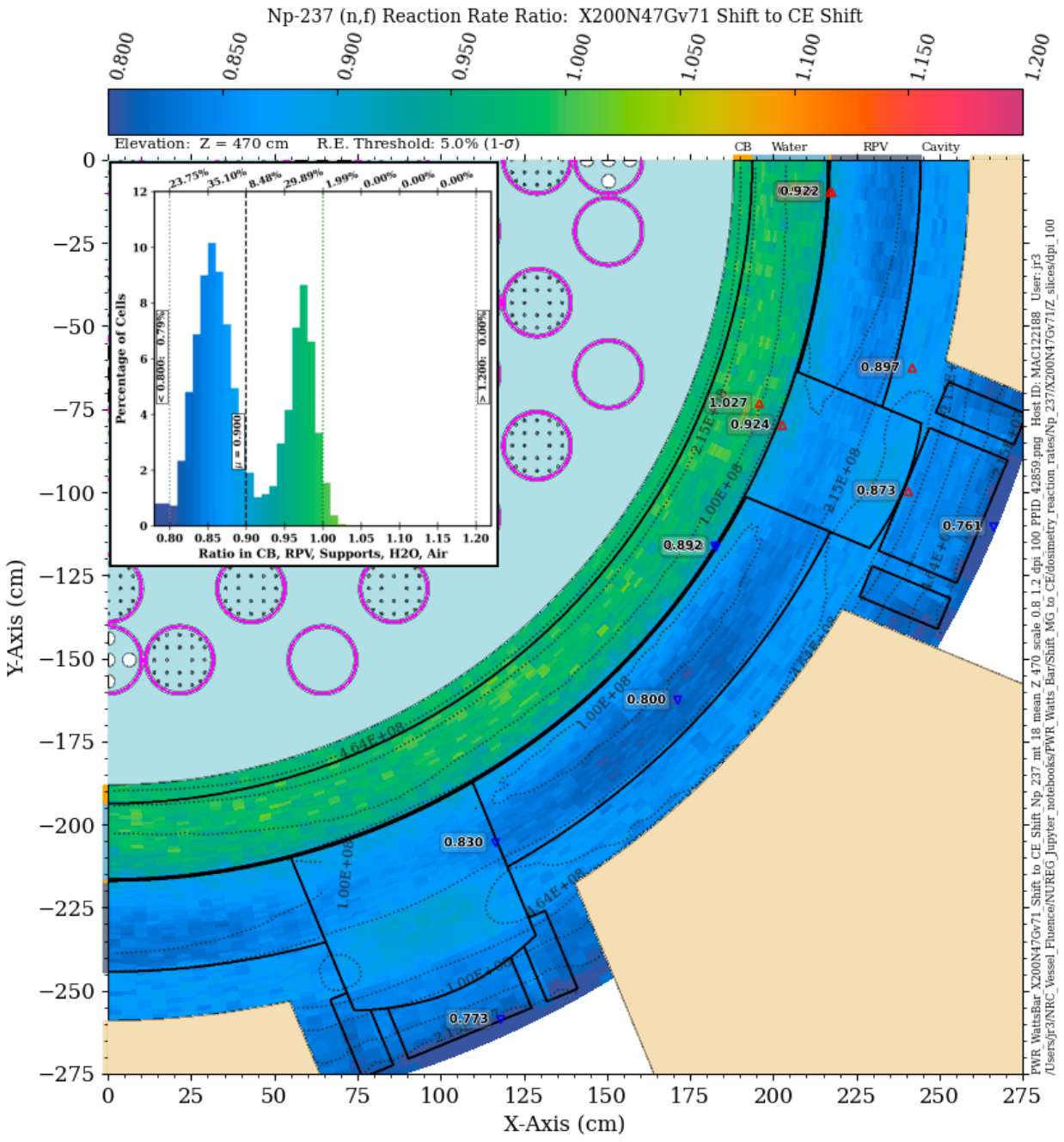

Figure 3-78 **^{237}Np (n,f) reaction rate ratio in the PWR model: 200N47Gv71 Shift/CE Shift. Plan view at Z = 470 cm. The contour lines are the reaction rate values from the CE solution**

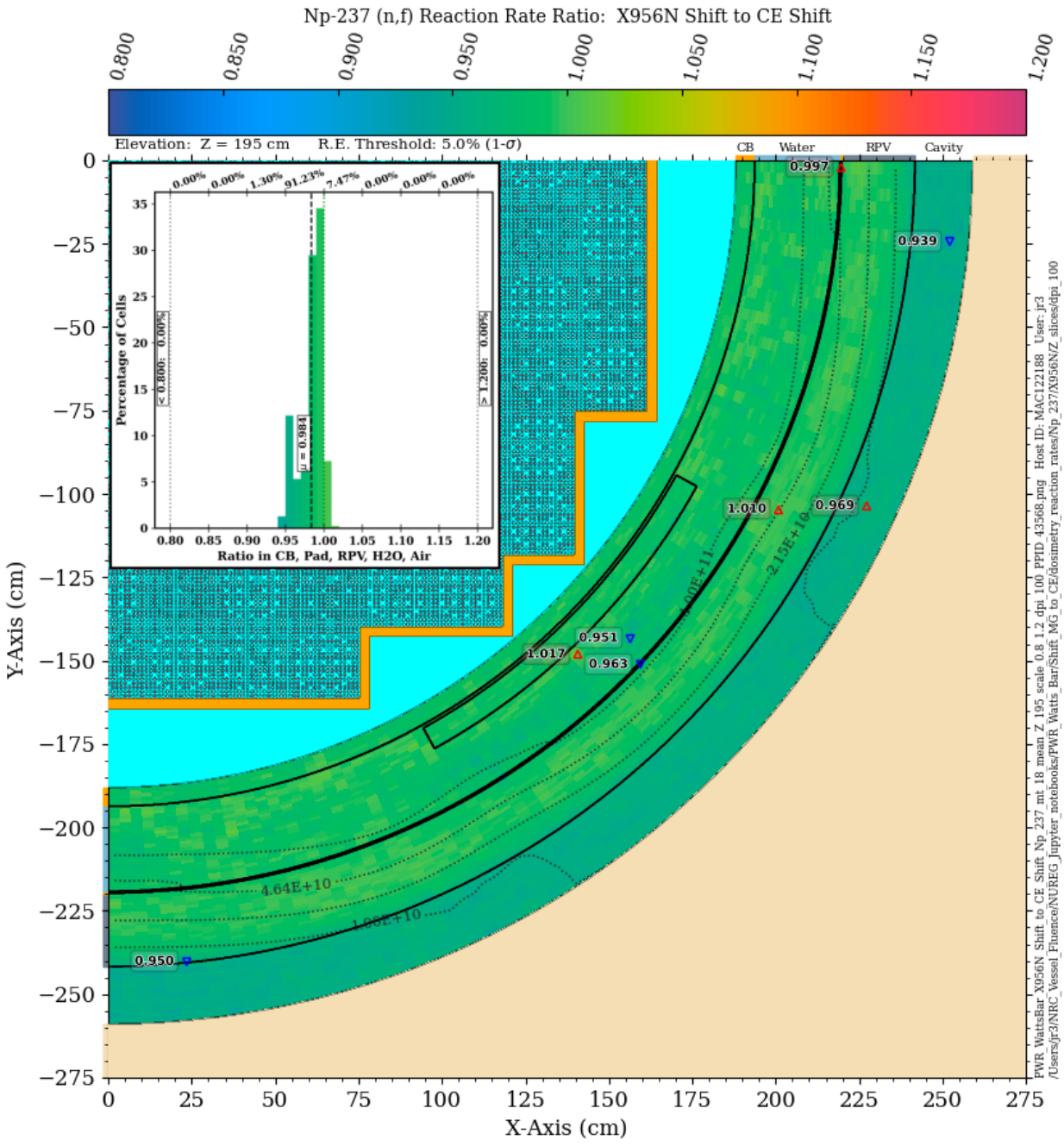

Figure 3-79 **^{237}Np (n,f) reaction rate ratio in the PWR model: X956N Shift/CE Shift. Plan view at Z = 195 cm. The contour lines are the reaction rate values from the CE solution**

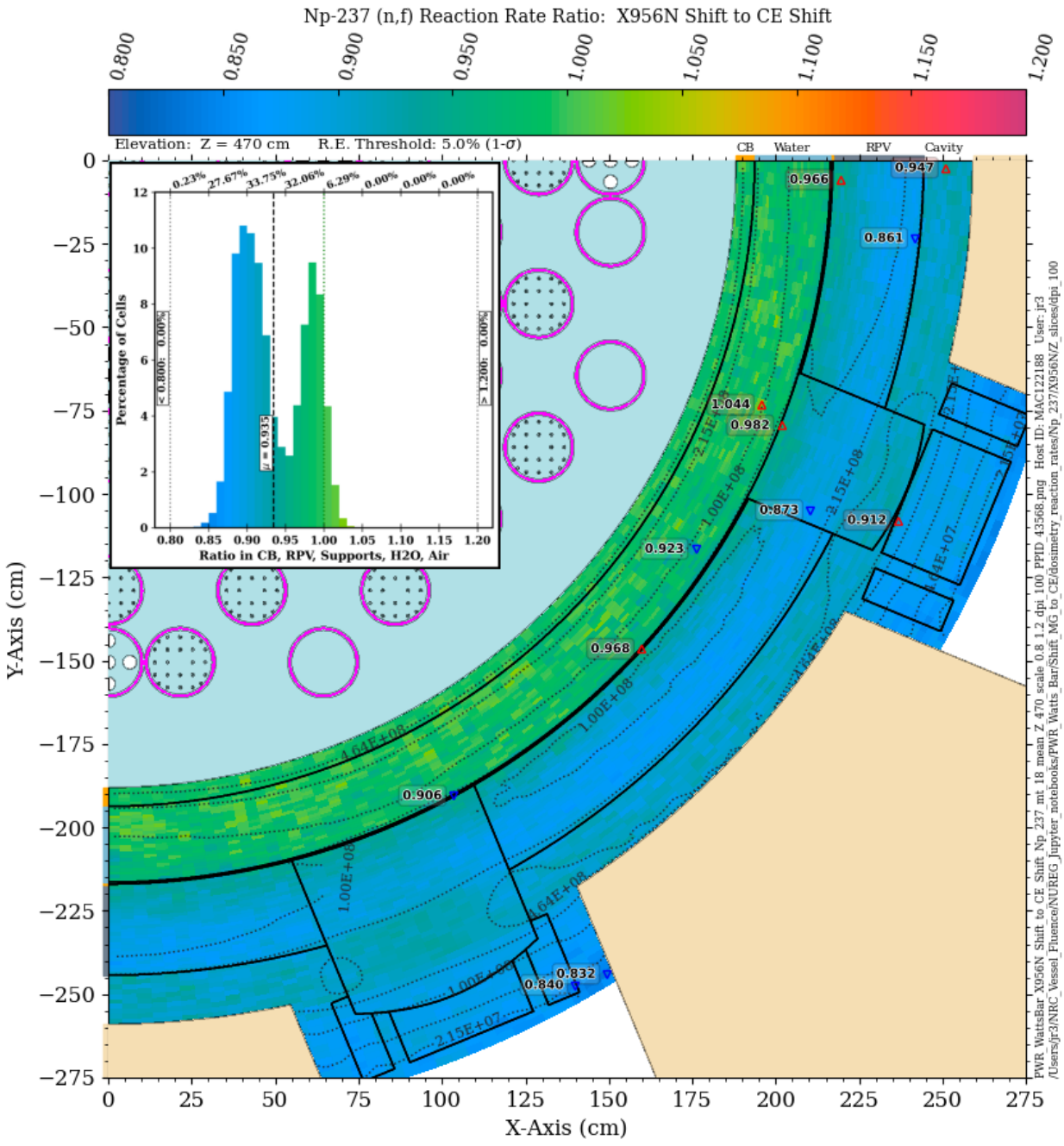

Figure 3-80 **^{237}Np (n,f) reaction rate ratio in the PWR model: X956N Shift/CE Shift. Plan view at Z = 470 cm. The contour lines are the reaction rate values from the CE solution**

3.5 Summary of multigroup studies

The analyses presented in this section provide insights into the adequacy and limitations of MG cross sections for the calculation of RPV fluence, dpa rates, and common dosimetry reactions. The results address both the traditional and extended beltline regions.

All of the MG libraries considered in this study are capable of providing accurate fast fluence estimates (i.e., values which agree very well with CE calculations) in the inner portion of the RPV within the traditional beltline region. However, with the exception of the X642N and X956N libraries which were developed specifically to improve the calculation of neutron transport through iron in the energy range of ~1 to ~3 MeV, all of the MG solutions underpredict the CE solution by ~10% at the outer surface of the RPV. Although this location is not important for RPV fluence calculations in the traditional beltline region, it is important for locations in the extended beltline region, where cavity streaming becomes an important contributor to neutron flux levels. An underprediction of the fast neutron flux at the outer surface of the RPV will result in an underprediction of the flux of neutrons that scatter from the concrete bioshield back into the cavity gap. This will result in erroneously low calculated fluxes in regions where cavity streaming is important. At the elevation of the vessel supports, all of the MG libraries except X642N and X956N underpredict the CE solution at all locations of interest, particularly in the vessel supports, where the solution differences can exceed 15% or more. In contrast, the X642N and X956N libraries provide fast fluence predictions that agree with the CE solution at the vessel support elevation within 5% in nearly all the locations of interest.

For dpa rate calculations, the results are more complex. The widely used BUGLE-B7 library underpredicts the dpa rate at all locations in the RPV at the traditional beltline elevation, with a maximum difference of more than 20% at the outer edge of the RPV. At the elevation of the vessel supports, the BUGLE-B7 solution underpredicts the CE solution by more than 20% at nearly all locations, with differences in the range of 35% at some locations in the vessel supports. Solutions using the VITAMIN-B7, X200N47Gv71, and X642N libraries overpredict as well as underpredict the dpa rate at the traditional midplane elevation, with the majority of locations agreeing with the CE solution within 5%. At the elevation of the vessel supports, these libraries produce solutions that underpredict the CE solution in all locations, with differences of 15% and more occurring in the vessel supports. The MG/CE agreement is markedly improved with the X956N library. Near the core midplane, the agreement is excellent, with differences of less than 2.5% in over 99% of the mesh tally voxels. At the elevation of the vessel supports, the MG solution again underpredicts the CE solution, but to a much lesser extent than the other libraries. The ratio values are tightly clustered with an apparent bias of ~6%.

The MG/CE agreement for the dosimetry rate calculations is strongly dependent on the reaction cross section being considered. For the three reactions with threshold energies above 2 MeV [^{27}Al(n,α), ^{63}Cu (n,α), and ^{46}Ti (n,p)], the MG/CE agreement is reasonably good at both of the elevations considered, with the exception of the ^{46}Ti (n,p) reaction rate calculated with the BUGLE-B7 and VITAMIN-B7 libraries. As noted in Section 3.4.3, the poor agreement obtained with the BUGLE-B7 and VITAMIN-B7 libraries is likely caused by differences in the ^{46}Ti (n,p) cross-section data rather than the transport cross sections.

Results for the ^{54}Fe (n,p) and ^{58}Ni (n,p) reactions—with threshold energies of 700 and 400 keV, respectively—are very similar. In each case, the BUGLE-B7 and X200N47Gv71 libraries provide good agreement with the CE solution in the traditional beltline region. At the elevation of the vessel supports, the BUGLE-B7 solutions are uniformly low, particularly toward the inner

surface of the RPV, where differences approach 10%. The X200N47Gv71 solution provides improved agreement at this elevation, with more than 92% of the tally values agreeing with the CE solution to within 5%.

For the ^{115}In (n,n′) and ^{103}Rh (n,n′) reactions, the BUGLE-B7 solutions agree well with the CE solution from the core barrel through the inner portion of the RPV at the traditional beltline location. However, at the outer edge of the RPV and in the cavity gap, the BUGLE-B7 solutions underpredict the CE solutions by up to ~10%. The agreement is degraded at the elevation of the vessel supports, where differences of 20% and more occur, particularly in the vessel supports. The X956N library solution for these two reaction rates is in excellent agreement with the CE solution at the traditional beltline elevation, with MG/CE differences of less than 5% in 99.9% of the mesh tally voxels. The agreement is degraded somewhat at the elevation of the vessel supports, but it is markedly improved relative to the BUGLE-B7 solution, with MG/CE agreement of 10% in more than 99% of the mesh tally voxels.

For the ^{238}U (n,f) reaction, the BUGLE-B7 solution consistently underpredicts the CE solution. At the traditional beltline elevation, the BUGLE-B7/CE differences are up to ~10% at the outer edge of the RPV and in the cavity gap. At the elevation of the vessel supports, the BUGLE-B7/CE agreement is further degraded, with differences of 15% or more in some locations. The MG/CE agreement at the core midplane is improved with the X200N47Gv71 library, with differences typically less than 5% except in the cavity gap, where the X200N47Gv71 solution underpredicts the CE solution by up to nearly 10%. At the elevation of the vessel supports, the solution agreement is degraded, particularly in the outer portion of the RPV and the vessel supports, where the X200N47Gv71 underprediction can reach 20%. The X956 library provides substantial improvements in the MG/CE ratios, particularly at the vessel support elevation, where the solutions agree to within 10% in more than 99% of the mesh tally cells and to within 5% in nearly 91% of the mesh tally cells.

Of all of the dosimetry reaction rates considered, the MG/CE differences are greatest at both the core midplane and the vessel support elevation for the ^{237}Np (n,f) reaction rate. This is not surprising, as the 90% energy response range for this reaction is the lowest of the nine reactions considered (Figure C-2). The BUGLE-B7 solution underpredicts the CE solution by ~10–13% throughout the cavity gap at the core midplane elevation. At the vessel support elevation, the BUGLE-B7/CE differences range from 10–20% in the RPV, nozzles, and cavity gap, with differences exceeding 20% in some vessel support locations. The X200N47Gv71 solution provides some improvement relative to the BUGLE-B7 solution, but there are still differences of 20% or more in some vessel support locations. Although the X956N solution agrees with the CE solution to within 5% in over 98% of the mesh tally cells at the core midplane elevation, the MG/CE differences with this library at the vessel support elevation are still relatively high, with differences exceeding 10% in in nearly 28% of the mesh tally cells, and differences of up to ~15% at locations in the vessel supports.

The results of the MG/CE comparisons for these 11 neutron responses (fast flux, dpa rate, and nine dosimetry reaction rates) suggest that while the widely used BUGLE-B7 library is generally adequate for the calculation of these quantities at locations radially out through the inner portion of the RPV in the traditional beltline region, it is not well suited to the calculation of most of these 11 responses at locations in the extended beltline region. In some cases, the differences between a BUGLE-B7 solution and a more accurate CE solution exceed 20%. This suggests that for a discrete ordinates calculation (which is also subject to the approximations made in

space and angle) using the BUGLE-B7 library, it may not be possible to obtain calculational results that are within the 20% uncertainty value prescribed by RG 1.190.

Improved agreement between MG and CE solutions can be obtained by using very fine energy-group structures that are specifically developed to accurately model neutron transport through iron over important resonance ranges. However, these very-fine-group libraries may have 10 times or more the number of groups in the BUGLE-B7 library. Because the MG libraries have 2D arrays for all the group-to-group scattering probabilities, the memory requirements for a discrete ordinates calculation scale as N^2 rather than N for a library with N groups. The computing resources required to perform 3D discrete ordinates calculations with these libraries can thus easily become prohibitive.

4. SCATTERING CROSS-SECTION EXPANSION (P_N) ORDER SENSITIVITY IN THE EXTENDED BELTLINE REGION

The angular distribution of scattered radiation in MG discrete ordinates calculations is modeled using Legendre polynomial expansions. The degree to which these expansions can adequately represent a scattering distribution is dependent on the degree of anisotropy in the MG scattering cross sections. A discussion of the causes of anisotropic MG scattering cross sections and examples of the scattering characteristics of some common nuclides and materials in LWR shielding analyses are provided in APPENDIX D.

As noted in APPENDIX D, MG scattering cross sections tend to be more anisotropic for light elements and for high-energy neutrons. Thus, scattering of neutrons within the RPV wall is less sensitive to the scattering expansion order than the scattering of neutrons within hydrogenous materials such as the coolant and the concrete bioshield. This behavior has implications for not only the penetration of neutrons through the RPV and the concrete, but also for scattering from the concrete back into the cavity gap. Consequently, it is possible that the calculation of neutron fluxes, dpa rates, and dosimetry reaction rates in the extended beltline region may be more sensitive to the scattering expansion order than similar calculations within the traditional beltline.

For RPV fluence calculations with typical LWR configurations in the beltline region, RG 1.190 requires a minimum P_3 expansion order. No suggestion is made as to the potential need for higher-order scattering in locations where cavity streaming is important.

It should be noted that the amount of memory required for a discrete ordinates calculation varies as $(N+1)^2$, where N is the order of the scattering expansion. Thus, a P_5 calculation requires more than twice the memory needed for a P_3 calculation, and a P_7 calculation requires four times the memory of a P_3 calculation. For this reason, as well as the increase in computational time with higher-order scattering, there is a strong incentive to avoid the use of higher expansion orders (i.e., greater than P_3) if the flux solution is relatively insensitive to the additional scattering moments.

This section describes evaluation of the effect of higher-order ($> P_3$) scattering on the fast neutron flux, dpa rate, and selected dosimetry reaction rates in the extended beltline region. In all cases, the comparisons are between P_3 and P_5 scattering.

4.1 Effect of scattering order on fast flux levels and dpa rates

The effect of increasing the scattering order from P_3 to P_5 has an insignificant impact on fast neutron flux and dpa rate calculations not only in the traditional beltline region (as expected), but also in the extended beltline region. Figure 4-1 illustrates the P_5/P_3 fast ($E > 1.0026$ MeV) neutron flux ratio at elevations of 200 and 465 cm. Within the RPV, nozzles, and RPV supports, the solution differences are less than 1%. The greatest difference in these solutions is seen deep in the concrete bioshield and is no more than 3%.

The dpa rate sensitivity is shown in Figure 4-2. As with the fast flux comparison, the differences between the P_3 and P_5 solutions are less than 1%. Note that because the dpa rate is only meaningful in carbon steel, the ratio data are only shown in the RPV, nozzles, and RPV supports.

These comparisons suggest that P_3 scattering expansions are adequate for calculation of fast fluence and dpa in the extended beltline region of RVs, as well as in the traditional beltline region.

4.2 Effect of scattering order on dosimetry reaction rates

Although P_3 expansions are adequate for fast fluence and dpa calculations in the extended beltline region, it is possible that higher-order scattering may be appropriate for the calculation of neutron reaction rates with high energy thresholds. Because neutron dosimetry reactions are used to benchmark calculational methods, any decrease in the accuracy of calculating these reaction rates has implications for methods validation studies.

Section 3.4 presents comparisons of calculated reaction rates for nine commonly used dosimetry isotopes using MG and CE cross-section libraries. Three of the dosimetry reactions—^{27}Al (n,α), ^{63}Cu (n,α), and ^{46}Ti (n,p)—have energy thresholds above 2 MeV. Because angular distributions of scattered neutrons are more anisotropic at high energies (see, for example, Figure D-6, Figure D-7, and Figure D-8), it is possible that calculation of those dosimetry reaction rates may be more sensitive to higher-order scattering moments compared to fast fluence and dpa calculations.

Figure 4-3 shows the ratio of the calculated ^{27}Al (n,α) reaction rate at Z = 200 cm and Z = 465 cm. Near the core midplane, there is very little difference between the P_3 and P_5 solutions except within the bioshield. However, at the elevation of the RPV supports, there are significant differences in the solutions within the cavity gap, nozzle, and outermost portion of the RV. These differences, which can exceed 20%, could affect the accuracy of calculations for ^{27}Al dosimeters that may be placed in the extended beltline region.

Figure 4-4 shows the ratio of the calculated ^{63}Cu (n,α) reaction rate at the same elevations. The agreement near the core midplane is very good, but at the elevation of the RPV supports, there are again significant differences between the P_3 and P_5 solutions. These solution differences are less than those for the ^{27}Al (n,α) reaction, which is consistent with the lower threshold energy for the ^{63}Cu (n,α) reaction.

Figure 4-5 shows the ratio of the calculated ^{46}Ti (n,p) reaction rate at the same elevations. Consistent with the lower energy threshold of this reaction of 2.10 MeV, the solution differences at the elevation of the RV supports are again reduced, with no values exceeding 8%.

For the ^{54}Fe (n,p) reaction, which has a threshold energy of 700 keV, there are only small differences, typically less than 3% between the P_3 and P_5 solutions (Figure 4-6).

Based on these findings, it is reasonable to ask whether P_5 scattering expansions are adequate for calculation of high-energy threshold reactions. Calculations of the ^{27}Al and ^{63}Cu (n,α) reaction rates using P_7 scattering show insignificant (< 2%) differences, even at the elevation of the RPV supports.

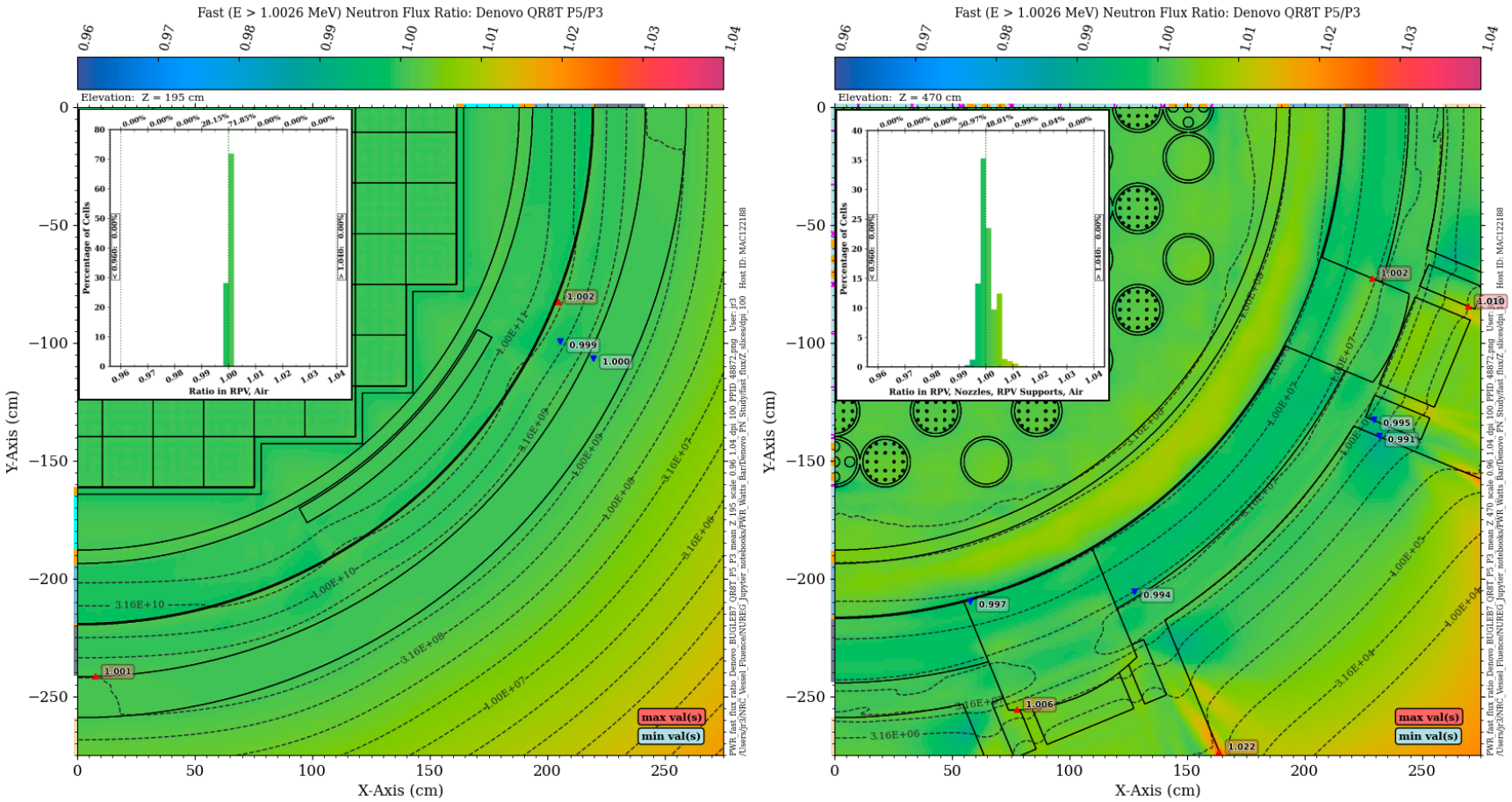

Figure 4-1 Ratio of the fast neutron flux (E > 1.0026 MeV) from a P5 Denovo solution to a P3 Denovo solution at elevations of Z = 195 cm and Z = 470 cm

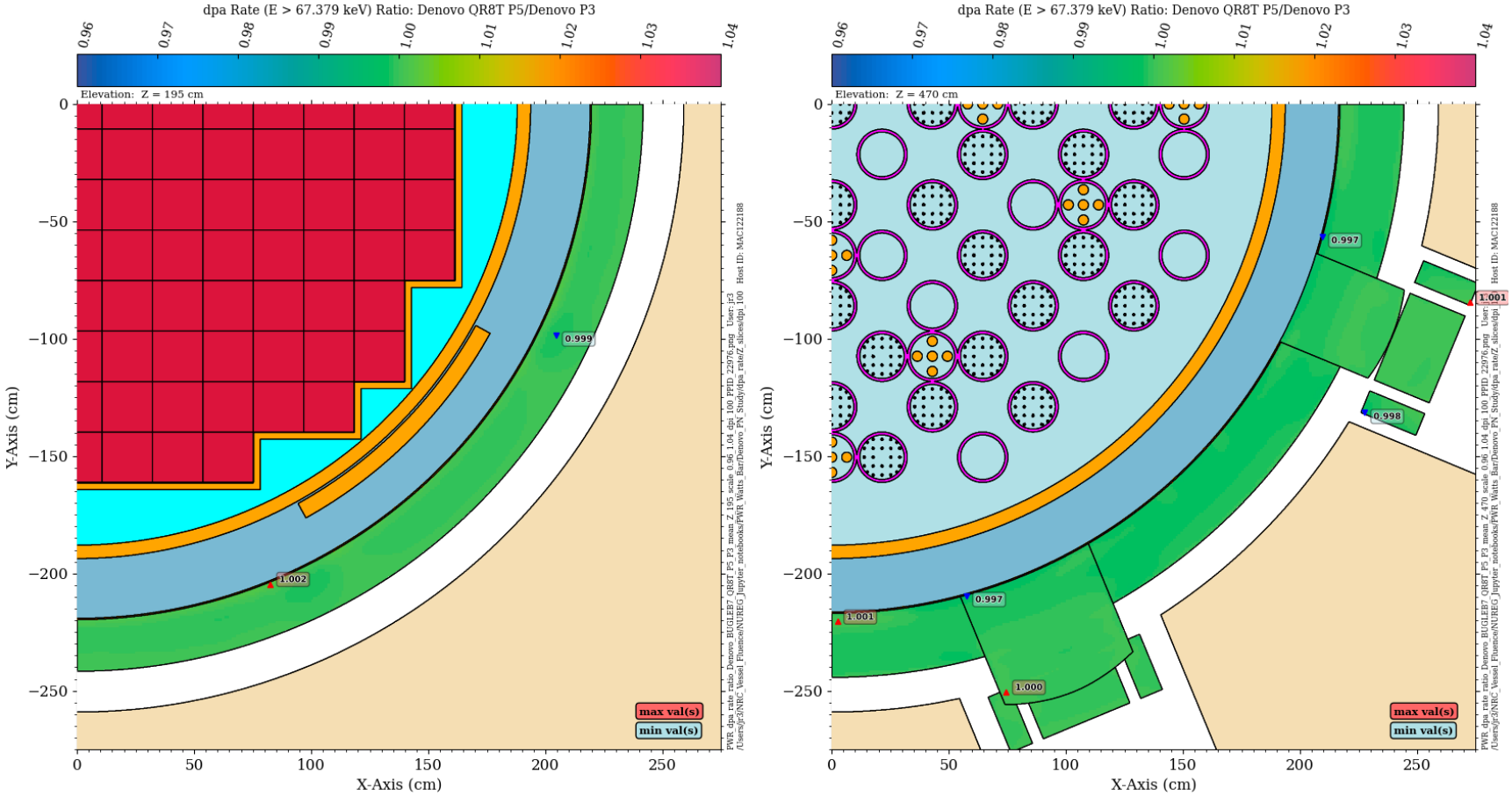

Figure 4-2 Ratio of the dpa rate for E > 67.379 keV from a P5 Denovo solution to a P3 Denovo solution at elevations of Z = 195 cm and Z = 470 cm

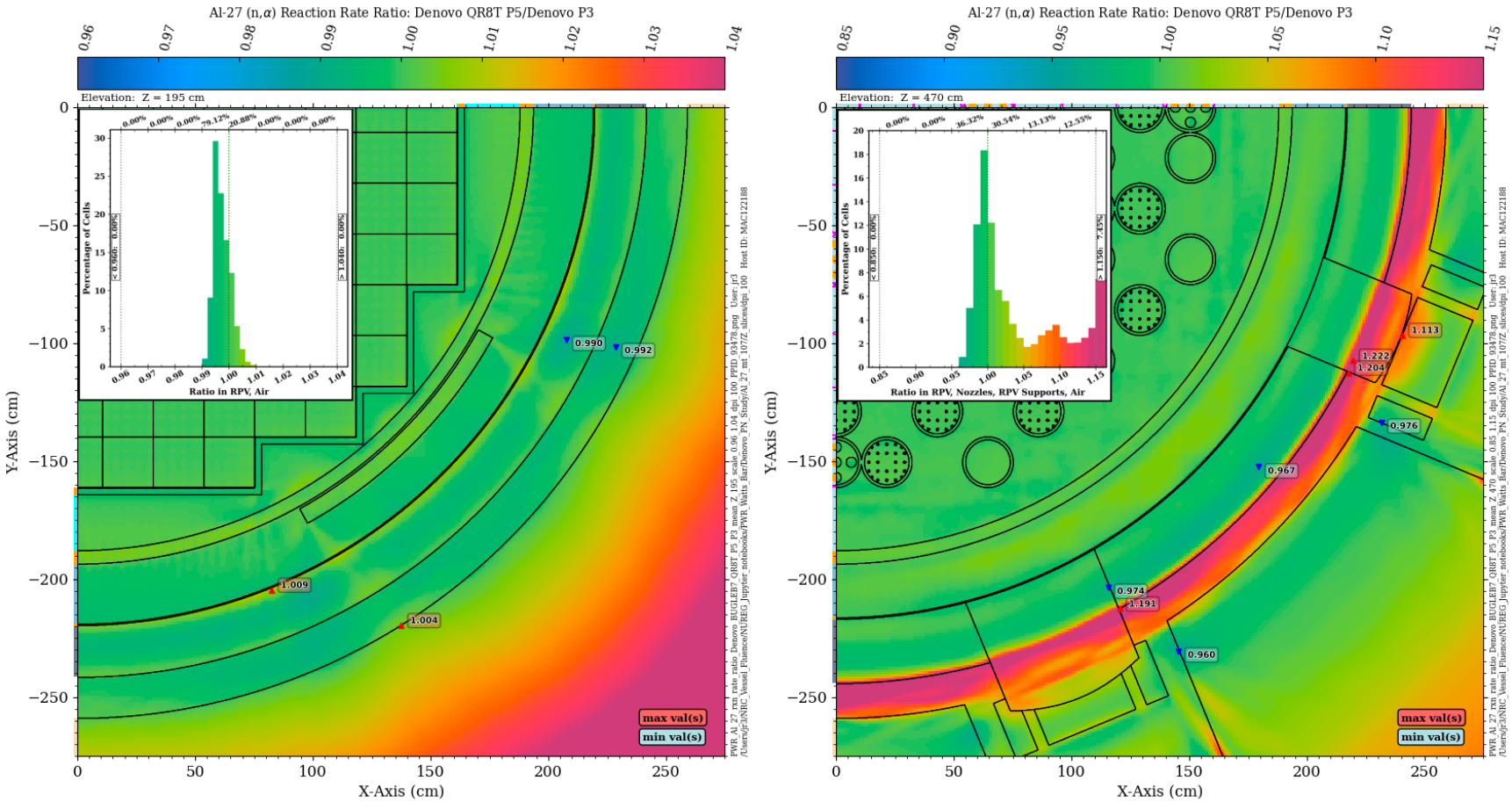

Figure 4-3 Ratio of the ^{27}Al (n,α) reaction rate from a P5 Denovo solution to a P3 Denovo solution at elevations of Z = 195 cm and Z = 470 cm. Note the change in the ratio scale between the two elevations

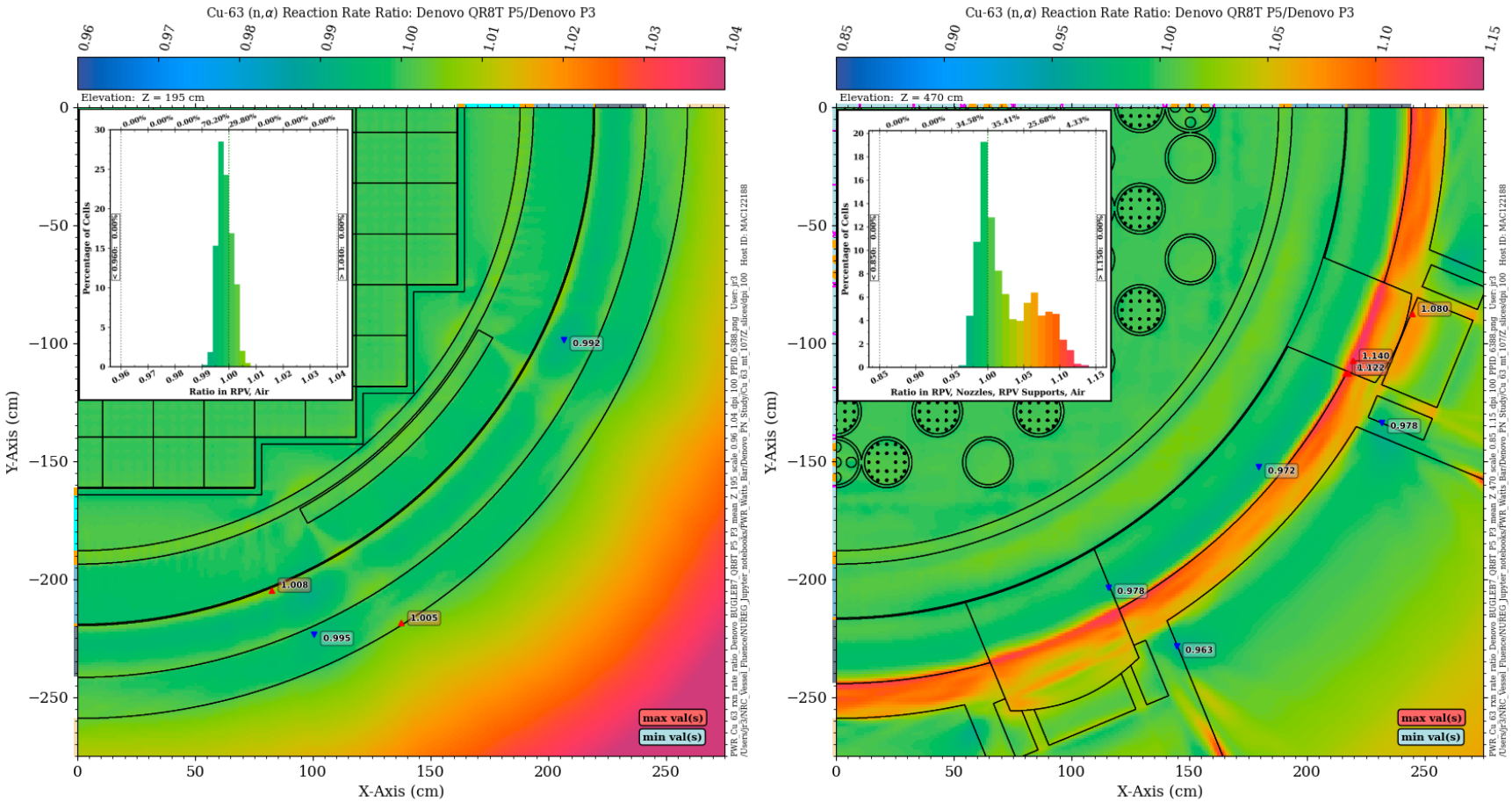

Figure 4-4 Ratio of the ^{63}Cu (n,α) reaction rate from a P5 Denovo solution to a P3 Denovo solution at elevations of Z = 195 cm and Z = 470 cm. Note the change in the ratio scale between the two elevations

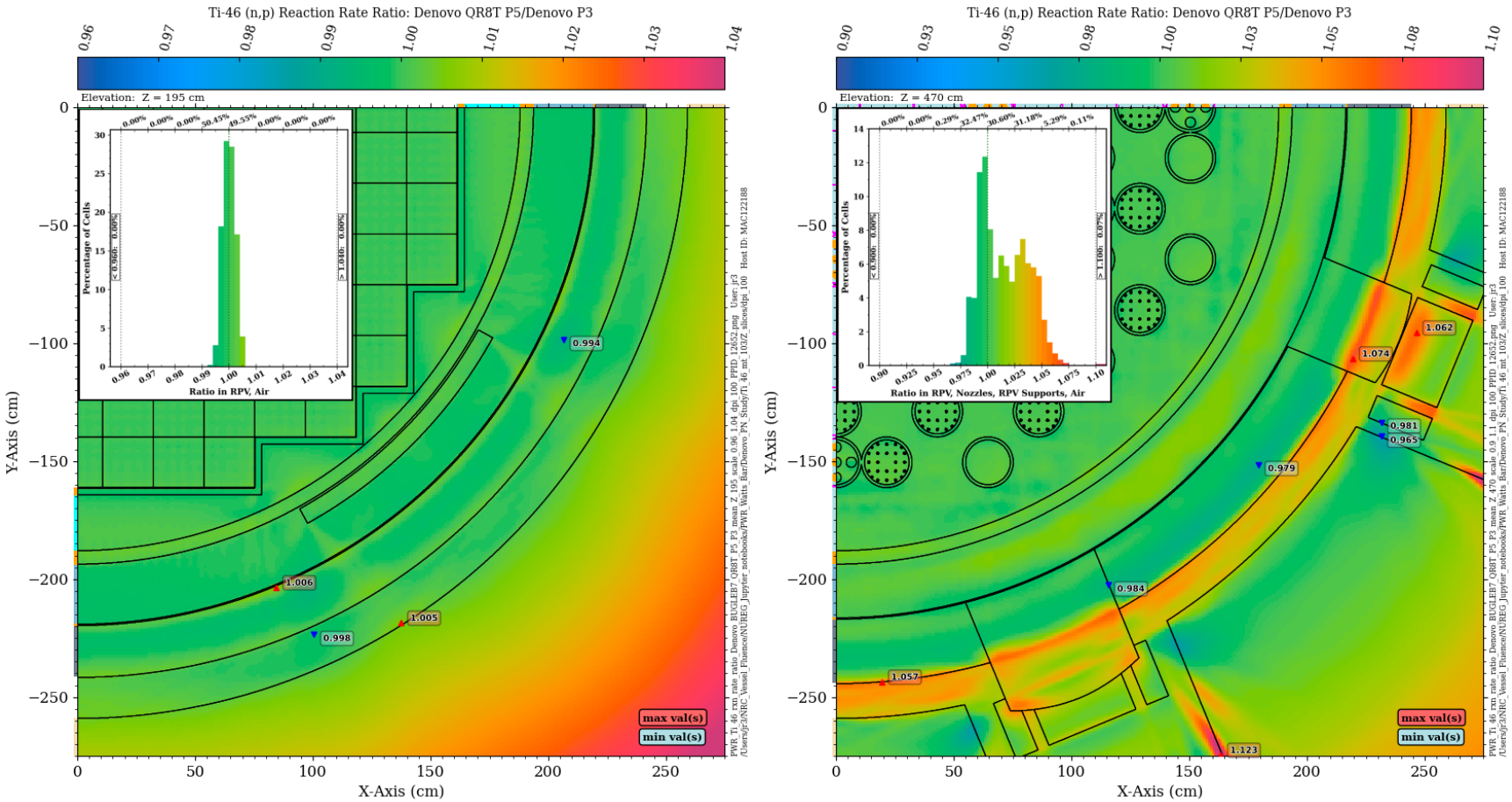

Figure 4-5 Ratio of the ^{46}Ti (n,p) reaction rate from a P5 Denovo solution to a P3 Denovo solution at elevations of Z = 195 cm and Z = 470 cm. Note the change in the ratio scale between the two elevations

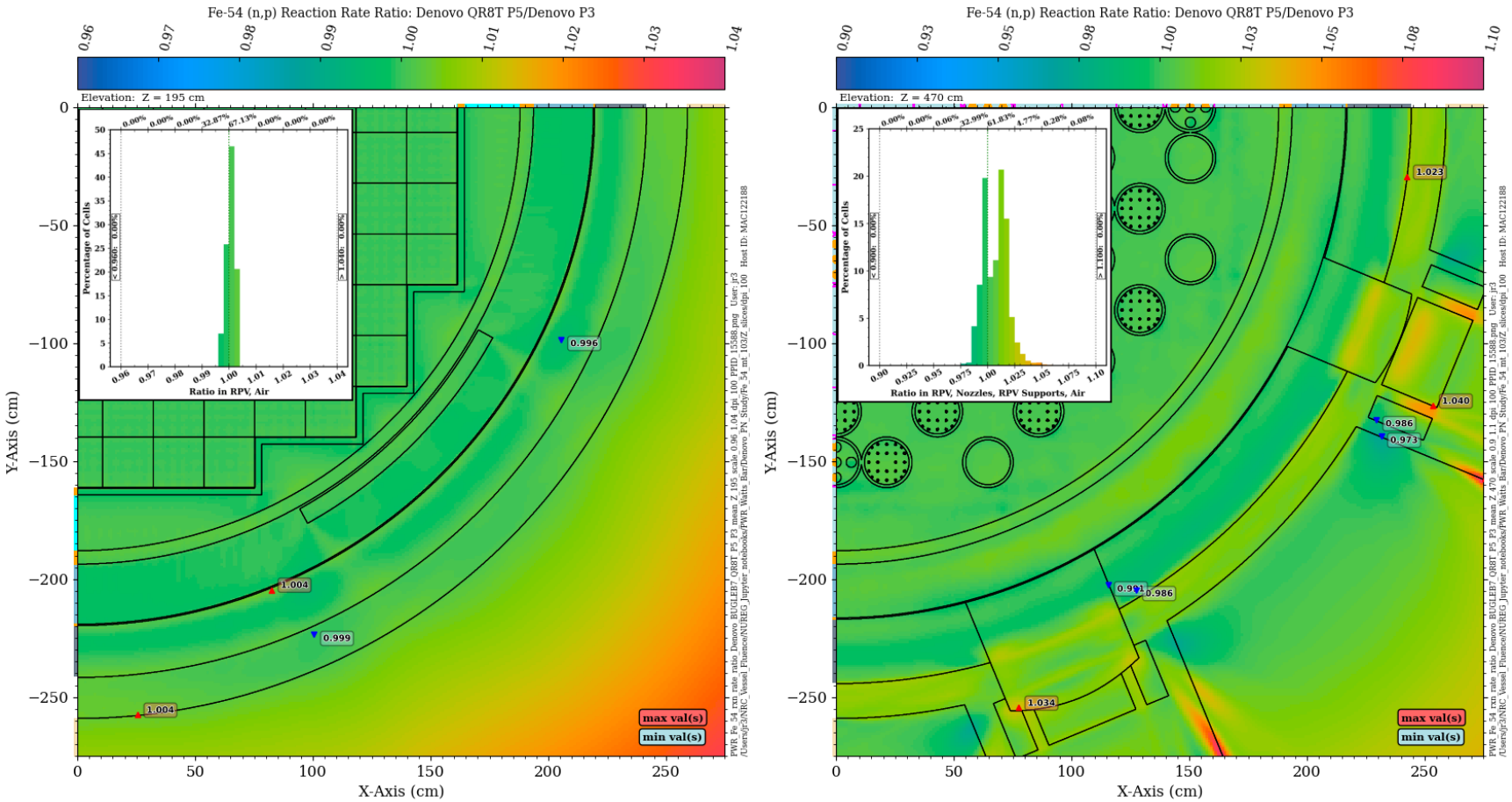

Figure 4-6 Ratio of the ^{54}Fe (n,p) reaction rate from a P5 Denovo solution to a P3 Denovo solution at elevations of Z = 195 cm and Z = 470 cm. Note the change in the ratio scale between the two elevations

4.3 Summary of scattering order studies

The results of the analyses presented in Sections 4.1 and 4.2 can be summarized by the following points:

1. The requirement of a minimum scattering order of P_3 from RG 1.190 is adequate for the extended beltline region when the BUGLE-B7 MG library is used. However, this does not provide validation that P_3 scattering would be adequate for finer MG energy structures such as those considered in Section 3. Because the angular scattering limits for MG elastic scattering become narrower with finer group structures, as shown in Eq. (D-1) and Eq. (D-2) of APPENDIX D, the scattering distributions become more anisotropic. Use of P_3 scattering expansions with a fine-group library would require validation on a case-by-case basis.
2. For the analysis of cavity dosimetry in the extended beltline region, the commonly used P_3 scatting expansion may not be adequate. In fact, the sensitivity to scattering order for dosimetry calculations involving high-energy reactions can easily exceed 10% and may even exceed 20%. As with the calculation of fast fluence and dpa, use of group structures finer than the BUGLE-B7 energy structure may be even more sensitive to higher-order scattering moments and would need to be assessed on a case-by-case basis.

5. NEUTRON FLUENCE UNCERTAINTY AND BIAS ESTIMATES

5.1 Neutron Fluence Uncertainty and Bias Estimates

The overall uncertainty and bias estimates for a neutron fluence calculational methodology are described in RG 1.190 and are determined using:

(1) analytic uncertainty and bias, and
(2) calculational uncertainty and bias.

The analytic uncertainty analysis is performed by determining input parameters that may not have been used precisely. Examples of such input parameters are the core neutron source, as well as the reactor's geometrical dimensions, coolant temperatures, and material compositions. Methodology-specific parameters should also be considered, such as angular quadrature, Legendre scattering order of cross sections, and MG cross-section libraries for deterministic radiation transport calculations. A range of variation in each selected input parameter is determined, and a sensitivity analysis is performed to estimate the analytical uncertainty. Individual analytic uncertainties are typically combined using root-sum-of-squares to obtain the total analytic uncertainty. Any identified analytic biases are combined algebraically with their associated signs (plus or minus) to obtain the total analytic bias.

The calculational uncertainty is determined by comparing calculational results with measurements from benchmarks. Benchmarks may involve the use of research reactors such as the Oak Ridge National Laboratory Pool Critical Assembly benchmark [22], [23], [24], [25], VENUS-1 and VENUS-3 benchmarks [26], [27], [28], [29], [30], [31]) or operating reactor benchmarks such as the H. B. Robinson Unit 2 Cycle 9 RPV benchmark [32], [33], [34]. A calculational bias may be determined from a measurement database that has been formed by combining measurements from benchmarks and measurements from operating reactors. The measurement database should have sufficient quality and quantity to allow for the estimate.

The overall uncertainty estimate may be calculated from the root-sum-of-squares of the analytical and calculational uncertainties and should be considered as the one-sigma uncertainty. The overall bias may be applied as a multiplicative factor to the calculated fluences to determine best-estimate values.

5.2 Need for Extended Beltline Benchmark Data

The uncertainty and bias estimate determination described in RG 1.190 was developed without considering the RPV extended beltline region. To determine the analytic uncertainty of the RPV extended beltline region when performing a sensitivity study, an expanded set of parameters will be required. This was not required when determining the uncertainty and bias estimate for the traditional beltline region.

The parameter studies presented by Risner et al. [8] and in this report may serve as an example of the scope of such studies that should be carried out. These parameter studies were based on an extensive set of parameter studies using the Denovo [9] discrete ordinates code and the hybrid transport methodology with the Shift Monte Carlo code. The studies noted that when using the widely used discrete ordinates method, there are intrinsic limitations resulting from the use of multigroup (MG) cross-section data, and to a lesser extent, from angular quadrature sets.

These limitations may make it very difficult to achieve a calculation uncertainty less than 20% in extended beltline locations.

The 47-neutron-group BUGLE-B7 MG library is often used for RPV fluence estimates. Use of the BUGLE-B7 library in a Shift calculation with a reference PWR model leads to differences of 15% or more compared to a more accurate continuous energy (CE) Shift calculation in portions of the vessel supports (Figure 3-6). Even the use of the 199-neutron-group VITAMIN-B7 library results in locations in the vessel supports where the MG solution underpredicts the more accurate CE solution by nearly 20% (Figure 3-8). In addition to the fast flux underprediction, dpa rates in portions of the PWR vessel supports are underpredicted by 30% or more with the BUGLE-B7 library (Figure 3-19) and by up to 20% with the VITAMIN-B7 library (Figure 3-21).

While these results provide some indication of an analytic uncertainty for discrete ordinates calculations in the extended beltline region, specific uncertainties must be developed for other discrete ordinates codes, as the numerical techniques they employ may differ.

Risner et al. [8] also address the lack of publicly available benchmark dosimetry measurement data in the RPV extended beltline region. Without such data, a calculational uncertainty cannot be determined. This lack of data prevents a quantitative assessment of an overall uncertainty and bias estimate for the hybrid transport method as applied to extended beltline locations. However, the analytic uncertainty with the hybrid transport method will be less than that of the discrete ordinates method, as the set of "methods parameters" (e.g., angular quadrature and MG library selection) is significantly reduced when CE Monte Carlo transport simulations are used.

Extended beltline benchmark dosimetry data should continue to be pursued, but acquisition of such benchmark data for a plant design—other than the Westinghouse 4-loop design used for the PWR reference model by Risner et al. [8]—would require development of a new model, which is outside the scope of this project.

Uncertainty Estimation Techniques for Combining Fluence Estimates

With regard to uncertainties in RPV fluence calculations, RG 1.190 is restricted to the use of a single transport methodology:

> *The NRC staff has not previously approved the combination of two methodologies for determining neutron fluence. Furthermore, the guidance provided in RG 1.190 is limited to the use of a single fluence method to determine RPV fluence for the entire irradiation period. The uncertainty analysis and methodology qualification regulatory positions do not provide any guidance for determining an accurate uncertainty estimate or qualifying the fluence estimate used from a combination of methods. As such, the staff concluded that combining fluence values from two separate methods does not adhere to the guidance contained in RG 1.190. Therefore, the staff considered this a deviation from NEDC-33178P-A, and the staff requested a supplement to the application.* [35]

The licensee subsequently recalculated the fluences using a single analysis methodology.

One approach for developing an uncertainty estimation for fluence estimates that combine two or more methodologies is to use time-weighting (in effective full power years) with the analytic and calculational uncertainties and combine those using a root-weighted-sum-of-squares. However, it may be more appropriate to address this on a case-specific basis. Furthermore, if an applicant adopts an improved methodology (such as the hybrid transport method), then it would be

reasonable for the applicant to apply that methodology to the entire analysis instead of combining it with fluence estimates from previous methods. This is particularly likely for fluence estimates in the extended beltline region, where previous analyses (i.e., those that cover plant lifetimes where the extended beltline region is not a concern) might require uncertainties that exceed 30%.
RG 1.190 states that if the overall fluence uncertainty exceeds 30%, then “the methodology of this regulatory guide is not applicable and the application will be reviewed on an individual basis.”

6. SUMMARY AND CONCLUSIONS

The primary objective of this report is to evaluate radiation transport methodologies that are best suited to the analysis for fast fluence and dpa in LWR RPVs. This work makes extensive use of large 3D transport calculations employing the Denovo discrete ordinates code and the Shift Monte Carlo code. The Shift calculations all employed the hybrid transport method, which utilizes both discrete ordinates and Monte Carlo calculations and is the current state of the art in radiation transport applications.

Both PWR and BWR models were utilized in these parametric studies. Particular emphasis was placed on identifying aspects of current methodologies that may be appropriate for traditional beltline fluence analyses, but not for extended beltline applications. Understanding those issues provides guidance on changes that might be appropriate for extended beltline analyses, either with regard to parameter guidance with discrete ordinates calculations, or with recommendations on the use of improved transport methods that have come into use since the issuance of many of the existing guidelines for RPV fluence analyses.

One of the most significant changes in radiation transport analysis methodology over the past 10 to 20 years has been the increasing use of hybrid methods These methods provide improved accuracy in modeling of the systems being analyzed and in the physics of particle transport compared with discrete ordinates methods. The hybrid methods are capable of producing well-converged, spatially detailed Monte Carlo solutions with reasonable run times (e.g., overnight solutions on computing clusters with on the order of a hundred CPUs).

The sensitivities of extended beltline fluence calculations to physical aspects of RPV models and the selection of appropriate quadrature sets for discrete ordinates were addressed in [8]. The sensitivity of transport calculations to MG libraries was addressed in this report. The MG library studies raise important questions about the level of accuracy that can be obtained for not only fast fluence evaluations, but also for calculations used to benchmark a transport methodology against measured dosimetry data.

6.1 Multigroup cross-section library considerations

One of the most significant areas of potential solution inaccuracy in discrete ordinates calculations is the use of MG cross-section libraries. With respect to RPV fluence calculations, this is particularly an area of concern for extended beltline regions, where the neutron flux spectra may be significantly different from those used to generate an MG library.

One way to examine the sensitivity of discrete ordinates calculations to the MG library selection would be to run those calculations with successively refined MG libraries. However, this approach has two limitations: (1) the vast amount of computer memory required to run a large 3D discrete ordinates calculation with an MG library that may contain hundreds of groups (compared to the 47 neutron groups in the BUGLE-B7 library), and (2) the fact that such comparisons necessarily involve substituting one approximation—a baseline MG library—with another—a refined MG library.

The method chosen to evaluate MG libraries in this study involved the use of Shift calculations. Because Shift can be run with either MG or CE cross-section data, these calculations provide a means of comparing various MG libraries with a more accurate CE solution.

In determining the impact of MG library selection for RPV fluence calculations, an extensive set of neutron response functions was considered. This set includes fast neutron flux (E > 1 MeV), neutron dpa rate, and nine dosimetry reactions based on commonly used dosimetry isotopes. This set of comparisons provides an indication of how well an MG library models neutron interactions over a wide range of energies rather than just the fast flux. The dosimetry comparisons are important because they form the basis for calculated-to-measured ratios for benchmark calculations.

A variety of MG libraries were evaluated, including VITAMIN-B7 (199 neutron energy groups) and BUGLE-B7 (47 neutron groups). These libraries were developed specifically for LWR shielding analyses. MG libraries from the SCALE code system containing from 200 to 1,597 neutron groups were evaluated. In addition, two libraries developed specifically to address neutron transport through energy ranges of particular importance for RPV flux and response calculations were also evaluated. All calculations were performed using the PWR model.

Details of the MG study are provided in Section 3. The results can be briefly summarized as follows.

6.1.1 Fast flux calculations

All of the MG libraries considered in this study are capable of providing accurate fast flux estimates (i.e., values which agree very well with CE calculations) in the inner portion of the RPV within the traditional beltline region. Of course, those locations are of primary concern with respect to the peak damage levels in the RPV. However, with the exception of the two fine-group libraries that were developed specifically for this application—one with 642 groups (X642N) and one with 956 groups (X956N)—all of the MG calculations underpredict the CE solution by more than 10% at the outer surface of the RPV. At the elevation of the vessel supports, all of the MG libraries except X642N and X956N underpredict the CE solution at all locations of interest, particularly in the vessel supports, where the solution differences can exceed 15%.

6.1.2 DPA rate calculations

For dpa rate calculations, the results are more complex. MG calculations using the BUGLE-B7 library underpredict the dpa rate at all locations in the RPV in both the traditional and extended beltline regions. At the core midplane, those differences range from ~5 to ~20%. At the elevation of the vessel supports, the BUGLE-B7 solution underpredicts the CE solution by more than 20% at nearly all locations of interest, with differences of up to 35% at some locations in the vessel supports. With the exception of the X956N library, all of the tested MG libraries underpredict the dpa rate at the elevation of the vessel supports, with differences of 15% and more occurring in the vessel supports.

6.1.3 Dosimetry reaction rate calculations

The accuracy of MG calculations used for dosimetry reaction rate calculations is strongly dependent on the reaction being considered. For reactions that have energy response ranges above the resolved resonances in the iron cross section (APPENDIX B and APPENDIX C), relatively broad group structures like BUGLE-B7 might be expected to provide accurate MG solutions. As the energy response range for a reaction rate extends over lower energies, where transport of neutrons through significant resonance regions occurs, MG transport calculations would be expected to exhibit more sensitivity to a library's group structure.

The energy response ranges for the nine reaction rates considered in this study are provided in Table C-1. The three dosimetry reactions with the highest energy response ranges were ^{27}Al (n,α), ^{63}Cu (n,α), and ^{46}Ti (n,p). For these reactions, the MG/CE agreement is reasonably good both at the core midplane and at the extended beltline vessel support elevation, except for the ^{46}Ti (n,p) reaction rate calculated with the VITAMIN-B7 or BUGLE-B7 libraries. The apparent reason for the poor VITAMIN-B7 and BUGLE-B7 results, which are discussed in Section 3.4.3, is not a function of the group structures of those libraries, but it probably is due to the differences in the ^{46}Ti (n,p) dosimetry cross-section data from these two libraries.

As noted above, for the remainder of the reactions, the MG/CE agreement became increasingly poor as the energy response ranges of the various reactions extended to lower neutron energies. For the ^{237}Np (n,f) reaction, which has the lowest 90% energy response range, the BUGLE-B7 solution underpredicted the CE reaction rate in the cavity gap at the core midplane elevation by ~10 to ~13%, and it underpredicted the CE solution by up to 20% and more in portions of the RPV, cavity gap, and vessel supports. Even the X956N solution underpredicted the ^{237}Np (n,f) rate from the CE solution by up to 15% at the vessel support elevation.

6.1.4 Multigroup library summary

The results of the MG/CE comparisons for these 11 neutron responses (fast flux, dpa rate, and nine dosimetry reaction rates) suggest that while the widely used BUGLE-B7 library is generally adequate for the calculation of these quantities at locations radially out through the inner portion of the RPV in the traditional beltline region, it is not well suited for calculation of most of the 11 responses at locations in the extended beltline region. In some cases, the differences between a BUGLE-B7 solution and a more accurate CE solution exceed 20%. This suggests that for a discrete ordinates calculation (which is also subject to the approximations made in space and angle) using the BUGLE-B7 library, it may not be possible to obtain calculational results within the 20% uncertainty value prescribed by RG 1.190.

While the accuracy of MG solutions can be improved by using a very-fine-group structure, libraries with the potential to contain several hundred energy groups could increase the amount of memory required for cross-section storage by more than two orders of magnitude and would also lead to much longer run times. As such, their use may not be practical for routine RPV analyses.

6.2 Cross-section scattering order

Regulatory Guide 1.190 requires a minimum P_3 expansion order for RPV fluence calculations with typical LWR configurations in the traditional beltline region. The sensitivity to scattering order for discrete ordinates calculations in the extended beltline region was evaluated for calculations of fast flux, dpa rate, and selected dosimetry reaction rates.

Denovo calculations using P_3, P_5, and P_7 scattering were considered. The use of P_3 scattering for fast flux and dpa rate calculations was shown to be adequate even in the extended beltline region. However, for calculation of neutron reaction rates for isotopes that have high energy thresholds [such as ^{27}Al (n,α)], P_3 calculations can easily underpredict P_5 calculations by 10% in the extended beltline region, with differences in some locations exceeding 20%. Increasing the scattering order from P_5 to P_7 in those cases was shown to result in insignificant differences, suggesting that P_5 scattering is adequate for those calculations when the BUGLE-B7 library is used.

It may be possible that for MG libraries with a finer group structure, higher scattering orders would be required. Use of P_3 (or possibly even P_5) scattering with a fine-group library would require validation on a case-by-case basis.

6.3 Recommendations on analysis methodology

The analyses performed in this study and in [8] suggest that the discretization of the angular and energy variables in MG discrete ordinates transport calculations poses significant challenges for RPV fluence evaluations in the extended beltline region. While it may be possible to adequately address quadrature effects without a significant cost increase in computing requirements, the use of MG cross-section libraries, even those with hundreds of energy groups, was shown to produce solutions that often underpredict more accurate CE calculations in extended beltline locations, including the vessel supports in the PWR model. This underprediction is particularly noteworthy for calculation of dpa rates and of some dosimetry reaction rates.

The use of hybrid radiation transport methods provides a significant advantage in these analyses, as the Monte Carlo calculations that are the final stage of the hybrid calculational sequence are not subject to angular discretization or to the approximations made in MG cross-section libraries.

7. REFERENCES

[1] Gary L. Stevens, “Evaluation of the Beltline Region for Nuclear Reactor Pressure Vessels,” U.S. Nuclear Regulatory Commission Technical Letter Report TLR-RES/DE/CIB-2013-01, November 14, 2014.

[2] U.S. Nuclear Regulatory Commission, “Calculational and Dosimetry Methods for Determining Pressure Vessel Neutron Fluence,” Regulatory Guide 1.190, 2001. ADAMS Accession No. ML010890301.

[3] U.S. Nuclear Regulatory Commission, “Domestic Licensing of Production and Utilization Facilities,” Title 10, Code of Federal Regulations, Part 50.

[4] ASTM E185-82, “Standard Practice for Design of Surveillance Programs for Light-Water Moderated Nuclear Power Reactor Vessels,” ASTM International, 1982.

[5] U.S Nuclear Regulatory Commission, “Reactor Pressure Vessel Status Report,” NUREG/CR-1511, December 1994. ADAMS Accession No. ML082030506.

[6] IAEA Nuclear Energy Series, “Integrity of Reactor Pressure Vessels in Nuclear Power Plants: Assessment of Irradiation Embrittlement Effects in Reactor Pressure Vessel Steels,” International Atomic Energy Agency, 2009.

[7] Pavel V. Tsvetkov, Editor, *Nuclear Power – Control, Reliability, and Human Factors*,” Intech, 2011.

[8] J. Risner, A. Alpan, and J. Yang, “Calculational Methods for Reactor Pressure Vessel Fluence in Extended Beltline Locations,” ORNL SPR-2020-1882, April 2021.

[9] T. M. Evans et al., “Denovo: A New Three-Dimensional Parallel Discrete Ordinates Code in SCALE,” *Nucl. Technol*., 171(2):171-200, 2010.

[10] ASTM E693-17, “Standard Practice for Characterizing Neutron Exposures in Iron and Low Alloy Steels in Terms of Displacements Per Atom (dpa),” ASTM International, August 2017.

[11] ASTM E1035-18, “Determining Neutron Exposures for Nuclear Reactor Vessel Support Structures,” ASTM International, June 2018.

[12] T. M. Pandya et al., “Implementation, Capabilities, and Benchmarking of Shift, a Massively Parallel Monte Carlo Radiation Transport Code,” *J. Comput. Physics*, 308:239-272, 2016.

[13] I. Remec, “Study of the Neutron Flux and Dpa Attenuation in the Reactor Pressure-Vessel Wall,” ORNL/NRC/LTR-99/5, Oak Ridge National Laboratory, June 1999.

[14] Eric N. Jones, “Comparison of Regulatory Guide 1.99 Fluence Attenuation Methods,’ *J. ASTM Intl.*, **9**(4):390–398, 2012. doi:10.1520/JAI104028.

[15] U.S. Nuclear Regulatory Commission, “Radiation Embrittlement of Reactor Vessel Materials,” Regulatory Guide 1.99, Revision 2, 1988.

[16] N. P. Baumann, “Gamma-ray Induced Displacements in D2O Reactors,” *Proceedings of the Seventh ASTM-EURATOM Symposium on Reactor Dosimetry*, Strasbourg, France, August 27-31, 1990.

[17] U.S. Nuclear Regulatory Commission, “Production and Testing of the VITAMIN-B7 Fine-Group and BUGLE-B7 Broad-Group Coupled Neutron/Gamma Cross-Section

Libraries Derived from ENDF/B-VII.0 Nuclear Data," NUREG/CR-7045, September 2011.

[18] B. T. Rearden and M. A. Jessee, Eds., "*SCALE 6.2: A Comprehensive Modeling and Simulation Suite for Nuclear Safety Analysis and Design; Includes ORIGEN and AMPX*," ORNL/TM-2005/39 Version 6.2, Oak Ridge National Laboratory, April 2016.

[19] Materials Reliability Program (MRP): Attenuation in U.S. RPV Steels (MRP-56), Electric Power Research Institute, Palo Alto, CA, 2002.

[20] U.S. Nuclear Regulatory Commission, "Expanded Materials Degradation Assessment (EMDA)," NUREG/CR-7153, Vol. 3, October 2014.

[21] International Rector Dosimetry File 2000 (IRDF-2002). Technical report, International Atomic Energy Agency, 2006.

[22] W. N. McElroy, "LWR Pressure Vessel Surveillance Dosimetry Improvement Program: PCA Experiments and Blind Test," NUREG/CR-1861 (HEDL-TME 80-87), July 1981.

[23] I. Remec and F. B. K. Kam, "Pool Critical Assembly Pressure Vessel Facility Benchmark," NUREG/CR-6454 (ORNL/TM-13205), July 1997.

[24] F. W. Stallmann et al., "Reactor Calculation 'Benchmark' PCA Blind Test Results," NUREG/CR-1872 (ORNL/NUREG/TM428), January 1981.

[25] D. K. Min, A. L. Aronson, and J. F. Carew, "Analysis of the ORNL Pool Critical Assembly Pressure Vessel Dosimetry Benchmark Experiment," BNL-NUREG-29047, Brookhaven National Laboratory, February 1981.

[26] R. E. Maerker, "Analysis of the VENUS-3 Experiments," Proceedings of the Seventh ASTM-Euratom Symposium on Reactor Dosimetry, Strasbourg, France, 27-31 August 1990, ASTM, Kluwer Academic Publishers, 1992.

[27] G. Hehn and B.C. Na, "New NEA Benchmarks Reveal Decisive Improvements in Calculating Fast Neutron Fluence for Predictions of Embrittlement in Reactor Pressure Vessels," Reactor Dosimetry, ASTM STP 1398 (J.G. Williams et al., Eds.), ASTM, West Conshohoken, PA, 2000.

[28] A. Haghighat, H. Ait Abderrahim, and G.E. Sjoden, "Accuracy and Performance of PENTRAN^{TM} Using the VENUS-3 Benchmark Experiment," Reactor Dosimetry, ASTM STP 1398 (J.G. Williams et al., Eds.). ASTM, West Conshohoken, PA, 2002.

[29] P. D'hondt et al, "Contribution of the VENUS-Engineering Mock-up Experiment to the LWR-PV Surveillance," Proceedings of the Seventh ASTM-Euratom Symposium on Reactor Dosimetry, Strasbourg, France, 27-31 August 1990, ASTM, Kluwer Academic Publishers, 1992.

[30] "Prediction of Neutron Embrittlement in the Reactor Pressure Vessel: VENUS-1 and VENUS-3 Benchmarks," Nuclear Energy Agency, 2000.

[31] A. H. Fero and E. T. Hayes, "Analysis of the VENUS-1 Benchmark Using TORT and BUGLE-96," Proceedings of the 11th International Symposium on Reactor Dosimetry. Reactor Dosimetry in the 21st Century. World Scientific Publishing Co. Pte. Ltd., 2003.

[32] I. Remec and F. B. K. Kam, "H. B. Robinson-2 Pressure Vessel Benchmark," NUREG/CR-6453 (ORNL/TM-13204, February 1998.

[33] M. L. Williams and M. Asgari, “Impact of ENDF/B-VI Cross-Section Data on H.B. Robinson Cycle 9 Dosimetry Calculations,” NUREG/CR-6071 (ORNL/TM-13204), October 1993.

[34] E. P. Lippincott et al., “Evaluation of Surveillance Capsule and Reactor Cavity Dosimetry from H.B. Robinson Unit-2, Cycle 9,” NUREG/CR-4576 (WCAP-11104), U. S. Nuclear Regulatory Commission, February 1987.

[35] U.S. Nuclear Regulatory Commission, “LaSalle County Station, Unit 1, Issuance of Amendment Revising Pressure and Temperature Limits (TAC No. MF3270)”, November 25, 2014. ADAMS Accession No. ML14220A517.

[36] I. I. Bondarenko, *Group Constants for Nuclear Reactor Calculations*, Consultants Bureau, New York, 1964.

[37] ANSI/ANS-6.1.2-2013, “Group-Averaged Neutron and Gamma-Ray Cross Sections for Radiation Protection and Shielding Calculations for Nuclear Power Plants,” American Nuclear Society, August 2013.

[38] J. Kenneth Shultis and Richard E. Faw, *Radiation Shielding*, American Nuclear Society, 2000.

[39] James J. Duderstadt and Louis J. Hamilton, *Nuclear Reactor Analy*sis, John Wiley and Sons, 1976.

[40] John R. Lamarsh, *Introduction to Nuclear Reactor Theory*, Addison-Wesley, 1972.

[41] H. Brockmann, “Treatment of Anisotropic Scattering in Numerical Neutron Transport Theory,” *Nucl. Sci. Eng.*, **77**(4):377–414, 1981.

[42] E. A. Attia and A. A. Harms, “A New Expansion for Highly Anisotropic Neutron-Nuclear Scattering,” *Nucl. Sci. Eng.*, **59**(4):319–325, 1975.

[43] ASTM E844-18, “Standard Guide for Sensor Set Design and Irradiation for Reactor Surveillance,” ASTM International, July 2018.

8. GLOSSARY

adjoint flux	The flux (see below) calculated using the adjoint form of the transport equation. The adjoint flux has the physical interpretation of representing the importance of particles to a specified response (e.g., flux or dpa rate).
discrete ordinates	A widely used method for solving the transport equation by discretizing the spatial, energy, and angular variables and solving the resulting set of algebraic equations using numerical methods. Discrete ordinates calculations are also referred to as deterministic calculations.
displacements per atom (dpa)	The mean number of times each atom in a crystal lattice structure is displaced from its lattice site as a result of radiation interactions.
fast fluence, fast flux	The fluence or flux of particles (e.g., neutrons) with energy above a specified threshold. While there is no standard definition of *fast neutron flux*, a commonly used energy cutoff for fast neutrons is 1 MeV. Within this report, the cutoff energy is either 1 MeV or 1.0026 MeV. The latter is used with MG cross-section libraries and with CE solutions that are compared directly with MG solutions.
fluence	The number of particles (e.g., neutrons) (dN) incident on a hypothetical sphere of cross-sectional area dA. *Fluence* can also be defined as the sum of the particle track lengths within the sphere. Fluence has units of inverse area (cm^{-2} or m^{-2}).
fluence rate	The number of particles entering a sphere, or the sum of the particle track lengths within a sphere per unit time.
flux	A more commonly used term for *fluence rate*.
hybrid	A class of techniques used to obtain a solution to the transport equation using a combination of determination and stochastic calculations.
lethargy	A measure of the amount of energy a neutron has lost as a result of scattering collisions. Lethargy is defined as $u = ln\left(\frac{E_0}{E}\right)$ where E is the neutron energy and E_0 is the maximum neutron energy (typically 20 MeV for neutron shielding calculations)

Monte Carlo	A stochastic method of obtaining a solution to the transport equation by simulating the behavior of a large number of particle histories.

APPENDIX A AN OVERVIEW OF THE MESH TALLIES AND PLOTTING METHODS USED IN THIS REPORT

Much of the data analysis in this report consists of plots of fast (E > 1 MeV) neutron flux distributions, dpa rates, and ratios of solutions from parametric studies. The majority of the solutions are from Shift Monte Carlo calculations with cylindrical mesh tallies. The scattering order sensitivity studies in Section 4 utilized Denovo discrete ordinates calculations.

This appendix briefly describes the level of detail in the Shift mesh tallies and provides examples of the types of plots that are used to present the analysis results. Examples of typical relative errors in the Shift calculations are also presented.

A.1 Cylindrical mesh tallies in the PWR and BWR models

The majority of the results presented in this report are based on cylindrical mesh tallies from continuous energy (CE) Shift calculations. The mesh tally intervals were selected to provide a high degree of spatial resolution while also providing solutions with mesh tally relative errors that are typically less than 1% in all locations of interest.

In the PWR model, the cylindrical mesh tally radial intervals are ~1 cm from the outer radius of the neutron pad to the outer radius of the RPV. In the cavity gap and the concrete bioshield the radial intervals are ~2 cm. The axial mesh intervals are ~2.5 cm over the height of the model. The azimuthal mesh intervals are uniform at 1°. Plots showing the radial, azimuthal, and axial mesh tally voxel boundaries for the PWR model are shown in Figure A-1 and Figure A-2. The Cartesian mesh in the Denovo calculations of Section 4 was uniform at 1 cm in X, Y, and Z. Comparison of Denovo solutions for the PWR model with Shift solutions using the identical MG cross-section library as Denovo demonstrated that this spatial mesh grid structure provides convergence with respect to mesh in the Denovo calculations.

In the BWR model, the cylindrical mesh tally radial intervals are ~2 cm over the radial extent from ~10 cm inboard of the core barrel to the inner radius of the RPV, ~1 cm through the RPV, ~3 cm in the cavity gap, and ~2 cm in the concrete bioshield. The axial mesh intervals are ~2.5 cm over the height of the model. The azimuthal mesh intervals are uniform at 1°. Plots showing the radial, azimuthal, and axial mesh tally voxel boundaries for the BWR model are shown in and Figure A-3 and Figure A-4.

A.2 Fast neutron flux plots

Fast neutron flux solutions are plotted using a combination of material color assignments, contour lines, and flooded contours. Contour lines are typically shown over an extent of the cylindrical mesh tallies ranging from the water region inboard of the RPV radially out into the concrete bioshield. Within the RPV and other carbon steel regions (nozzles and nozzle supports), flooded contours are used to emphasize the fast flux behavior in these key components. Maximum and minimum values of the fast flux within each distinct carbon steel component (RPV, nozzles, nozzle supports) are indicated. In some plots the mesh tally voxel boundaries are shown. For elevation plots, the top of the active fuel (TAF) and bottom of the active fuel (BAF) elevations are indicated. Example fast neutron flux plots from the PWR model are shown in Figure A-5 and Figure A-6.

A.3 DPA rate plots

DPA rate plots are presented in nearly the same way as fast flux plots. The sole difference is that the dpa rate contour lines and flooded contours are shown only in the carbon steel components, as the dpa cross sections from [10] apply only to iron and low-alloy steels. Example dpa rate plots from the PWR model are shown in Figure A-7 and Figure A-8.

A.4 Ratio plots

Ratio plots are used in parametric studies to show the effect of changes in solution or model parameters. Many of the ratio plots in this report use contour lines and flooded contours only in the RPV, nozzles, and nozzle supports. Ratio plots also typically include an inset plot with a histogram of the ratio values in specified regions, which may include the RPV, nozzles, nozzle supports, and cavity gap. The abscissa labels on the histogram plots indicates which regions are included in the distribution. Numeric values on the upper edge of the ratio plot show the percentage of values that fall within each major interval of the abscissa.

An example ratio plot from a Shift parametric study is shown in Figure A-9.

Ratio plots for the Denovo parameter study in Section 4 are somewhat different from the ratio plots for the Shift parameter studies in Section 3. In Section 4 the ratio of two solutions is shown over the entire plot extent. An example Denovo parameter study ratio plot is shown in Figure A-10.

A.5 Mesh tally relative errors

As noted in Section A.1 relative errors for the Shift solutions in this report are typically less than 1% in all locations of interest. Example plots showing relative errors in the fast neutron flux for the PWR model are shown in Figure A-11 and Figure A-12. These correspond to the fast flux plots in Figure A-5 and Figure A-6.

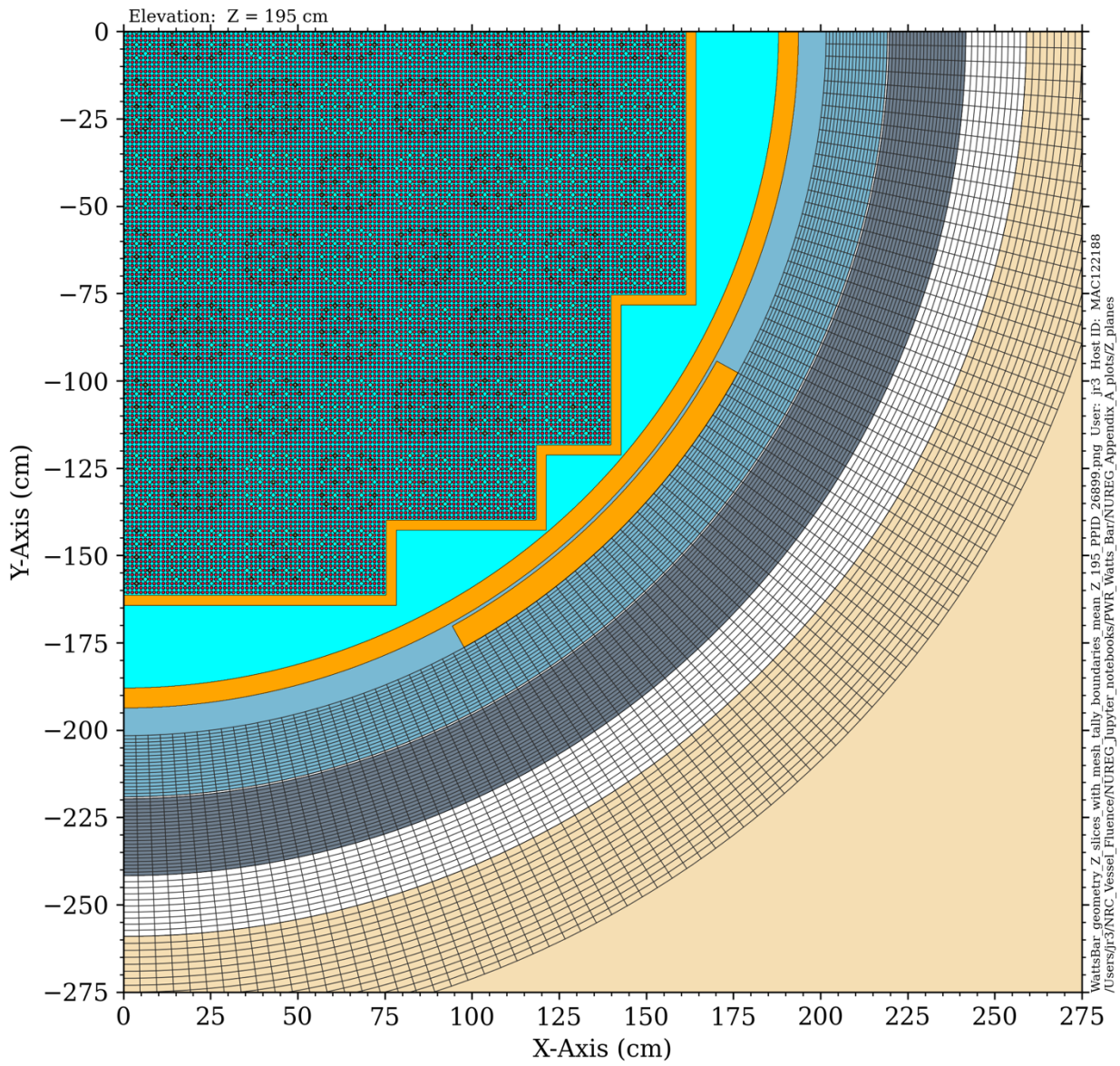

Figure A-1 Radial and azimuthal cylindrical mesh tally intervals in the PWR model. Plan view at the core midplane

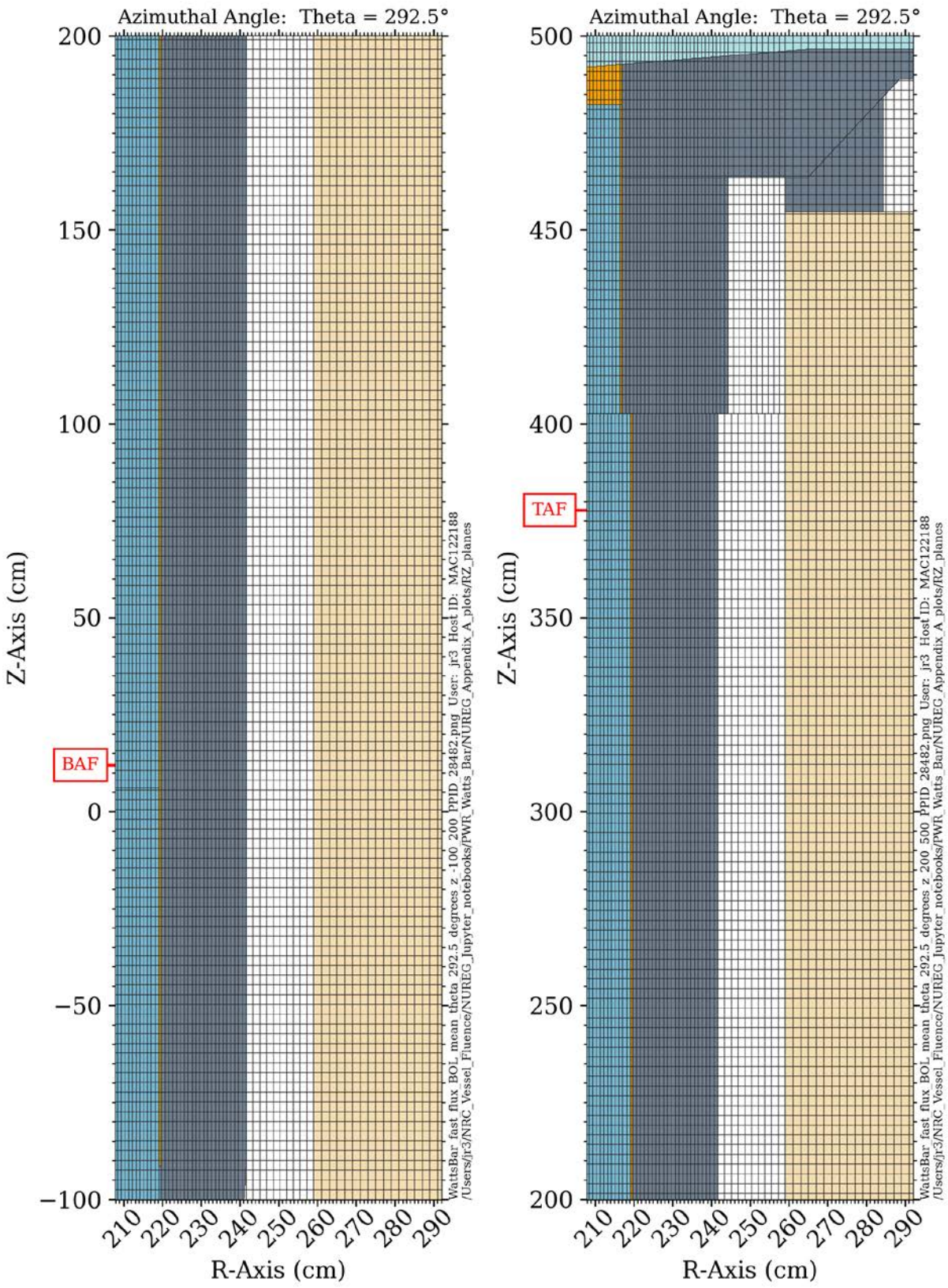

Figure A-2 Axial cylindrical mesh tally intervals in the PWR model. Elevation view at an azimuthal angle of 292.5°

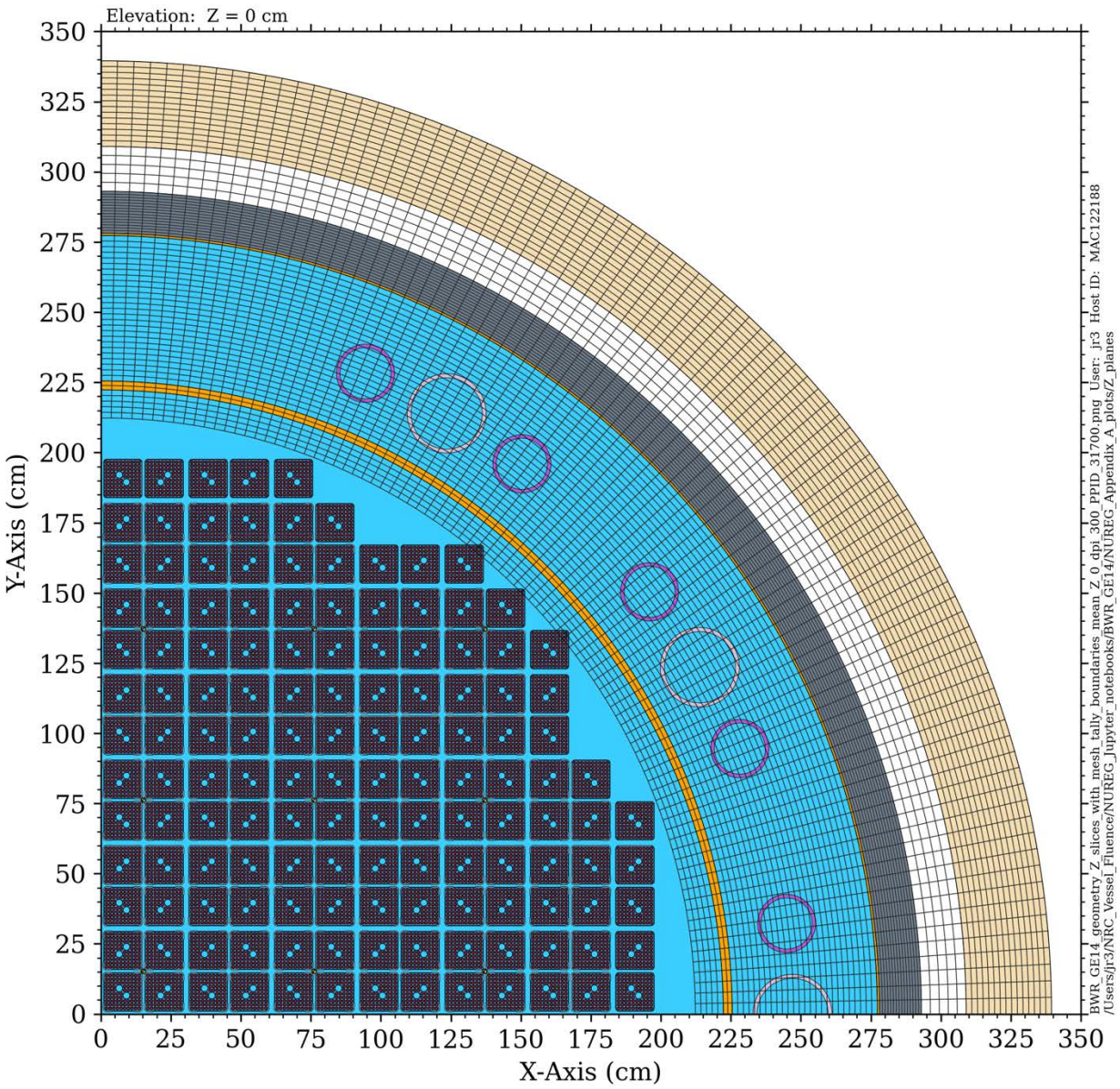

Figure A-3 Radial and azimuthal cylindrical mesh tally intervals in the BWR model. Plan view at the core midplane

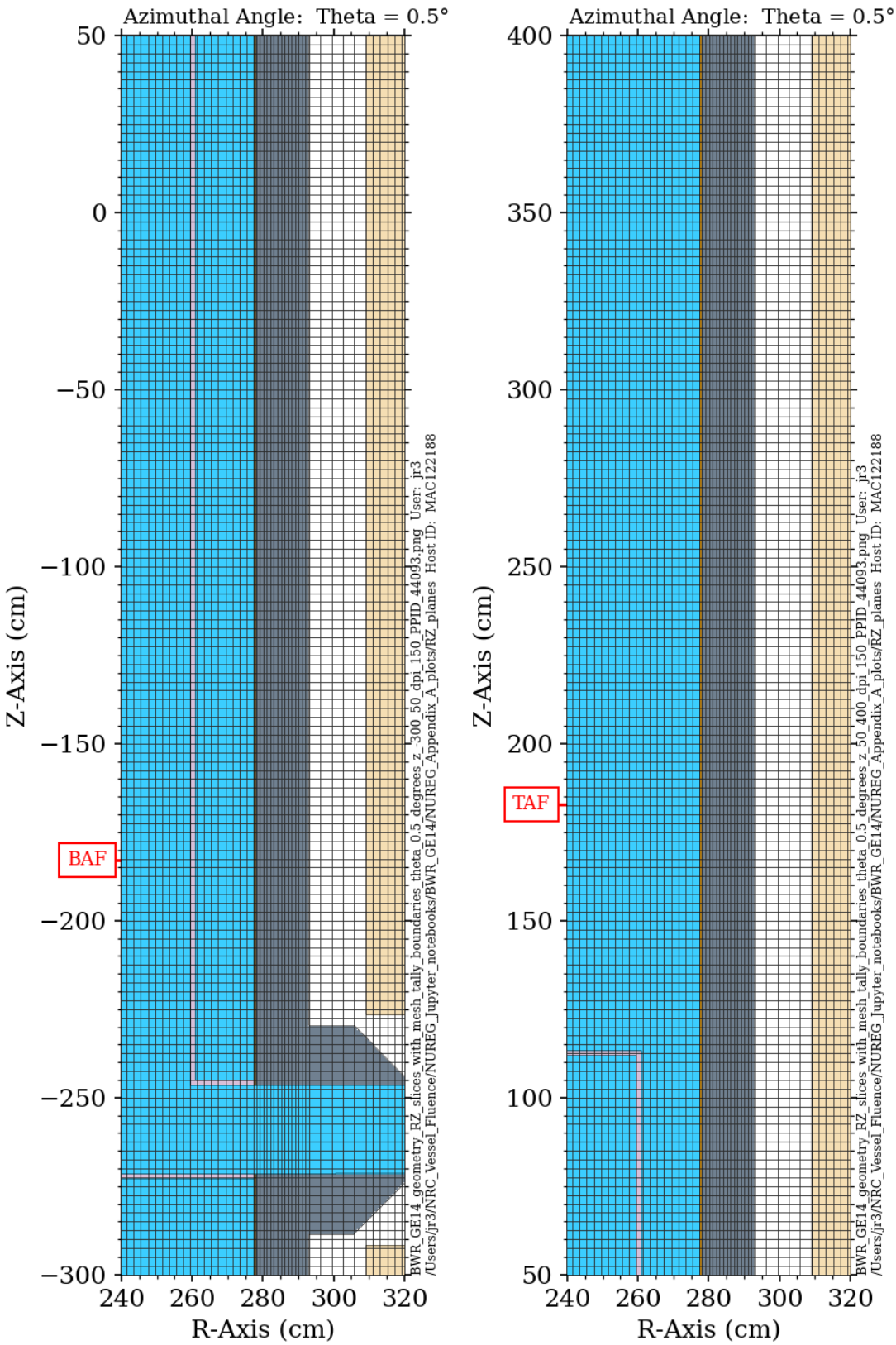

Figure A-4 Axial cylindrical mesh tally intervals in the BWR model. Elevation view at an azimuthal angle of 0.5°

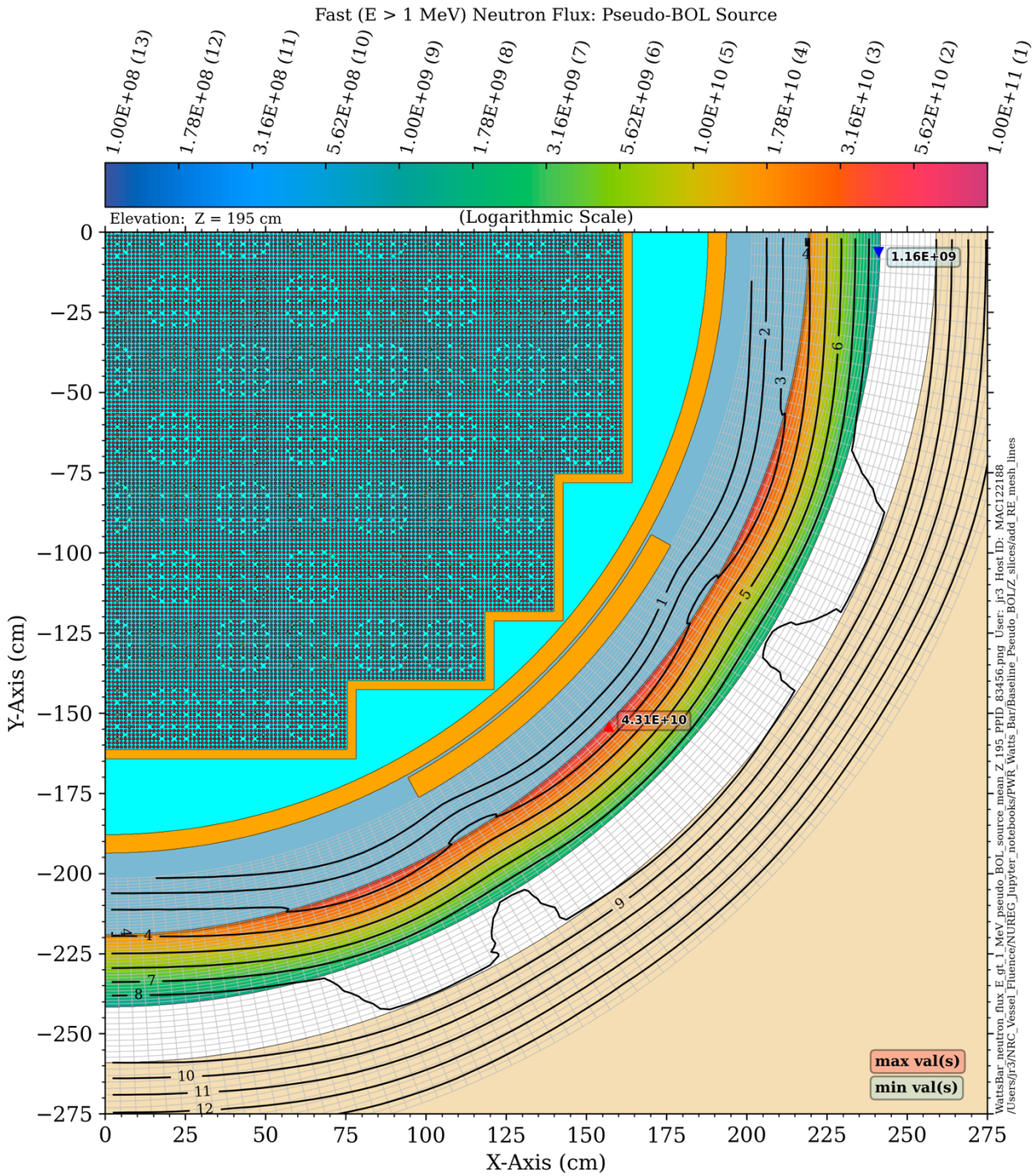

Figure A-5 **Fast neutron flux at the core midplane in the PWR model. Regions other than the RPV are colored by material assignment. Contour lines show the fast neutron flux over the full extent of the cylindrical mesh tally. Flooded contours are used to highlight the fast flux in the RPV, which is the primary region of interest. Maximum and minimum fast flux values in the RPV are indicated. The cylindrical mesh tally boundaries are shown on this plot but are not present on all plots of this type**

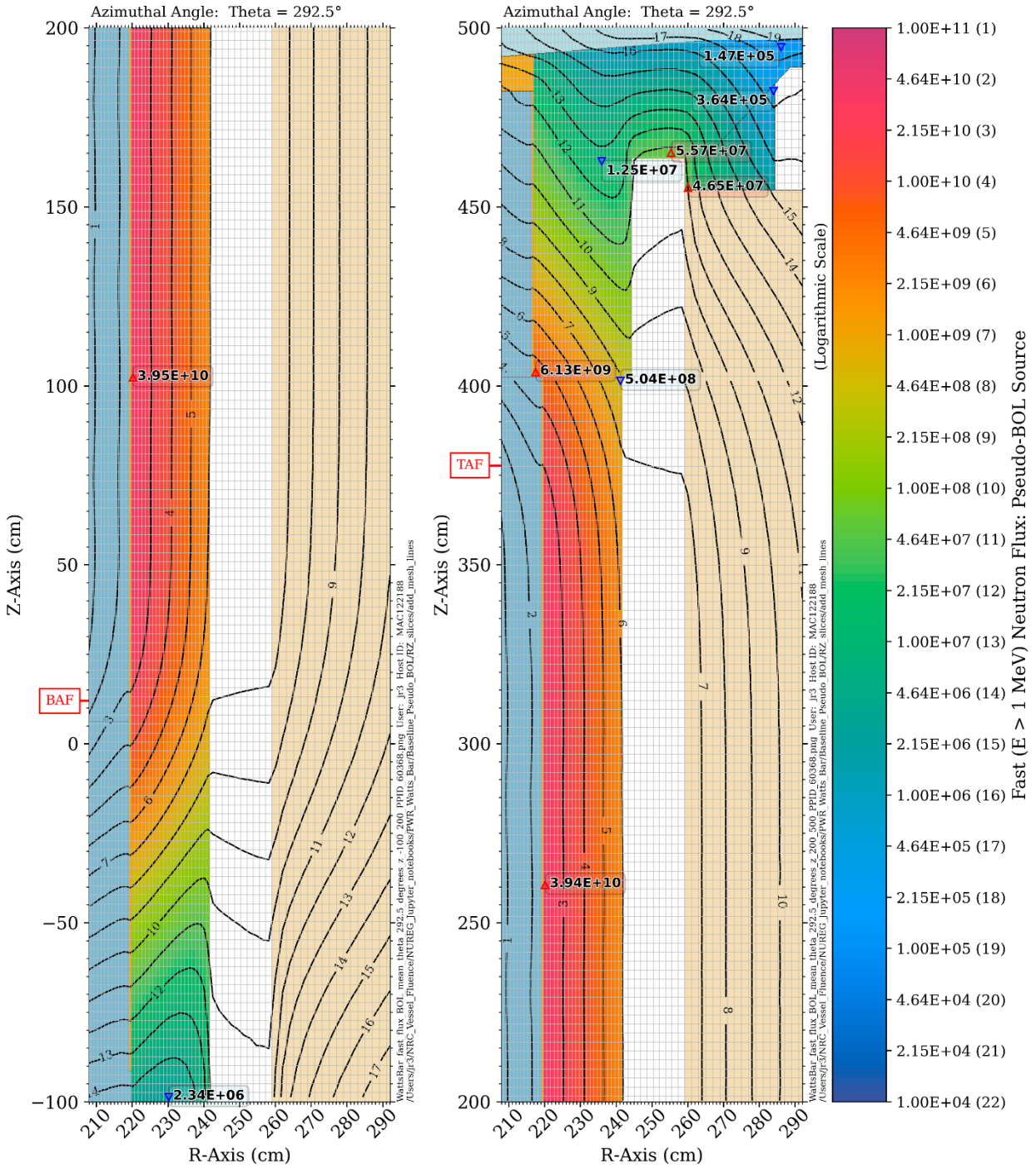

Figure A-6 **Fast neutron flux in the PWR model at an azimuthal angle of 292.5°. Regions other than the RPV are colored by material assignment. Contour lines show the fast neutron flux in all regions. Flooded contours are used to highlight the fast flux in the RPV, which is the primary region of interest. Maximum and minimum fast flux values in the RPV, RPV nozzle, and nozzle support are indicated. Maximum and minimum values in the RPV in the right-hand-side view are indicated above and below Z = 402.59 cm, where the thickness of the RPV changes. BAF and TAF are the bottom and top elevations of the active fuel**

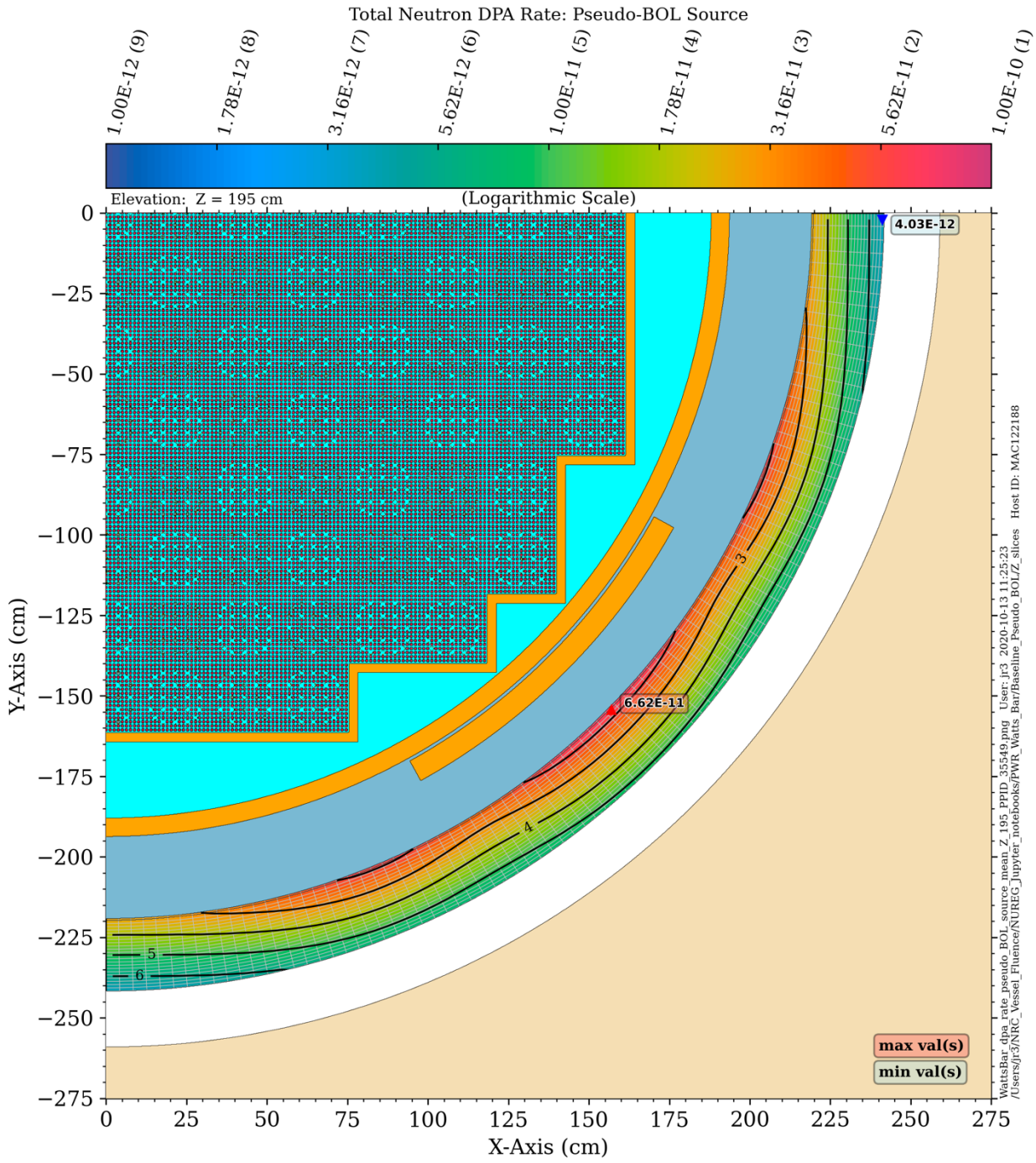

Figure A-7 DPA rate at the core midplane in the PWR model. Regions other than the RPV are colored by material assignment. Flooded contours show the dpa rate in the RPV. Maximum and minimum dpa rate values are indicated. The cylindrical mesh tally boundaries are shown only in the RPV, which is the only region where the dpa rate is meaningful at this elevation

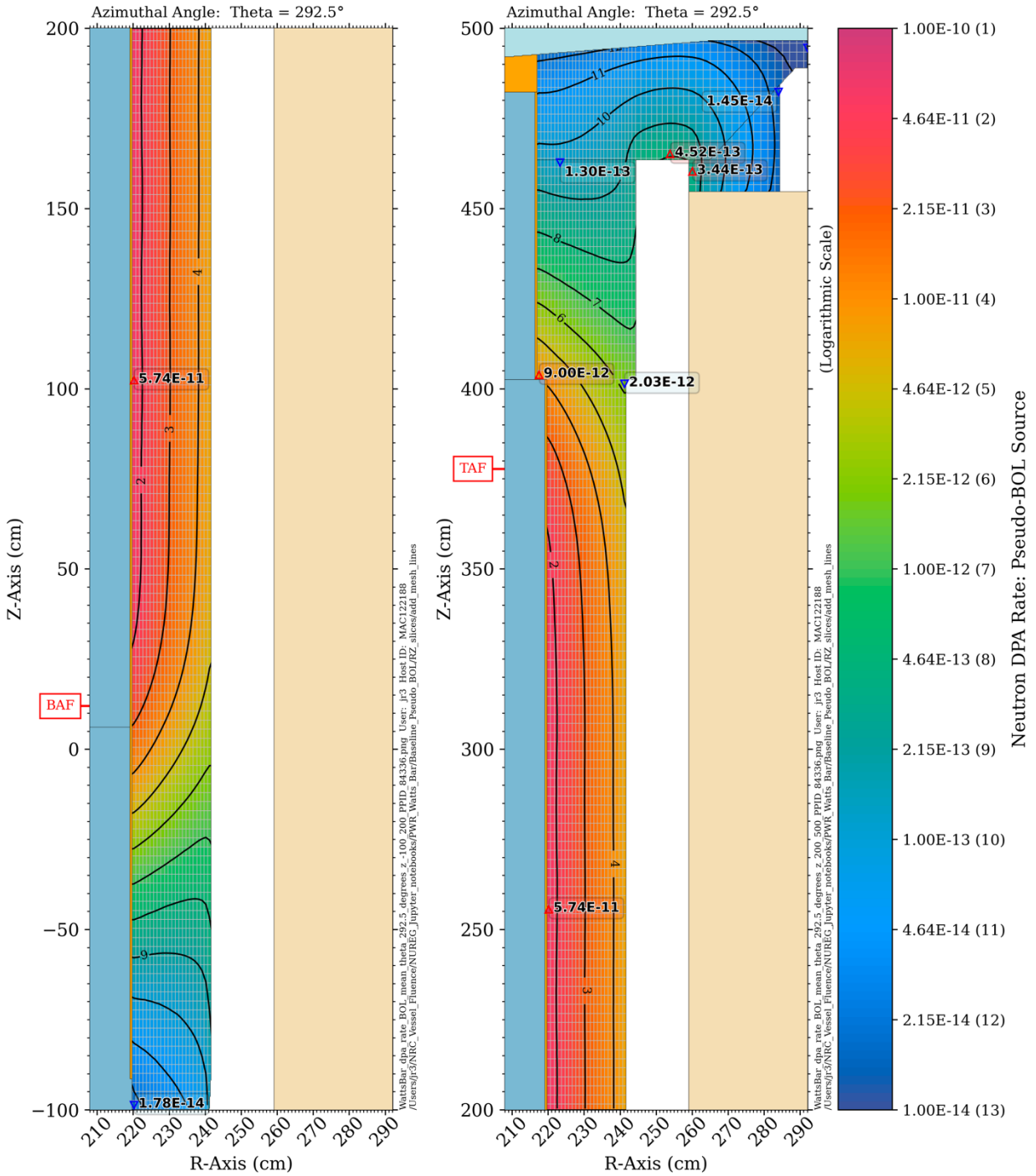

Figure A-8 **DPA rate in the PWR model at an azimuthal angle of 292.5°. Regions other than the RPV are colored by material assignment. Flooded contours show the dpa rate in the RPV, RPV nozzle, and nozzle support. Maximum and minimum dpa rate values in the RPV, RPV nozzle, and nozzle support are indicated. Maximum and minimum values in the RPV in the right-hand-side view are indicated above and below Z = 402.59 cm, where the thickness of the RPV changes. BAF and TAF are the bottom and top elevations of the active fuel**

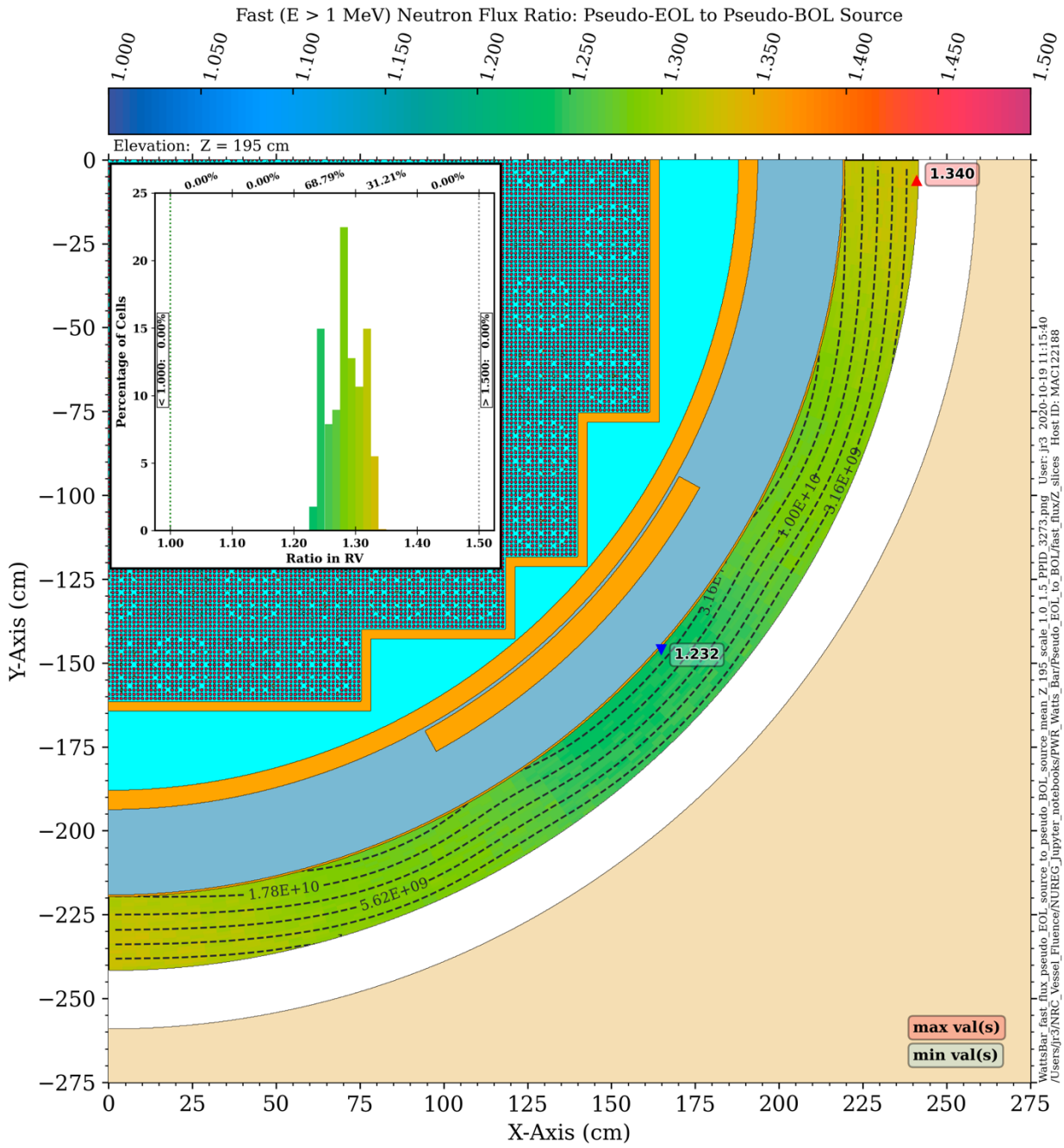

Figure A-9 Fast neutron flux ratio at the core midplane in the PWR model: pseudo-EOL source to pseudo-BOL source. Flooded contours show the fast flux ratio in the RPV. Minimum and maximum ratio values are indicated. The dashed contour lines represent the pseudo-BOL solution. The inset histogram plot shows the distribution of ratio values in the RPV

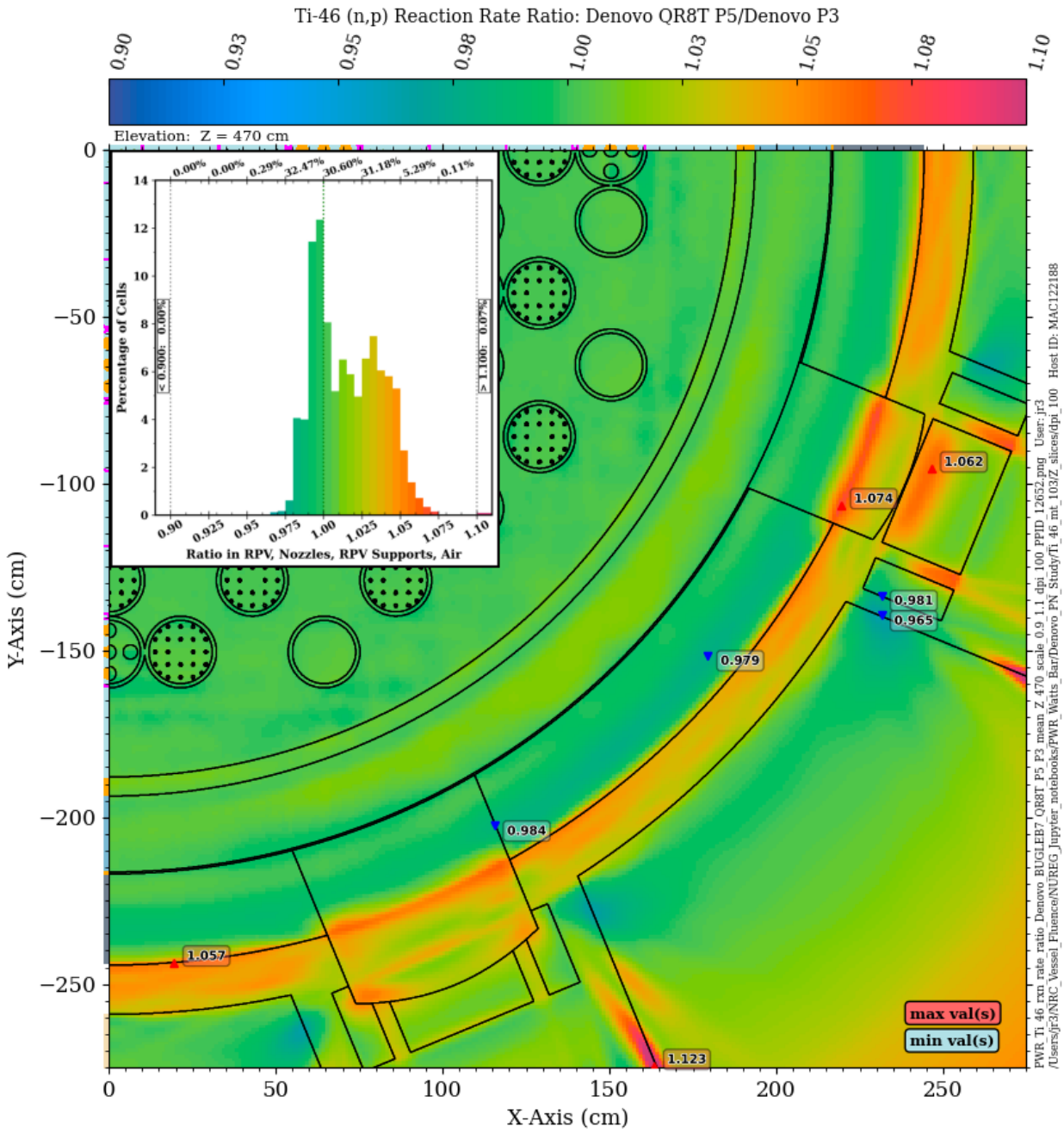

Figure A-10 Ratio of the ^{46}Ti (n,p) reaction rate from a P5 Denovo solution to a P3 Denovo solution at an elevation of Z = 470 cm.

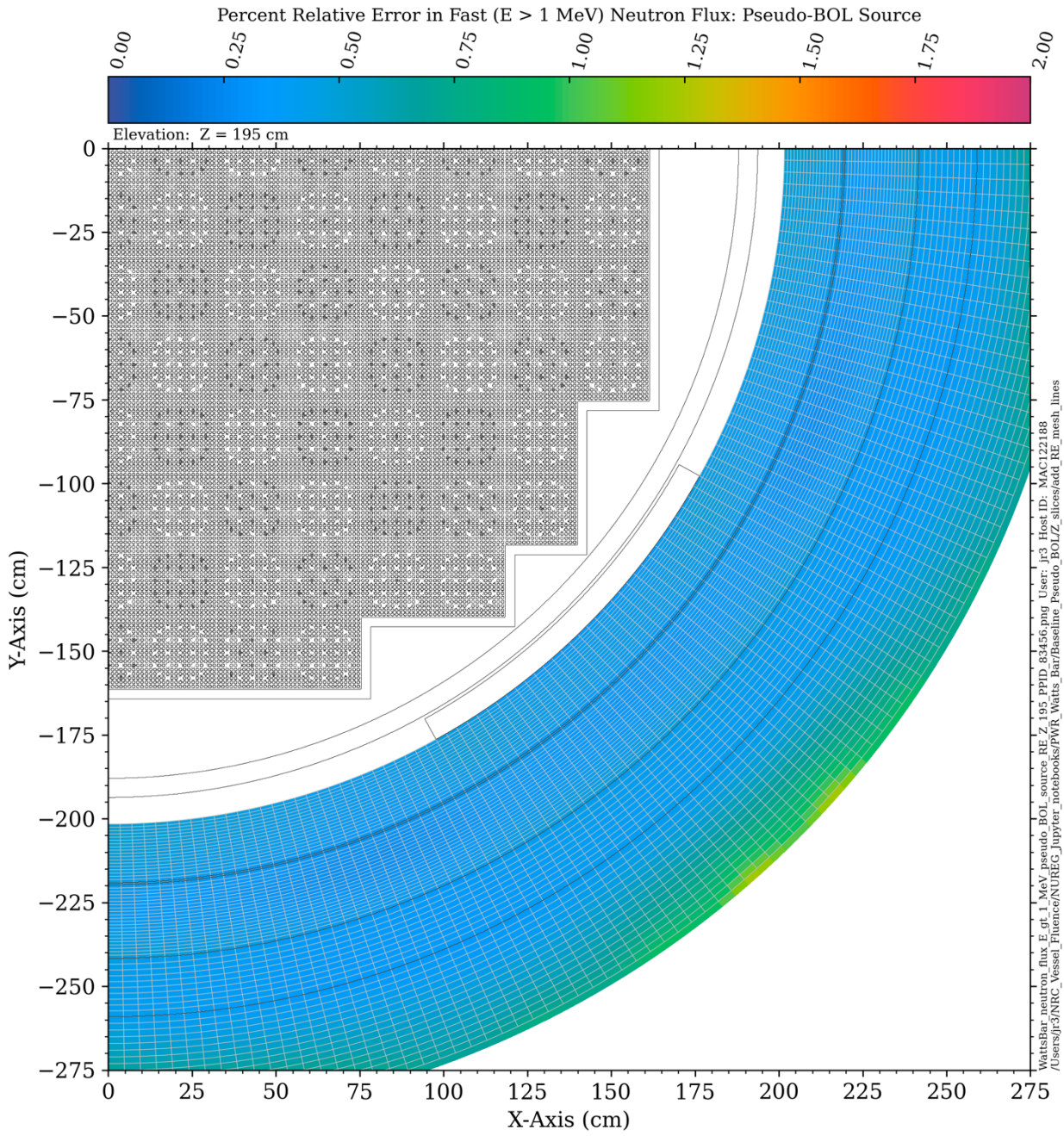

Figure A-11 Relative error in the fast neutron flux at the core midplane in the PWR model (see Figure A-5)

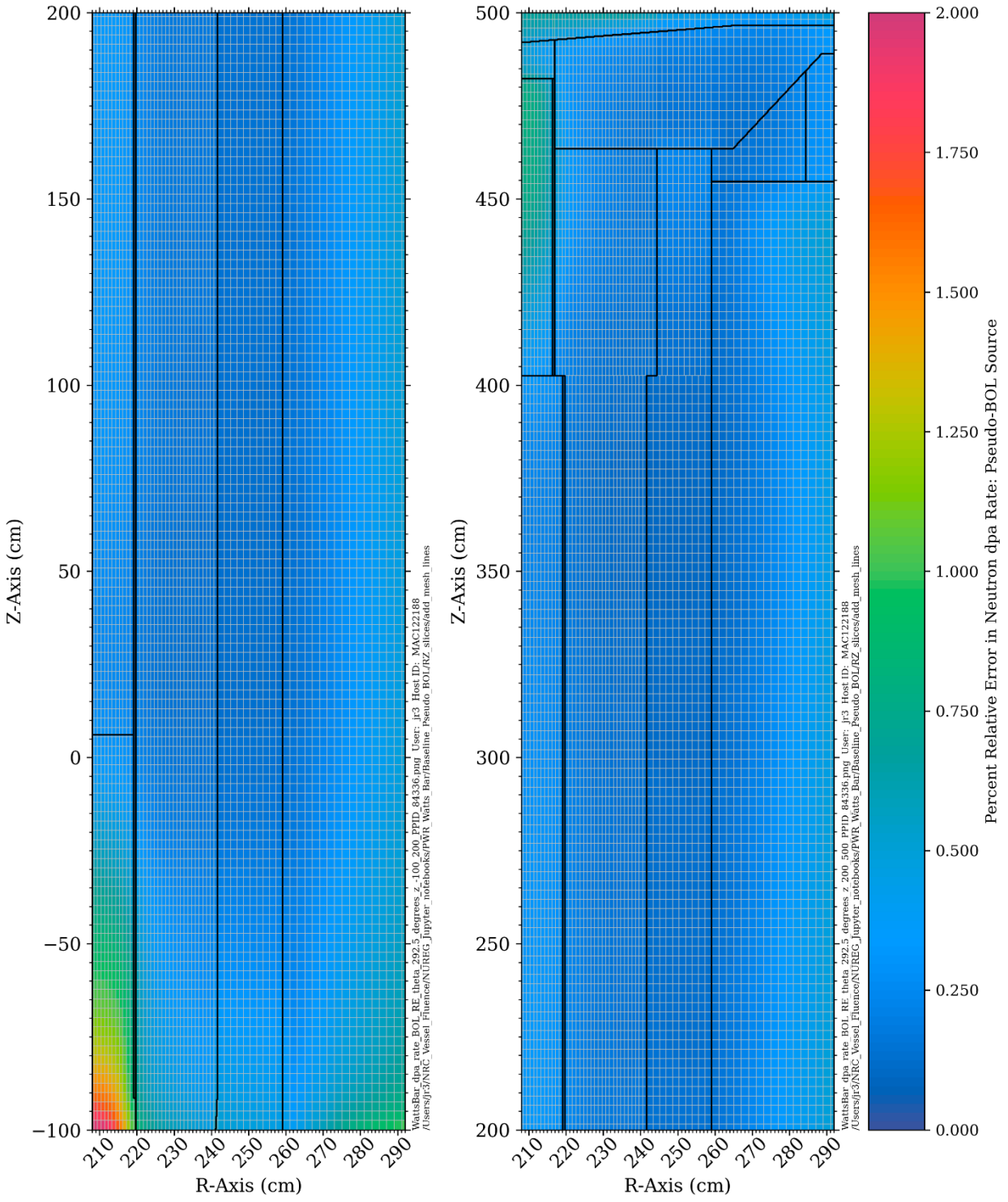

Figure A-12 Relative error in the fast neutron flux in the PWR model at an azimuthal angle of 292.5° (see Figure A-6)

APPENDIX B AN OVERVIEW OF MULTIGROUP CROSS-SECTION LIBRARIES

MG cross-section libraries used in radiation transport analyses are generally categorized as *fine group* or *broad group*. Fine-group libraries, which typically contain hundreds of energy groups, are generated by collapsing (averaging) pointwise cross-section data over a specified set of energy groups using a standard weighting spectrum. For LWR shielding analyses, the weighting spectrum used to average the pointwise data is typically a combination of a fission spectrum, a 1/E slowing-down spectrum, and a Maxwellian thermal spectrum. Fine-group libraries include a sufficient number of groups so that differences between the flux spectrum used to produce the groupwise cross sections and the actual flux spectra in a given application should have a negligible effect on the fine-group data.

Broad-group libraries, which typically contain tens of groups, are produced by collapsing (averaging) fine-group data using flux spectra that closely approximate the spectra that are encountered in specific locations in a particular transport application. A broad-group library that is developed using appropriate weighting spectra can produce calculated fluxes more quickly, and with fewer computing resources, with little loss in accuracy compared to a fine-group calculation.

MG libraries may also be categorized as *master libraries* and *working libraries*. A master library, which is typically a fine-group library,[2] contains cross-section data for multiple temperatures to address Doppler broadening of resonances and to provide thermal Maxwellian spectra and multiple Bondarenko background cross sections for resonance self-shielding effects [36]. Working libraries contain data for a single temperature and account for energy self-shielding by applying Bondarenko factors for each isotope in a mixture based on the material composition. Working libraries are thus problem-specific in the sense that they should only be used for calculations involving models similar to those used to develop the working library. For example, the BUGLE-B7 library was developed specifically for LWR shielding applications and may not be appropriate for other types of analysis.

All MG libraries contain 1D and 2D data. The 1D data contain reaction cross sections for each energy group, while the 2D data contain group-to-group transfer matrices. Master libraries and working libraries typically contain 1D data for numerous reaction types (e.g., elastic scattering, inelastic scattering, capture). Master libraries typically contain 2D data for multiple reaction types, while working libraries contain only a single 2D transfer matrix that accounts for all processes which result in a particle in group *g* due to a particle interaction in group *g'*.

Figure B-1 shows the 1D total microscopic cross section for ^{56}Fe from three MG libraries, as well as the CE data from which the MG libraries were created. Figure B-2 and Figure B-3 show the 2D transfer matrices (for the neutron groups only) for ^{1}H in PWR core coolant and ^{56}Fe at one quarter of the distance (¼T) through a PWR RPV from the BUGLE-B7 library.

The 2D transfer matrix plots show the magnitude of the group-to-group cross section from a source group on the abscissa to a sink group on the ordinate. The group numbers on these plots start with 0, the convention used by Denovo. The far-left column of each 2D plot thus shows the cross sections for scattering from the highest energy group to all lower energy groups. The values along the diagonal, from [0,0] to [46,46], represent the in-group cross

[2] The SCALE code system contains both fine-group and broad-group master libraries.

sections. Note that all out-of-group transfers are to lower energy groups (i.e., *downscattering*), except in the thermal groups, where upscatter can occur.

Figure B-4 illustrates the effect of inelastic scattering in the ^{56}Fe. For all groups below group 18, downscatter can occur to only the first sink group below the source group because the maximum energy loss for elastic scattering in ^{56}Fe is only ~7%. Inelastic scattering in ^{56}Fe occurs only for energies above 862.5 keV. The inelastic scattering accounts for all downscatters of more than one group.

Fine-group master libraries appropriate for LWR shielding analyses include the VITAMIN-B7 library and the coupled 200-neutron-group 47-gamma-group libraries (XN200G47v7.0 and XN200G47v7.1) in the SCALE code system. The VITAMIN-B7 fine-group master library has 199 neutron groups and 42 gamma groups. The VITAMIN-B7 neutron group structure is the same as that of the SCALE XN200G47v7.0 library, except that it does not include an energy group from 19.64 to 20.0 MeV, as the upper energy limit of the VITAMIN-B7 library is 19.64 MeV.

The SCALE code system also contains a broad-group master library with 56 neutron groups for physics calculations, as well as a broad group coupled neutron/gamma library with 28 neutron groups and 19 gamma groups. The 28n/19g library is used primarily for discrete ordinates adjoint flux calculations to generate importance maps for hybrid radiation transport.

This appendix briefly describes the fine- and broad-group libraries that were used in this study. More details of each library can be found in the reference documents.

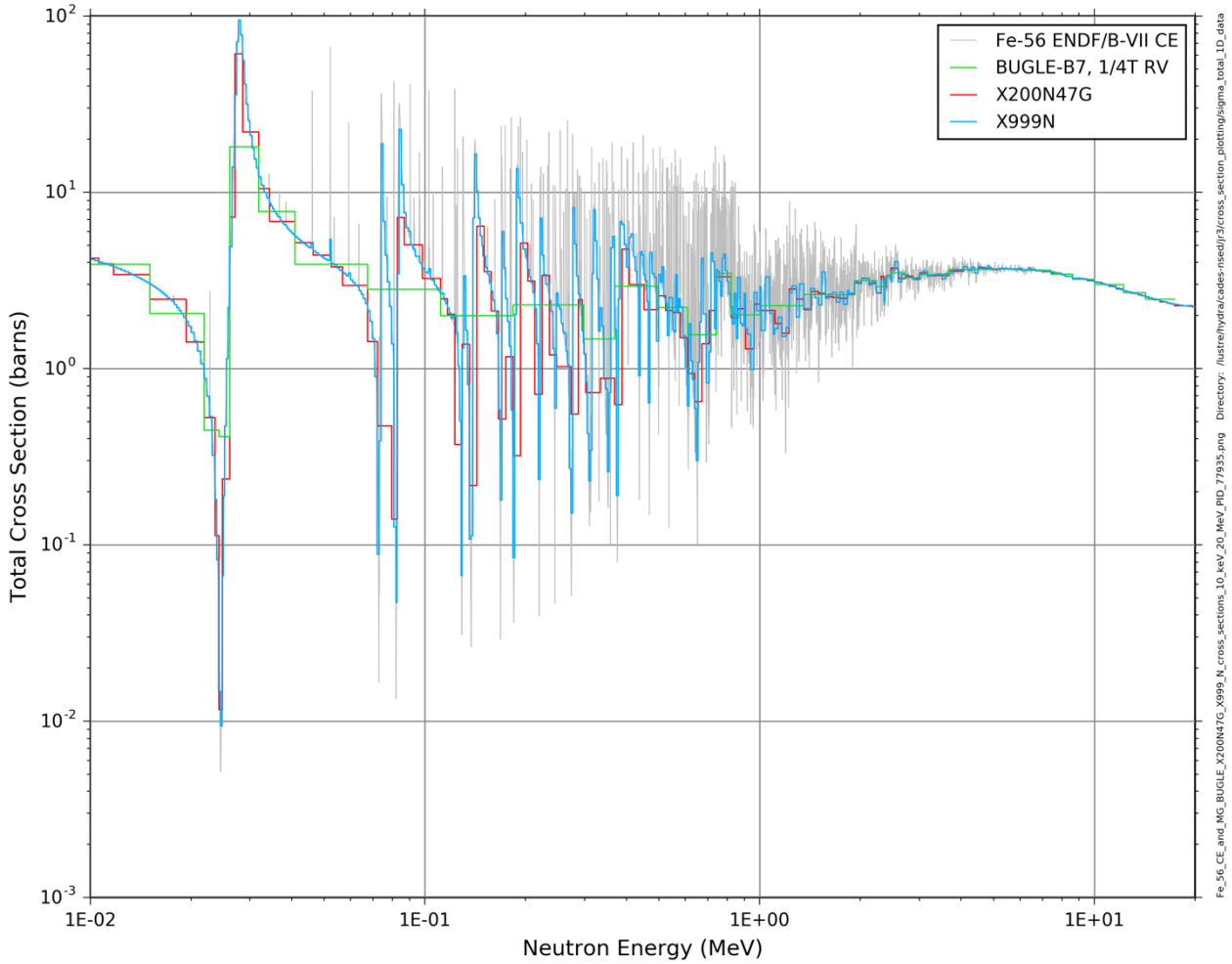

Figure B-1 Total microscopic cross section for ^{56}Fe from three MG libraries (BUGLE-B7, XN20047G, and XN999) and the SCALE ENDF/V-VII.1 CE library. The BUGLE-B7 data is for ^{56}Fe that has been collapsed from the VITAMIN-B7 library using a neutron flux spectrum at one quarter of the distance through the RPV

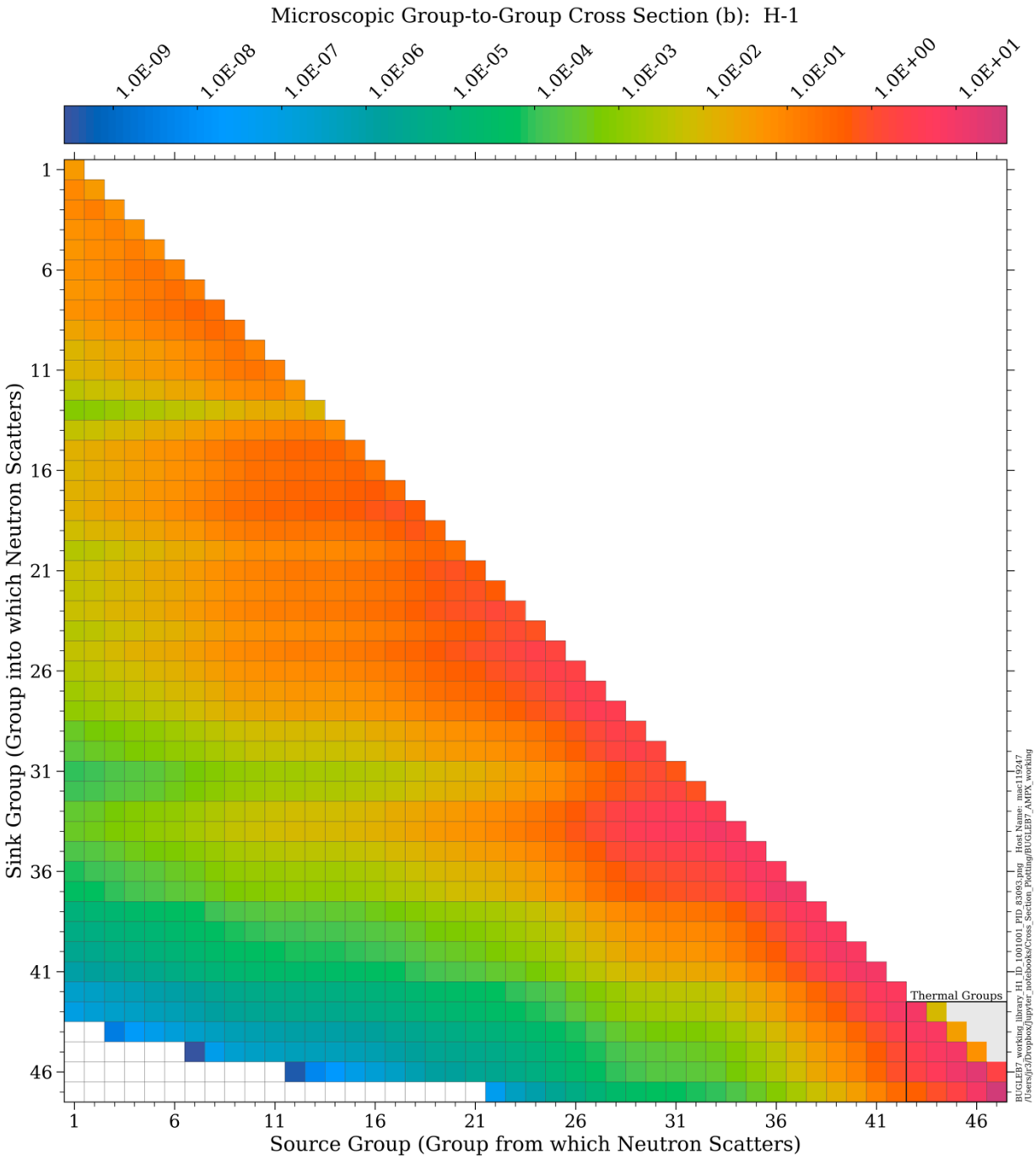

Figure B-2 Two-dimensional transfer matrix for ^{1}H from the BUGLE-B7 working library

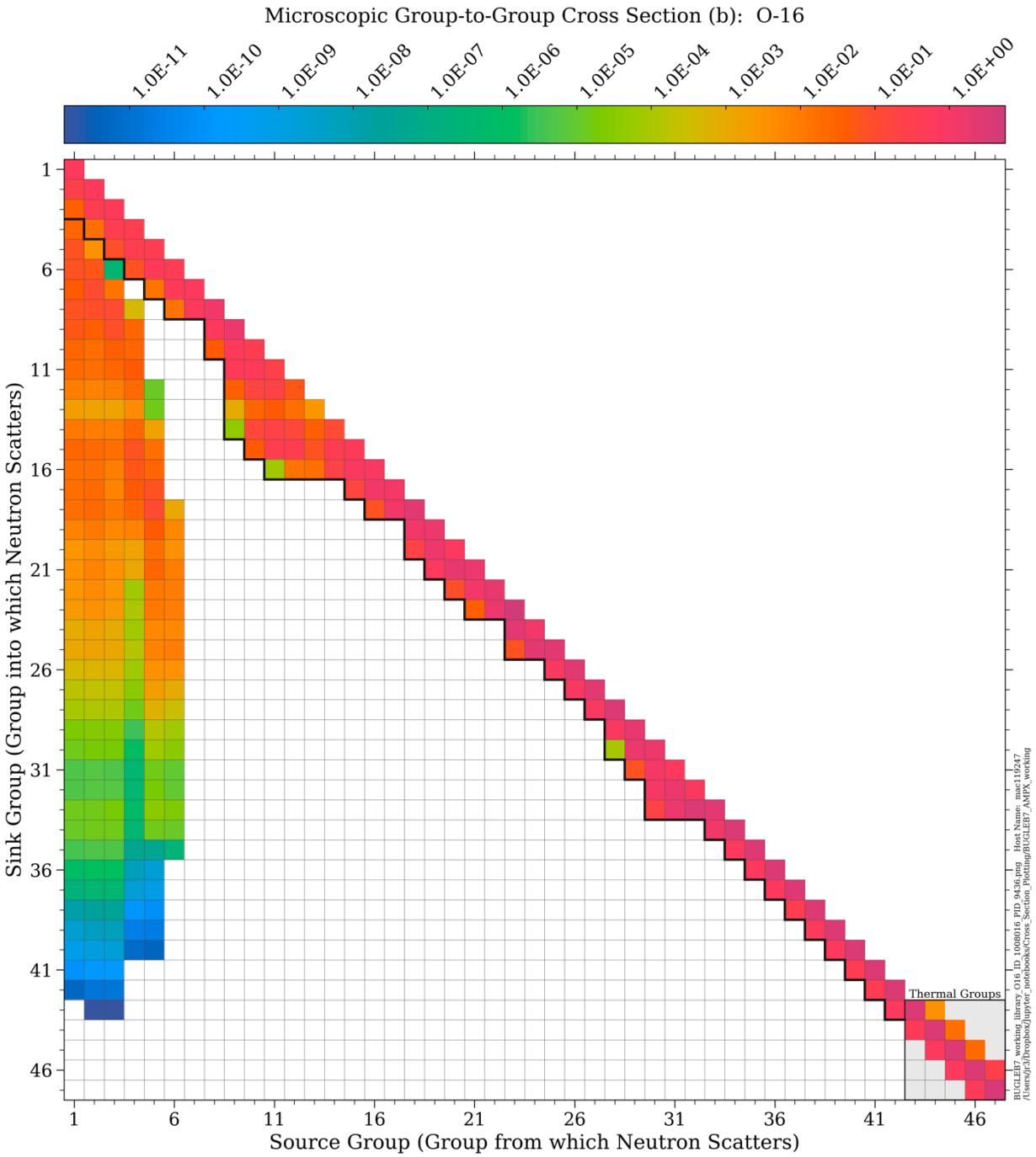

Figure B-3 **Two-dimensional transfer matrix for ^{16}O from the BUGLE-B7 working library. The weighting spectrum is for coolant in the core of a PWR model (Section B.4). The solid black line marks the minimum group into which elastic scattering can occur. The lowest energy group in which inelastic scattering occurs in ^{16}O is group 6**

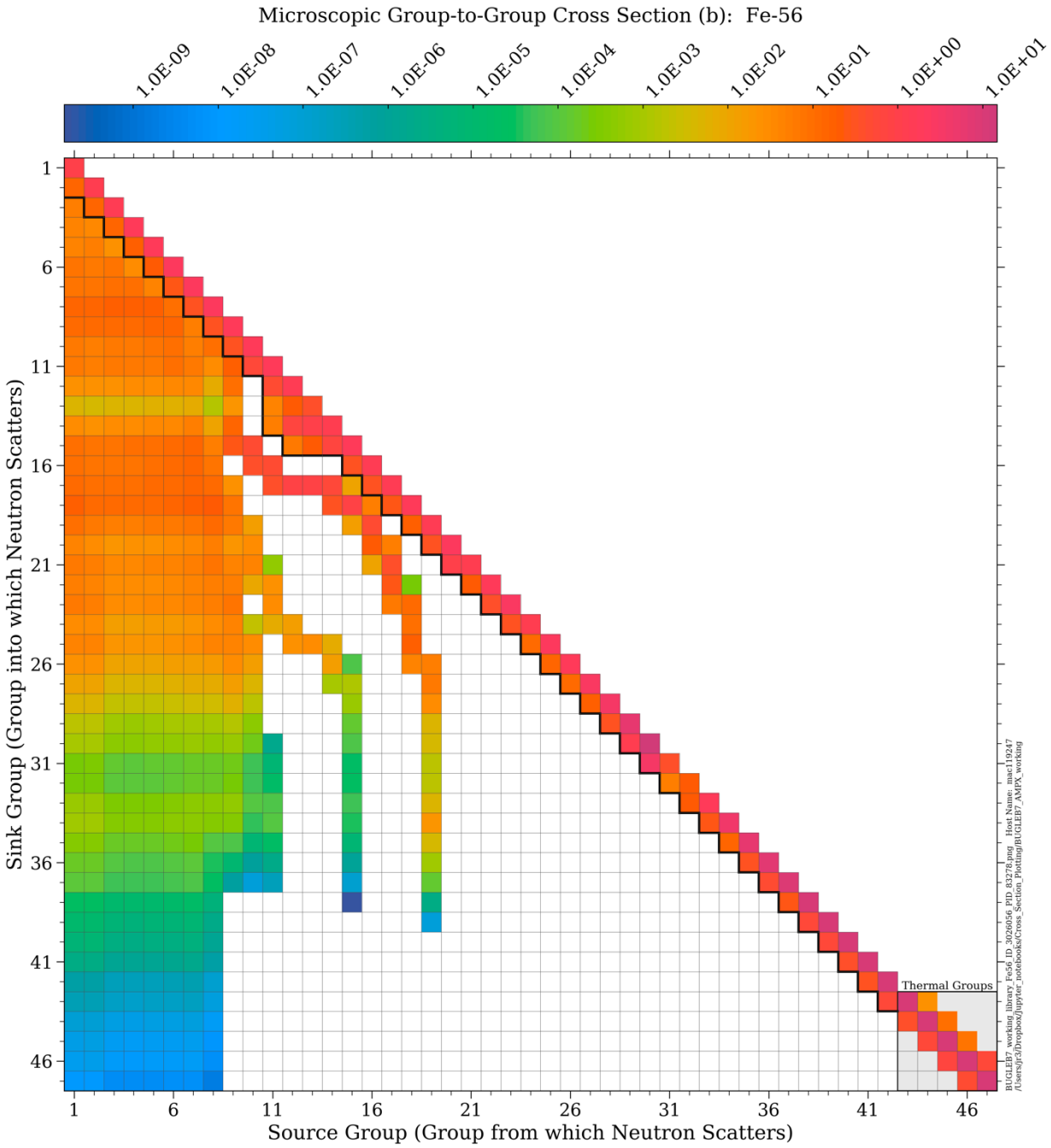

Figure B-4 Two-dimensional transfer matrix for ^{56}Fe at one-quarter of the RPV thickness from the BUGLE-B7 working library. The weighting spectrum is for the 1/4T thickness in the RPV of a PWR model (Section B.4). The solid black line marks the minimum group into which elastic scattering can occur. The lowest energy group in which inelastic scattering occur in ^{56}Fe is group 19

B.1 The XN200G47 Fine-Group Libraries

The XN200G47 libraries are part of the SCALE code system. There are two XN200G47 libraries: XN200G47v7.0, based on ENDF/B-VII.0 data, and XN200G47v7.1, based on ENDF/B-VII.1 data. The XN200G47v7.0 neutron energy group structure has 200 groups, with an upper energy limit of 20.0 MeV. The thermal energy range, which includes upscattering cross sections, has an upper boundary of 5.0435 eV and includes 36 groups. The neutron groups typically have uniform lethargy[3] widths ranging from 0.025 to 0.25 for energies above 1.445 eV, with additional boundaries to resolve resonance minima important for shielding calculations (e.g., the ^{16}O minimum at ~2.36 MeV and the ^{56}Fe minimum at ~24.5 keV). The energy group boundaries and group lethargy widths for the XN200G47v7.0 library are listed in Table B-1. The energy group boundaries for the XN200G47v7.1 library are identical to those of the XN200G47v7.0 library, except the upper energy of the first thermal group is 5.0 eV rather than 5.0435 eV.

The neutron weighting spectrum used to generate the XN200G47 libraries is shown in Figure B-5. It consists of a 1/E slowing-down spectrum above 10 MeV, a Watt fission spectrum from 80 keV to 10 MeV, a 1/E slowing-down spectrum from 0.125 eV to 80 keV, and a Maxwellian thermal spectrum below 0.125 eV. Scattering cross sections in the XN200G47 libraries are limited to P_5 expansions for all nuclides.

B.2 The VITAMIN-B7 Fine-Group Library

The VITAMIN-B7 library was developed for use in LWR shielding applications, including vessel fluence and dosimetry analyses. VITAMIN-B7 was generated using ENDF/B, Version VII, Release 0 (ENDF/B-VII.0). The processing methodology used to generate the VITAMIN-B7 library, as well as the BUGLE-B7 library, is consistent with the guidelines specified in ANSI/ANS 6.1.2 [37].

The VITAMIN-B7 neutron energy group structure has 199 groups, with an upper energy limit of 19.64 MeV. The energy groups are identical to groups 2 to 200 of the XN200G47v7.0 library (Table B-1). The weighting spectrum used to generate the VITAMIN-B7 library is shown in Figure B-5. It consists of a fission spectrum for neutron energies above 820.8 keV, a 1/E slowing-down spectrum for energies between 0.125 eV and 820.8 keV, and a Maxwellian spectrum for energies below 0.125 eV.

The angular distribution of neutron scattering cross sections in VITAMIN-B7 is represented using Legendre polynomial expansions with P_7 order for Z values up to 30 (Zn), and P_5 order for Z values above 30.

B.3 The XN999 Fine-Group Library

The XN999 library is available for use in Denovo and Shift but is not a standard SCALE library. XN999 libraries are available for ENDF/B-VII.0 and ENDF/B-VII.1 data. Scattering expansions are limited to P_3 for all nuclides.

[3] The lethargy width of an energy group g in an MG library is defined as $\Delta u = ln(E_g/E_{g+1})$. MG structures are often defined based on lethargy widths.

Table B-1 Neutron group boundaries and lethargy widths for the SCALE XN200G47v7.0 library.[4] The thermal groups are shaded in gray. The 199 VITAMIN-B7 groups are the same as groups 2–200 of the XN200G47v7.0 library

Grp	Upper Energy (eV)	Lethargy Width	Grp	Upper Energy (eV)	Lethargy Width	Grp	Upper Energy (eV)	Lethargy Width	Grp	Upper Energy (eV)	Lethargy Width
1	2.0000E+07	0.0182	51	2.0190E+06	0.0500	101	1.4264E+05	0.0500	151	1.6702E+02	0.2500
2	1.9640E+07	0.1250	52	1.9205E+06	0.0500	102	1.3569E+05	0.0500	152	1.3007E+02	0.2500
3	1.7332E+07	0.0249	53	1.8268E+06	0.0500	103	1.2907E+05	0.0500	153	1.0130E+02	0.2500
4	1.6905E+07	0.0250	54	1.7377E+06	0.0500	104	1.2277E+05	0.0499	154	7.8893E+01	0.2500
5	1.6487E+07	0.0500	55	1.6530E+06	0.0500	105	1.1679E+05	0.0500	155	6.1442E+01	0.2500
6	1.5683E+07	0.0500	56	1.5724E+06	0.0500	106	1.1109E+05	0.1250	156	4.7851E+01	0.2500
7	1.4918E+07	0.0250	57	1.4957E+06	0.0500	107	9.8037E+04	0.1250	157	3.7266E+01	0.2500
8	1.4550E+07	0.0250	58	1.4227E+06	0.0499	108	8.6517E+04	0.0475	158	2.9023E+01	0.2500
9	1.4191E+07	0.0250	59	1.3534E+06	0.0500	109	8.2503E+04	0.0371	159	2.2603E+01	0.2500
10	1.3840E+07	0.0249	60	1.2874E+06	0.0500	110	7.9499E+04	0.0991	160	1.7604E+01	0.2500
11	1.3499E+07	0.0501	61	1.2246E+06	0.0501	111	7.1998E+04	0.0663	161	1.3710E+01	0.2500
12	1.2840E+07	0.0250	62	1.1648E+06	0.0500	112	6.7379E+04	0.1750	162	1.0677E+01	0.2500
13	1.2523E+07	0.0250	63	1.1080E+06	0.1000	113	5.6562E+04	0.0750	163	8.3153E+00	0.2500
14	1.2214E+07	0.0500	64	1.0026E+06	0.0417	114	5.2475E+04	0.1250	164	6.4760E+00	0.2500
15	1.1618E+07	0.0499	65	9.6164E+05	0.0583	115	4.6309E+04	0.1250	165	5.0435E+00	0.2500
16	1.1052E+07	0.0500	66	9.0718E+05	0.0500	116	4.0868E+04	0.1750	166	3.9279E+00	0.2500
17	1.0513E+07	0.0500	67	8.6294E+05	0.0500	117	3.4307E+04	0.0750	167	3.0590E+00	0.2500
18	1.0000E+07	0.0500	68	8.2085E+05	0.0500	118	3.1828E+04	0.1104	168	2.3824E+00	0.2500
19	9.5123E+06	0.0500	69	7.8082E+05	0.0500	119	2.8501E+04	0.0541	169	1.8554E+00	0.2500
20	9.0484E+06	0.0500	70	7.4274E+05	0.0500	120	2.7000E+04	0.0355	170	1.4450E+00	0.1057
21	8.6071E+06	0.0500	71	7.0651E+05	0.0500	121	2.6058E+04	0.0500	171	1.3000E+00	0.1443
22	8.1873E+06	0.0500	72	6.7206E+05	0.0500	122	2.4788E+04	0.0250	172	1.1253E+00	0.0411
23	7.7880E+06	0.0500	73	6.3928E+05	0.0500	123	2.4176E+04	0.0250	173	1.0800E+00	0.0377
24	7.4082E+06	0.0500	74	6.0810E+05	0.0500	124	2.3579E+04	0.0750	174	1.0400E+00	0.0392
25	7.0469E+06	0.0500	75	5.7844E+05	0.0500	125	2.1875E+04	0.1250	175	1.0000E+00	0.1319
26	6.7032E+06	0.0167	76	5.5023E+05	0.0500	126	1.9305E+04	0.2500	176	8.7643E-01	0.0912
27	6.5924E+06	0.0333	77	5.2340E+05	0.0500	127	1.5034E+04	0.2500	177	8.0000E-01	0.1588
28	6.3763E+06	0.0500	78	4.9787E+05	0.1000	128	1.1709E+04	0.1000	178	6.8256E-01	0.0880
29	6.0653E+06	0.0500	79	4.5049E+05	0.1000	129	1.0595E+04	0.1500	179	6.2506E-01	0.1620
30	5.7695E+06	0.0500	80	4.0762E+05	0.0500	130	9.1188E+03	0.2500	180	5.3158E-01	0.0612
31	5.4881E+06	0.0500	81	3.8774E+05	0.0500	131	7.1017E+03	0.2500	181	5.0000E-01	0.1888
32	5.2205E+06	0.0500	82	3.6883E+05	0.1000	132	5.5308E+03	0.2500	182	4.1399E-01	0.1210
33	4.9659E+06	0.0500	83	3.3373E+05	0.1000	133	4.3074E+03	0.1500	183	3.6680E-01	0.1210
34	4.7237E+06	0.0500	84	3.0197E+05	0.0116	134	3.7074E+03	0.1000	184	3.2500E-01	0.1671
35	4.4933E+06	0.1000	85	2.9849E+05	0.0043	135	3.3546E+03	0.1000	185	2.7500E-01	0.2007
36	4.0657E+06	0.1000	86	2.9721E+05	0.0091	136	3.0354E+03	0.1000	186	2.2500E-01	0.2012
37	3.6788E+06	0.1000	87	2.9452E+05	0.0250	137	2.7465E+03	0.0500	187	1.8400E-01	0.2043
38	3.3287E+06	0.0500	88	2.8725E+05	0.0500	138	2.6126E+03	0.0500	188	1.5000E-01	0.1823
39	3.1664E+06	0.0500	89	2.7324E+05	0.1000	139	2.4852E+03	0.1000	189	1.2500E-01	0.2231
40	3.0119E+06	0.0500	90	2.4724E+05	0.0500	140	2.2487E+03	0.1000	190	1.0000E-01	0.3567
41	2.8651E+06	0.0500	91	2.3518E+05	0.0500	141	2.0347E+03	0.2500	191	7.0000E-02	0.3365
42	2.7253E+06	0.0500	92	2.2371E+05	0.0500	142	1.5846E+03	0.2500	192	5.0000E-02	0.2231
43	2.5924E+06	0.0500	93	2.1280E+05	0.0500	143	1.2341E+03	0.2500	193	4.0000E-02	0.2877
44	2.4660E+06	0.0333	94	2.0242E+05	0.0500	144	9.6112E+02	0.2500	194	3.0000E-02	0.3567
45	2.3852E+06	0.0084	95	1.9255E+05	0.0500	145	7.4852E+02	0.2500	195	2.1000E-02	0.3704
46	2.3653E+06	0.0083	96	1.8316E+05	0.0500	146	5.8295E+02	0.2500	196	1.4500E-02	0.3716
47	2.3457E+06	0.0167	97	1.7422E+05	0.0500	147	4.5400E+02	0.2500	197	1.0000E-02	0.6931
48	2.3069E+06	0.0333	98	1.6573E+05	0.0500	148	3.5357E+02	0.2500	198	5.0000E-03	0.9163
49	2.2313E+06	0.0500	99	1.5764E+05	0.0499	149	2.7536E+02	0.2500	199	2.0000E-03	1.3863
50	2.1225E+06	0.0500	100	1.4996E+05	0.0500	150	2.1445E+02	0.2500	200	5.0000E-04	3.9120

[4] The upper energy of group 165 (the first thermal group) in the XN200G47v7.1 library is 5.0 eV.

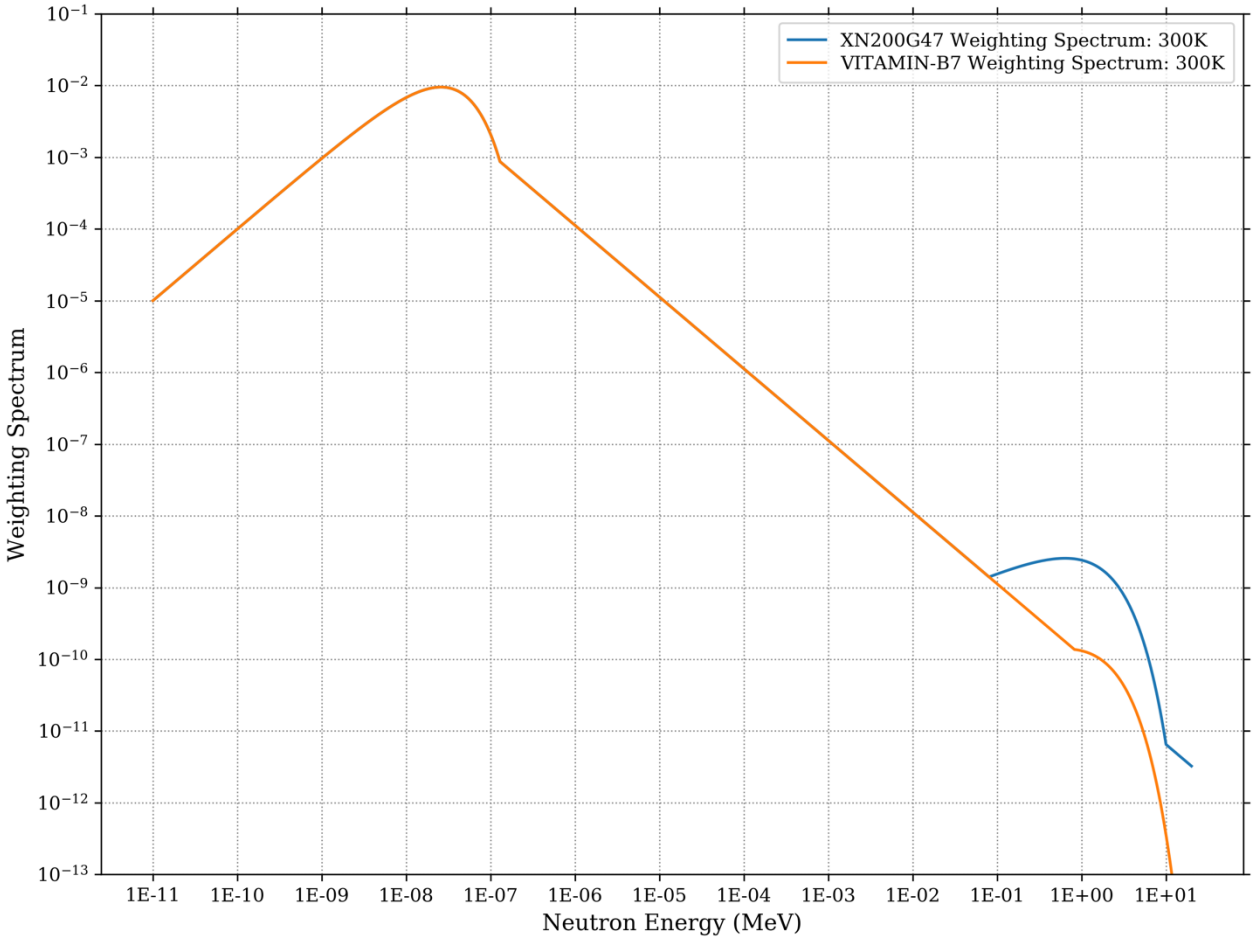

Figure B-5 The weighting spectra used to generate the VITAMIN-B7 and SCALE XN200G47 MG libraries from ENDF/B-VII pointwise data

B.4 The BUGLE-B7 Broad-Group Library

The BUGLE-B7 library is widely used in RPV fluence analyses. It includes 47 neutron energy groups with an upper energy limit of 17.332 MeV. The thermal energy range has an upper boundary of 5.043 eV and includes five groups. There are options in the BUGLE-B7 libraries to explicitly model upscatter or to apply an approach referred to as the "ANISN upscatter approximation." The energy group boundaries and group lethargy widths for the BUGLE-B7 library are listed in Table B-2.

The BUGLE-B7 library was produced by collapsing the VITAMIN-B7 library using weighting spectra from key regions of one-dimensional PWR and BWR models. These weighting spectra are representative of the following locations in the PWR and BWR models:

1. Off-center in the core region of the BWR model
2. Off-center in the core region of the PWR model
3. In the PWR downcomer region
4. Within the PWR RPV at one-fourth the vessel thickness
5. Within the PWR concrete biological shield

The fine-group (based on the VITAMIN-B7 group structure) spectra in each of these regions are shown in Figure B-6.

The angular distribution of neutron scattering cross sections in BUGLE-B7 is represented using Legendre polynomial expansions with P_7 order for Z values up to 30 (Zn), and P_5 order for Z values above 30.

Table B-2 Neutron energy group boundaries and lethargy widths for the BUGLE-B7 library. The thermal groups are shaded in gray. The fine groups correspond to the VITAMIN-B7 library

Grp	Upper Energy (eV)	Lethargy Width	Fine Groups	Grp	Upper Energy (eV)	Lethargy Width	Fine Groups
1	1.7332E+07	0.1999	2-7	26	1.8316E+05	0.5000	95-104
2	1.4191E+07	0.1500	8-12	27	1.1109E+05	0.5000	105-110
3	1.2214E+07	0.2000	13-16	28	6.7379E+04	0.5000	111-114
4	1.0000E+07	0.1500	17-19	29	4.0868E+04	0.2500	115-116
5	8.6071E+06	0.1500	20-22	30	3.1828E+04	0.2000	117-119
6	7.4082E+06	0.2000	23-27	31	2.6058E+04	0.0750	120-121
7	6.0653E+06	0.2000	28-31	32	2.4176E+04	0.1000	122-123
8	4.9659E+06	0.3000	32-35	33	2.1875E+04	0.3750	124-125
9	3.6788E+06	0.2000	36-38	34	1.5034E+04	0.7500	126-129
10	3.0119E+06	0.1000	39-40	35	7.1017E+03	0.7500	130-133
11	2.7253E+06	0.1000	41-42	36	3.3546E+03	0.7500	134-140
12	2.4660E+06	0.0417	43-44	37	1.5846E+03	1.2500	141-145
13	2.3653E+06	0.0083	45	38	4.5400E+02	0.7500	146-148
14	2.3457E+06	0.0500	46-47	39	2.1445E+02	0.7500	149-151
15	2.2313E+06	0.1500	48-50	40	1.0130E+02	1.0000	152-155
16	1.9205E+06	0.1500	51-53	41	3.7266E+01	1.2500	156-160
17	1.6530E+06	0.2000	54-57	42	1.0677E+01	0.7500	161-163
18	1.3534E+06	0.3000	58-62	43	5.0435E+00	1.0000	164-167
19	1.0026E+06	0.2000	63-66	44	1.8554E+00	0.7500	168-174
20	8.2085E+05	0.1000	67-68	45	8.7643E-01	0.7500	175-180
21	7.4274E+05	0.2000	69-72	46	4.1399E-01	1.4207	181-188
22	6.0810E+05	0.2000	73-76	47	1.0000E-01	9.2103	189-199
23	4.9787E+05	0.3000	77-80				
24	3.6883E+05	0.2159	81-84				
25	2.9721E+05	0.4841	85-94				

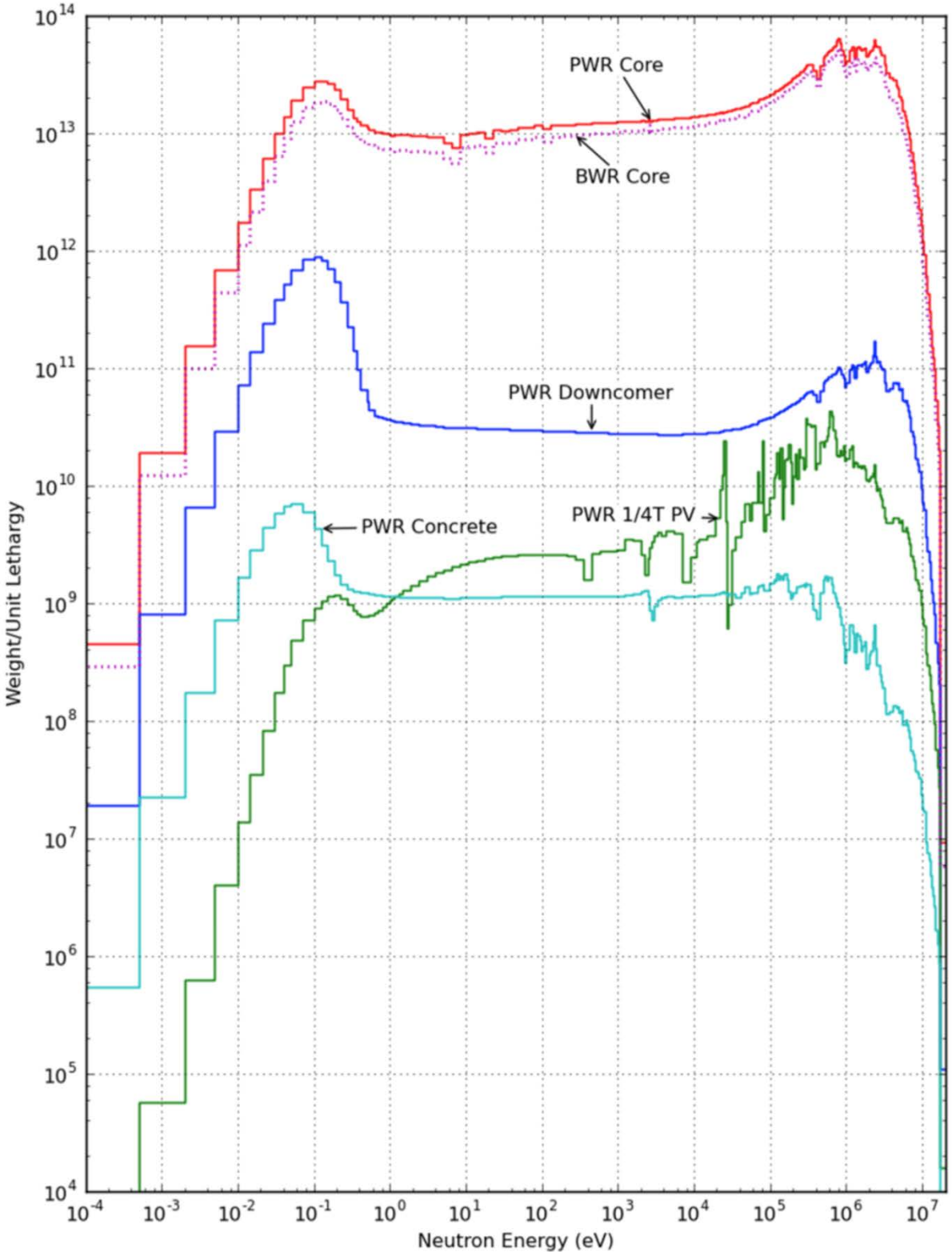

Figure B-6 The weighting spectra used to generate the BUGLE-B7 MG data for problem-specific analyses

APPENDIX C DOSIMETRY CROSS SECTIONS USED IN LWR RPV FLUENCE BENCHMARK CALCULATIONS

Benchmark calculations for RPV fluence analyses typically involve comparing measured activities of several isotopes from dosimetry capsules at specific locations in the benchmark experiment. Radiation transport calculations are then performed to estimate the isotopic activities, with the resulting calculated/measured (C/M) ratios indicating how well the transport calculations model the physical experiment.

The accuracy that can be obtained in calculating the activation of an isotopic target is dependent on both the accuracy of the neutron transport calculation and the accuracy of the cross sections for the reactions that produce the activated dosimetry isotopes.

For this analysis, nine isotopic reactions are considered that have been used in the H.B. Robinson, ORNL Pool Critical Assembly [Pressure Vessel Facility] (PCA), and VENUS-3 benchmarks [17]. These reactions are listed in Table C-1. Seven of the nine reactions are threshold reactions, with threshold energies ranging from 40.14 keV to 3.25 MeV. The remaining two are fission reactions, which have no minimum energy threshold. Characterizing a neutron field requires use of multiple dosimetry isotopes which span the desired range of neutron energies.

A commonly used set of reaction cross sections for reactor dosimetry applications is IRDF-2002 [21]. Cross sections from IRDF-2002 for the reactions listed in Table C-1 are shown in Figure C-1 and Figure C-2. Figure C-2 shows the pointwise data for energies above 100 keV and the 90% energy response ranges listed in Table C-1. For each reaction, the data symbols plotted along the abscissa indicate the threshold energies, below which the cross-section values are identically zero.

Table C-1 Dosimetry reactions that are commonly used for RPV fluence benchmark measurements and calculations

Target isotope	Reaction	Product isotope	Product half life	Reaction threshold	Energy response range (MeV)[5] [43]
^{27}Al	(n,α)	^{24}Na	14.97 h	3.25 MeV	6.45–11.9
^{63}Cu	(n,α)	^{60}Co	5.271 y	2.25 MeV	4.53–11.0
^{46}Ti	(n,p)	^{46}Sc	83.81 d	2.10 MeV	3.70–9.43
^{54}Fe	(n,p)	^{54}Mn	312.1 d	700 keV	2.27–7.54
^{58}Ni	(n,p)	^{58}Co	70.88 d	400 keV	1.98–7.51
^{115}In	(n,n′)	^{115m}In	4.485 h	339.2 keV	1.12–5.86
^{103}Rh	(n,n′)	^{103m}Rh	56.12 m	40.14 keV	0.731–5.73
^{238}U	(n,f)	F.P.	--------	--------	1.44–6.69
^{237}Np	(n,f)	F.P.	--------	--------	0.684–5.61

[5] The energy range over which 90% of the detector response occurs in a ^{235}U fission spectrum.

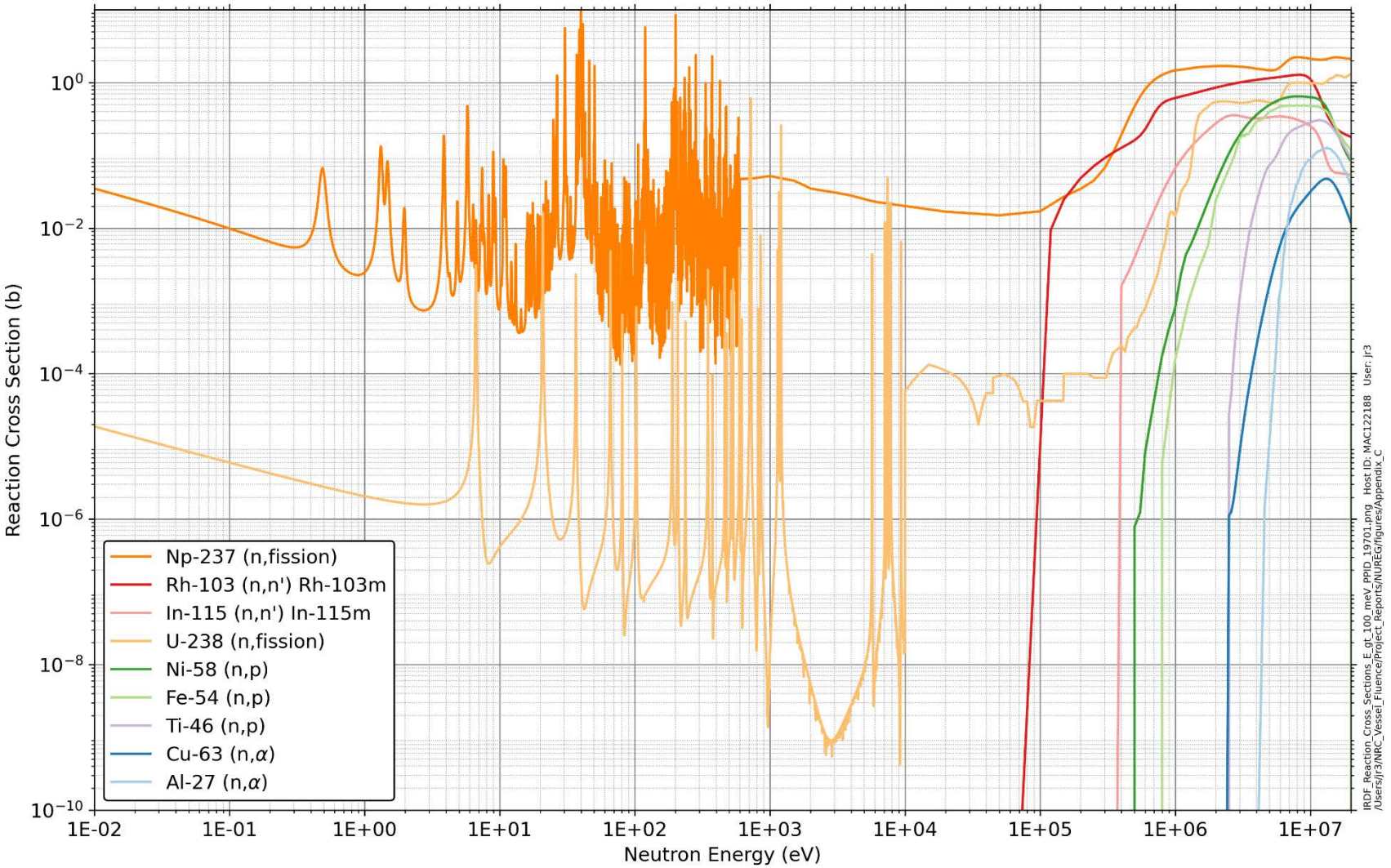

Figure C-1 Cross-section data for dosimetry reactions used in RPV benchmarks

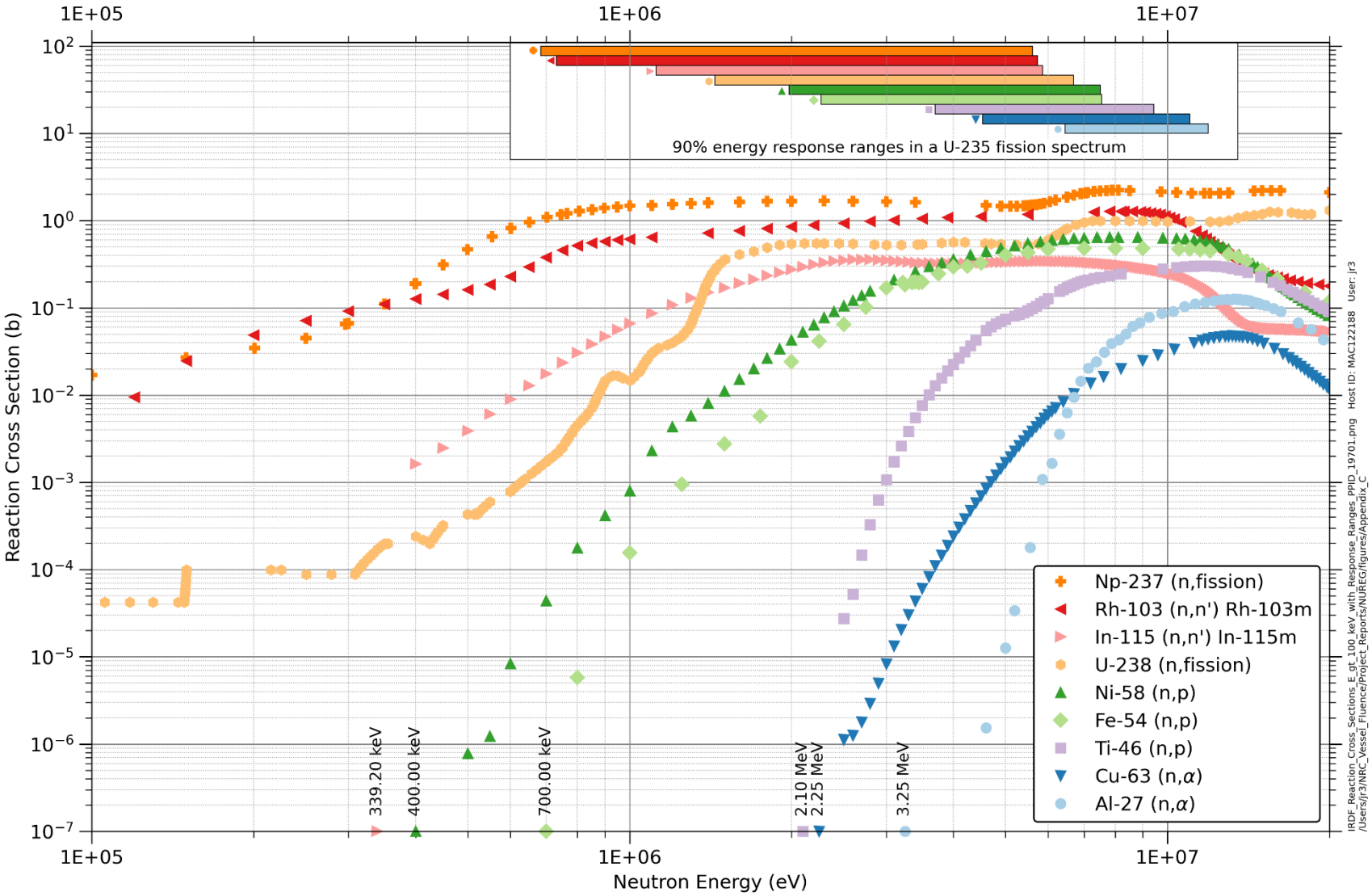

Figure C-2 Cross-section data for dosimetry reactions used in RPV benchmarks: E > 100 keV. The symbols on the abscissa indicate the reaction threshold energies for ^{115}In, ^{58}Ni, ^{54}Fe, ^{46}Ti, ^{63}Cu, and ^{27}Al

APPENDIX D REPRESENTATION OF ANGULAR SCATTERING DISTRIBUTIONS IN MULTIGROUP CROSS-SECTION LIBRARIES

The angular distribution of scattered radiation in MG discrete ordinates calculations is typically modeled using Legendre polynomial expansions. The extent to which these expansions can accurately model the scattering distributions is dependent on two factors: the kinematics of neutron scattering, and the MG energy boundaries. Those two factors are briefly discussed in this appendix, and examples of scattering angular distributions for some common materials encountered in LWR shielding analyses are provided. Implications of these scattering angular distributions for MG neutron transport calculations are briefly discussed.

D.1 Neutron scattering kinematics

A discussion of neutron scattering kinematics is well beyond the scope of this report, but a few key points can be made here. Further details can be found in the literature [38], [39], [40].

Two types of neutron scattering are of importance in typical shielding calculations: *capture scattering* and *potential scattering*. In capture scattering, the incident neutron is absorbed by the scattering nucleus, which subsequently decays by the emission of a neutron. Capture scattering can be either elastic or inelastic. With elastic scattering, the residual nucleus is left in the ground state. With inelastic scattering, the residual nucleus is left in an excited state, which returns to the ground state by the emission of a gamma ray. Potential scattering does not involve the formation of a compound nucleus and is always elastic.

The kinematics of neutron scattering events are dependent on the incident neutron energy and the scattering nucleus. Although no absolute statements can be made regarding the angular distribution of scattered neutrons as a function of the neutron energy and the specific scattering nucleus, the following behaviors are typical [41]:

1. Neutron scattering tends to become more anisotropic with increasing neutron energy for any scattering nucleus.
2. Neutron scattering tends to become more anisotropic as the mass of the scattering nucleus decreases.

Therefore, scattering anisotropy tends to be most pronounced in the scattering of high-energy neutrons from nuclei of low mass numbers. This behavior is illustrated below in Section D.3

D.2 Multigroup energy structures

The degree of anisotropy in MG calculations can also be dependent on the MG energy structure. This effect is not due to scattering kinematics but is rather an artifact of MG libraries. Because of energy-momentum constraints that govern the minimum and maximum scattering angles for MG neutron elastic scattering, light element scattering often produces group-to-group scattering cross sections that are highly anisotropic.

Consider the scattering of a neutron from a scattering nucleus through a scattering angle θ (Figure D-1). For elastic scattering from a source group g′ to a sink group g, the lower and upper limits (ω_{min} and ω_{max}) for the cosine of the scattering angle are given by Attia and Harms [42]:

$$\omega_{min} = \frac{1}{2}\left[(A+1)\sqrt{\frac{E_g}{E_{g'-1}}} - (A-1)\sqrt{\frac{E_{g'-1}}{E_g}}\right], \quad \text{(D-1)}$$

and

$$\omega_{max} = \frac{1}{2}\left[(A+1)\sqrt{\frac{E_{g-1}}{E_{g'}}} - (A-1)\sqrt{\frac{E_{g'}}{E_{g-1}}}\right], \quad \text{(D-2)}$$

where

A	=	relative mass of the scattering isotope (the mass of the isotope divided by the neutron mass)
$E_{g'-1}$	=	upper energy of the source group
$E_{g'}$	=	lower energy of the source group
E_{g-1}	=	upper energy of the sink group
E_g	=	lower energy of the sink group

Equations (D-1) and (D-2) are valid if

$$\alpha E_{g'-1} \leq E_{g'}, \quad \text{(D-3)}$$

where

$$\alpha = \left(\frac{A-1}{A+1}\right)^2. \quad \text{(D-4)}$$

Note that ω_{min} and ω_{max} are restricted to the range [-1, 1]:

$$-1 \leq \omega_{min} \leq \omega_{max} \leq 1. \quad \text{(D-5)}$$

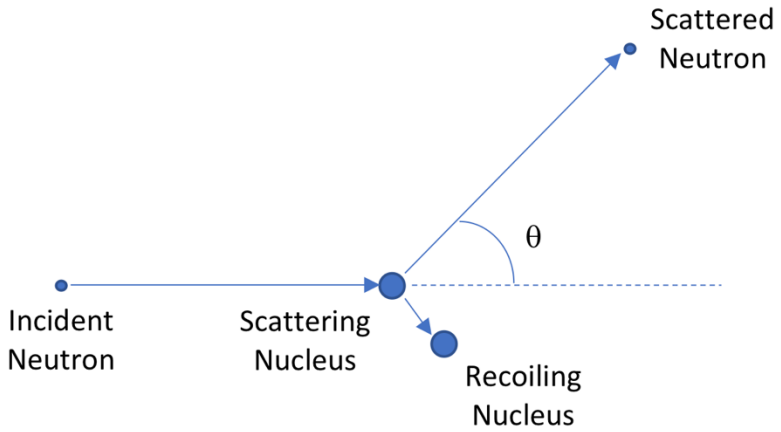

Figure D-1 Diagram illustrating the scattering angle θ (with cosine ω) for neutron scattering.

The value of α provides a measure of the minimum possible energy of a neutron that scatters elastically from a nucleus of mass A. For example, neutron scattering from ^{1}H has an α value of 1.735E-7. A neutron which scatters from group 1 of the BUGLE-B7 library, with a lower energy limit of 14.191 MeV, has a minimum possible energy of 2.46 eV, which is in group 43 of the

BUGLE-B7 library. This is shown in the leftmost column of Figure B-2, where the scattering cross section from group one into groups 44 through 47 is zero.

Neutrons which undergo elastic scattering in ^{56}Fe can lose 6.9% of their energy at most in a single scatter. This behavior can be seen in Figure B-4. In all BUGLE-B7 energy groups other than groups 11–13, elastic scattering in ^{56}Fe can only occur within the scattering group or to the next group number. The exception for groups 11–13 is due to the narrow group widths of groups 12–14 (Table B-2). For neutron energies below 862.5 eV, which is in group 19, inelastic scattering cannot occur in ^{56}Fe.

Because there is no inelastic scattering of neutrons from the isotopes of H, Eq. (D-1) and Eq. (D-2) hold for all scattering events from those nuclides. For all other nuclides, inelastic scattering is possible, and Eq. (D-1) and Eq. (D-2) are valid only for neutron energies below the lowest inelastic scattering threshold for each nuclide. Note that the lower and upper limits of the cosine of the scattering angle depend on the energy bounds of the source and sink groups, as shown in Eq. (D-1) and Eq. (D-2). Examples of scattering anisotropy for ^{1}H, ^{16}O, and ^{56}Fe can be seen in Figure D-2 through Figure D-4 for different group-to-group scattering cross sections; the true scattering anisotropy in each plot is shown by the black lines, which are obtained from MCNP calculations using CE cross-section data.

D.3 Multigroup scattering angular distribution examples

D.3.1 Scattering from a single nuclide: ^{1}H, ^{16}O, and ^{56}Fe

For the first example, consider the scattering of neutrons from three important nuclides in LWR shielding analyses: ^{1}H, ^{16}O, and ^{56}Fe. Legendre expansions of data from the BUGLE-B7 library are compared with scattering distributions obtained using cosine- and energy-binned current tallies for singly scattered neutrons from MCNP simulations in which a monodirectional beam of neutrons impinges on a target of the isotope being studied. This simulation provides an accurate representation of the angular scattering distribution from one BUGLE group to another. The MCNP calculations are run using CE cross-section data. The BUGLE-B7 group structure is imposed on the MCNP simulation using a neutron source with a uniform strength over the energy range of the source group, as well as tallied data with energy ranges over the sink groups. The true group-to-group scattering angular distributions from these CE MCNP calculations are shown by blank lines.

Figure D-2 illustrates the CE tally data and the Legendre polynomial expansions of the angular distributions for scattering from ^{1}H for groups 1-to-1, 1-to-2, 1-to-3, 1-to-10, 1-to-18, and 1-to-26. Because all scattering from ^{1}H is elastic, the permissible range of ω values is prescribed by Eq. (D-1) and Eq. (D-2). For each of these scattering distributions, the range of permissible ω values is quite narrow, resulting in highly anisotropic MG scattering distributions. This is reflected in the CE scattering distributions. It can also be seen that for narrow, highly peaked scattering distributions, such as for groups 1-to-10, 1-to-18, and 1-to-26, even a P_7 Legendre expansion (the highest order available in the BUGLE-B7 library) provides a poor representation of the true scattering behavior.

For each of the ^{1}H scattering distributions plotted in Figure D-2, every expansion order (with the exception of the P_1 expansion for scattering from group 1-to-18 and group 1-to-26) has regions in which the Legendre expansion produces negative cross-section values. These negative regions, which are a mathematical artifact of the Legendre expansion, can produce nonphysical behavior in MG flux solutions.

Figure D-3 shows the group-to-group scattering distributions for the same energy groups (1, 2, 3, 10, 18, and 26) for ^{16}O. Note that both elastic and inelastic scattering can occur from ^{16}O, with inelastic scattering being responsible for all scatters from group 1 to group 4 and lower energy groups (Figure B-3). Because there is no elastic scattering occurring from group 1 to groups 10, 18, and 26, it is not surprising that those scattering distributions are much less anisotropic.

Figure D-4 shows the group-to-group scattering distributions for the same energy groups (1, 2, 3, 10, 18, and 26) for ^{56}Fe. As is the case with ^{16}O, inelastic scattering of neutrons is possible for all of these group-to-group transfers and is responsible for scattering into all groups below group 2 (Figure B-4). Consequently, the anisotropy for scattering from group 1 is most pronounced for scattering into groups 1 and 2, and the higher-order Legendre expansions approximate the CE MCNP results much more closely than those from lighter elements.

In-group scattering angular distributions (as opposed to group-to-group) are shown in Figure D-5 for ^{1}H, ^{16}O, and ^{56}Fe in groups 1 and 30. These two groups have equivalent lethargy widths[6] of 0.2, so the range of permissible scattering angles in ^{1}H is equivalent for group 1-to-1 and group 30-to-30. For ^{16}O, with an inelastic scattering threshold of 6.475 MeV, Eq. (D-1) and Eq. (D-2) are valid for group 30, but not for group 7. For ^{56}Fe, the condition of Eq. (D-3) is not met for group 30 (which is below the inelastic scattering threshold of 862.5 keV), so Eq. (D-1) and Eq. (D-2) are not valid.

The following observations can be made from Figure D-2 through Figure D-5:

1. Neutron scattering from ^{1}H in MG libraries is highly anisotropic at all energies. Because of the scattering angle limitations for elastic scattering (which is the only type of scattering that occurs in ^{1}H), the range of permissible scattering angles is narrow, which is a major source of the scattering anisotropy. In addition, it can be seen that even a scatter from BUGLE-B7 group 1 to group 18 (the group with a lower energy limit of 1.0026 MeV) is a forward scatter, which means that the scattering angle is less than 90°. In fact, scattering kinematics indicate that there is no backscattering of neutrons from ^{1}H at any energy. The only way in which a neutron can change its direction by more than 90° when the scattering occurs from ^{1}H is through multiple small angle scatters.
2. For ^{16}O and ^{56}Fe, MG neutron scattering cross sections generally exhibit decreasing anisotropy as neutron energies decrease. This is seen in downscattering cross sections (Figure D-3 and Figure D-4) and in within group scattering (Figure D-5). In addition, the degree of anisotropy for a given group-to-group scattering cross section tends to decrease with increasing mass of the scattering nucleus.
3. With the exception of in-group scattering in high-energy groups and downscattering to adjacent groups, the scattering angular distributions for ^{16}O and ^{56}Fe are well represented by P_3 Legendre polynomial expansions. For ^{1}H, all of the scattering expansions show marked differences as the expansion order is increased. This suggests that the sensitivity of an MG transport calculation to scattering order should be most pronounced for transport through hydrogenous material such as water or concrete. Neutron transport through metal regions is unlikely to be sensitive to scattering expansion orders greater than P_3.

These observations are consistent with the discussion in Section D.1 .

[6] The lethargy width of an energy group g in an MG library is defined as $\Delta u = ln(E_g/E_{g+1})$. MG structures are often defined based on lethargy widths.

D.3.2 Scattering from three common materials in LWR shielding analyses: water, concrete, and steel

This section addresses three common materials in LWR shielding analyses: water, concrete, and steel. The compositions of these materials are provided in Table D-1.

Table D-1 Composition of the water, concrete, and RPV steel used for the scattering angular distribution plots in Figure D-6 through Figure D-8. Elemental compositions are listed in units of atoms/b-cm (1 b-cm = 10^{-24} cm^2)

Element	Water	Type 04 concrete	RPV steel
H	4.9540E-2	7.7671E-3	
C			9.8100E-4
O	2.4470E-2	4.4076E-2	
Na		1.0478E-3	
Mg		1.4866E-4	
Al		2.3882E-3	
Si		1.5910E-2	3.7100E-4
S		5.6343E-5	
K		6.9312E-4	
Ca		2.9151E-3	
Cr			1.2700E-4
Mn			1.1200E-3
Fe		3.1273E-4	8.1900E-2
Ni			4.4400E-4

The scattering distributions for these materials are shown in Figure D-6 through Figure D-8 for the water, concrete, and RPV steel, respectively. As expected, the behavior of these distributions is consistent with those shown for ^{1}H, ^{16}O, and ^{56}Fe. The scattering distributions for water are highly anisotropic and are very sensitive to the Legendre expansion order. Consistent with the scattering distributions for ^{1}H, the higher-order expansions (greater than P_1) all have regions in which the scattering expansion has negative values. The primary constituents of Type 04 concrete by atom fraction are O, Si, and H. Type 04 concrete exhibits a high degree of anisotropy, although not as pronounced as the water. Unlike the scattering distributions for water, the concrete data exhibit very few angular regions for cases in which the expansions are negative. The RPV steel consists primarily of Fe, which has an ^{56}Fe atom fraction of 91.754%. Therefore, its scattering distributions are nearly identical to those of ^{56}Fe.

D.4 Implications for Multigroup Neutron Transport Calculations

The material discussed in Sections D.1 and D.2 and the examples provided in Section D.3 have clear implications for MG neutron transport calculations used in LWR shielding analyses. Light nuclides, particularly ^{1}H, exhibit a high degree of scattering anisotropy due to scattering kinematics. In addition, the use of MG cross-section libraries imposes restrictions on the permissible scattering angles for group-to-group transfers. Therefore, the sensitivity of a MG neutron calculation should be highest in regions that are characterized by deep penetration through hydrogenous materials, including water and concrete.

For RPV fluence calculations with typical LWR configurations in the beltline region, Regulatory Guide 1.190 requires a minimum P_3 expansion order. As shown in Figure D-4, the scattering distributions for ^{56}Fe in the BUGLE-B7 library are fairly well approximated for this case within the beltline region.

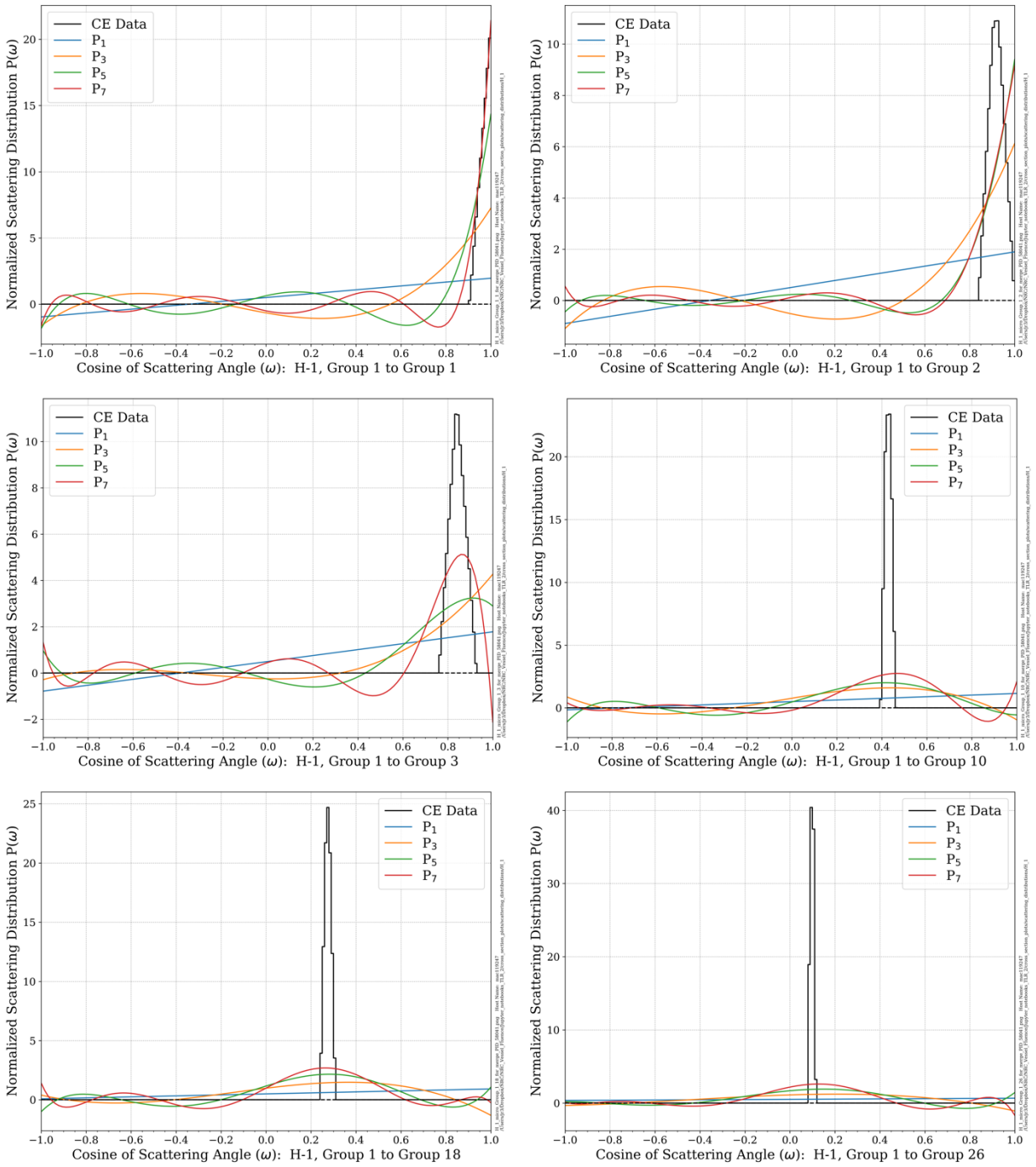

Figure D-2 Group-to-group angular scattering distributions for ^{1}H from the BUGLE-B7 library as a function of scattering order from P_1 to P_7. The group energy boundaries and lethargy widths can be found in Table B-2. The CE data are based on cosine- and energy-binned tallies for singly scattered neutrons from an ^{1}H target

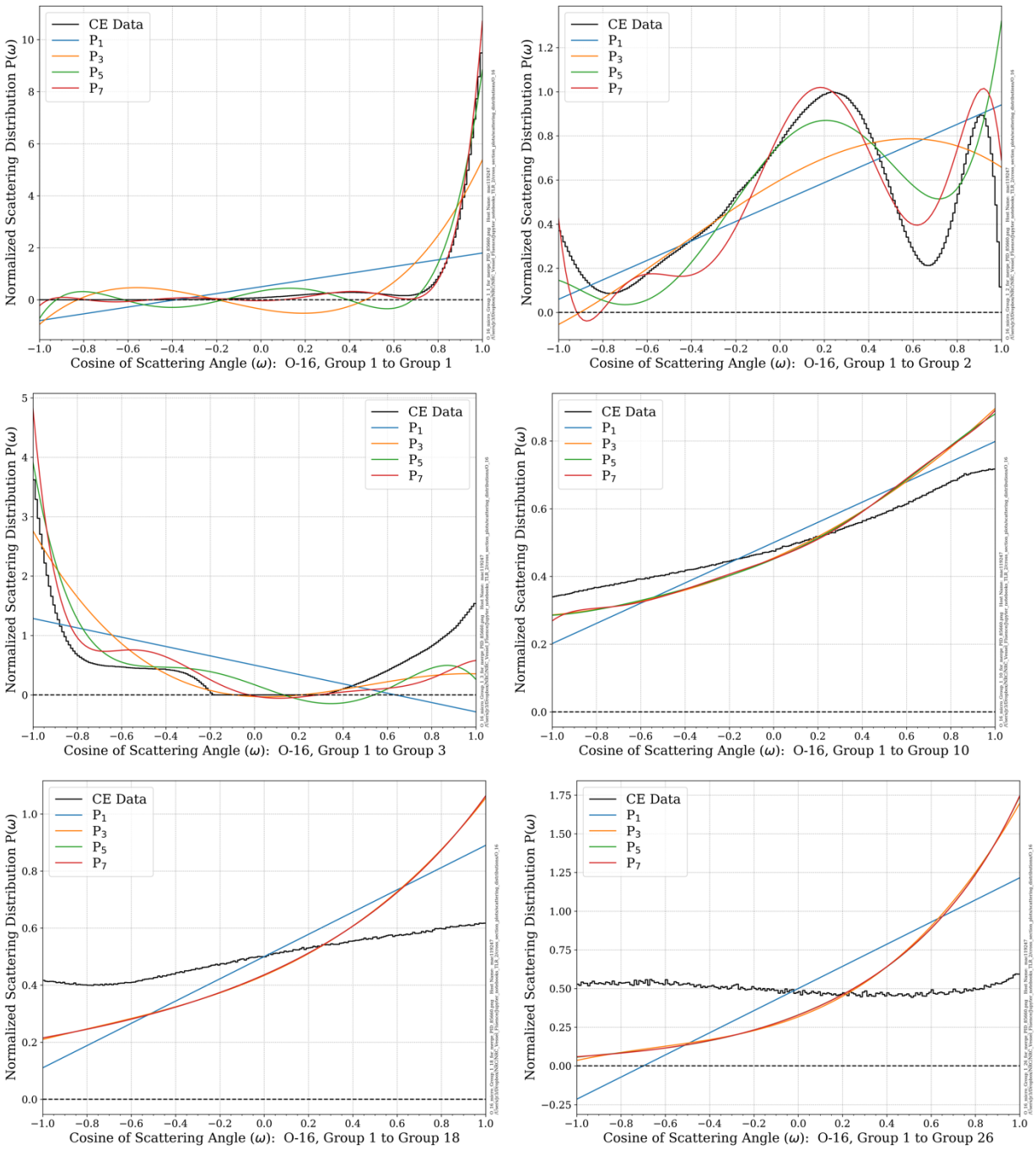

Figure D-3 Group-to-group angular scattering distributions for ^{16}O from the BUGLE-B7 library as a function of scattering order from P_1 to P_7. The group energy boundaries and lethargy widths can be found in Table B-2. The CE data are based on cosine- and energy-binned tallies for singly scattered neutrons from an ^{16}O target

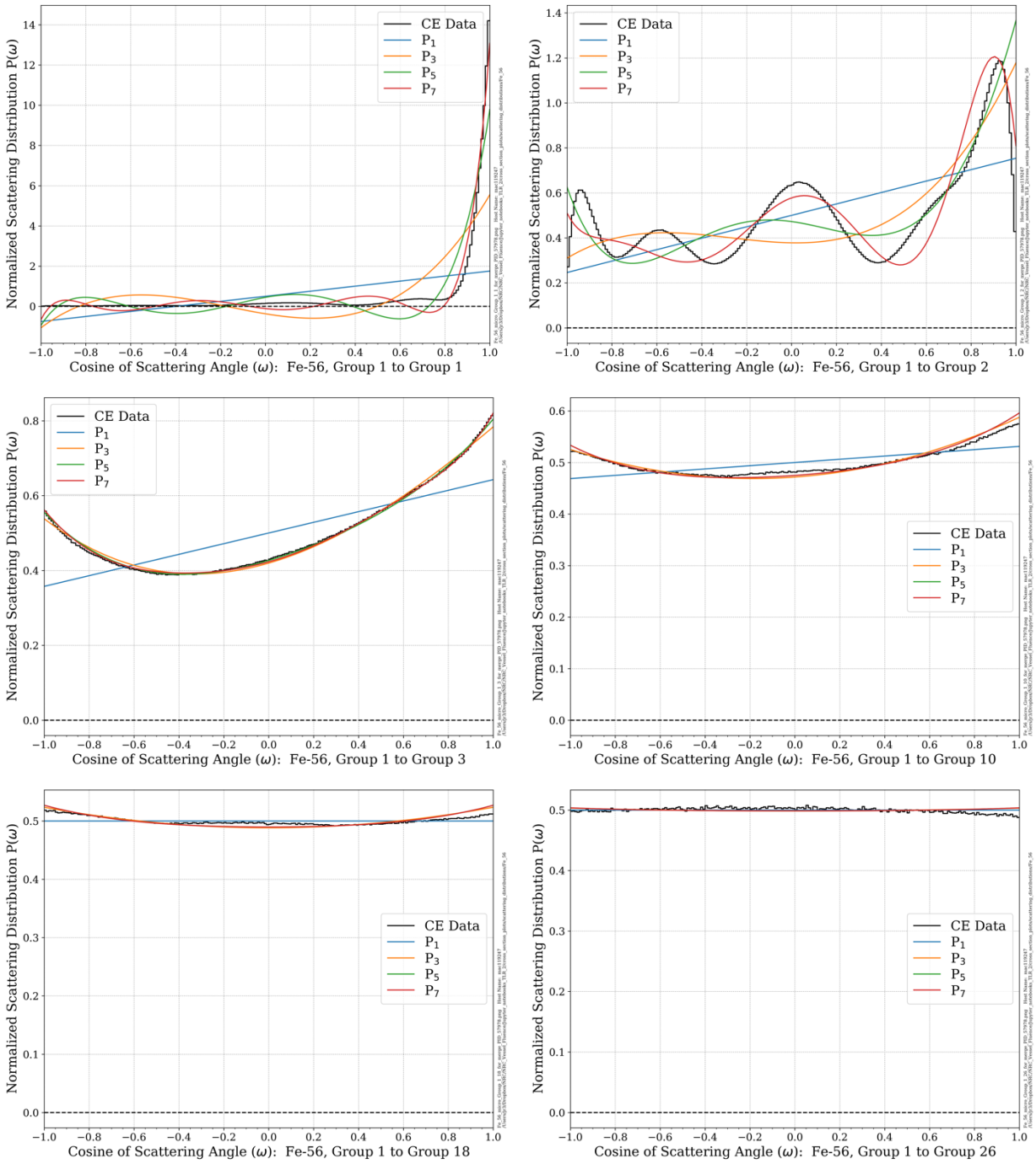

Figure D-4 Group-to-group angular scattering distributions for ^{56}Fe from the BUGLE-B7 library as a function of scattering order from P_1 to P_7. The group energy boundaries and lethargy widths can be found in Table B-2. The CE data are based on cosine- and energy-binned tallies for singly scattered neutrons from an ^{56}Fe target

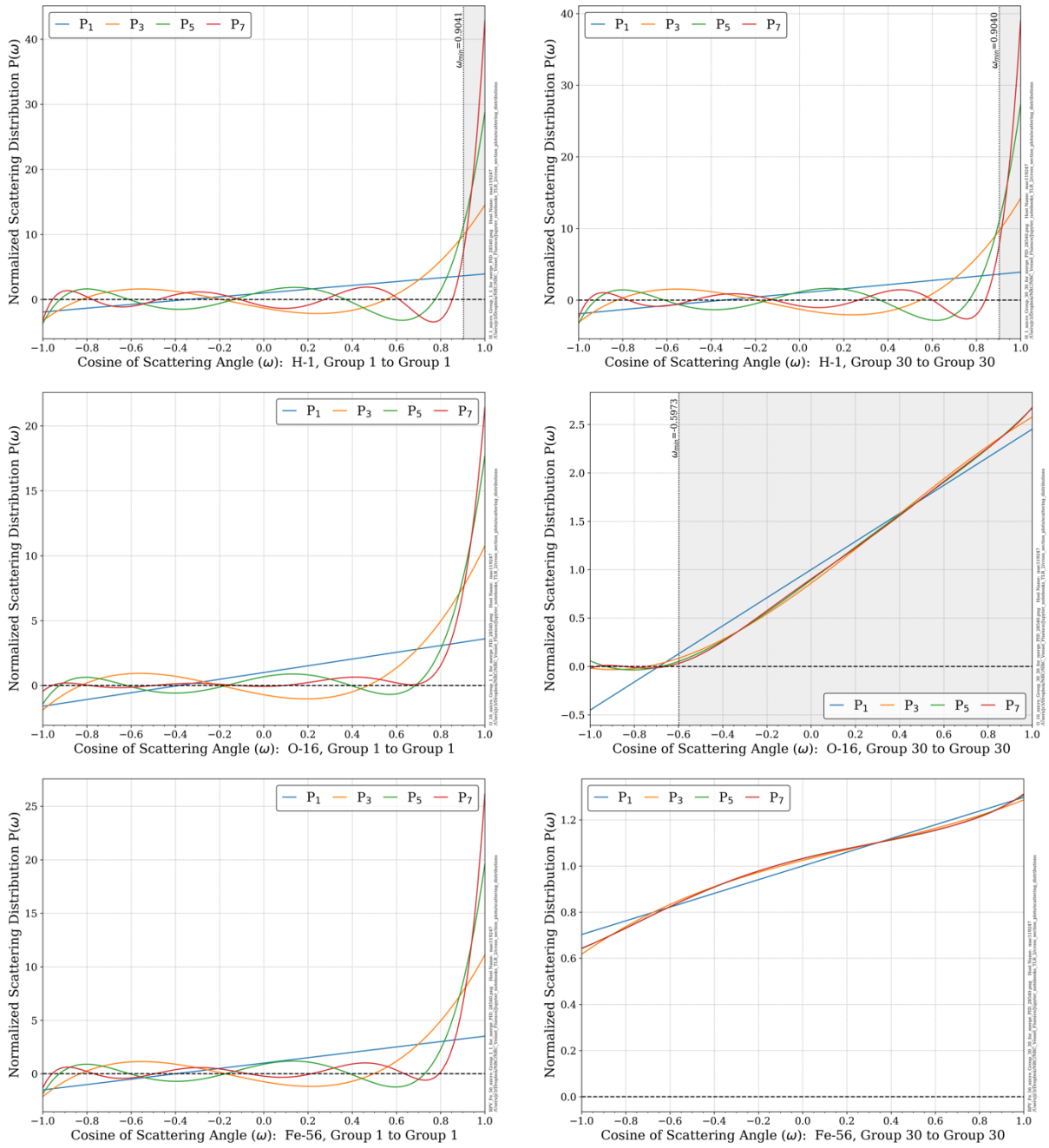

Figure D-5 In-group angular scattering distributions for ^{1}H, ^{16}O, and ^{56}Fe in groups 1 and 30 of the BUGLE-B7 library as a function of scattering order from P_1 to P_3. The group boundaries are Group 1, 17.332–14.191 MeV; and Group 30, 31.828–26.058 keV. The areas shaded in gray for ^{1}H and ^{16}O represent the range of permissible scattering angles based on Eq. (D-1) and Eq. (D-2)

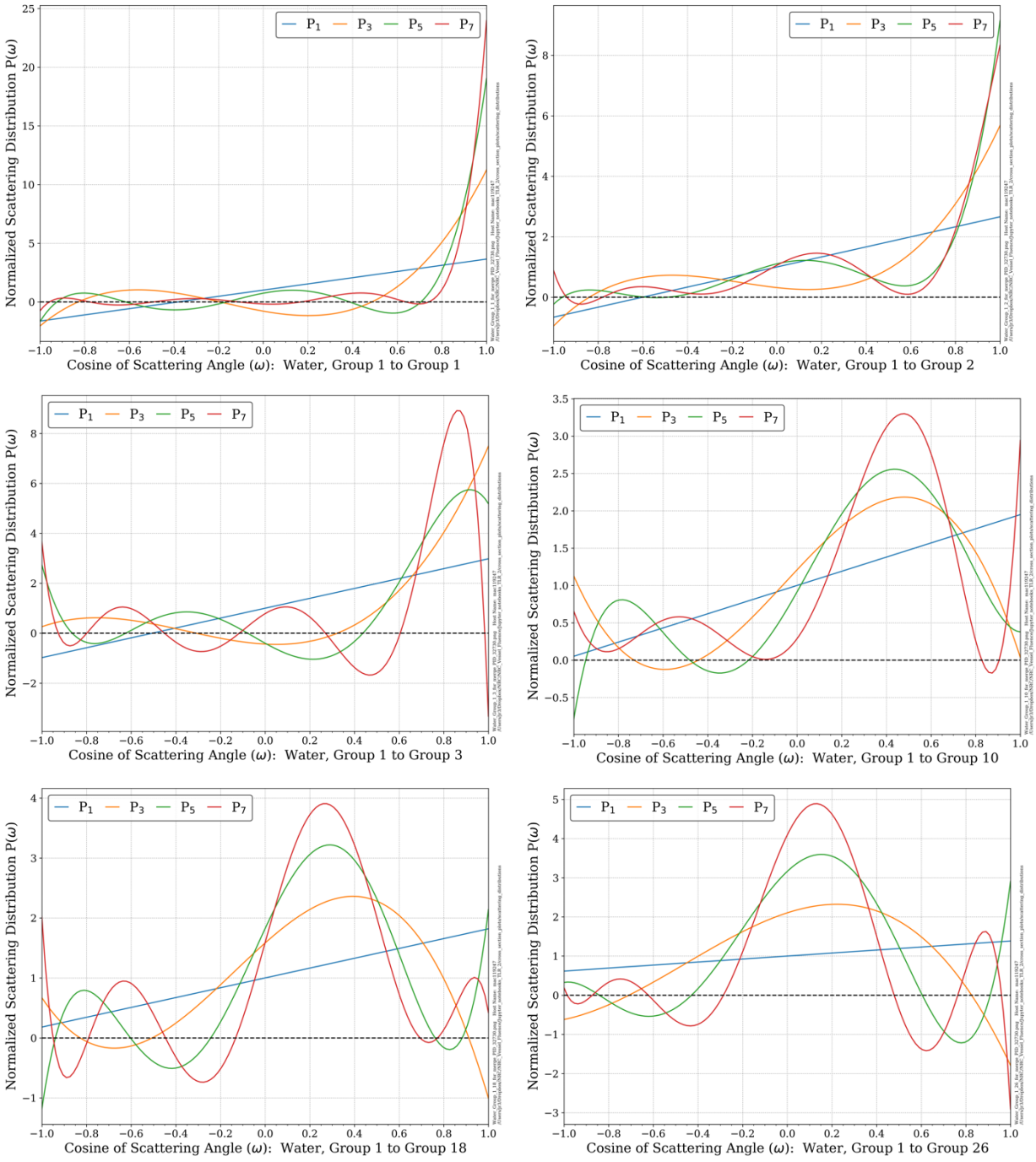

Figure D-6 Group-to-group angular scattering distributions for water from the BUGLE-B7 library as a function of scattering order from P_1 to P_7. The group energy boundaries and lethargy widths can be found in Table B-2

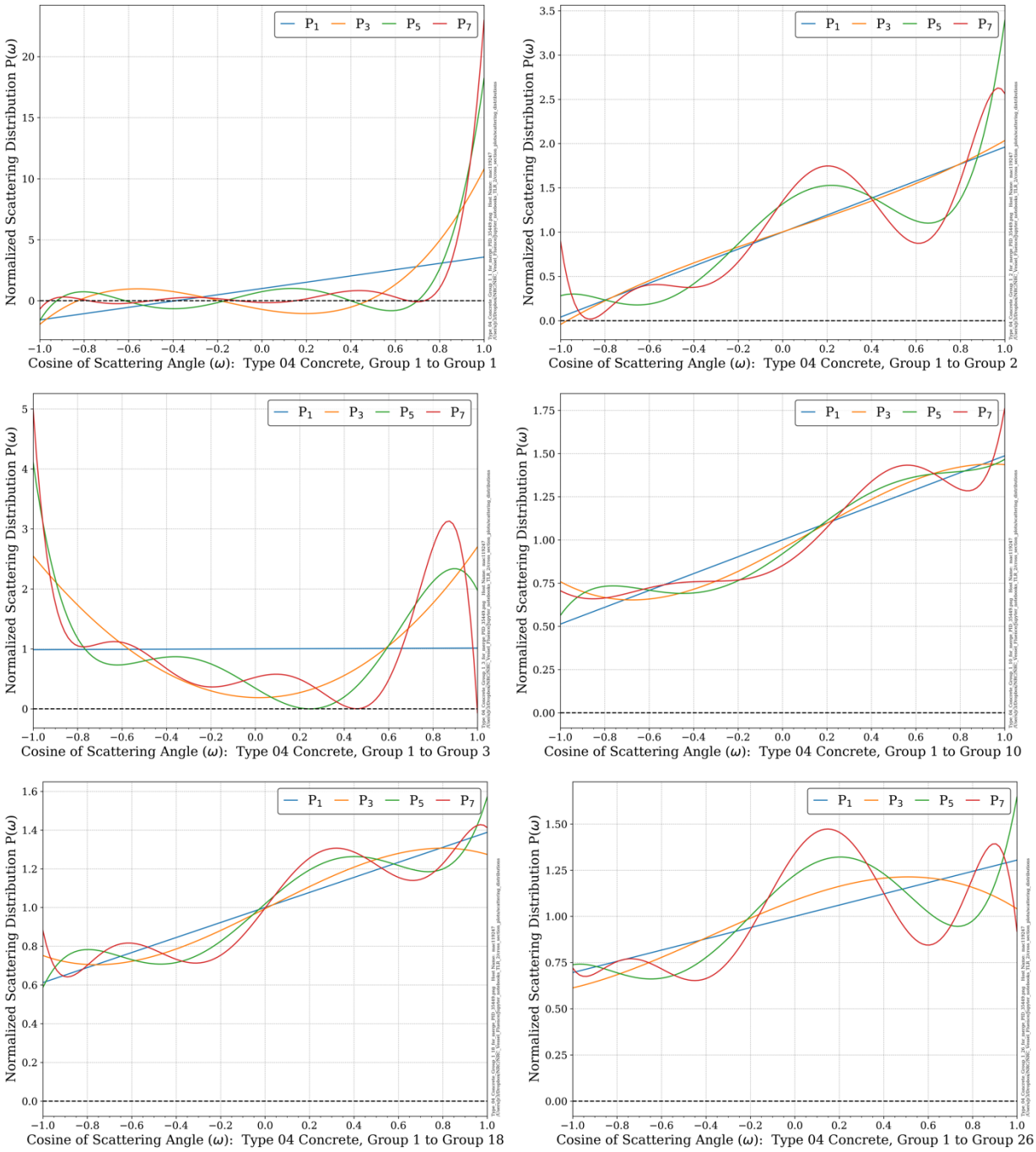

Figure D-7 Group-to-group angular scattering distributions for Type 04 concrete from the BUGLE-B7 library as a function of scattering order from P_1 to P_7. The group energy boundaries and lethargy widths can be found in Table B-2

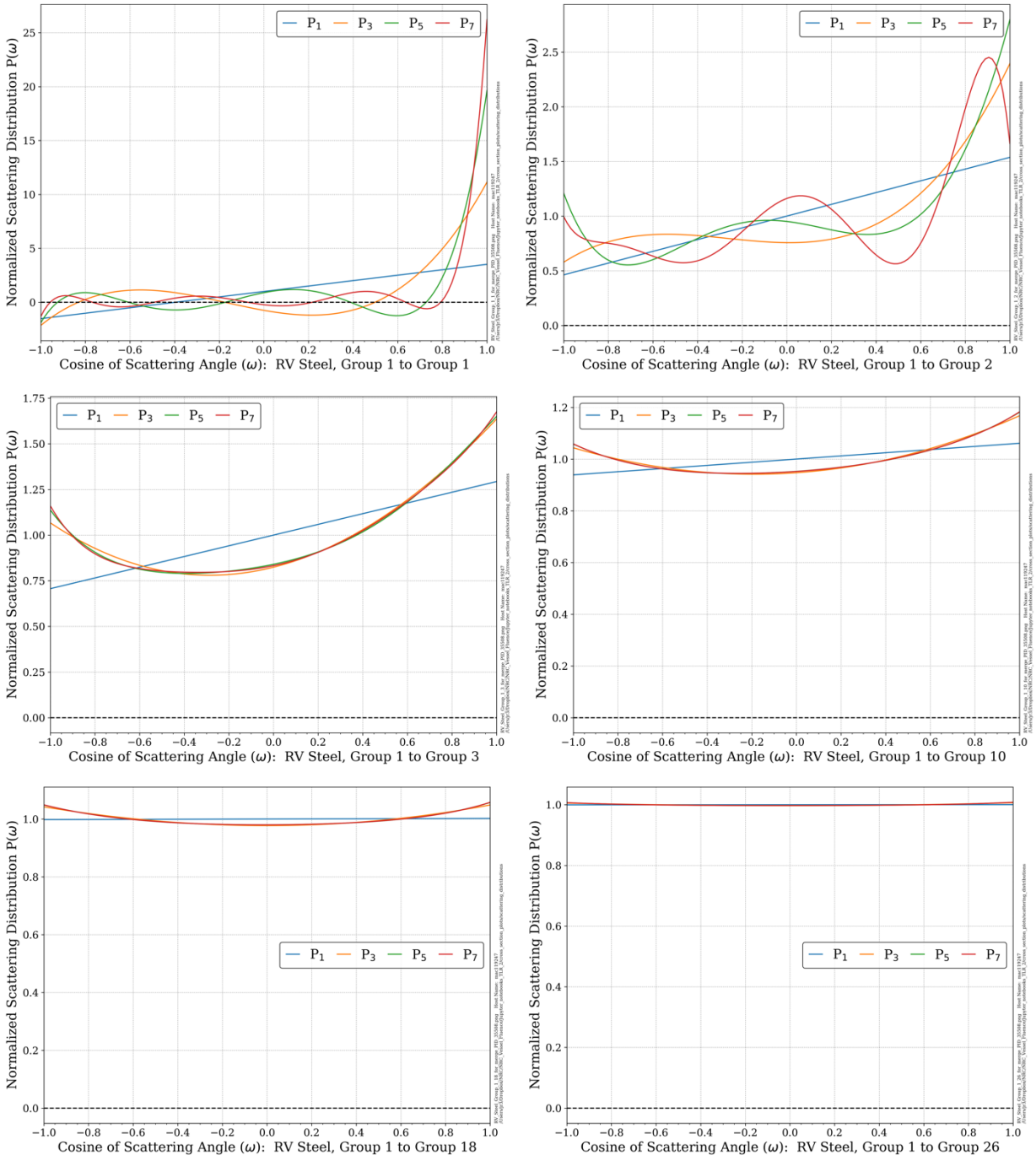

Figure D-8 Group-to-group angular scattering distributions for RPV steel from the BUGLE-B7 library as a function of scattering order from P_1 to P_7. The group energy boundaries and lethargy widths can be found in Table B-2